Analytical Modelling of Microstrip Travelling Wave Antennas

Thesis Submitted by Kaushik Patra

Doctor of Philosophy (Engineering)

Department of Electronics and Telecommunication Engineering
Faculty Council of Engineering and Technology
Jadavpur University, Kolkata, India

2018

JADAVPUR UNIVERSITY

KOLKATA – 700 032, INDIA

INDEX NO. 133/15/E

1. **Title of the thesis:** Analytical Modelling of Microstrip Travelling Wave Antennas
2. **Name, Designation & Institution of the Supervisors:**

Supervisor 1 : Professor Bhaskar Gupta

Professor, Electronics and Telecommunication Engineering Department

Jadavpur University, Kolkata – 700 032, West Bengal

Supervisor 2 : Dr. Sayantan Dhar

Assistant Professor, Electronics and Communication Engineering Department

Heritage Institute of Technology, Kolkata – 700 107, West Bengal

3. **List of publications :**

[1] "**Design Guidelines for Single and Dual Wide Band Leaky Periodic Microstrip Line Antennas**" by K Patra, S Dhar and B Gupta, accepted for publication in International Journal of RF and Microwave Computer Aided Design, February, 2018

[2] "**Transmission Line Model For Analysis Of Microstrip Travelling Wave Antennas With Right Angled Bends**", by Kaushik Patra, Sayantan Dhar and Bhaskar Gupta, *AEÜ - International Journal of Electronics and Communications*, Vol. 84, pp. 375-86, February 2018.

[3] "**Analysis of Arbitrarily Curved Microstrip Lines for Radiated Emission**" by Kaushik Patra, Sayantan Dhar and Bhaskar Gupta, *IEEE Transaction on Electromagnetic Compatibility*, vol. 60, No. 3, pp. 572-79, June 2018.

4. **List of patents :** Nil

5. **List of Presentations in National / International Conferences:**

[1] **"Radiation from simple and perturbed arbitrarily curved microstrip lines,"** by K Patra, S Dhar and B Gupta, *2016 Asia-Pacific Microwave Conference (APMC)*, New Delhi, December, 2016, pp. 1-4

CERTIFICATE FROM THE SUPERVISORS

This is to certify that the thesis entitled "**Analytical Modelling of Microstrip Travelling Wave Antennas**" submitted by **Shri Kaushik Patra,** who got his name registered on **14th August 2015** for the award of Ph.D. (Engg.) degree of Jadavpur University is absolutely based upon his own work under the supervision of **Prof. Bhaskar Gupta**, Department of Electronics and Telecommunication Engineering, Jadavpur University, Kolkata and **Dr. Sayantan Dhar**, Department of Electronics and Communication Engineering, Heritage Institute of Technology, Kolkata and that neither his thesis nor any part of the thesis has been submitted for any degree/diploma or any other academic award anywhere before.

1. _____

Signature of the Supervisor and date with Official Seal

2. _____

Signature of the Supervisor and date with Official Seal

Acknowledgement

The road up to this point has been long and the journey quite rewarding in itself. Everybody who I came in touch with during this time, I consider them to be, my travelling companion of sorts. I would like to take this opportunity to thank and acknowledge all my travelling companions.

Firstly I would like to express my deepest and sincerest gratitude to my supervisors Prof. Bhaskar Gupta and Dr. Sayantan Dhar. I am grateful to Prof. Gupta for his constant support and encouragement over the years. His simple approach to a problem of any order of difficulty has really untangled several knots in my own head. His Zen-like patience and the trust he has on his students have made a deep impact. I am thankful to Dr. Dhar for helping me at every turn. He has been like an elder brother. Oddest of times, most idiotic of questions, myriad of demands – He tackled with a smile and tried his best to keep the wheels from rolling down the slope.

I am grateful to all the faculty members of the Department of Electronics and Telecommunication Engineering, Jadavpur University for providing me with valuable suggestion. Advice from Prof. D R Poddar, Prof. S B Roy, Prof. Sayan Chatterjee, Prof. M Biswas, Prof. A Konar have really helped at all times. Technical discussions with Prof. A K. Bandyopadhaya and his evening classes have really enriched and motivated me.

The entire duration of my research has been carried out in Microstrip lab, Jadavpur University. I take this opportunity to acknowledge the help I received from the research scholars and post-graduate scholars I came in touch with. Proceeding chronologically I would like to thank Dr. S Sankaralingam, Mr. Sharanbasappa Belamgi, Mrs. Ayona Chakraborty, Dr. Rajeev Wakodkar, Dr. Sanghamitra Dasgupta, Dr. Sriparna Bhattacharya, Dr. Arkaprovo Das, Dr. Amrita Chakraborty, Dr. Arindam Deb, Mr. Sumit Mitra,

Dr. Buddhadev Pradhan, Mr. Ardhendu Kundu, Mr. Mishor Biswas, Mrs. Rinki Ghoshal, Mr. Joydeep Pal, Ms. Baisakhi Banerjee are a few to name.

Mr. Arka Bhattacharyya and Mr. Suman Pradhan deserve special thanks for their insightful technical discussions. Discussion with Dr. Sudipta Maity over theoretical and measurement issues has really been fun and enriching.

Special mention of a few names must be made. Dr. Rajendra Prosad Ghosh had been, since the time of my post graduation, a person who I would ask any problems – He never said no and never got irritated. I learned a lot from him. Another person would be Mr. Amartya Banerjee. His selfless nature has time and again forced me to introspect.

Finally, this acknowledgement will not be complete without recognizing the support I have received from my family. Insane timing of works, negligible contribution to the household, living almost a detached life – they have weathered with great patience. Without the blessings of my parents, I could not have been what I am now.

Kaushik Patra

Contents

List of Figures

List of Tables

Chapter 1

Introduction

Contents	
	1.1. Preface 1.2. Travelling wave antennas: what and why 1.3. Leaky wave antennas: what and why 1.4. Analysis efforts 1.5. Motivation of the thesis 1.6. Novel aspects 1.7. Thesis outline

1.1 PREFACE

Travelling wave antennas as a part of a receiving system dates back to the early 1920s when H H Beverage [1] used a very long horizontal wire over earth to receive wireless signals across the Atlantic. This long wire "travelling wave antenna" was commissioned by Radio Corporation of America for trans-Atlantic communication through long waves at 10 KHz to 100 KHz frequency range. This has been the oldest known application of such travelling wave antennas. Since then this class of antennas have evolved immensely to delve into the domains of microstrip [2-4], waveguide [5, 6] and hybrid planar waveguide technologies [7], bringing with it great advantages of frequency controlled beam steering [2-7], low interference [1] and polarization agility [8, 9] among many others.

1.2 TRAVELLING WAVE ANTENNAS: WHAT AND WHY

Semantically, "travelling wave antennas" denote a class of antennas where the current distribution on the antenna length/surface/volume is of travelling wave type [10]. Unlike conventional resonant antennas where a spatial variation of field magnitude is created at the frequency of resonance, the travelling wave antennas

exhibit a spatial distribution of phase of the internal fields instead of the magnitude. Field magnitude remains essentially constant along such antenna leading to an inherent wideband nature while the phase variation gives rise to beam steering with frequency [11]. The internal electric and magnetic fields are in these cases mostly of a slow wave nature bound in the structure to a Quasi TEM mode of propagation. All slow wave structures being essentially non-radiating in nature, they require open or semi open structures with considerable introduction of discontinuities for substantial radiation to occur. Higher order modes generated near such discontinuities tend to become "fast" locally and eventually contribute to the total radiation from such structures. Typical examples of these kind of slow wave based travelling wave antennas are long wire antenna [12], rhombic antenna [13], bend based microstrip line antennas (Rampart line [8], Crank line [9], Franklin line antennas [14]) etc.

As is evident from the radiation mechanism itself, these travelling wave antennas tend to exhibit very interesting properties. In most cases, the antenna is excited from one end and the other end is terminated in matched impedance. This gives rise to wide impedance bandwidth as well as minimized load reflections resulting in reduced side lobe levels. This is a very interesting feature in designing receiving systems with lower interference. The most remarkable feature of a travelling wave antenna is its beam scanning with frequency. This feature along with controllable scan rate [15] (by controlling the amount of loading) and narrow beam width (using a longer antenna length) is very suitable for use in radar [16] and microwave imaging applications [17]. Finally, it has been shown by P S Hall [8] and Nakano *et. al.* [9] that some of these travelling wave arrays can very easily be designed to obtain circular polarization without incorporation of complicated feed networks or tedious geometry modifications.

1.3 LEAKY WAVE ANTENNAS: WHAT AND WHY

Leaky wave antennas are a special group of antennas inside the travelling wave antenna family that have some distinctive features forcing them to be recognized independently. Based mostly on microstrip [3, 18], semi-open waveguide [15] and hybrid-waveguide technologies [19], these antennas are of the fast wave nature. The internal electric and magnetic fields are loosely bound to the structure through a higher order mode with a leaky region just above the cut off frequency of the concerned mode [18]. The fast wave nature of the structure allows power to radiate all along the length of the structure without necessitating the introduction of discontinuities. In microstrip configuration, there are two different sub classes of the leaky wave antenna, namely the uniform leaky wave antenna [3, 20] and the periodic leaky wave antenna [21, 22]. In case of the uniform leaky wave antenna, a higher order microstrip line mode (TE_{01} [23] or TE_{02} [24] mostly) is excited in the structure and the leaky region near cut off is utilized. In case of the periodic leaky wave antenna on the other hand, a propagating mode bound to the structure is perturbed using periodic loads. Dictated by the Floquet theorem, a bunch of spatial harmonics are generated some of which enter the leaky fast wave region and tend to radiate substantially [25].

Starting with the first leaky wave antenna introduced by W Menzel [3] and successful analysis by A A Oliner [18], they have since been applied in multitude of applications ranging from beam steering in automotive radar, near field focusing arrays, multi-beam antennas and many others.

1.4 ANALYSIS EFFORTS

Among all the configurations of both travelling wave and leaky wave antennas the ones based on microstrip technology have become the most popular one owing to their ease of fabrication, conformal nature and simplicity in design and analysis. Analysis techniques based on transmission line model [8, 26] and

circuit based techniques [27] have been popular for Quasi TEM mode based travelling wave antennas. Subsequently some full wave techniques based on MoM [28] technique have also been applied afterwards. On the other hand leaky fast wave antennas were initially analyzed using a hybrid transmission line-cavity model by Menzel [3] but later on steepest descent techniques [18] and rigorous full wave techniques [29] were preferred for complete description of the complex nature of the leaky wave fields.

1.5 MOTIVATION OF THE THESIS

Recent advancement of radar technologies and fast growing requirement of automotive and vehicular radars have necessitated the use of antennas capable of beam scanning with frequency as well as scanning at constant frequency. Complications in designing the feed networks of phased array antennas have naturally put travelling wave antennas to the task.

In this context, travelling wave antennas based on Quasi TEM mode based slow wave type have become a major candidate. As was discussed earlier, introduction of discontinuities of non-periodic or periodic nature is a must for such antennas. Consequently, bent and non uniform microstrip lines have been used to cater to applications demanding beam steering, polarization agility and wide impedance bandwidth. Our work aims at development of analytical models capable of analyzing such bent and non uniform microstrip line based antennas in an approximate manner while describing the underlying physics in comprehensive detail. To this end, we start with a simple transmission line model for microstrip line antennas with right angle bends and thereafter introduce empirical models for acute and obtuse angle bends and finally interface a simple model for inter-segment mutual coupling into the transmission line model. This leads to a comprehensive transmission line model with very wide applicability. The propagation constant along the microstrip line however becomes spatially varying

when the bends become continuous instead of discrete i.e. for an arbitrarily curved microstrip line. There is very little literature apart from some full wave analysis efforts and some analytical developments for curved and twisted waveguides by Lewin [30]. We have developed a mode matching based rigorous technique for analyzing arbitrarily curved microstrip lines supporting both fundamental Quasi TEM as well as higher order modes. As a natural extension, non uniform microstrip lines came up next. Most of the literatures available for such lines have used various techniques for solving one dimensional non linear Riccatti equations thereby ignoring any transverse field variation completely. Such minimal transverse fields are hardly the case for an antenna application. We applied the mode matching technique for analyzing arbitrarily non uniform microstrip lines supporting fundamental or higher order modes.

Finally, there has been a very rapid expansion in the leaky wave antenna domain focusing on periodic leaky wave antennas. In recent years several periodic leaky wave antennas in microstrip configuration have been developed based mainly on slot or stub loading. These works have focused on designing leaky wave antennas with multiband or specific beam scanning behavior. Most of the analysis is dependent on either simplified ABCD matrix technique or very tedious full wave technique. The ABCD matrix technique is heavily reliant on some simplified circuit model of the periodic antenna which is not always available or is difficult to formulate (for example, in case of a microstrip line supporting the first higher order mode loaded periodically with open stubs or in case of a half width ladder line). We have addressed this problem by developing a technique combining the mode matching technique and Floquet modal theorem for analyzing the dispersion characteristics of periodically perturbed microstrip line supporting fundamental or higher order modes.

In the end, design guidelines are outlined for designing microstrip leaky wave antennas based on dual stubs (open and shorted) with single or dual wideband behavior.

1.6 NOVEL ASPECTS

Following are the novel aspects aimed at this thesis:

- Development of a transmission line model capable of analyzing any bend based microstrip travelling wave antenna.
- Development of mode matching based techniques for analyzing arbitrarily curved and non-uniform microstrip line antennas.
- Analysis and observation of the dispersion characteristics for periodically loaded, width modulated and non uniformly periodic microstrip lines and applying the same for perturbing the radiation characteristics of a Rampart line antennas.
- Development of a mode matching and Floquet theorem based technique for analyzing the dispersion characteristics of single/multiple stub loaded microstrip lines, half width ladder line and SIW based periodic leaky wave antennas.
- Outlining design guidelines for wideband leaky wave antennas with frequency beam steering.

1.7 THESIS OUTLINE

This thesis presents a comprehensive theoretical analysis approach suitable for microstrip travelling wave and leaky wave antennas. Analytical models are developed for discretely bent and arbitrarily curved microstrip lines, arbitrarily non uniform microstrip lines as well as for periodic leaky wave

antennas. A brief historical perspective along with a basic introduction to the working of travelling wave antennas as well as a leaky wave antenna is presented in Chapter 1.

Chapter 2 is divided in two parts. The first part deals with a brief account of the development of Quasi TEM mode based microstrip travelling wave antennas. Different analytical and computational techniques used over the years for such slow wave travelling wave antennas are discussed. A reference to their practical applications has also been included. Chronological evolution of microstrip leaky wave antennas is presented in the second part of Chapter 2. Development of various uniform and periodic leaky wave antennas along with proposed applications is discussed. Different Analytical and numerical techniques for analyzing these antennas are outlined.

Chapter 3 presents a transmission line model for the analysis of bend based travelling wave antennas. First, the transmission line model considering local and load reflection is presented in the context of a right angle bend based microstrip line geometry. Next an empirical formula suitable for both acute and obtuse angle bends is derived to extend the model for inclusion of geometries with no-right angle bends.

The simplified transmission line model applicable to discretely bent microstrip lines can no more be used in case of a continuously curved microstrip line. The spatially varying curvature gives rise to spatially varying propagation constant in the line. This problem of analyzing arbitrarily curved microstrip lines is taken up in Chapter 4. First a piecewise linear technique is presented for lines with smaller curvature. Next, a rigorous mode matching based technique is utilized for curved microstrip lines with arbitrary curvature and arbitrary line width.

Chapter 5 deals with the problem of non uniform microstrip lines. First a Fourier series based technique is outlined for non uniform microstrip lines with smaller amount of non uniformity and smaller line width. A Quasi TEM mode of propagation is assumed and the telegrapher's equation is solved. Non uniform microstrip lines with arbitrary amount of non uniformity and arbitrary line width is analyzed in the latter part of this chapter. A rigorous mode matching based technique is used for field description and matching.

Chapter 6 onwards, the thesis concentrates primarily on microstrip leaky wave antennas. A brief account and comparison of the dispersion characteristics of higher order modes in microstrip lines are presented. Higher order modes both in a uniform and a periodic microstrip leaky wave antenna are discussed.

The problem of periodic leaky wave antenna is taken up in Chapter 7. A combination of mode matching and Floquet theory is used to calculate the dispersion characteristics and outline the leaky region for different periodic leaky wave antennas. Open and shorted stub loaded lines are considered. Perturbations of the fundamental as well as higher order modes due to introduction of periodicity are analyzed.

Chapter 8 is concentrated on the application of leaky wave antenna. Design guidelines are outlined for developing wideband leaky wave antennas based on dual stub loading of microstrip line to obtain single or dual beam behavior.

In the last chapter conclusions are drawn with brief discussion on future scopes in the domain of travelling and leaky wave antennas.

REFERENCES:

[1] H. H. Beverage, C. W. Rice and E. W. Kellogg, "The Wave Antenna A New Type of Highly Directive Antenna," in *Transactions of the American Institute of Electrical Engineers*, vol. XLII, pp. 215-266, Jan. 1923.

[2] J. R. James and P. S. Hall, "Microstrip antennas and arrays. Part 2: New array-design technique," in *IEE Journal on Microwaves, Optics and Acoustics*, vol. 1, no. 5, pp. 175-181, September 1977.

[3] W. Menzel, "A New Travelling Wave Antenna in Microstrip," *1978 8th European Microwave Conference*, Paris, France, 1978, pp. 302-306.

[4] C. Wood, "Curved microstrip lines as compact wideband circularly polarised antennas," *Microwaves, Optics and Acoustics, IEE Journal on* , vol.3, no.1, pp.5, January 1979.

[5] W. W. Hansen, *Radiating electromagnetic wave guide*. U.S. Patent 2,402,622. Leland Stanford Junior University, 1946.

[6] L. Goldstone, and A. A. Oliner, "Leaky-wave antennas I: Rectangular waveguides," *IRE Transactions on Antennas and propagation*, *7*(4), pp.307-319, 1959.

[7] A. J. Martinez-Ros, J. L. Gómez-Tornero, V. Losada, F. Mesa and F. Medina, "Non-Uniform Sinusoidally Modulated Half-Mode Leaky-Wave Lines for Near-Field Focusing Pattern Synthesis," *IEEE Transactions on Antennas and Propagation*, vol. 63, no. 3, pp. 1022-1031, March 2015.

[8] P. S. Hall, "Microstrip linear array with polarisation control," *Microwaves, Optics and Antennas, IEE Proceedings H* , vol.130, no.3, pp.215-224, April 1983.

[9] H. Nakano, T. Oka, K. Hirose and J. Yamauchi, "Analysis and measurements for improved crank-line antennas," IEEE Transactions on Antennas and Propagation, vol. 45, no. 7, pp. 1166-1172, Jul 1997.

[10] C. H. Walter, *Traveling wave antennas*. Dover Publications, 1970.

[11] W. L. Stutzman, and G. A. Thiele, *Antenna theory and design*. John Wiley & Sons, 2012.

[12] E. Bruce, E, "Developments in Short-Wave Directive Antennas," *Proceedings of the Institute of Radio Engineers* , vol.19, no.8, pp. 1406- 1433, Aug. 1931

[13] D. Foster, "Radiation from Rhombic Antennas," *Proceedings of the Institute of Radio Engineers* , vol.25, no.10, pp. 1327- 1353, Oct. 1937.

[14] S. Nishimura, K. Nakano, and T. Makimoto, "Franklin type microstrip line antenna," *Antennas and Propagation Society International Symposium, 1979*, Seattle, WA, USA, 1979, pp. 134-137.

[15] A. J. Martinez-Ros, J. L. Gomez-Tornero, and G. Goussetis, "Planar leaky-wave antenna with flexible control of the complex propagation constant," *IEEE Transactions on Antennas and Propagation*, *60*(3), pp.1625-1630, 2012.

[16] H. Moheb, L. Shafai and M. Barakat, "Design of 24 GHz microstrip travelling wave antenna for radar application," *IEEE Antennas and Propagation Society International Symposium. 1995 Digest*, Newport Beach, CA, USA, pp. 350-353 vol.1, 1995.

[17] C. Vázquez, C. García, Y. Álvarez, S. Ver-Hoeye and F. Las-Heras, "Near Field Characterization of an Imaging System Based on a Frequency Scanning Antenna Array," in *IEEE Transactions on Antennas and Propagation*, vol. 61, no. 5, pp. 2874-2879, May 2013.

[18] A. A. Oliner and K. S. Lee, "The nature of the leakage from higher modes on microstrip line," In *Microwave Symposium Digest, 1986 IEEE MTT-S International* (pp. 57-60), IEEE, June 1986.

[19] J. Liu, D. R. Jackson and Y. Long, "Substrate Integrated Waveguide (SIW) Leaky-Wave Antenna With Transverse Slots," in *IEEE Transactions on Antennas and Propagation*, vol. 60, no. 1, pp. 20-29, Jan. 2012.

[20] G. M. Zelinski, G. A. Thiele,M. L. Hastriter, M. J. Havrilla, and A. J. Terzuoli, "Half width leaky wave antennas,". *IET Microwaves, Antennas & Propagation*, *1*(2), pp.341-348, 2007.

[21] M. H. Rahmani, and D. Deslandes, "Circularly polarised periodic leaky-wave antenna with filtering capability," *IET Microwaves, Antennas & Propagation*, 2018.

[22] D. K. Karmokar, Y. J. Guo, P. Y. Qin, S. L. Chen, and T. S. Bird, "Substrate Integrated Waveguide-Based Periodic Backward-to-Forward Scanning Leaky-Wave Antenna with Low Cross-Polarization," *IEEE Transactions on Antennas and Propagation*, 2018.

[23] D. Xie, L. Zhu and X. Zhang, "An EH_0-Mode Microstrip Leaky-Wave Antenna With Periodical Loading of Shorting Pins," in *IEEE Transactions on Antennas and Propagation*, vol. 65, no. 7, pp. 3419-3426, July 2017.

[24] D. Xie, L. Zhu, X. Zhang and N. Liu, "Gain-enhanced EH_1 mode microstrip leaky-wave antenna with periodical loading of shorting pins," in *IET Microwaves, Antennas & Propagation*, vol. 12, no. 2, pp. 230-236, 7 2 2018.

[25] A. A. Oliner, "Radiating periodic structure: analysis in terms of k vs. β diagrams", in *Short Course on Microwave Field and Network Techniques,* Polytechnic Institute of Brooklyn, New York, 1963.

[26] M. Manteghi, A. Shooshtari, and S. Safavi-Naeini, "A leaky transmission line method for the analysis of the microstrip line traveling wave antennas," *IEEE Antennas and Propagation Society International Symposium*, vol. 2, pp. 1138-1141, Jul 1997.

[27] Y. Kami, and R. Sato, "Analysis of radiation characteristics of a finite-length transmission line using a circuit-concept approach," IEEE Transactions on Electromagnetic Compatibility, vol. 30, no. 2, pp. 114-121, May 1988.

[28] M. I. Aksun and R. Mittra, "Spurious radiation from microstrip interconnects," in *IEEE Transactions on Electromagnetic Compatibility*, vol. 35, no. 2, pp. 148-158, May 1993.

[29] F. Mesa, and D. R. Jackson, "Investigation of integration paths in the spectral-domain analysis of leaky modes on printed circuit lines" *IEEE transactions on microwave theory and techniques*, *50*(10), pp.2267-2275, 2002.

[30] L. Lewin, Electromagnetic Waves and Curved Structures, New York:IEEE Press, 1977, pp. 36.

Chapter 2

Literature Review

Contents

2.1 INTRODUCTION

Travelling wave antennas are a class of non resonant antennas that support a travelling wave type current distribution on the antenna surface. Excited from one end and usually terminated in the other, they exhibit beam scanning property, wide bandwidth, narrow beam-width and low side lobe levels. It is easy to obtain polarization agility using some form of travelling wave antennas. This class of antennas has expanded from its wire configuration in initial years through metallic waveguide, microstrip, coplanar waveguide, slot lines, dielectric guide. Many researchers have analyzed various configurations of travelling wave antennas while some have focused on the design and synthesis aspects.

2.2 INITIAL RESEARCH ON TRAVELLING WAVE ANTENNAS: HISTORICAL PERSPECTIVE

In 1923, Beverage and Peterson [1] were working on a method to measure electric field strengths at a large distance from the transmitter antenna and subsequently developed sensitive receivers toward that end. This was the beginning into what would later become one of the most distinct classes of

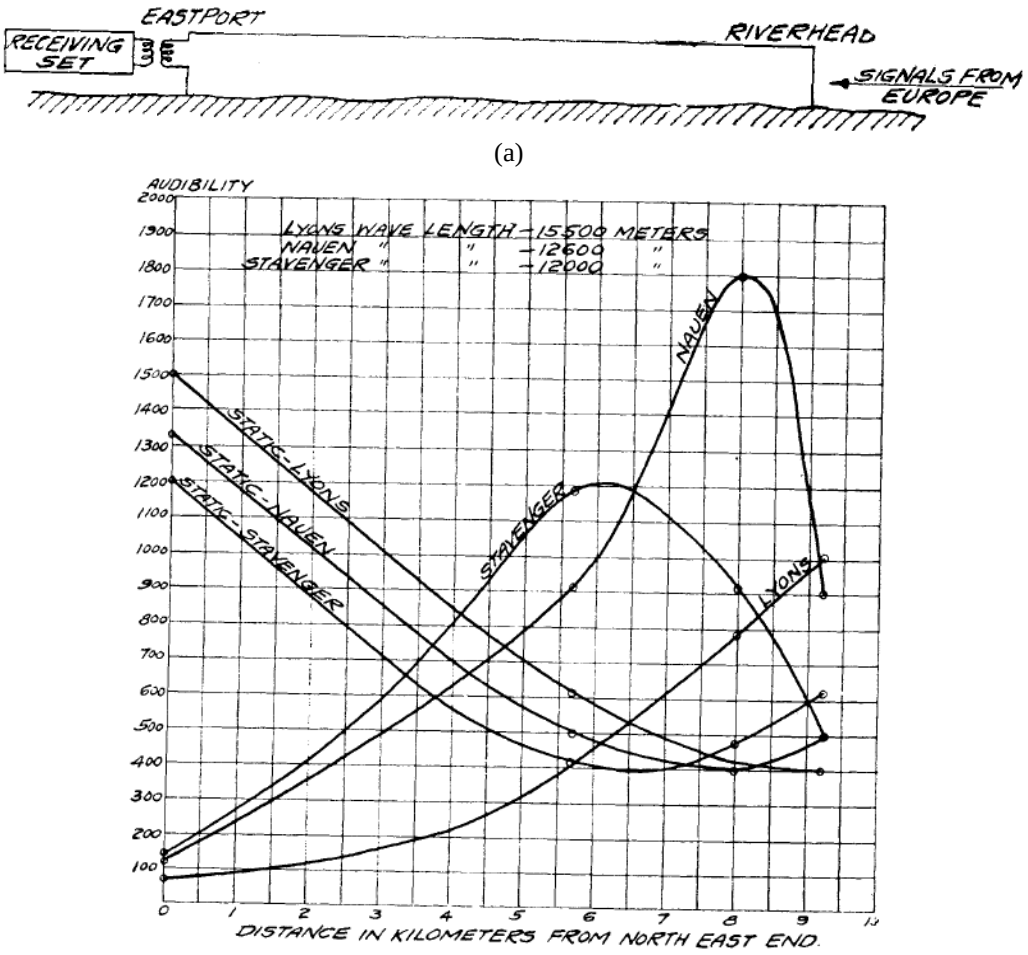

Fig. 2.1: (a) The Beverage antenna and (b) signal strength with distance along the antenna. [1] ©IEEE

antennas in the field of radio transmission. Later in the same year Beverage's group published an article [2] describing the "Atlantic coast ear of the Radio America for reception of wireless signals from England, France Germany and Norway". The antenna used was a very simple one: Two parallel wires supported by poles running over earth. He called this a 'ground antenna' or 'Wave antenna'. This antenna had great advantages in terms of drastically minimized interference and static due to termination of the antenna at the far end from Europe. They made measurements of signal strengths along the line at every mile and found that

the antenna was as if collecting energy *i.e.* the signal strength was intensifying as one moved toward the far end of the antenna. The antenna schematic and the plot of signal strength as presented by them are shown in Fig. 2.1 for convenience. Subsequent research by several groups in Radio Corporation of America (RCA) focused on the solving the problems of fading and interference [3] faced by short wave communication in connection with radio transmission and reception. Combinations and variants of the long wire antenna were developed to increase the directivity [4] which later led to the development of the travelling wave vee and Rhombic antenna [5-6]. They had considerably increased directivity and were less prone to interference from noise signals.

Extension of the concept of the travelling wave antenna into the microstrip domain took some time. In 1977, James and Hall presented a radiating system of microstrip travelling wave array [7]. The antenna system comprised of simple microstrip lines loaded with open stubs at periodic intervals. They optimized the array to obtain wideband behavior at J band and also designed a low side lobe array for use in the same band.

In years to follow travelling wave antenna developed greatly in the microstrip domain as well as in waveguides and SIW lines in recent times.

I. TRAVELLING WAVE ANTENNAS BASED ON QUASI-TEM MODES IN MICROSTRIP LINES

2.3 TRAVELLING WAVE ANTENNAS WITH DISCRETE BENDS

Travelling wave antennas with right angle, acute or obtuse angle bends have dominated the travelling wave antenna domain for a long time. A summary of analysis techniques and applications of this class of travelling wave antennas are presented below.

ANALYSIS TECHNIQUES

2.4.1 Transmission Line Model

One of the most appropriate models for microstrip travelling wave antennas is the Transmission line model. It yields results with sufficient accuracy under the approximation of a Quasi TEM mode of propagation.

The basic transmission line model was the one utilized by P S Hall in evaluating axial ratio and the radiation from Rampart lines [8] shown in Fig. 2.2 to develop polarization agile microstrip travelling wave array. He followed the technique proposed by Wood [9] and ignored reflections from the right angle corners of the line (champhered bends). This greatly simplified the analysis and allowed a closed from solution to be calculated. In their work, far field radiation from magnetic currents on the sidewalls of the Rampart line was considered. In both these works, an equivalent decay constant was computed from the power radiated from the structure. This effective decay constant was then reintroduced in the analysis in subsequent iterations of the calculation. The basic transmission line model along with the magnetic current model was later utilized by several other researchers [10-12] to analyze bent microstrip line based travelling wave antennas.

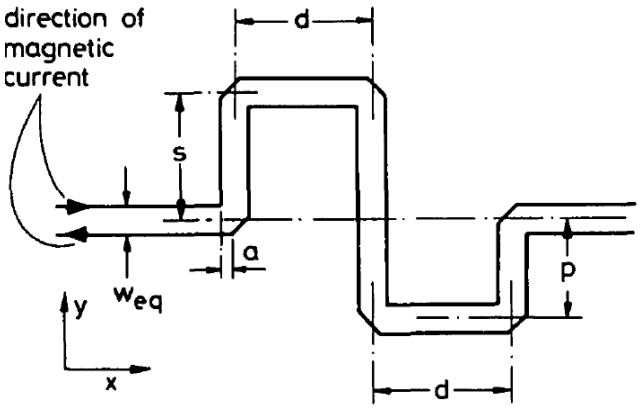

Fig. 2.2: Rampart line antenna with the magnetic currents [8]. ©IEEE

An iterative technique was used by [13] where the per unit length resistance of the line was iteratively updated from the power radiated by the line. A layered media Green's function was used by them to calculate the radiated far field. The iteration algorithm used by them was:

$$\frac{1}{2}R^{(i+1)}\int_L \left|I^{(i)}(l)\right|^2 dl = P_r(R^{(i)}) + \frac{1}{2}R_c\int_L \left|I^{(i)}(l)\right|^2 dl \tag{2.1}$$

where $R^{(i)}$, $I^{(i)}, P_r(R^{(i)})$ are the per unit length resistance, current on the line and the power lost on the line due to $R^{(i)}$ for the i^{th} iteration while R_c accounts for the ohmic losses in the line.

Another technique similar to this had been used by several other researchers [14] where the basic voltage-current relationship in a lossless transmission line is modified with unknown losses ($\alpha(l)$, $\beta(l)$) in the following manner:

$$\begin{aligned}\frac{\partial v(l)}{\partial l} &= -j\omega L(l)i(l) + \alpha(l)i(l)\\ \frac{\partial i(l)}{\partial l} &= -j\omega L(l)v(l) + \beta(l)v(l)\end{aligned} \tag{2.2}$$

These unknown losses are evaluated by using the voltage and currents calculated from full wave MoM based technique. This is basically an inverse extraction technique.

2.4.2 Full Wave Techniques

Full wave techniques have always been a prime choice for researchers to analyze bent travelling wave antenna geometries. L Shafai in his 1984 paper [15] attempted to numerically analyze a serpent line antenna for its radiation characteristics. He used an Electric Field Integral Equation (EFIE) technique by modeling the line with short segments of thin wires over the infinite ground. He modeled the excitation as voltage source and the termination as a matched load.

His technique yielded accurate results when the substrate permittivity approached unity. In a later publication by Aksun and Mittra [16], a closed form Green's function in the spatial domain was used to compute the current distribution on microstrip traces in a PCB environment. Their analysis was greatly generalized as it could accommodate any number of traces with arbitrary complex loads and arbitrary excitation. Also the choice of operating in spatial domain instead of spectral domain allowed them to avoid evaluation of Sommerfeld integrals. They used the currents calculated using the MoM technique with rooftop basis functions to calculate the spurious radiation from such traces. They subsequently extended the concept to asymmetrical multi trace situations as well [17]. In 1994 Nakano and Hirose applied the MoM technique to analyze crank line based microstrip travelling wave arrays [18] to be used in the X band. They used a spectral domain Galerkin technique using piecewise sinusoidal basis functions to analyze the crank line antennas shown in Fig. 2.3. In a later publication they modified the antenna by gradually tapering the substrate thickness for the crank line to improve the radiation characteristics. Sommerfeld type integrals in the spectral domain had to be solved [19].

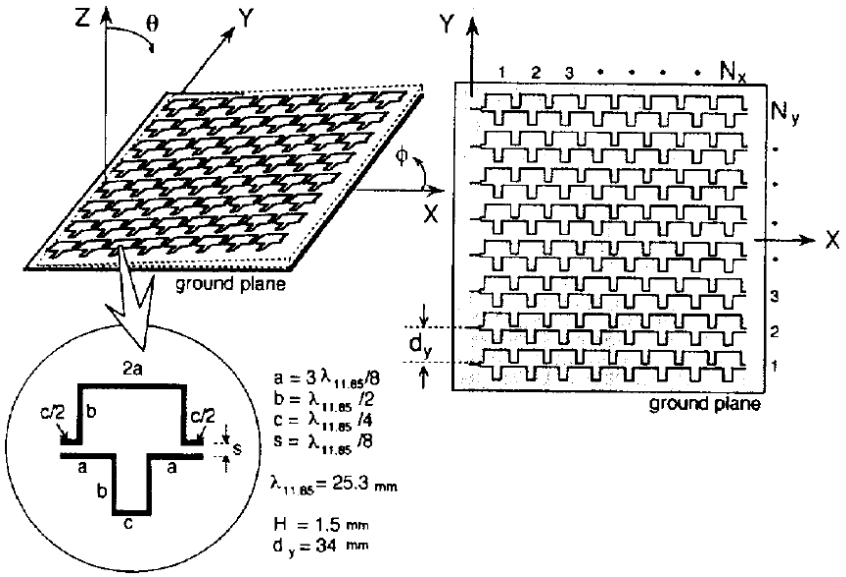

Fig. 2.3: Crank line antenna. [18]©IEEE

2.4.3 Green's Function Technique

One of the most efficient techniques for analyzing radiation from microstrip lines and line based antennas is the Green's function technique. They were primarily used in the context of calculating spurious radiation in a EMI scenario. A layered media far field Green's function was developed by Hill *et al.* for horizontal and vertical current elements located on top of the substrate [20, 21]. They used a simple theory of reciprocity to calculate the radiated far fields. This was a great simplification over the conventional full wave techniques since current on the strip surface were approximated using transmission line theory instead of approximating them using a basis. This Green's function was later utilized by M Leone [22] to calculate the radiated emissions from microstrip lines with complex terminations. In [23] the nature of the propagating wave was of Quasi Tem type which is quite common in a transmission line.

However, modifications in the Green's function technique became imminent for lines supporting higher order modes in microstrip lines. Consequently, as a natural extension of the transmission line model, the Enhanced Transmission Line model (ETL) [24] was developed. This model startS with the Standard Transmission Line technique (STL) with line parameters calculated using full wave integral equation approach. Next, the line parameters (which are essentially algebraic in nature in STL) are modified to a more general convolution type. This allows the enhanced model to be applied to frequencies and situations where the guided wavelength in the substrate becomes comparable to the substrate thickness. At lower frequencies and geometries with smaller width and conductor separation the ETL converges onto the STL. Later extension to the ETL was presented to accommodate multiple microstrip lines and a mixed mode propagation environment supporting even and odd modes.

Although lines with non right angle bends have not received as much attention as their right angle counterpart, there have been some efforts directed at them. Pioneered by Nakamura the travelling wave mode method [25] had been applied to calculate the terminal and radiation characteristics of bends of wire antennas over ground planes. In [26] an acute angle bend was analyzed by decomposing the currents in the adjacent arms of the bend into even and odd modes. Subsequently, the TWMM was applied to each of the two modes to find the radiation characteristics.

2.4.4 Other techniques

Apart from the techniques presented above there have been some other techniques employed to analyze microstrip travelling wave antennas in general. In 1989-90, A K Bhattacharyya [27] observed that the fields inside a long rectangular patch antenna with single feed tend to become more of the travelling nature than the conventional standing wave type. Consequently, he approached the problem with cavity model type formulation with wall admittances wherein the wave equation was solved underneath the line. The results he finally obtained for the propagation constants indicated the existence of the travelling wave.

Tammen and Mayes [28] introduced an eigenvalue technique for computation of complex propagation constant of a travelling wave antenna. Starting with perfect electric walls for the top and bottom of the microstrip line and perfect magnetic sidewalls, they calculated complex wall admittance from the radiated near field from the structure. This wall admittance was then utilized to formulate a transcendental equation on the transverse phase constant of the line. Upon successfully solving this transverse problem, the longitudinal complex propagation constant was computed.

A very interesting circuit approach was presented by Kami and Sato [29] to model the radiation from straight as well as bent transmission lines in general.

They modeled the radiation problem using a three terminal network. Extremities of the transmission line were modeled as two terminals while the external observing horn antenna was considered as the third one. Currents excited on the external antenna due to currents imposed at the transmission line were observed after evaluation of the Z- matrix of the network. Analytical solution for the radiated fields from a finite length transmission was finally presented.

Another popular technique for calculation of radiated fields from transmission line has been the Hertzian dipole technique [30, 31]. This technique starts by segmenting the line into several smaller sections and consider each subsection as a radiating Hertzian dipole. Total radiated far field is computed by adding the contributions from each such dipoles.

APPLICATIONS

Classically, the onset of research on the travelling wave array using bent or curved microstrip lines had started with the aim of designing polarization diverse antennas. In the 1983 paper by Hall [8], the microstrip rampart line antenna was investigated for designing antennas with polarization control. It was shown that the arm lengths of the Rampart line could be tuned to obtain linear or circular polarization. In the same year Nishimura [32] and later Nakano and Hirose [33, 34] utilized a combination of Rampart unit cells to design what they called a Crank type antenna. This antenna was seen to be able to obtain circular polarization along with high gain and low side lobe level (SLL). Another interesting geometry for obtaining circular polarization had been the cross antenna. It was introduced by Roscoe and Shafai in 1989 [35] and later extended by Roederer in 1990 [36]. Shown in Fig. 2.4, this antenna basically replaced a continuous circular loop with radiating units of microstrip discontinuities. These units and the separation between them could be calculated for circularly polarized radiation.

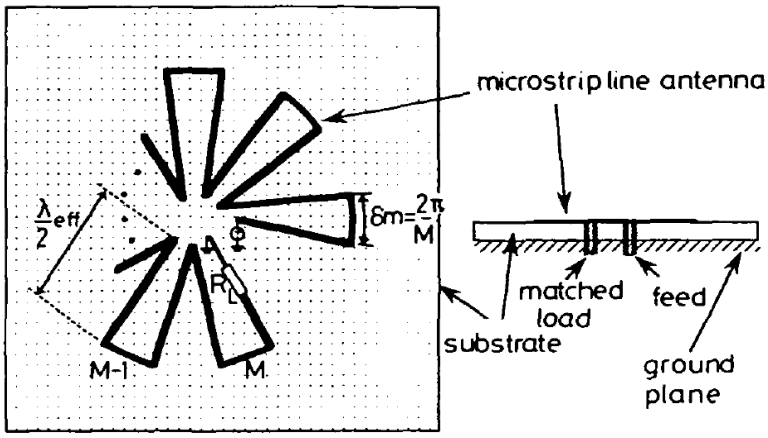

Fig. 2.4: The travelling wave cross antenna [35]. © IET

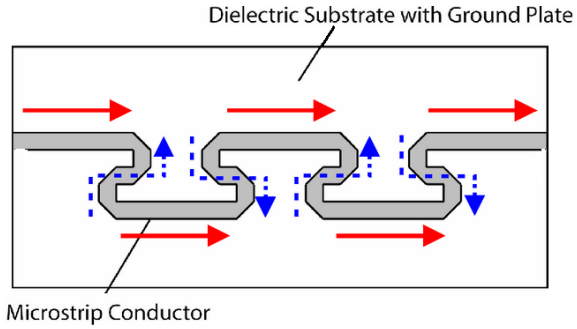

(b)

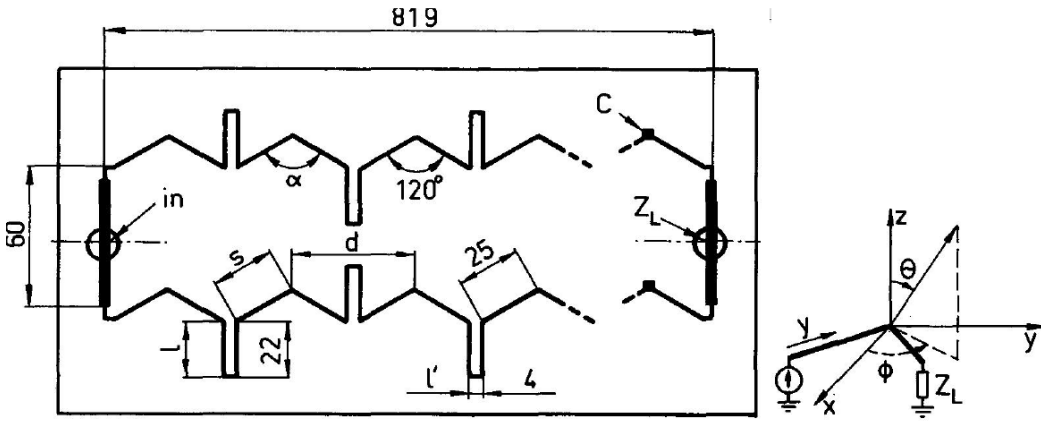

(c)

Fig.2.5: The Franklin type antenna [12] and (b) chain antenna [11]. ©IEEE

One of the most interesting characteristic of a travelling wave antenna is beam scanning with frequency. This gives them one distinct advantage over conventional phased array systems used for beam steering: they do not require any complex feeding network and the scan rate or the side lobe levels can be adjusted to some extent by controlling the antenna geometry. The Franklin antenna shown in Fig. 2.5a [12] and the chain antenna shown in Fig. 2.5b [11] were one of the earliest bend based travelling wave geometries which came up in 1979.

In recent years, this beam scanning property of travelling wave antennas have been applied to millimeter wave imaging applications as well. In 2013, Vazquez *et al.* used a travelling wave array [37] in the K_u band (in the 15 GHz to 18 GHz band) to develop a sensitive scanning apparatus assisting a versatile imaging system. They characterized the complete near field of the antenna under consideration and were able to obtain a sensitive scanning rate of almost 1.17^0/100 MHz. Later in 2016 their concept was extended in [38] to design Rampart line antennas for an imaging system in the Ka band (29.5 GHz to 36 GHz range) with wide scan range (56^0 in one case and 98^0 in another) and impedance bandwidth (about 6 GHz).

Apart from these, microstrip travelling wave antennas have also been used in RFID [39-41] applications and vehicular radar [42, 43] applications. Right angle bend based 'snake antenna' [39], meander line antenna [40] and Rampart line antenna [41] had been used in the UHF frequency range (865 MHz – 928 MHz). On the other hand, the 24 GHz band reserved for use in automotive radar, has been used in vehicular radar designing using Rampart line array [42] and comb line array [43].

2.4 TRAVELLING WAVE ANTENNAS WITH ARBITRARY CURVATURE

Propagation of electromagnetic waves on a curved structure had been a topic of interest in the context of MMIC design. They radiated smaller amount of power as compared to sharply bent lines. A variety of analysis techniques involving the simple transmission line model, conformal mapping, perturbation techniques, circuit models and full wave techniques have been developed over the years. These curved microstrip lines have been applied both in MMIC circuits, and in antenna design problems.

ANALYSIS TECHNIQUES

2.4.1 Approximate Models

The simple transmission line model is the most natural model for analyzing curved microstrip lines. Owing to the reduced amount of reflection from the curvatures, this model works fine as long as the curvature is not of a great degree. It had been very popular in the context of circular spiral [44] and circular loop [45, 46] antennas. In most [45, 46] of these works, the curved line is modeled as a lossy transmission line accounting for the radiation losses and a correspondence between the curved structure and a straight transmission line is evaluated in an approximate manner. In [47] an Archimedean spiral antenna was analyzed after modeling the spiral using a straight transmission line. Characteristic impedance of the transmission line was taken equal to the input impedance of the spiral while in [44] a cascaded ABCD matrix formulation was used to calculate the properties of a closed microstrip circular ring. The problem of radiation from arbitrary planar spiral antennas had been addressed recently by Barton et al. in 2010 using standard radiation integrals [48].

The perturbation technique had been a very elegant method for calculating the propagation constant as well as the modified electric and magnetic fields

inside a curved guiding structure. Lewin [49, 50] developed this technique in the context of a curved metallic waveguide in 1977. In this technique, the propagation constant and the internal electric/magnetic field were expressed as weighted sum of linearly independent functions. The weighing factors were chosen to be the curvature of the waveguide and its higher powers. The propagation constant and the internal electric field are thus expressed as follows:

$$E_{np} = e^{-j\beta_{np}s}\left\{\phi_{0p} + \chi_n\phi_{1p} + \chi_n^2\phi_{2p} + \ldots\right\} \tag{2.3}$$

$$\beta_{np} = \begin{cases} k_e\sqrt{\left\{1-\dfrac{W_e^2\chi_n^2}{12}\left(1-\dfrac{2}{5}k_e^2W_e^2\right)\right\}} & \text{for p=0} \\ \sqrt{k_e^2\left(1-\dfrac{p^2\pi^2}{k_e^2W_e^2}\right)+\dfrac{\pi^2\chi_n^2}{6}\left[p^2+\dfrac{12-p^2\pi^2}{2p^2\pi^4}k_e^2W_e^2-\dfrac{21+p^2\pi^2}{2p^4\pi^6}k_e^4W_e^4\right]} & \text{for p>0} \end{cases} \tag{2.4}$$

$$\phi_{0p} = \cos\left[\frac{p\pi}{W_e}\left(\xi-\frac{W_e}{2}\right)\right] \tag{2.5}$$

The unknown linearly independent functions were calculated after substituting the said fields and the propagation constants onto the original differential equation for the curved guide. This concept was very simple and worked very well in case of a waveguide with constant and small curvature. Later in 1984, Wolff and Tripathi imported this concept to microstrip when they analyzed an open [51] and a closed microstrip ring [52]. Weisshaar and Tripathi furthered the analysis [53, 54] dealing with circularly curved microstrip bends shown in Fig. 2.6. In this latter work, they modeled the curved microstrip bend using planar waveguide theory [55] and subsequently applied a mode matching analysis [56] to calculate the frequency dependent terminal characteristics of a curved microstrip bend.

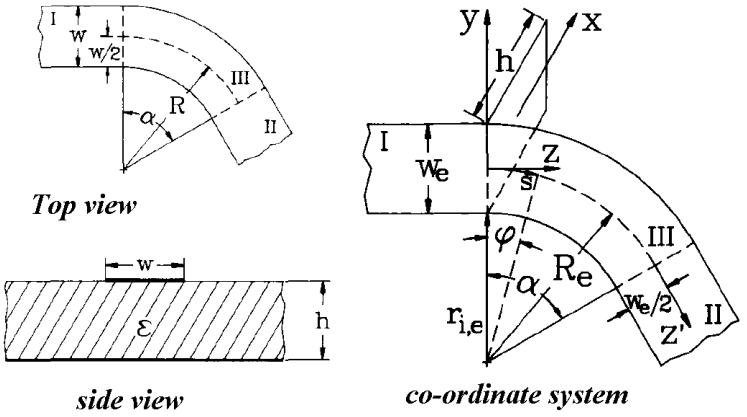

Fig. 2.6: Curved microstrip bend geometry [55]. © IEEE

Researchers have also used the conformal mapping techniques to map the curved microstrip line structure onto manageable straight or linear structures and calculated the line characteristics thereof. Using this procedure, Roy *et al.* developed an empirical formula for the effective dielectric constant for curved microstrip lines [57, 58] in early 1990s. Expression for the frequency dependent effective dielectric constant evaluated by them is shown below:

$$\varepsilon_{ec}(f) = \varepsilon_r - \frac{\left\{ \varepsilon_r - \varepsilon_e(0)\, e^{\frac{1}{12}\sqrt[4]{\frac{h}{r}}} \right\}}{1+\left(\frac{f}{f_c}\right)^2} \tag{2.6}$$

Here usual notations are used with $fc = \left(3\times10^8\right)/\left(4h\sqrt{\varepsilon_r - 1}\right)$, $\varepsilon(0)$ is the static permittivity of a rectangular microstrip line and '*r*' is the radius of the circularly curved microstrip line. (2.6) was shown to be valid $2 \le \varepsilon_r \le 12$, $0.8 \le W/h \le 5$, $\frac{\lambda_g}{4\pi h} \le r/h \le \infty$ and $0 \le f \le 12$. Later more complex Schwarz-Christoffel transformation technique was developed for analyzing singly curved transmission lines in an efficient manner [59].

Apart from these, there are some works involving a circuit modeling of the curved microstrip structure. [60] used a curve fitted empirical model for circuit equivalent of a curved section of microstrip line.

2.4.2 Full Wave Analysis

Simplicity of techniques described in the last section is affected by the range of their applications. They fail to handle Microstrip lines or transmission lines in general with greater curvature or variable curvature. To alleviate this problem, full wave analysis involving the method of moment (MoM) technique was utilized [15] by Shafai and Sebak using the Electric Field Integral Equation (EFIE) using short piecewise segments for the line. They analyzed a serpent line antenna. Weisshaar et al. developed a full wave MoM technique in conjunction with mode matching technique to calculate the transmission characteristics of a E and a H plane waveguide bend [61] in 1992. Later in 1997, Khamas and Cook presented a MoM based technique for analyzing the input impedance and current distributions of arbitrary printed wire spirals [62]. They used a piecewise sinusoidal basis function in the sub-domain technique. Similar curved segmentation techniques involving curvilinear basis and testing functions in MoM had been used by several researchers afterwards for curved wire antennas [63] and printed antennas [64-67]. Integral equation based technique was also presented in [68] for parabolically bent dipole antenna and general wire loop antennas [69].

APPLICATIONS

Planar and wire structures with arbitrary curvature are popular for both circuit and antenna applications. Archimedean Spirals for UWB applications [70, 71] have been a very widely. These curved antennas have also been used for antenna miniaturization. In [72] authors compared the performances of a meander and a sinusoidal line antenna for use in the GSM (900 MHz) band. Later in 2009, Kakoyiannis et al. presented a sinusoidal monopole antenna [73, 74] shown in

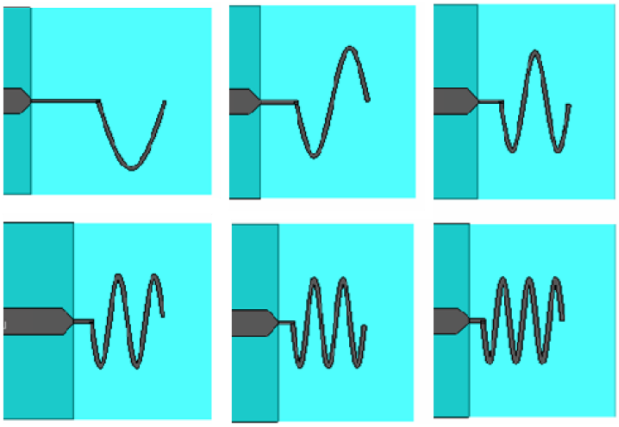

Fig. 2.7: Different number of unit cells of the sinusoidal line geometry [74]. ©IET

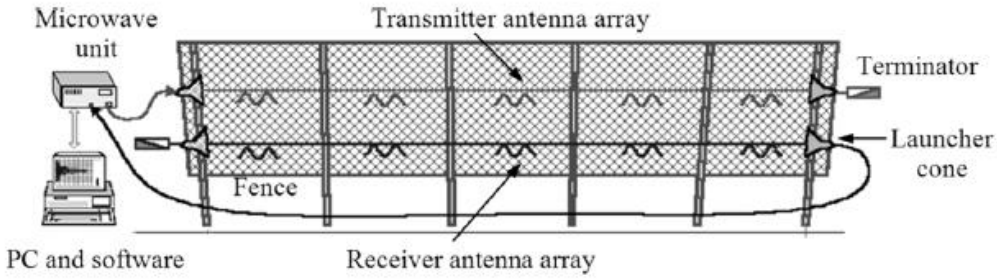

Fig. 2.8: Sinusoidally curved wire antennas deployed in security fence radar [86]. ©IEEE

Fig. 2.7 with different number of units for sensors and portable devices working in 2-3 GHz band. They observed the effect of ground plane on the radiation characteristics of such small monopoles as well. First in 1982 [77] and later in

2002 [78], focus was given on obtaining shaped radiation pattern by optimizing the structure of curved wire antennas. The wire was modeled using piecewise parabolas optimized using Genetic Algorithm (GA) to synthesize given radiation pattern. Curved microstrip lines can be designed to radiate circularly polarized waves. As shown in 1979 by Wood [9], curved microstrip edges could be optimized to radiated directive CP waves. CP radiating printed spiral antenna using genetic algorithm [79], circularly polarized loop antennas [80, 81] and printed figure of eight antennas [82] have also been designed. Apart from these, sinusoidally curved microstrip line antennas have also been utilized in K band and mm wave frequencies to obtain transverse polarization [83, 84]. In recent years, sinusoidal curved wire antennas shown in Fig. 2.8 have been deployed in security fence radar in household security systems [85-87].

2.5 TRAVELLING WAVE ANTENNAS WITH NON-UNIFORM LINE WIDTH

Non uniform microstrip lines have been in use for circuit designing and impedance matching since a long time. Consequently, there is an anthology of analysis technique for non uniform microstrip lines with specific types of non uniformity. In most cases either the second order non linear differential equation underneath the non uniform strip has been solved or a multiport circuit analysis has been employed. In later years newer techniques for arbitrarily non uniform microstrip lines involving both approximate and full wave methods have developed.

ANALYSIS TECHNIQUES

2.4.3 Approximate Analysis

Starting from the early 20s upto almost the late sixties, researchers attempted to analyze the non uniform transmission line problem by solving the

non linear Riccati differential equation in input reflection co-efficient or input impedance of the line.

In 1932, A T Starr reduced the non uniform transmission line problem to a variable co-efficient second order differential equation and solved it for a line with power law characteristic impedance [88]. He found the solutions using a combination of Bessel functions. Later in 1946, Walker and Wax, showed a method to convert the coupled voltage-current equations in a non uniform line to a single first order non linear Riccati type differential equation on the input reflection co-efficient [89]. Cohn [90] used a reversion technique outlined by Pipes [91] to solve the non-uniform transmission line problem. In 1955, Kaufman published an article [92] which contains a comprehensive list of research on non uniform transmission line up to that time. The non linear differential equation on input impedance was later solved by Pipes [93] through a substitution obtaining a linear second order differential equation. He solved the problem for uniform, exponential and power indexed lines. In the same year, Bollinder developed a Fourier series based technique [94] with limited number of terms to solve the non linear Riccati equation on input impedance. This technique is similar to the conventional small reflection model. The small reflection technique on the other hand motivated Collin [95] to design an optimal matching section using tapered transitions. In this perod (1950-1960) may other researchers endeavored to solve the non linear Riccati equation in voltage reflection co-efficient and input impedance [96-102] to calculate the characteristics of various non uniform lines. In 1964 S C Dutta Roy developed a terminal two port network technique [103] for transmission lines of General Hyperbolic Class (GHC) and General Electric Class (GEC).

Simple or modified transmission line techniques have also been applied to the case of non uniform microstrip lines. Cascaded piecewise segments [104] and tapered segments [105] to approximate the non uniform microstrip lines have been reported (shown in Fig. 2.9a and Fig. 2.9b respectively). In both cases the

ABCD matrices for the individual segments were multiplied to obtain the overall characteristics.

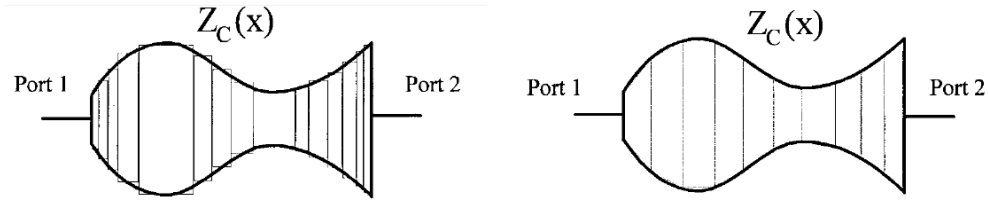

(a) (b)

Fig. 2.9: (a) Piecewise linear and (b) piecewise tapered analysis of non uniform microstrip line [105]. ©IEEE

Later in 1990, Nwoke developed a matrix relationship between voltage and currents on a non uniform transmission line [106]. He expressed it as:

$$\begin{bmatrix} V(x) \\ I(x) \end{bmatrix} = \begin{bmatrix} \cosh\left(\int_{x_0}^{x} \sqrt{Z(t)Y(t)}dt\right) & -Z_0 \sinh\left(\int_{x_0}^{x} \sqrt{Z(t)Y(t)}dt\right) \\ -\frac{1}{Z_0}\sinh\left(\int_{x_0}^{x} \sqrt{Z(t)Y(t)}dt\right) & \cosh\left(\int_{x_0}^{x} \sqrt{Z(t)Y(t)}dt\right) \end{bmatrix} \begin{bmatrix} V_0 \\ I_0 \end{bmatrix} \quad (2.7)$$

Recently in 2014, a two step perturbation method in the spectral domain for non uniform lines was presented in [107]. The authors considered the non uniformity as perturbation on unloaded line and subsequently reduced the telegrapher's equation to a second order differential equation with source terms. Later in 2016 [108] Nguyen *et.al.* developed a transmission line model for non uniform leaky wave antennas. They used a simple transmission line model harboring the first higher order mode. Propagation constant of the higher order mode was calculated by standard techniques available for leaky wave antennas. Radiation from non uniform microstrip lines [109] had been analyzed by Cheldavi [110] where he considered the radiation from the structure in time domain and calculated co-relation between power radiated and the terminal voltages and currents.

Most of these works attempted the non uniform transmission line problem from analytical point of view. This restricted the solutions to specific types of solvable lines. In 2006, Amirhosseni presented two series based techniques (Taylor series [111] and Fourier series [112]) for approximately solving the non uniform transmission line problems. In these techniques, the voltage and current are replaced by a series sum and the unknown co-efficients of the series are calculated after a term by term comparison.

Apart from these approximate techniques, there have been some efforts put into analyzing these non uniform lines using full wave techniques [113-116] as well. In 1984, Glandorf and Wolff used a combination of spectral domain method of moment and Floquet theorem [113] to analyze periodically non uniform microstrip lines of the type shown in Fig. 2.10. A sub-domain technique

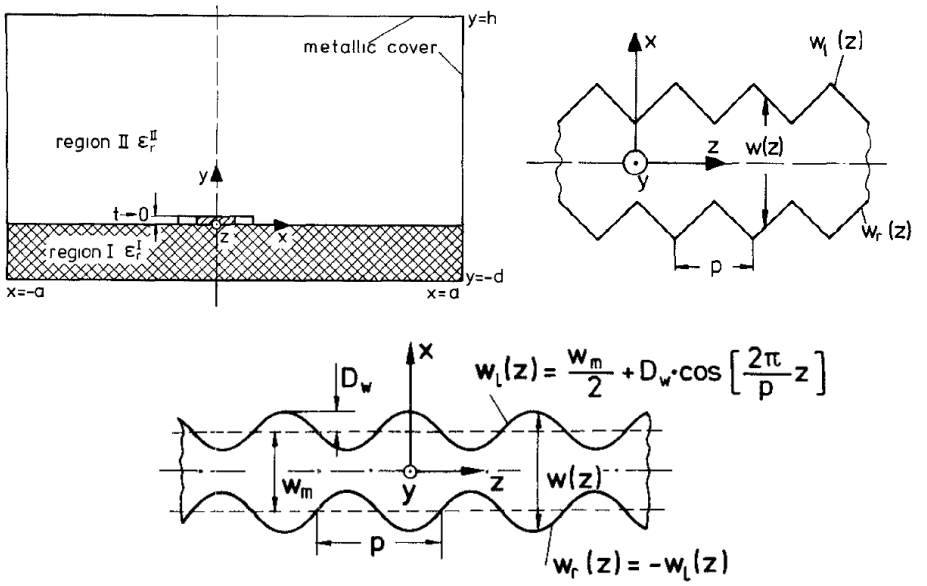

Fig. 2.10: Non uniform microstrip line antenna analyzed by Glandorf et.al. using the spectral domain technique [113]. ©IEEE

based MoM formulation was used in [114, 115] for strip line and microstrip lines with non uniform width. Later in 2008, the integral equation corresponding to the non uniform microstrip line was solved in [116].

APPLICATIONS

Non uniform microstrip lines have found applications in a multitude of circuit and antenna problems ranging from filter and circuit design to design of leaky wave antenna for beam focusing. It had been a popular choice for suppression of spurious pass bands in microstrip coupled line filters [117], band stop filters [118], multi band [119] and ultra wideband [120] Wilkinson power divider, as guard trace for cross talk minimization [121], in pulse shaping networks [122, 123] and as onboard analog signal processing units [124, 125]. In recent years, versions of the non uniform microstrip lines have been used in designing leaky wave antennas for beam scanning [126] and in near field focusing array with periodic width modulated lines [127, 128].

II. TRAVELLING WAVE ANTENNAS BASED ON LEAKY HIGHER ORDER MODES IN MICROSTRIP LINES

Leaky wave antennas, since their inception in the early 70s, have become a very important topic of research in recent years. They can be classified into two groups namely the uniform leaky wave antennas and the periodic leaky wave antennas. Uniform leaky wave antennas, as the name suggests, are basically guiding structures (waveguides/microstrip lines/Coplanar waveguide (CPW) or Substrate integrated waveguide (SIW) lines) where a higher order mode is excited and the fundamental Quasi Tem bound mode is suppressed. On the other hand, a periodic leaky wave antenna, as the name suggests, basically comprises a guiding structure (waveguide/ microstrip line/CPW line/SIW line) periodically perturbed with some loading network. Some higher order Floquet modes thus generated becomes leaky with phase constant values smaller than that of the free space phase constant at the concerned frequency.

2.6 UNIFORM LEAKY WAVE ANTENNAS

First known form of Leaky wave antenna was introduced by W Hansen in 1940 [129]. He developed a metallic semi open waveguide with slit on the narrow wall that radiated electromagnetic energy. After this they have evolved greatly. Numerous works were done on metallic wave guiding structures and dielectric slabs in the initial years. After 1977, when Menzel presented a leaky wave antenna in microstrip configuration, research flourished on planar technologies. Since then, various microstrip , CPW, slot lines and SIW guides have been considered as leaky wave antennas.

2.6.1. Initial Research

In 1956 Marcuvitz pointed out the existence of non-eigenmodes as field solutions in source free electromagnetic problem with open boundaries [130].

These solutions tended to violate the singularity at infinite distance from the structure in the transverse or the cross-sectional plane. Consequently they had a continuous spectrum and were termed as improper modes. This concept was utilized by Goldstone and Oliner to analyze the nature of complex waves inside semi open waveguides. They facilitated a transverse resonance technique to calculate the complex propagation constant inside a rectangular guide [131] in 1958 and a cylindrical guide in 1960 [132]. Later in 1963, Tamir and Oliner came up with a very comprehensive work on leaky waves in guiding structures [133, 134]. They showed that these leaky waves having complex propagation constants are primarily results of contributions from various poles in the integral representation of the electromagnetic fields. They utilized a steepest-descent technique for their analysis and justified the improper modal nature of these complex waves. The interface fields calculated in [133] were used in a later work [134] to find co-relation between the leaky modes in a structure and the electromagnetic field pattern radiated by it. They made an interesting observation

that smaller attenuation constant tend to make the main beam of the radiated far field at a specific angle from the structure. This observation was furthered by Garg *et.al.* [135] when they presented a slow leaky wave antenna with a huge attenuation. Such a high value of attenuation pushed the main beam toward the broadside direction. Antenna structure used by them was a rectangular waveguide with one of its wall replaced by a thin conducting screen (thickness less than skin depth). Most of the analysis efforts and applications up to this point were focused on metallic waveguide with partial openings. It was only after 1978 starting with Menzel's work that the research delved into the planar technology domain.

2.6.2. Semi Analytical approaches

W Menzel [136] in his 1978 paper facilitated a transmission line model with the longitudinal propagation constant calculated by modeling the line with planar waveguide model [55] (Menzel's antenna shown in Fig. 2.11). Later in

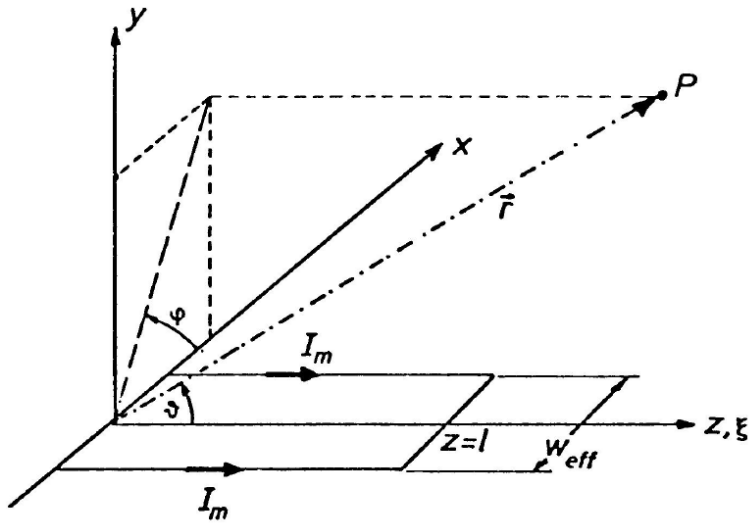

Fig. 2.11: Menzel's [136] travelling wave antenna. ©IEEE

1990, A K Bhattacharyya [137] came up with a technique to solve the wave equation inside a long microstrip patch antenna. The complex internal fields and the propagation constant were evaluated assuming an impedance boundary

condition on the cavity walls. The wall admittances accounted for the radiation losses in the structure. Afterwards in 1997, the simplest form of cavity model was applied by Luxey and Latheurte in [138] to calculate the radiated far fields from a microstrip leaky wave antenna in an approximate manner.

One of the most comprehensive works on leaky wave antennas had been presented during 1986, by Oliner and Lee [139, 140]. They attempted to put forth an explanation of the observations made by Ermert [141, 142] and Menzel [136]. What they found was very interesting. They analyzed microstrip lines with and without top covers using a Wiener- Hopf formulation. Propagation wave numbers were calculated using a transverse resonance technique. They observed that leakage occur in a combination of space and surface wave modes and the relative proportion of power in them depend on the height of the top cover. Subsequently in 1988, Oliner and Jackson presented a Steepest-Descent formulation to analyze narrow beam radiation from multilayer planar leaky wave antennas [ ] . They presented asymptotic expressions for antenna characteristics for ready design. A similar steepest descent technique was applied in [143] for analyzing microstrip lines on a lossy substrate. They observed a spectral region present only when the dielectric losses are non-zero.

In 1999, Villegas *et al.* [144] used two different asymptotic techniques to calculate the leakage fields radiated by a semi-infinite microstrip line. They used the stationary phase technique and a uniform asymptotic evaluation.

Burghignoli et al. developed an equivalent circuit model suitable for leaky wave antennas. The feeding line was considered to be supporting the quasi Tem mode while the radiating leaky line harbored the leaky higher order mode. Equivalent circuit parameters and consequent S- parameters were calculated from full wave MoM simulations [145].

2.6.3. Full Wave Analysis

Several researchers had attempted the problem of higher order modes in microstrip lines using the spectral domain method of moment technique. Most of them however calculated the dispersion characteristics upto the fast wave region and did not enter the leaky fast wave region. In 1956, T T Wu published his work [146] on evaluating the propagation constant of microstrip line using the Fourier transformation technique. He concluded that the higher order modes, below a certain frequency, would yield improper modes not diminishing away from the structure in the transverse plane. Later in 1976 H Ermert [141, 142] approached the problem of higher order modes in microstrip lines by considering infinitely extending standing wave pattern in the transverse plane of the line thereby yielding only real phase constants. One of the first works to have calculated the complex propagation constant of the first higher order mode in microstrip line had been done by Jansen and Boukamp in 1983 [147]. They carefully chose the integration path in the inverse Fourier domain to appropriately include the effects

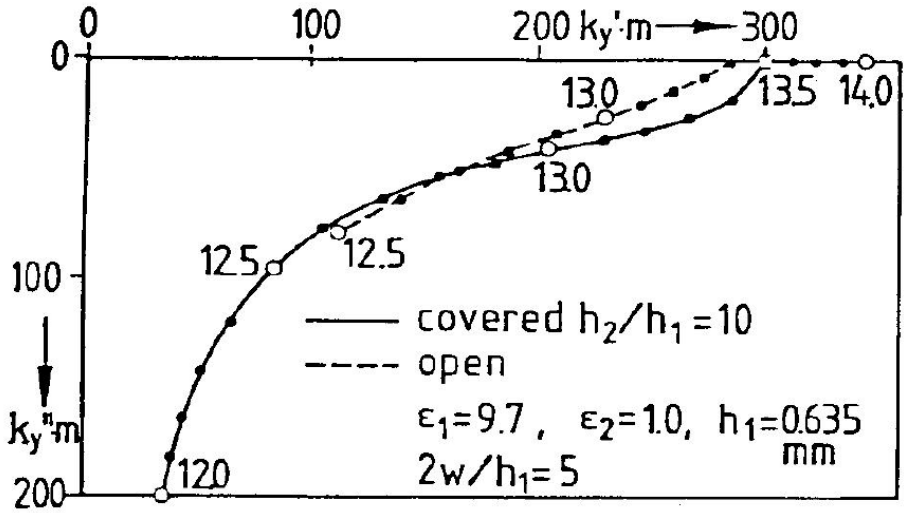

Fig. 2.12: Real and imaginary parts of the propagation constant as calculated by Jansen and Boukamp [147]. ©IEEE

of the surface wave pole. The propagation characteristics of the first higher order mode as calculated by them is shown Fig. 2.12. Bagby and Nyquist picked up later in 1993 to calculate the propagation regimes [148] for open microstrip lines using spectral domain MoM with entire domain basis functions. The spectral domain MoM technique was also applied afterwards to analyze the leakage from coupled microstrip lines and coupled discontinuities [149].

Looking for a faster convergence and reduced number of singularities, Michalski and Zheng developed a Mixed Potential Integral Equation (MPIE) in [150] based full wave technique for analyzing the leaky modes in microstrip lines. They used respectively a 'pulse' and 'triangle' basis functions to represent the longitudinal and the transverse component of the electric current on the strip surface respectively. Later same year they extended this technique to analyze microstrip lines with arbitrary cross-sections [151]. They validated their analysis with a microstrip line of rectangular, trapezoidal ad circular cross-sections. Specific discourse on the power flow along the leaky line and along the transverse plane of the line had been presented by Lin and Sheen in 1997 [152]. In this work they distinguished between the radiation mode and the reactive mode of a leaky wave antenna. It had been observed by many researchers that the integration path in the spectral domain technique has serious implications on the results obtained. Consequently, in 2002, Mesa and Jackson published their work on various integration paths in the spectral domain inverse transformation and various physical and non-physical results arising thereof [153].

In 1991, Chow *et.al.* diverted from the usual spectral domain technique and developed a closed form spatial Green's function [154] for analysis of microstrip leaky wave antennas. They avoided the complexity of performing the Sommerfeld integrals by approximating the Green's function with few terms depending on the substrate permittivity and thickness. Contributions from surface waves were introduced. Later in 1993, Grimm and Nyquist [155] came up with an

Electric Field Integral Equation (EFIE) based technique to identify the continuous radiation spectrum typical of open microstrip structures. The EFIE technique was furthered by Mesa *et. al.* using a delta gap source excitation [156] for a leaky microstrip line. They showed the existence of residual currents on open microstrip structures.

Later in 1995, Mesa and Marques presented a hybrid technique for analyzing leaky covered lines [157]. They represented the Green's function in a integral form in the spatial domain and afterwards solved the MoM problem in the spectral domain. One of the biggest advantages of this approach was that they could pose the strip currents as sources of radiation instead of using them as boundary conditions. As later as in 1999, Mesa and Jackson [158] evaluated the power radiated into the surface wave and space waves from an excited microstrip line. They used a Vertical Electric Dipole (VED) for excitation source and a semi analytical three dimensional (3D) Green's function to solve the problem using spectral domain analysis.

In 2008, very simple and efficient empirical formulae for the first higher order mode had been developed by Liu *et al.* Their formulae were based on a complex effective line width and yielded results within 10% accuracy [159]. Empirical formula for the propagation constant as calculated by them is shown below:

$$k = \beta - j\alpha = \sqrt{k_0^2 \varepsilon_{eff} - \frac{\pi^2}{W_e^2}} \tag{2.8}$$

$$W_e = W + 2\left(\Delta W - jb\right) \tag{2.9}$$

$$\Delta W = h\left[1 + 0.8874\left(\frac{1}{\varepsilon_r + 0.375}\right)\left(\frac{\frac{W}{h} - 11}{\frac{W}{h} + 20.26}\right)\right] \tag{2.10}$$

$$b = \frac{h}{2\varepsilon_{eff}} \tag{2.11}$$

These formulae are claimed to be accurate within an error of 10% for $W/h \geq 5.5$ and $\varepsilon_r \leq 12$.

Later in 2015, a transmission line model [108] was developed where the propagation constant of the propagating mode was extracted from full wave simulations.

APPLICATIONS

Classically, the uniform microstrip leaky wave antenna has been applied in beam scanning applications [160, 161]. However, the open stopband near the broad side direction proved to be a disadvantage in using them in scan-through-boresight applications. Looking to remedy this problem, Lovat *et al.* made a very interesting observation that when the phase constant and the attenuation constant of the radiating leaky mode is made equal, a single beam at broadside with considerable amount of radiation appears [162]. Exploiting the odd symmetry of the first higher order mode in microstrip leaky wave antennas, Zelinski et al.

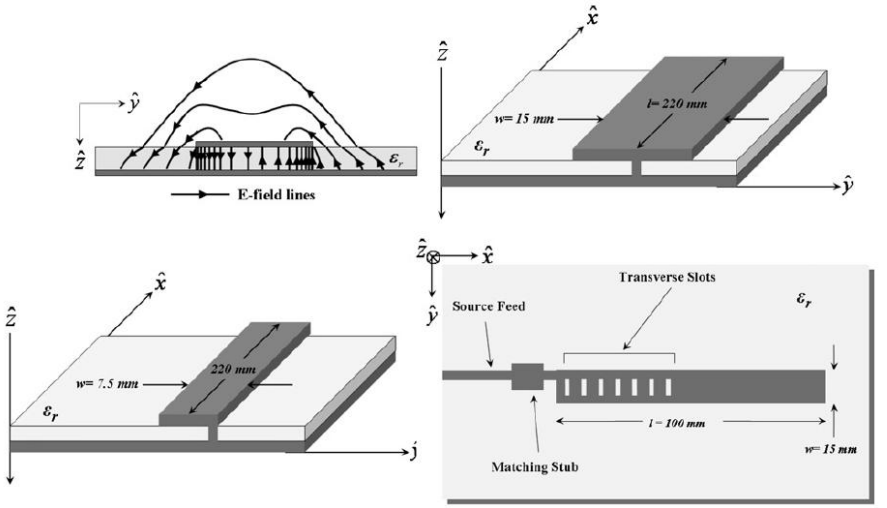

Fig.2.13: Half width leaky wave antenna presented by Zelinski *et al* [163]. ©IEEE.

developed the half width leaky wave antenna [163] shown in Fig. 2.13. This was a very important landmark in leaky wave antenna design. By doing this, all even modes, particularly the fundamental quasi TEM one, were automatically suppressed and at the same time the antenna footprint was reduced Building on this idea of using symmetry for mode suppression, use of shorting posts for mode suppression has been extensively studied [164]. This study eventually led to designing of microstrip leaky wave antennas supporting the EH_0 [165] and the EH_1 [166] modes.

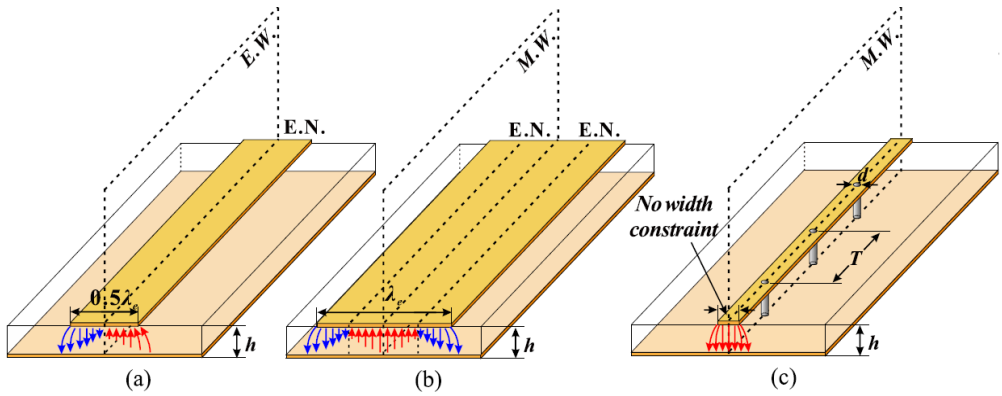

Fig. 2.14: Shorting post loaded microstrip lines [165] with excitation of (a) first higher order (EH_1) modes, (b) second higher order (EH_2) mode and (c) the fundamental Quasi TEM (EH_0) mode.© IEEE

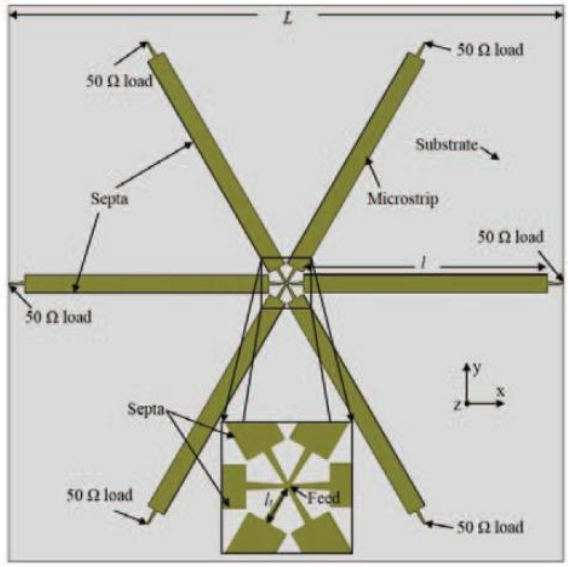

Fig. 2.15: Star shaped array of half width leaky wave antennas [169]. ©IEEE

These are shown in Fig. 2.14a and b respectively. Array of uniform leaky wave antennas shown in Fig. 2.15, have also been developed to increase antenna gain [167, 168] and obtain conical beam antenna [169]

2.7 PERIODIC LEAKY WAVE ANTENNAS

Periodically loaded microstrip lines have been in literature since a long time [170-175]. Classically they were used to design filters and slow wave structures because of the inherent slow wave propagation inside them. Phase velocity of the propagating wave inside these structures is much less than that in the free space. Consequently, they do not radiate power implicitly. However, it was shown by Oliner [176] that while periodically loading a semi-open or open transmission line (such as microstrip line), higher order Floquet modes are generated. Each of these higher order Floquet modes have different phase velocity. It is possible to design the structure in such a way that in a particular frequency range, the phase velocities of one or more than one Floquet modes become greater than the speed of light in vacuum. If such a condition prevails, then the structure would radiate substantially and such Floquet modes could be called 'leaky'. In 1986 Tsuji *et al.* presented a network model appropriate for analysis of periodic stepped dielectric guides [177] and subsequently in 1987, a metallic strip loaded dielectric slab was investigated by Guilelmo and Oliner [178] for their respective dispersion characteristics and the leaky regions. Majumdar *et al.* [179] investigated this metallic strip loaded dielectric guide. They utilized a steepest descent technique to investigate the spectral gap arising from the transition of the main radiating mode from improper to proper regime. The same structure was then analyzed by Burghignoli *et al.* using a combination of transverse resonance technique and full wave analysis [180] for its complete dispersion characteristics at low frequencies. They observed the existence of different proper and improper modes co-existing in the structure.

General microstrip based one dimensional periodic structures were analyzed by Baccarelli et al. in 2005 [181]. They employed a full wave MoM in the spectral domain to calculate a modified Brillouin dispersion diagram. This new dispersion diagram provided physical insight into the functioning of different modes excited in the structure. Later in 2006, they solved the same problem with a MPIE formulation using spatial domain MoM [182].

In 2006, Burghignoli *et al.* proved that broadside radiation from a 1D leaky periodic structure is possible even if one operates very close to the open stopband frequencies [183]. They investigated the structure with an equivalent network model combined with asymptotic Bloch theorem. Later in 2009, Paulotto *et al.* developed a technique [184] where they used a quarter wavelength long stub per unit cell to mitigate the effects of open stopbands and achieve broadside radiation.

In recent years (2017), Fuscaldo *et al.* [185] developed a closed form formula for evaluating the beam-width ($\Delta\theta$) of a one-dimensional periodic leaky wave antenna. It is given by

$$\Delta\theta_h = \cos^{-1}\left[\frac{\beta}{k_0} - \frac{2.783}{k_0 L}\left\{1 - \tanh\left(0.021\frac{\alpha L}{2}\right)\right\} - \frac{\alpha}{k_0}\tanh\left(0.21\frac{\alpha L}{2}\right)\right] - \theta_0 \quad (2.12)$$

α, β, k_0 and L are respectively the attenuation constant, phase constant, free space phase constant and the length of the antenna while θ_0 is the direction of the main beam radiated by the antenna.

Since its inception, microstrip periodic leaky wave antennas have been applied repeatedly in applications demanding frequency beam steering [186-190], and constant frequency electronic beam steering [191-192].

Otto *et al.* had worked on the problems of symmetric unit cells for periodic leaky wave antennas and showed that they suffer from the low broadside

radiation. He proposed a remedy in the form of asymmetrical unit cells and subsequently solved the broadside radiation problem [187, 188] Geometries used by him are shown in Fig. 2.16. Karmokar *et al.* used half width microstrip leaky

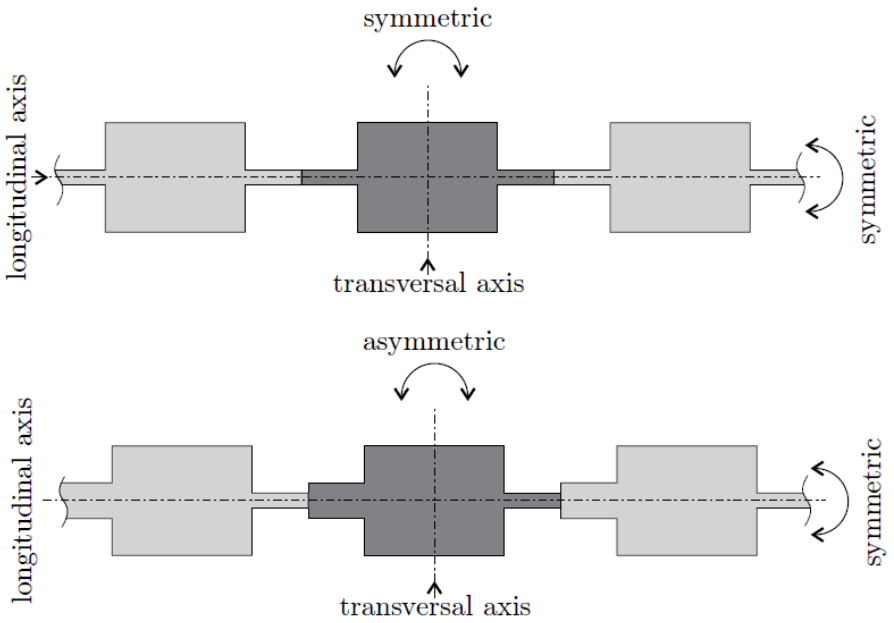

Fig. 2.16: Geometries used by Otto [187] to remedy the broadside radiation problem. © S. Otto.

wave antennas with L-shaped slots [189] to obtain a triple band leaky wave antenna with three pass bands respectively in C band, X band and K_u bands. Beam scanning with frequency was observed in all of these bands. In a later publication they presented a microstrip line based leaky wave antenna with excitation of the second higher order mode for simultaneous dual beam scanning [190] in the frequency range 6.92 GHz to 8.75 GHz. Both these antennas are shown in Fig. .

Apart from the beam scanning with frequency which is the characteristics of any leaky wave antenna, there have been works on leaky wave antennas where beam scanning at a single frequency is obtained using PIN diodes or varactors. In this context, Karmokar *et al.* designed a stub and slot loaded half width microstrip line with binary switches for beam steering at a constant frequency [191]. Later, a

leaky wave antenna array was designed in [192] for constant frequency beam scanning at 5 GHz where a steering ranges of -46^0 to 48^0 was obtained.

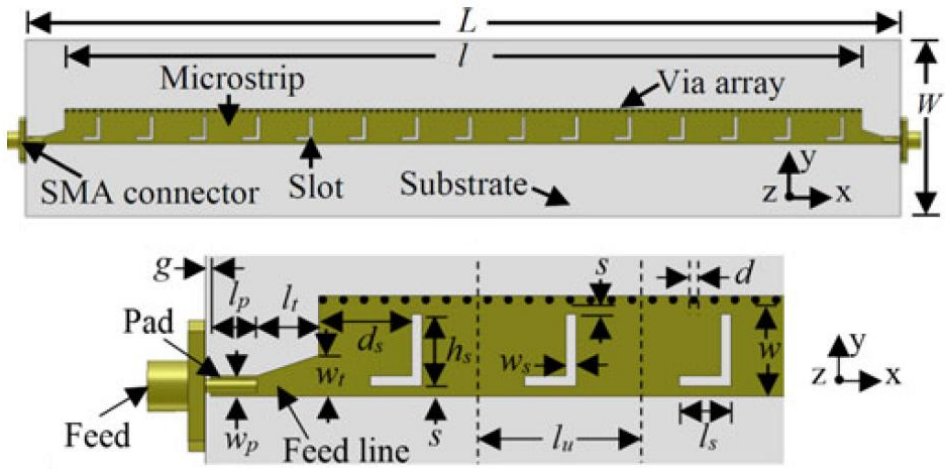

Fig. 2.17: Beam scanning leaky wave antenna designed by Karmokar et al. [189]. ©IEEE

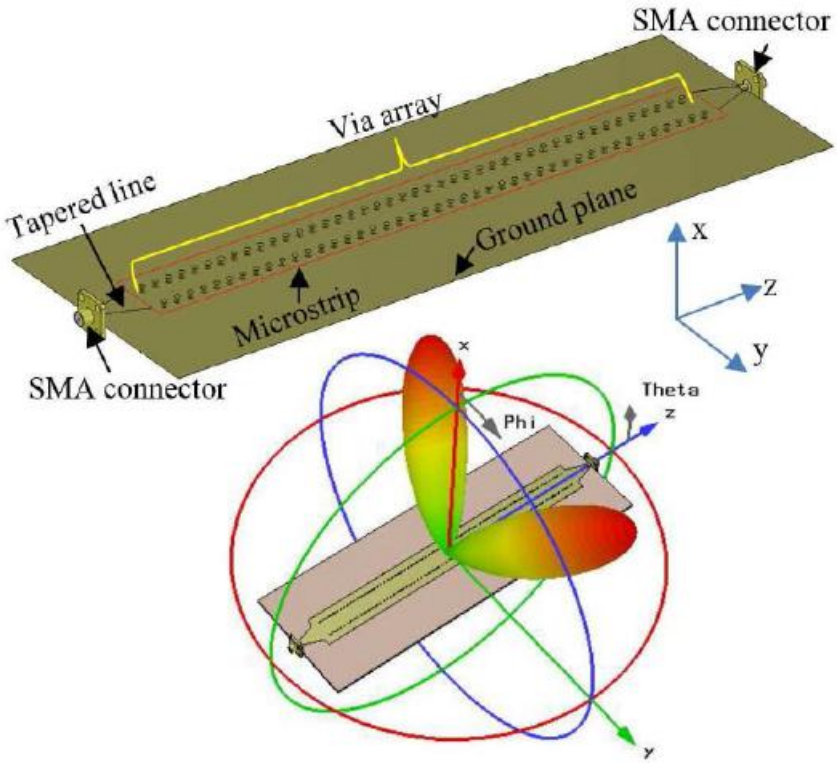

Fig. 2.18: Dual beam leaky wave antenna through excitation of the second higher order mode in microstrip line [190]. ©IEEE

REFERENCES:

[1] H. H. Beverage, C. W. Rice and E. W. Kellogg, "The Wave Antenna A New Type of Highly Directive Antenna," in *Transactions of the American Institute of Electrical Engineers*, vol. XLII, pp. 215-266, Jan. 1923.

[2] H. H. Beverage and H. O. Peterson, "Radio Transmission Measurements on Long Wave Lengths," *Proceedings of the Institute of Radio Engineers* , vol.11, no.6, pp. 661- 673, Dec. 1923.

[3] E. Bruce, "Developments in Short-Wave Directive Antennas," *Proceedings of the Institute of Radio Engineers* , vol.19, no.8, pp. 1406- 1433, Aug. 1931

[4] H. T. Friis and C. B. Feldman, "A Multiple Unit Steerable Antenna for Short-Wave Reception," *Proceedings of the Institute of Radio Engineers* , vol.25, no.7, pp. 841- 917, July 1937.

[5] E. Bruce, A. C Beck and L. R. Lowry, "Horizontal Rhombic Antennas," *Proceedings of the Institute of Radio Engineers* , vol.23, no.1, pp. 24- 46, Jan. 1935

[6] D. Foster, "Radiation from Rhombic Antennas," *Proceedings of the Institute of Radio Engineers* , vol.25, no.10, pp. 1327- 1353, Oct. 1937.

[7] J. R. James and P. S. Hall, "Microstrip antennas and arrays. Part 2: New array-design technique," in *IEE Journal on Microwaves, Optics and Acoustics*, vol. 1, no. 5, pp. 175-181, September 1977.

[8] P. S. Hall, "Microstrip linear array with polarisation control," *Microwaves, Optics and Antennas, IEE Proceedings H* , vol.130, no.3, pp.215-224, April 1983

[9] C. Wood, "Curved microstrip lines as compact wideband circularly polarised antennas," *Microwaves, Optics and Acoustics, IEE Journal on* , vol.3, no.1, pp.5, January 1979

[10] H. Nakano, T. Oka, K. Hirose and J. Yamauchi, "Analysis and measurements for improved crank-line antennas," IEEE Transactions on Antennas and Propagation, vol. 45, no. 7, pp. 1166-1172, Jul 1997.

[11] J. Henriksson, K. Markus and M. Tiuri, "A Circularly Polarized Traveling-Wave Chain Antenna," Microwave Conference, 1979. 9th European, Brighton, UK, 1979, pp. 174-178

[12] S. Nishimura, K. Nakano and T. Makimoto, "Franklin type microstrip line antenna," *Antennas and Propagation Society International Symposium, 1979*, Seattle, WA, USA, 1979, pp. 134-137

[13] M. Manteghi, A. Shooshtari and S. Safavi-Naeini, "A leaky transmission line method for the analysis of the microstrip line traveling wave antennas," *IEEE Antennas and Propagation Society International Symposium*, vol. 2, pp. 1138-1141, Jul 1997.

[14] Y. W. Liu, K. K. Mei and J. S. Hong, "Radiation extraction for transmission-line interconnects," *IEEE Antennas and Propagation Society International Symposium. 2001 Digest. Held in conjunction with: USNC/URSI National Radio Science Meeting (Cat. No.01CH37229)*, Boston, MA, USA, 2001, pp. 580-583 vol.1.

[15] L. Shafai and A. Sebak, "Radiation characteristics of microstrip serpent antennas," *Antennas and Propagation Society International Symposium*, 1984, Boston, MA, USA, 1984, pp. 55-57.

[16] M. I. Aksun and R. Mittra, "Estimation of spurious radiation from microstrip etches using closed-form Green's functions," IEEE Transactions on Microwave Theory and Techniques, vol. 40, no. 11, pp. 2063-2069, Nov 1992.

[17] M. I. Aksun and R. Mittra, "Spurious radiation from microstrip interconnects," in *IEEE Transactions on Electromagnetic Compatibility*, vol. 35, no. 2, pp. 148-158, May 1993

[18] H. Nakano and K. Hirose, "Numerical analysis of a crank-line array antenna," *Antennas and Propagation Society International Symposium, 1994. AP-S. Digest* vol.3, no., pp.1526-1529 vol.3, 20-24 Jun 1994

[19] H. Nakano, T. Oka, K. Hirose and J. Yamauchi, "Analysis and measurements for improved crank-line antennas," in *IEEE Transactions on Antennas and Propagation*, vol. 45, no. 7, pp. 1166-1172, July 1997..

[20] D. A. Hill, D. G. Camell, K. H. Cavcey, and G. H. Koepke, "Radiated emissions and immunity of microstrip transmission lines: Theory and reverberation chamber measurements," IEEE Trans. Electromagn. Compat., vol. 38, no. 2, pp. 165–172, May 1996.

[21] D. A. Hill, D. G. Camell, K. H. Cavcey, G. H. Koepke, *Radiated emissions and immunity of microstrip transmission lines: Theory and measurements*, 1995.4

[22] M. Leone, "Closed-Form Expressions for the Electromagnetic Radiation of Microstrip Signal Traces," IEEE Transactions on Electromagnetic Compatibility, vol. 49, no. 2, pp. 322-328, May 2007.

[23] A. Maffucci, G. Miano and F. Villone, "An enhanced transmission line model for conducting wires," in *IEEE Transactions on Electromagnetic Compatibility*, vol. 46, no. 4, pp. 512-528, Nov. 2004

[24] A. G. Chiariello, A. Maffucci, G. Miano, F. Villone and W. Zamboni, "A Transmission-Line Model for Full-Wave Analysis of Mixed-Mode Propagation," in *IEEE Transactions on Advanced Packaging*, vol. 31, no. 2, pp. 275-284, May 2008..

[25] T. Nakamura, K. Oda and S. Yokokawa, "Equivalent transmission lines of wire antennas and the radiation mechanism," *Electronics and Communications in Japan (Part I: Communications)*, *72*(8), pp.85-94, 1989.

[26] T. Nakamura, N. Hayashi, H. Fukuda and S. Yokokawa, "Radiation from the transmission line with an acute bend," in *IEEE Transactions on Electromagnetic Compatibility*, vol. 37, no. 3, pp. 317-325, Aug. 1995.

[27] A. K. Bhattacharyya, A.K.; , "Radiation characteristics of a long rectangular patch antenna," *Antennas and Propagation Society International Symposium, 1989. AP-S. Digest* , vol., no., pp.1692-1695 vol.3, 26-30 June 1989

[28] D. J. Tammen and P. E. Mayes, "An eigenvalue technique for analysis of traveling-wave microstrip antennas", Antennas and Propagation Society International Symposium, 1993. AP-S. Digest, vol. 3, 1993 ,pp. 1450 – 1453.

[29] Y. Kami and R. Sato, "Analysis of radiation characteristics of a finite-length transmission line using a circuit-concept approach," IEEE Transactions on Electromagnetic Compatibility, vol. 30, no. 2, pp. 114-121, May 1988.

[30] F. J. Meng, Y. X. Teo, D. W. P. Thomas and C. Christopoulos, "Fast Prediction of Transmission Line Radiated Emissions Using the Hertzian Dipole Method and Line-End Discontinuity Models," IEEE Transactions on Electromagnetic Compatibility, vol. 56, no. 6, pp. 1295-1303, Dec. 2014.

[31] M. Z. Mohd Jenu, and A. M. Sayegh, "Prediction of radiated emissions from high-speed printed circuit board traces using dipole antenna and imbalance difference model," in IET Science, Measurement & Technology, vol. 10, no. 1, pp. 28-37, 1 2016.

[32] S. Nishimura, Y. Sugio and T. Makimoto, "Crank-type circularly polarized microstrip line antenna," *1983 Antennas and Propagation Society International Symposium*, Houston, TX, USA, 1983, pp. 162-165.

[33] K. Hirose and H. Nkano, "A crank-line array antenna radiating a circularly polarized wave," in *IEEE Transactions on Antennas and Propagation*, vol. 45, no. 12, pp. 1881-1883, Dec. 1997.

[34] K. Hirose, K. Orihara and H. Nakano, "Formation of a circularly polarized tilted beam using radiation cells of a crank-line antenna," *Electronics and Communications in Japan (Part I: Communications)*, *84*(8), pp.23-30, 2001.

[35] D. Roscoe, L. Shafai and A. Ittipiboon, "Circularly polarised travelling-wave printed line antennas," in *Electronics Letters*, vol. 25, no. 20, pp. 1407-1408, 28 Sept. 1989.

[36] A. G. Roederer, "The cross antenna: a new low-profile circularly polarized radiator," in *IEEE Transactions on Antennas and Propagation*, vol. 38, no. 5, pp. 704-710, May 1990.

[37] C. Vázquez, C. García, Y. Álvarez, S. Ver-Hoeye and F. Las-Heras, "Near Field Characterization of an Imaging System Based on a Frequency Scanning Antenna Array," in *IEEE Transactions on Antennas and Propagation*, vol. 61, no. 5, pp. 2874-2879, May 2013.

[38] M. Ranjbar Naeini, M. Fakharzadeh and F. Farzaneh, "Travelling-wave Ka-band Frequency Scanning Antennas for millimeter-wave imaging applications," *2016 8th International Symposium on Telecommunications (IST)*, Tehran, 2016, pp. 591-595.

[39] A. Michel, A. Buffi, R. Caso, P. Nepa, G. Isola and H. T. Chou, "Design and performance analysis of a planar antenna for near-field UHF-RFID desktop readers," *2012 Asia Pacific Microwave Conference Proceedings*, Kaohsiung, 2012, pp. 1019-1021.

[40] A. Michel, R. Caso, A. Buffi, P. Nepa and G. Isola, "An array of meander Travelling Wave Antennas for near-field UHF-RFID readers," *2013 IEEE Antennas and Propagation Society International Symposium (APSURSI)*, Orlando, FL, 2013, pp. 1732-1733.

[41] D. B. Oliveira and E. J. Silva, "Design of the compact UHF RFID meander-line antenna loaded with CPW elements," *AEU-International Journal of Electronics and Communications*, *77*, pp.57-60, 2017.

[42] A. D. Searle *et al*., "Millimetre wave antennas for vehicle based telematic applications," *IEE Colloquium MM-Wave Circuits and Technology for Commercial Applications (Ref. No. 1999/007)*, London, UK, 1999, pp. 9/1-9/6.

[43] H. Moheb, L. Shafai and M. Barakat, "Design of 24 GHz microstrip travelling wave antenna for radar application," *IEEE Antennas and Propagation Society International Symposium. 1995 Digest*, Newport Beach, CA, USA, 1995, pp. 350-353 vol.1.

[44] D. Jaisson, "Quasi-static model for circular transmission lines," *Proceedings of 1995 SBMO/IEEE MTT-S International Microwave and Optoelectronics Conference*, Rio de Janeiro, Brazil, 1995, pp. 825-828 vol.2.

[45] Cheng-Cheh Yu and Kai Chang, "Transmission-line analysis of a capacitively coupled microstrip-ring resonator," in *IEEE Transactions on Microwave Theory and Techniques*, vol. 45, no. 11, pp. 2018-2024, Nov. 1997.

[46] P. Gardner and D. K. Paul, "Transmission line analysis of symmetrical ring resonators," in *IEE Proceedings - Microwaves, Antennas and Propagation*, vol. 143, no. 2, pp. 184-188, April 1996.

[47] T. K. Chen and G. H. Huff, "Transmission line analysis of the Archimedean spiral antenna in free space," *Journal of Electromagnetic Waves and Applications*, *28*(10), pp.1175-1193, 2014.

[48] R. J. Barton, P. J. Collins, P. E. Crittenden, M. J. Havrilla and A. J. Terzuoli, "Analytical Development of the Far-Zone Radiation Integral for an Arbitrary Planar Spiral Antenna," in *IEEE Antennas and Propagation Magazine*, vol. 52, no. 2, pp. 19-30, April 2010.

[49] L. Lewin, Electromagnetic Waves and Curved Structures, New York:IEEE Press, 1977, pp. 36.

[50] L. Lewin, Theory of waveguides: Techniques for the solution of waveguide problems. *New York, Halsted Press, 1975. 356 p.*, 1975.

[51] I. Wolff and V. K. Tripathi, "The Microstrip Open-Ring Resonator," in *IEEE Transactions on Microwave Theory and Techniques*, vol. 32, no. 1, pp. 102-107, Jan. 1984.

[52] V. K. Tripathi and I. Wolff, "Perturbation for Open Analysis and Design Equations and Closed-Ring Microstrip Resonators," in *IEEE Transactions on Microwave Theory and Techniques*, vol. 32, no. 4, pp. 405-410, Apr. 1984.

[53] A. Weisshaar and V. K. Tripathi, "Perturbation analysis and modeling of curved microstrip bends," in *IEEE Transactions on Microwave Theory and Techniques*, vol. 38, no. 10, pp. 1449-1454, Oct. 1990.

[54] A. Weisshaar, 1991. Generalized modal analysis of electromagnetic-and quantum-waveguide structures and discontinuities, Ph. D. thesis, Oregon State University.

[55] G. Kompa and R. Mehran, "Planar waveguide model for calculating microstrip components," in *Electronics Letters*, vol. 11, no. 19, pp. 459-460, 18 September 1975.

[56] E. Kühn, "A mode-matching method for solving field problems in waveguide and resonator circuits", *Arch. Elek. übertragung.*, vol. 27, pp. 511-513, Dec. 1973.

[57] J. S. Roy, D. R. Poddar, A. Mukherjee and S. K. Chowdhury, "Dispersion characteristics of curved microstrip transmission lines," in *IEEE Transactions on Microwave Theory and Techniques*, vol. 38, no. 9, pp. 1366-1370, Sep 1990.

[58] J. S. Roy, D. R. Poddar and S. K. Chowdhury, "High-frequency behaviour of curved microstrip lines," *International Journal of Electronics Theoretical and Experimental*, *70*(1), pp.183-193, 1991.

[59] K. Hosseini and Z. Atlasbaf, "Analysis and Synthesis of Singly-Curved Microstrip Structures Utilizing Modified Schwarz-Christoffel Transformation," Antennas and Propagation, IEEE Transactions on. 61. 5940-5947, 2013.

[60] Z. Zhang, D. Gruner and G. Boeck, "Modeling of integrated microstrip bend structures on silicon substrates up to 110 GHz," *18-Th International Conference On Microwaves, Radar And Wireless Communications*, Vilnius, 2010, pp. 1-4.

[61] A. Weisshaar, S. M. Goodnick and V. K. Tripathi, "A rigorous and efficient method of moments solution for curved waveguide bends," in *IEEE Transactions on Microwave Theory and Techniques*, vol. 40, no. 12, pp. 2200-2206, Dec. 1992.

[62] S. K. Khamas and G. G. Cook, "Moment-method analysis of printed wire spirals using curved piecewise sinusoidal subdomain basis and testing functions," in *IEEE Transactions on Antennas and Propagation*, vol. 45, no. 6, pp. 1016-1022, June 1997.

[63] Rong-Lin Li and H. Nakano, "Numerical analysis of arbitrarily shaped probe-excited single-arm printed wire antennas," in *IEEE Transactions on Antennas and Propagation*, vol. 46, no. 9, pp. 1307-1317, Sept. 1998.

[64] S. K. Khamas and G. G. Cook, "Moment method analysis of printed eccentric spiral antennas using curved segmentation," in *IEE Proceedings - Microwaves, Antennas and Propagation*, vol. 146, no. 6, pp. 407-410, Dec. 1999.

[65] Hsueh-Yung Chao, Jun-Sheng Zhao and Weng Cho Chew, "Application of curvilinear basis functions and MLFMA for radiation and scattering problems involving curved PEC structures," in *IEEE Transactions on Antennas and Propagation*, vol. 51, no. 2, pp. 331-336, Feb. 2003.

[66] S. K. Khamas, P. L. Starke and G. G. Cook, "Design of a printed spiral antenna with a dielectric superstrate using an efficient curved segment moment method with optimisation using marginal distributions," in *IEE Proceedings - Microwaves, Antennas and Propagation*, vol. 151, no. 4, pp. 315-320, 15 Aug. 2004.

[67] S. K. Khamas, "Moment Method Analysis of an Archimedean Spiral Printed on a Layered Dielectric Sphere," in *IEEE Transactions on Antennas and Propagation*, vol. 56, no. 2, pp. 345-352, Feb. 2008.

[68] D. M. Petkovic and D. D. Krstic, "Parabolically Bent Dipole Antenna," *TELSIKS 2005 - 2005 uth International Conference on Telecommunication in ModernSatellite, Cable and Broadcasting Services*, Nis, 2005, pp. 471-474.

[69] S. D. Rogers and C. M. Butler, "An efficient curved-wire integral equation solution technique," in *IEEE Transactions on Antennas and Propagation*, vol. 49, no. 1, pp. 70-79, Jan 2001.

[70] S. D. Rogers, C. M. Butler and A. Q. Martin, "Realization of a genetic-algorithm-optimized wire antenna with 5: 1 bandwidth." *Radio Science*, *36*(6), pp.1315-1325, 2001.

[71] T. K. Chen and G. H. Huff, "On the constant input impedance of the Archimedean spiral antenna in free-space" *IEEE Transactions on Antennas and Propagation*, *62*(7), pp.3869-3872, 2014.

[72] M. Ali, S. S. Stuchly and K. Caputa, "An experimental study of small self-resonant antennas for wireless applications," *Microwave and Optical Technology Letters*, *35*(2), pp.143-145, 2002.

[73] C. G. Kakoyiannis, P. Gika and P. Constantinou, "Compact multi-element antennas of sinusoidal printed monopoles for sensors and portable devices," *2009 3rd European Conference on Antennas and Propagation*, Berlin, 2009, pp. 3423-3427.

[74] C. G. Kakoyiannis and P. Constantinou, "Radiation properties and ground-dependent response of compact printed sinusoidal antennas and arrays," *IET microwaves, antennas & propagation*, *4*(5), pp.629-642, 2010.

[75] D. K. Cheng and C. H. Liang, "Shaped wire antennas with maximum directivity," *Electronics Letters*, *18*(19), pp.816-818, 1982.

[76] K. C. Lee, "Optimization of bent wire antennas using genetic algorithms," *Journal of electromagnetic waves and applications*, *16*(4), pp.515-522, 2002.

[77] D. K. Cheng and C. H. Liang, "Shaped wire antennas with maximum directivity," in *Electronics Letters*, vol. 18, no. 19, pp. 816-818, 16 September 1982.

[78] K. C. Lee, "Optimization of bent wire antennas using genetic algorithms," *Journal of electromagnetic waves and applications*, *16*(4), pp.515-522, 2002.

[79] R. M. Edwards, G. G. Cook, S. K. Khamas, R. J. Aidley and B. Chambers, "Design of circularly polarised printed spiral antenna using dual objective genetic algorithm," in *Electronics Letters*, vol. 34, no. 7, pp. 608-609, 2 April 1998.

[80] Rong-Lin Li, V. F. Fusco and H. Nakano, "Circularly polarized open-loop antenna," in *IEEE Transactions on Antennas and Propagation*, vol. 51, no. 9, pp. 2475-2477, Sept. 2003.

[81] K. Hirose, Y. Nagata and H. Nakano, "Novel dual-loop antennas radiating a circularly polarized wave," *2013 IEEE Antennas and Propagation Society International Symposium (APSURSI)*, Orlando, FL, 2013, pp. 1466-1467.

[82] Rong-Lin Li and V. F. Fusco, "Printed figure-of-eight wire antenna for circular polarization," in *IEEE Transactions on Antennas and Propagation*, vol. 50, no. 10, pp. 1487-1490, Oct. 2002.

[83] A. O. Salman, H. Cetinkaya and A. A. Vertiy, "Actively and passively excited sinusoidal microstrip and PCB strip antennas operating at K and millimeter-wave bands," *Microwave and Optical Technology Letters*, *50*(5), pp.1302-1308, 2008.

[84] A. O. Salman, D. Dibekci, S. Gavrilov and A. A. Vertiy, "The millimeter wave radiation of a traveling wave sinusoidal wire antenna," *International Journal of Infrared and Millimeter Waves*, *29*(5), pp.465-485, 2008.

[85] A. A. Vertiy, S. P. Gavrilov, V. N. Stepanyuk and A. O. Salman, "mm-wave radiation by the undulator type wire antennas," *Infrared and Millimeter Waves, Conference Digest of the 2004 Joint 29th International Conference on 2004 and 12th International Conference on Terahertz Electronics, 2004.*, Karlsruhe, Germany, 2004, pp. 695-696

[86] A. O. Salman, D. Dibekci, S. P. Gavrilov and A. A. Vertiy, "The Radiation Properties of a Novel Wire Antenna for the Security Fence Radar," in *IEEE Transactions on Antennas and Propagation*, vol. 56, no. 9, pp. 2852-2864, Sept. 2008.

[87] A. A. Vertiy, S. P. Gavrilov, V. N. Stepanyuk and A. O. Salman, "Sommerfeld wave diffraction by the undulator wire segments," *The Fifth International Kharkov Symposium on Physics and Engineering of Microwaves, Millimeter, and Submillimeter Waves (IEEE Cat. No.04EX828)*, Kharkov, Ukraine, 2004, pp. 302-304 Vol.1.

[88] A. T. Starr, "The Nonuniform Transmission Line," in *Proceedings of the Institute of Radio Engineers*, vol. 20, no. 6, pp. 1052-1063, June 1932.

[89] L. R. Walker and N. Wax, "Non-uniform transmission lines and reflection coefficients," *Journal of Applied Physics*, *17*(12), pp.1043-1045, 1946.

[90] G. I. Cohn and B. Saltzberg, "Solution of nonlinear differential equations by the reversion method," *Journal of Applied Physics*, *24*(2), pp.180-186, 1953.

[91] L. A. Pipes, "The reversion method for solving nonlinear differential equations,". *Journal of Applied Physics*, *23*(2), pp.202-207, 1952.

[92] H. Kaufman, "Bibliography of nonuniform transmission lines," *IRE Transactions on Antennas and Propagation*, *3*(4), pp.218-220, 1955.

[93] L. A. Pipes "Computation of the impedances of nonuniform lines by a direct method," *Transactions of the American Institute of Electrical Engineers, Part I: Communication and Electronics*, *75*(5), pp.551-554, 1956.

[94] E. F. Bolinder, "Fourier transforms and tapered transmission lines," In *IRE Proc.* (Vol. 44, p. 557), 1956.

[95] R. E. Collin, "The optimum tapered transmission line matching section," *Proceedings of the IRE*, *44*(4), pp.539-548, 1956.

[96] B. G. Kazansky, "Outline of a theory of non-uniform transmission lines,". *Proceedings of the IEE-Part C: Monographs*, *105*(7), pp.126-138, 1958.

[97] I. Sugai, "D'Alemberts Method For Nonuniform Transmission Lines," *Proceedings Of The Institute Of Radio Engineers*, *49*(4), pp.823, 1961.

[98] I. Sugai, "Riccati's nonlinear differential equation." *The American Mathematical Monthly*, *67*(2), pp.134-139, 1960.

[99] I. Sugai, "The solutions for nonuniform transmission line problems," *Proceedings of the Institute of Radio Engineers*, *48*(8), pp.1489-1490, 1960.

[100] Sugai, I., 1961. Riccati's and Bernoulli's equations for nonuniform transmission lines. *IRE Transactions on Circuit Theory*, *8*(3), pp.359-360.

[101] C. P. Womack, "The use of exponential transmission lines in microwave components," *IRE Transactions on Microwave Theory and Techniques*, *10*(2), pp.124-132, 1962.

[102] J. Ekstrom, "The Z-matrix parameters of tapered transmission lines," *IRE Transactions on Circuit Theory*, *9*(2), pp.132-135, 1962.

[103] S. D. Roy, "Matrix parameters of nonuniform transmission lines," *IEEE Transactions on Circuit Theory*, *12*(1), pp.142-143, 1965.

[104] N. V. Nair, and A. K. Mallick, "An analysis of a width-modulated microstrip periodic structure," *IEEE transactions on microwave theory and techniques*, *32*(2), pp.200-204, 1984.

[105] K. Lu, "An efficient method for analysis of arbitrary nonuniform transmission lines," IEEE *Transactions on Microwave Theory and Techniques*, *45*(1), pp.9-14, 1997.

[106] C. Nwoke, "An exact solution for the nonuniform transmission line problem,". *IEEE Transactions on Microwave Theory and Techniques*, *38*(7), pp.944-946, 1990.

[107] M. Chernobryvko, D. De Zutter and D. V. Ginste, "Nonuniform Multiconductor Transmission Line Analysis by a Two-Step Perturbation Technique," in *IEEE Transactions on Components, Packaging and Manufacturing Technology*, vol. 4, no. 11, pp. 1838-1846, Nov. 2014.

[108] N. Nguyen-Trong, L. Hall and C. Fumeaux, "Transmission-Line Model of Nonuniform Leaky-Wave Antennas," in *IEEE Transactions on Antennas and Propagation*, vol. 64, no. 3, pp. 883-893, March 2016.

[109] N. H. Younan, B. L. Cox, C. D. Taylor and W. D. Prather, "An exponentially tapered transmission line antenna," *IEEE transactions on electromagnetic compatibility*, *36*(2), pp.141-144, 1994.

[110] A. Cheldavi, "Radiation from multiconductor transmission lines: exact time-domain analysis," Electromagnetics l(23): 55–70, 2003.

[111] M. Khalaj-Amirhosseini, "Analysis of coupled nonuniform transmission lines using Taylor's series expansion," *IEEE transactions on electromagnetic compatibility*, *48*(3), pp.594-600, 2006.

[112] M. Khalaj-Amirhosseini, "Analysis of periodic and aperiodic coupled nonuniform transmission lines using the Fourier series expansion," *Progress In Electromagnetics Research*, *65*, pp.15-26, 2006.

[113] F. J. Glandorf and I. Wolff, "A Spectral-Domain Analysis of Periodically Nonuniform Microstrip Lines," in *IEEE Transactions on Microwave Theory and Techniques*, vol. 35, no. 3, pp. 336-343, Mar 1987.

[114] A. H. Hamade, A. B. Kouki F. M. Ghannouchi, "An efficient approach suitable for the analysis and design of nonuniform transmission lines," *Microwave and Optical Technology Letters*, *10*(3), pp.146-150, 1995.

[115] N. Boulejfen, A. B. Kouki and F. M. Ghannouchi, "Frequency- and time-domain analyses of nonuniform lossy coupled transmission lines with linear and

nonlinear terminations," in *IEEE Transactions on Microwave Theory and Techniques*, vol. 48, no. 3, pp. 367-379, Mar 2000.

[116] M. Khalaj-Amirhosseini, "Analysis of coupled or single nonuniform transmission lines using the method of Moments," *International Journal of RF and Microwave Computer-Aided Engineering*, *18*(4), pp.376-382, 2008.

[117] T. Lopetegi *et al*., "New microstrip "Wiggly-Line" filters with spurious passband suppression," in *IEEE Transactions on Microwave Theory and Techniques*, vol. 49, no. 9, pp. 1593-1598, Sep 2001.

[118] D. Nesic, and B. Kolundzija, "Band-stop filter with suppression of requested number of spurious stopbands," *International Journal of Microwave and Wireless Technologies, 9*(5), 995-1002, 2017.

[119] K. Al Shamaileh, A. Qaroot, N. Dib and A. Sheta, "Design and analysis of multifrequency Wilkinson power dividers using nonuniform transmission lines." Int J RF and Microwave Comp Aid Eng, 21: 526–533, 2011.

[120] K. A. Shamaileh, M. Almalkawi, V. K. Devabhaktuni, N. I. Dib, B. Henin, and A. M. Abbosh, "Non-uniform transmission line ultra-wideband wilkinson power divider," *Progress In Electromagnetics Research C*, Vol. 44, 1-11, 2013.

[121] L. Tani and N. E. Ouazzani, "Minimizing crosstalk on printed circuit board using non uniform guard traces," *2016 International Conference on Information Technology for Organizations Development (IT4OD)*, Fez, 2016, pp. 1-4

[122] P. M. Narayanan, P. Rulikowski and J. Barrett, "Miniaturization of nonuniform transmission lines for ultra-wideband pulse shaping," *2011 IEEE International Conference on Microwaves, Communications, Antennas and Electronic Systems (COMCAS 2011)*, Tel Aviv, 2011, pp. 1-6.

[123] M. S. Liang, B. Z. Wang, Z. M. Zhang and S. Ding, "Simplified Pulse Shaping Network for Microwave Signal Focusing Based on Time Reversal," in *IEEE Antennas and Wireless Propagation Letters*, vol. 14, pp. 225-228, 2015.

[124] J. D. Schwartz, J. Azana and D. V. Plant, "Real-Time Microwave Signal Processing Using Microstrip Technology," *2006 IEEE MTT-S International Microwave Symposium Digest*, San Francisco, CA, 2006, pp. 1991-1994.

[125] M. A. G. Laso *et al*., "Real-time spectrum analysis in microstrip technology," in *IEEE Transactions on Microwave Theory and Techniques*, vol. 51, no. 3, pp. 705-717, Mar 2003.

[126] S. K. Podilchak, L. Matekovits, A. P. Freundorfer, Y. M. M. Antar and M. Orefice, "Controlled Leaky-Wave Radiation From a Planar Configuration of Width-Modulated Microstrip Lines," in *IEEE Transactions on Antennas and Propagation*, vol. 61, no. 10, pp. 4957-4972, Oct. 2013.

[127] A. J. Martínez-Ros, J. L. Gómez-Tornero, F. J. Clemente-Fernández and J. Monzó-Cabrera, "Microwave Near-Field Focusing Properties of Width-Tapered Microstrip Leaky-Wave Antenna," in *IEEE Transactions on Antennas and Propagation*, vol. 61, no. 6, pp. 2981-2990, June 2013.

[128] A. J. Martinez-Ros, J. L. Gómez-Tornero, V. Losada, F. Mesa and F. Medina, "Non-Uniform Sinusoidally Modulated Half-Mode Leaky-Wave Lines for Near-Field Focusing Pattern Synthesis," in *IEEE Transactions on Antennas and Propagation*, vol. 63, no. 3, pp. 1022-1031, March 2015.

[129] W. W. Hansen, Leland Stanford Junior University, 1946. *Radiating electromagnetic wave guide*. U.S. Patent 2,402,622.

[130] N. Marcuvitz, "On field representations in terms of leaky modes or eigenmodes," *IRE transactions on antennas and propagation*, *4*(3), pp.192-194, 1956.

[131] L. Goldstone and A. A. Oliner, "Leaky-wave antennas I: Rectangular waveguides," *IRE Transactions on Antennas and propagation*, *7*(4), pp.307-319, 1959.

[132] L. Goldstone and A. A. Oliner, "Leaky wave antennas II: Circular waveguides,". *IRE Transactions on Antennas and Propagation*, *9*(3), pp.280-290, 1961.

[133] T. Tamir and A. A. Oliner, "Guided complex waves. Part 1: Fields at an interface," In *Proceedings of the Institution of Electrical Engineers* (Vol. 110, No. 2, pp. 310-324). IET Digital Library, 1963.

[134] T. Tamir and A. A. Oliner, "Guided complex waves. Part 2: Relation to radiation patterns," In *Proceedings of the Institution of Electrical Engineers* (Vol. 110, No. 2, pp. 325-334). IET Digital Library, 1963.

[135] R. Garg, K. Gupta and R. Sharan, "A thin wall leaky waveguide antenna," *IEEE Transactions on Antennas and Propagation*, *23*(1), pp.107-112, 1975.

[136] W. Menzel, "A New Travelling Wave Antenna in Microstrip," *1978 8th European Microwave Conference*, Paris, France, 1978, pp. 302-306.

[137] A. K. Bhattacharyya, 'Long rectangular patch antenna with a single feed', *IEEE Transactions on Antennas and Propagation*, 1990, 38, (7), pp. 987–993

[138] C. Luxey and J. M. Laheurte, "Simple design of dual-beam leaky-wave antennas in microstrips," *IEE Proceedings-Microwaves, Antennas and Propagation*, *144*(6), pp.397-402, 1997.

[139] A. A. Oliner and K. S. Lee, "The nature of the leakage from higher modes on microstrip line," In *Microwave Symposium Digest, 1986 IEEE MTT-S International* (pp. 57-60). IEEE, 1986

[140] A. A. Oliner, *Scannable millimeter wave arrays volume II*, pp. 304-315, Apr. 1989

[141] H. Ermert, "Guided Modes and Radiation Characteristics of Covered Microstrip Lines", *A.E.U.*, vol. 30, pp. 65-70, February 1976.

[142] H. Ermert, "Guiding and Radiation Characteristics of Planar Waveguides", *IEE Microwave Optics and Acoustics*, vol. 3, pp. 59-62, March 1979.

[143] D. R. Jackson and A. A. Oliner, "A leaky-wave analysis of the high-gain printed antenna configuration," in *IEEE Transactions on Antennas and Propagation*, vol. 36, no. 7, pp. 905-910, July 1988.

[144] F. J. Villegas, D. R. Jackson, J. T. Williams and A. A. Oliner, "Leakage fields from planar semi-infinite transmission lines," in *IEEE Transactions on Microwave Theory and Techniques*, vol. 47, no. 4, pp. 443-454, April 1999.

[145] P. Burghignoli, C. Di Nallo, F. Frezza, A. Galli and P. Lampariello, "Efficient description of impedance and radiation features in printed-circuit leaky-wave structures-an unconventional scattering-matrix approach," in *IEEE Transactions on Microwave Theory and Techniques*, vol. 48, no. 10, pp. 1661-1672, Oct. 2000.

[146] T. T. Wu, "Theory of the microstrip," *Journal of Applied Physics*, *28*(3), pp.299-302, 1957.

[147] J. Boukamp and R. H. Jansen "Spectral domain investigation of surface wave excitation and radiation by microstrip lines and microstrip disk resonators," In *Microwave Conference, 1983. 13th European* (pp. 721-726). IEEE, 1983.

[148] J. S. Bagby, C. H. Lee, D. P. Nyquist and Y. Yuan, "Identification of propagation regimes on integrated microstrip transmission lines," *IEEE transactions on microwave theory and techniques*, *41*(11), pp.1887-1894, 1993.

[149] J. M. Grimm and D. P. Nyquist, "Spectral analysis considerations relevant to radiation and leaky modes of open-boundary microstrip transmission line," *IEEE transactions on microwave theory and techniques*, *41*(1), pp.150-153, 1993.

[150] K. A. Michalski and D. Zheng, "Rigorous analysis of open microstrip lines, of arbitrary cross section in bound and leaky regimes," *IEEE Transactions on Microwave Theory and Techniques*, *37*(12), pp.2005-2010, 1989.

[151] K. A. Michalski and D. Zheng, "On the leaky modes of open microstrip lines,". *Microwave and Optical Technology Letters*, *2*(1), pp.6-8, 1989.

[152] Y. D. Lin and J. W. Sheen, "Mode distinction and radiation-efficiency analysis of planar leaky-wave line source," *IEEE transactions on microwave theory and techniques*, *45*(10), pp.1672-1680, 1997.

[153] F. Mesa and D. R. Jackson, "Investigation of integration paths in the spectral-domain analysis of leaky modes on printed circuit lines," *IEEE transactions on microwave theory and techniques*, *50*(10), pp.2267-2275, 2002.

[154] Y. L. Chow, J. J. Yang, D. G. Fang and G. E. Howard, "A closed-form spatial Green's function for the thick microstrip substrate," *IEEE Transactions on Microwave Theory and Techniques*, *39*(3), pp.588-592, 1991.

[155] J. M. Grimm and D. P. Nyquist, "Spectral analysis considerations relevant to radiation and leaky modes of open-boundary microstrip transmission line," *IEEE transactions on microwave theory and techniques*, *41*(1), pp.150-153, 1993.

[156] R. Rodriguez-Berral, F. Mesa, P. Baccarelli and P. Burghignoli, "Excitation of a Periodic Microstrip Line by an Aperiodic Delta-Gap Source," in *IEEE Antennas and Wireless Propagation Letters*, vol. 8, pp. 641-644, 2009.

[157] F. Mesa and R. Marques, "Integral representation of spatial Green's function and spectral domain analysis of leaky covered strip-like lines," in *IEEE Transactions on Microwave Theory and Techniques*, vol. 43, no. 4, pp. 828-837, April 1995.

[158] F. Mesa, C. di Nallo and D. R. Jackson, "The theory of surface-wave and space-wave leaky-mode excitation on microstrip lines," in *IEEE Transactions on Microwave Theory and Techniques*, vol. 47, no. 2, pp. 207-215, Feb. 1999.

[159] J. Liu and Y. Long, "Formulas for complex propagation constant of first higher mode of microstrip line," in *Electronics Letters*, vol. 44, no. 4, pp. 261-262, 14 February 2008.

[160] Wanchu Hong, Tai-Lee Chen, Chi-Yang Chang, J. -. Sheen and Yu-De Lin, "Broadband tapered microstrip leaky-wave antenna," in *IEEE Transactions on Antennas and Propagation*, vol. 51, no. 8, pp. 1922-1928, Aug. 2003.

[161] G. Lovat, P. Burghignoli and D. R. Jackson, "Fundamental properties and optimization of broadside radiation from uniform leaky-wave antennas," in *IEEE Transactions on Antennas and Propagation*, vol. 54, no. 5, pp. 1442-1452, May 2006.

[162] V. R. Komanduri, D. R. Jackson and S. A. Long, "Radiation characteristics of finite-length 1D-uniform leaky wave antennas radiating at broadside," *2010 IEEE Antennas and Propagation Society International Symposium*, Toronto, ON, 2010, pp. 1-4.

[163] G. M. Zelinski, G. A. Thiele, M. L. Hastriter, M. J. Havrilla and A. J. Terzuoli, "Half width leaky wave antennas" *IET Microwaves, Antennas & Propagation*, *1*(2), pp.341-348, 2007.

[164] D. Xie and L. Zhu, "Microstrip Leaky-Wave Antennas With Nonuniform Periodical Loading of Shorting Pins for Enhanced Frequency Sensitivity," in *IEEE Transactions on Antennas and Propagation*, vol. 66, no. 7, pp. 3337-3345, July 2018.

[165] D. Xie, L. Zhu and X. Zhang, "An EH_0-Mode Microstrip Leaky-Wave Antenna With Periodical Loading of Shorting Pins," in *IEEE Transactions on Antennas and Propagation*, vol. 65, no. 7, pp. 3419-3426, July 2017.

[166] D. Xie, L. Zhu, X. Zhang and N. Liu, "Gain-enhanced EH_1 mode microstrip leaky-wave antenna with periodical loading of shorting pins," in *IET Microwaves, Antennas & Propagation*, vol. 12, no. 2, pp. 230-236, 7 2 2018.

[167] D. Killips, J. Radcliffe, L. Kempel, S. Schneider, "Radiation by a linear array of half-width leaky-wave antennas", *ACES J.*, vol. 21, no. 3, pp. 248-255, Nov. 2006.

[168] G. Cheng and C. C. Tzuang, "Closely coupled half-width leaky-wave antenna array," *2012 6th European Conference on Antennas and Propagation (EUCAP)*, Prague, 2012, pp. 957-960.

[169] D. K. Karmokar, K. P. Esselle, T. S. Bird and S. G. Hay, "Conical beaming using simple arrays of uniform half-width microstrip leaky-wave antennas," *2015 IEEE 4th Asia-Pacific Conference on Antennas and Propagation (APCAP)*, Kuta, 2015, pp. 90-91.

[170] L. Brillouin, 2003. *Wave propagation in periodic structures: electric filters and crystal lattices*. Courier Corporation.

[171] L. Brillouin, 2013. *Wave propagation and group velocity* (Vol. 8). Academic Press.

[172] R. E. Collin, 2007. *Foundations for microwave engineering*. John Wiley & Sons.

[173] A. Ishimaru, 1978. *Wave propagation and scattering in random media*. Academ. Press.

[174] R. E. Collin, 1960. Field theory of guided waves.

[175] A. F. Harvey, Periodic and Guiding Structures at Microwave Frequencies, IRE Trans. Microw. Theory Tech., vol. 8, no. 1, pp. 30-61, January 1960.

[176] A. A. Oliner, "Radiating periodic structure: analysis in terms of k vs. β diagrams", in *Short Course on Microwave Field and Network Techniques*, Polytechnic Institute of Brooklyn, New York, 1963

[177] M. Tsuji, H. Shigesawa and A. Oliner, "Microwave network design approach to dielectric perioic leaky-wave antennas," *1986 Antennas and Propagation Society International Symposium*, Philadelphia, PA, USA, 1986, pp. 145-148.

[178] M. Guglielmi and A. A. Oliner, "A Practical Theory for Dielectric Image Guide Leaky-Wave Antennas Loaded by Periodic Metal Strips," *1987 17th European Microwave Conference*, Rome, Italy, 1987, pp. 549-554.

[179] S. Majumder, D. R. Jackson and M. Guglielmi, "The nature of the spectral gap for leaky waves on a periodic strip grating structure," *1997 IEEE MTT-S International Microwave Symposium Digest*, Denver, CO, USA, 1997, pp. 479-482 vol.2.

[180] P. Burghignoli, L. Pajewski, F. Frezza, A. Galli and G. Schettini, "Improved quadrature formulas for boundary integral equations with conducting or dielectric

edge singularities," in *IEEE Transactions on Antennas and Propagation*, vol. 52, no. 2, pp. 373-379, Feb. 2004.

[181] P. Baccarelli, S. Paulotto, D. R. Jackson and A. A. Oliner, "A New Brillouin Dispersion Diagram for 1-D Periodic Printed Structures," in *IEEE Transactions on Microwave Theory and Techniques*, vol. 55, no. 7, pp. 1484-1495, July 2007.

[182] P. Baccarelli, C. Di Nallo, S. Paulotto and D. R. Jackson, "A full-wave numerical approach for modal analysis of 1-D periodic microstrip structures," in *IEEE Transactions on Microwave Theory and Techniques*, vol. 54, no. 4, pp. 1350-1362, June 2006.

[183] P. Burghignoli, G. Lovat and D. R. Jackson, "Analysis and Optimization of Leaky-Wave Radiation at Broadside From a Class of 1-D Periodic Structures," in *IEEE Transactions on Antennas and Propagation*, vol. 54, no. 9, pp. 2593-2604, Sept. 2006.

[184] S. Paulotto, P. Baccarelli, F. Frezza and D. R. Jackson, "A Novel Technique for Open-Stopband Suppression in 1-D Periodic Printed Leaky-Wave Antennas," in *IEEE Transactions on Antennas and Propagation*, vol. 57, no. 7, pp. 1894-1906, July 2009.

[185] W. Fuscaldo, D. R. Jackson and A. Galli, "A General and Accurate Formula for the Beamwidth of 1-D Leaky-Wave Antennas," in *IEEE Transactions on Antennas and Propagation*, vol. 65, no. 4, pp. 1670-1679, April 2017.

[186] Lei Liu, C. Caloz and T. Itoh, "Dominant mode leaky-wave antenna with backfire-to-endfire scanning capability," in *Electronics Letters*, vol. 38, no. 23, pp. 1414-1416, 7 Nov. 2002.

[187] S. Otto, 2016. Solution to the Broadside Problem and Symmetry Properties in Periodic Leaky-Wave Antennas.

[188] S. Otto, A. Rennings, K. Solbach, C. Caloz, "Transmission line modeling and asymptotic formulas for periodic leaky-wave antennas scanning through broadside," *IEEE Transactions on Antennas and Propagation*, *59*(10), pp.3695-3709, 2011.

[189] D. K. Karmokar, K. P. Esselle and T. S. Bird, "Wideband Microstrip Leaky-Wave Antennas With Two Symmetrical Side Beams for Simultaneous Dual-

Beam Scanning," in *IEEE Transactions on Antennas and Propagation*, vol. 64, no. 4, pp. 1262-1269, April 2016.

[190] D. K. Karmokar, Y. J. Guo, P. Qin, K. P. Esselle and T. S. Bird, "Forward and Backward Beam-Scanning Tri-Band Leaky-Wave Antenna," in *IEEE Antennas and Wireless Propagation Letters*, vol. 16, pp. 1891-1894, 2017.

[191] D. K. Karmokar, K. P. Esselle and S. G. Hay, "Fixed-Frequency Beam Steering of Microstrip Leaky-Wave Antennas Using Binary Switches," in *IEEE Transactions on Antennas and Propagation*, vol. 64, no. 6, pp. 2146-2154, June 2016.

[192] M. Wang, H. F. Ma, H. C. Zhang, W. X. Tang, X. R. Zhang and T. J. Cui, "Frequency-Fixed Beam-Scanning Leaky-Wave Antenna Using Electronically Controllable Corrugated Microstrip Line," in *IEEE Transactions on Antennas and Propagation*, vol. 66, no. 9, pp. 4449-4457, Sept. 2018.

Chapter 3

Transmission Line Model for Microstrip Travelling Wave Antennas

Contents

3.1 INTRODUCTION

Travelling wave antennas involving almost unidirectional wave propagation have been an interesting choice in designing directional antennas capable of frequency scanning [1, 2]. It had been applied in designing antenna systems with minimized interference and narrow beam-width and in applications demanding polarization agility [3]. Analysis of this class of antennas has been carried out primarily using a forward wave propagation assumption [4]. Other techniques and models involving circuit approach [5] and several full wave techniques [6] followed later. In this work we have adopted a transmission line based technique for analyzing bend based microstrip travelling wave antennas. Internal as well as terminal reflections are considered.

This chapter is organized in two sections. First the transmission line model is presented to calculate the terminal (S-parameters, Z parameters) and radiation

characteristics (pattern, realized gain, efficiency) for right angle bend based geometries. This is followed by the development of an empirical formula for arbitrary bends (acute/obtuse). The transmission line model is thus extended to analyze geometries based on such arbitrary bends.

3.2 PROBLEM FORMULATION

The first part of this chapter deals with microstrip travelling wave antennas based on right angle bends as shown in Fig. 3.1a. The side view of the geometry is shown in Fig. 3.1b. Input reflection co-efficient and radiation characteristics are calculated for the Rampart line (shown in Fig. 3.1a), Hilbert line (shown in Fig. 3.1c) and the Moore line (shown in Fig. 3.1d). Next, the model is extended to geometries based on non right angle bends (acute and obtuse angle bends) as shown in Fig. 3.1e. Empirical formulae for bend reactance are derived.

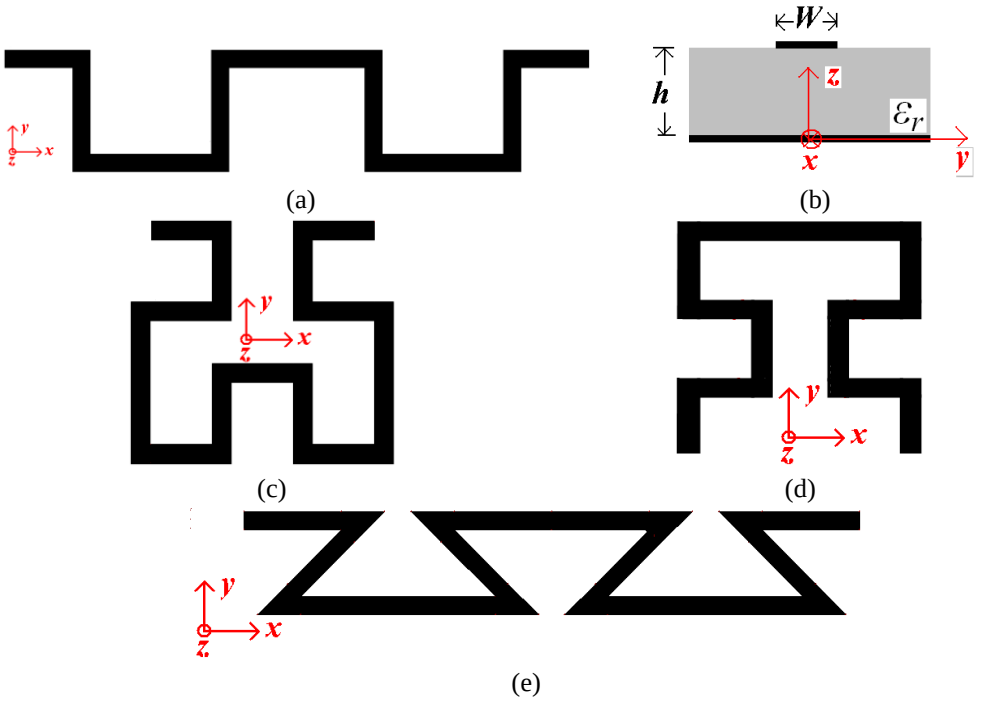

Fig. 3.1: (a) Right angle bend based geometry Rampart line, (b) acute angle based geometry triangular loop line, (c) Hilbert line and (d) Moore line taken for analysis

3.3 TRANSMISSION LINE MODEL FOR RIGHT ANGLE BEND BASED TRAVELLING WAVE ANTENNAS

The transmission line model for calculation of internal voltage-currents as well as radiated far fields from a right angle bend based travelling wave antenna is discussed in this section in the context of a microstrip Rampart line antenna. First the geometry is segmented into several linear sections. Input and terminating impedances for each such segments are calculated and the same are then used for evaluation of voltage along the line and equivalent electric and magnetic currents. These current densities are next used for calculation of radiated far fields from the line. Finally an equivalent attenuation constant is calculated to accommodate the radiated power into the analysis and all the antenna parameters are re-calculated in an iterative manner. These steps are discussed in detail in the sections to follow.

3.3.1. GEOMETRY SEGMENTATION AND NOTATIONS

First, the antenna geometry is segmented into 'N' linear segments as shown in Fig. 3.2 with segment numbers. This segmentation leads to generation of x-directed line segments, y-directed line segments and bend regions. In case of the Rampart line antenna N is taken as 13 with three x-directed and two y directed line segments per unit cell. In addition to these, there are a total of twelve bend regions in the entire geometry.

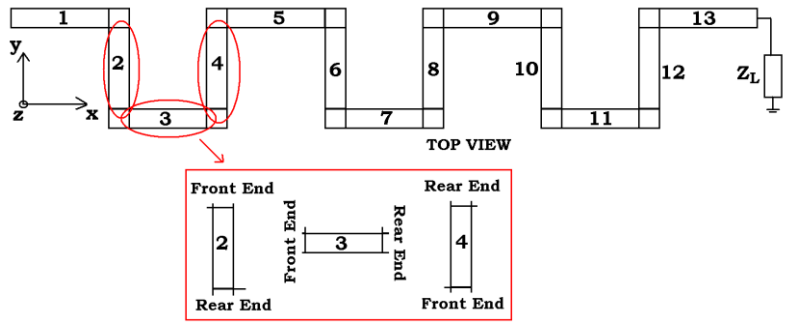

Fig. 3.2: Top view and side view with co-ordinate system and segment numbers for the Rampart line antenna

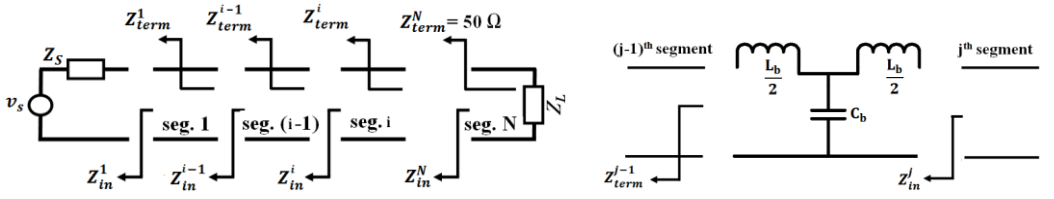

(a) (b)

Fig. 3.3: (a) Input and terminating impedance for each segments and (b) the right angle bend model for impedance calculation.

Front and rear end of a segment are defined with respect to the direction of wave propagation. These are marked for three different segments in Fig. 3.2. Input (Z^N_{in}) and terminating (Z^N_{term}) impedances for each of the segments are defined as the impedance looking towards the load respectively from the front end and the rear end of the concerned segment. These are shown in Fig. 3.3a. Terminal voltages for each of the segments are defined similarly as front voltage (V_f) and end voltage (V_e).

3.3.2. CALCULATION OF Z_{IN} AND S_{11}

Starting from the general complex load termination ($Z_{L,}$) at the end of the structure, impedance transformation is used to calculate the input impedance of the Nth (last) segment (Z^N_{in}). This Z^N_{in} is then combined with the lumped T circuit [7] for the right angled bend to get the terminal impedance of the preceding segment (Z^{N-1}_{term}) [as shown in Fig 3.3b for the i^{th} and (i-1)th segment in general]. This same technique is applied repeatedly to rest of the segments until the input impedances (Z^i_{in}) and the terminal impedances (Z^i_{in}) of all of them are found. Impedance transformation formula used here is shown below

$$Z^i_{in} = Z_{0i}\frac{Z^i_{term} + \mathrm{Z}_{0i}\tanh\left(\gamma_i L_i\right)}{\mathrm{Z}_{0i} + Z^i_{term}\tanh\left(\gamma_i L_i\right)} \tag{3.1}$$

Here $Z^i_{in}, Z^i_{term}, \mathrm{Z}_{0i}, \gamma_i$ and L_i are respectively the input impedance, terminating

impedance, characteristic impedance, complex propagation constant and length of the i^{th} line segment (Here it is assumed in general that the different line segments have different widths and hence different Z_{0i} and γ_i).

3.3.3. VOLTAGE ALONG THE LINE AND CURRENT DENSITIES

Using general transmission line theory, the voltage at any point within the i^{th} segment is given by,

$$v_i(\xi) = v_i^+ \left\{ e^{-\gamma_i(\xi-\xi_{ei})} + \Gamma_i e^{\gamma_i(\xi-\xi_{ei})} \right\} \tag{3.2}$$

where v_i^+ and $v_i(\xi)$ are respectively the amplitude of the forward travelling voltage wave in the i^{th} segment and voltage at any location 'ξ' in the i^{th} segment, Γ_i is the reflection co efficient for the i^{th} segment and is expressed as

$$\Gamma_i = \frac{Z_{term}^i - Z_{0i}}{Z_{term}^i - Z_{0i}} \tag{3.3}$$

ξ is the running co-ordinates in the current segment i.e. for horizontal segments ξ is 'x' while for a vertical segment it is 'y'. ξ_{ei} is the end co-ordinate of the i^{th} segment, i.e. for horizontal and vertical segments it is written as X_{ei} and Y_{ei} respectively. Here starting and end co ordinates as well as voltages are assumed with respect to the direction of wave propagation.

Next, the amplitude of the forward wave (v_i^+) is calculated for individual segments. First, the excitation to the antenna is modeled as a voltage source (v_s)

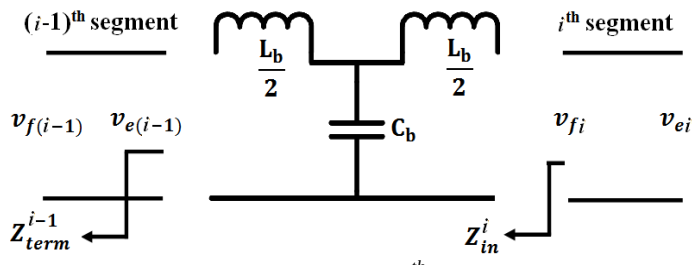

Fig. 3.4: Front and end voltages v_{fi} and v_{ei} for the i^{th} segment for calculation of $v_{e(i-1)}$

with a series source impedance (Z_s) as shown in Fig. 3.3a. Voltage at the front end of the first segment (v_{f1}) is calculated using this source model and the input impedance of the antenna (Z_{in}^1) calculated using (3.1), with the formula

$$v_{f1} = v_s \frac{Z_{in}^1}{Z_s + Z_{in}^1} \tag{3.4}$$

Then v_1^+(v^+ for the first segment) can be found from $v_1(0)$ using (3.2) and v_{f1} as

$$v_1(0) = v_1^+ \left\{ e^{\gamma_1 L_1} + \Gamma_1 e^{-\gamma_1 L_1} \right\} = v_{f1} \tag{3.5}$$

$$v_1^+ = \frac{v_{f1}}{\left\{ e^{\gamma_1 L_1} + \Gamma_1 e^{-\gamma_1 L_1} \right\}} \tag{3.6}$$

End voltage of the first segment (v_{e1}) is calculated from $v_1(\xi)$.

$$v_{e1} = v_1(\xi = X_{e1}) = v_1^+ (1 + \Gamma_1) \tag{3.7}$$

Next, the front voltage of the succeeding segment (v_{f2}) is calculated from v_{e1} and the bend reactances as can be seen from the Fig. 3.4. $v_2^+$is calculated From v_{f2} and $v_2(0)$. Proceeding in this fashion, magnitudes of the forward travelling voltage v_i^+ for all the segments are found. With v_i^+ calculated in such a manner, expressions for voltage in horizontal and vertical segments with propagation direction (±x and ±y) are expressed as

$v_i(x) = v_i^+ \left\{ e^{-\gamma_i (x - X_{ei})} + \Gamma_i e^{\gamma_i (x - X_{ei})} \right\}$ for +x directed propagation in i^{th} horizontal segment (3.8)

$v_i(x) = v_i^+ \left\{ e^{\gamma_i (x - X_{ei})} + \Gamma_i e^{-\gamma_i (x - X_{ei})} \right\}$ for -x directed propagation in i^{th} horizontal segment (3.9)

$v_i(y) = v_i^+ \left\{ e^{-\gamma_i (y - Y_{ei})} + \Gamma_i e^{\gamma_i (y - Y_{ei})} \right\}$ for +y directed propagation in i^{th} vertical segment (3.10)

$v_i(y) = v_i^+ \left\{ e^{\gamma_i (y - Y_{ei})} + \Gamma_i e^{-\gamma_i (y - Y_{ei})} \right\}$ for -y directed propagation in i^{th} vertical segment (3.11)

Here $v_i^+ = \frac{v_{fi}}{e^{\gamma_i L_i} + \Gamma_i e^{-\gamma_i L_i}}$, and x_{ie}, y_{ie} indicate the end co ordinates of a horizontal and a vertical segment respectively.

The structure leaks power from all along its length and the apertures on the sidewalls along the length are considered for radiation calculations. Since this is a line antenna and the line width is sufficiently small ($\sim \frac{\lambda_g}{10}$), the electric field underneath the line is assumed to be uniform along the width, i.e. a quasi TEM mode is considered for the entire analysis. Electric field along the periphery of the line is calculated from the voltage along the line expressed in (3.8)-(3.11). Aperture illumination is evaluated from this electric field using equivalence principle. Current density calculated from the voltage along the line is used to calculate the contribution of electric current on the total radiation.

Magnetic current density ($\vec{M}$):

There are two vertical apertures associated with every segment. For any segment, the aperture located higher along the co-ordinate axes are represented as top apertures and the ones located lower are represented as bottom apertures in our analysis. This representation is shown in Fig. 3.5a.

For the i^{th} *horizontal* segment (segment 1, 3, 5… in Fig. 3.1a), magnetic current on the top aperture ($\vec{M}_{Hi}^{Top}$) is calculated as

$$\vec{M}_{Hi}^{Top} = \vec{E} \times \hat{y} = \frac{v_i(x)}{h} \{-\hat{z}\} \times \hat{y} = \frac{v_i(x)}{h} \hat{x} \quad (3.12)$$

In this expression, $v_i(x)$ is calculated using (3.8.) or (3.9) depending on the direction of propagation.

For the i^{th} *vertical* segment (segment 2, 4, 7… in Fig. 3.1a), magnetic current on the top aperture ($\vec{M}_{Vi}^{Top}$) is calculated as

$$\vec{M}_{Vi}^{Top} = \vec{E} \times \hat{x} = \frac{v_i(y)}{h}\{-\hat{z}\} \times \hat{x} = \frac{v_i(y)}{h}(-\hat{y}) \tag{3.13}$$

Here $v_i(y)$ is calculated using (3.10) or (3.11) depending on the direction of propagation.

Since field variation along the width of any segment is neglected, the top and the bottom apertures are illuminated in the opposite phase, i.e. the direction of the aperture electric fields in them are identical to each other and consequently the direction of magnetic currents in them are opposite to each other. This leads to

$$\vec{M}_{Hi}^{Bottom} = -\vec{M}_{Hi}^{Top} \tag{3.14}$$

$$\vec{M}_{Vi}^{Bottom} = -\vec{M}_{Vi}^{Top} \tag{3.15}$$

These magnetic current densities are indicated in Fig. 3.5c.

Electric current density ($\vec{J}$):

Electric current density on the strip surface shown in Fig. 3.5b is calculated from expressions for voltage in (3.8)-(3.11) and Maxwell's equation using the following steps.

Magnetic field ($\vec{H}$) underneath the strip is calculated from the electric field underneath the strip surface using

$$\nabla \times \vec{E} = -j\omega\mu\vec{H} \tag{3.16}$$

Using $\vec{E} = v_i(x)/h\{-\hat{z}\}$ for a horizontal segment with +x directed wave propagation and under the approximation $\partial\vec{E}/\partial y = 0$ (No cross-sectional field variation), $\vec{H}$ is calculated as

$$\vec{H} = H_y \hat{y} = \frac{v_i^+ \gamma_i}{j\omega\mu_0 h}\left\{e^{-\gamma_i(x-X_{ei})} - \Gamma_i e^{\gamma_i(x-X_{ei})}\right\}\hat{y} \tag{3.17}$$

Next, electric current density $\vec{J}$ on the strip surface is calculated from $\vec{H}$ using $\vec{J} = -\hat{z} \times H_y \hat{y}$. With this, the final expression of $\vec{J}$ for the i^{th} horizontal segment with +x directed wave propagation is expressed as

$$\vec{J}_i = J_{0i}\left\{e^{-\gamma_i(x-X_{ei})} - \Gamma_i e^{\gamma_i(x-X_{ei})}\right\}\hat{x} \tag{3.18}$$

where $J_{0i} = \dfrac{v_i^+ \gamma_i}{j\omega\mu h}$

Proceeding in the similar manner, electric current densities in a segment with –x and ±y directed wave propagation are calculated as

For segments with –x directed propagation

$$\vec{J}_i = -J_{0i}\left\{e^{-\gamma_i(x-X_{ei})} - \Gamma_i e^{\gamma_i(x-X_{ei})}\right\}\hat{x} \tag{3.19}$$

For segments with +y directed propagation

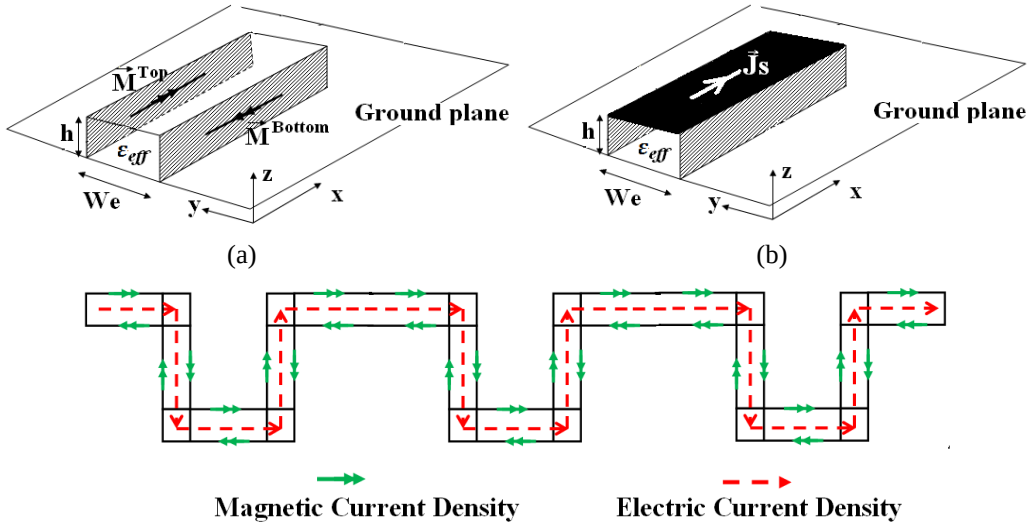

Fig. 3.5: (a) Location of the magnetic currents on the planar waveguide model for radiated far field analysis, (b) Location of the Electric currents on the planar waveguide model for radiated far field analysis and (c) Top view of Electric and Magnetic current densities on the Rampart line geometry.

$$\vec{J}_i = J_{0i}\left\{e^{-\gamma_i(y-Y_{ei})} - \Gamma_i e^{\gamma_i(y-Y_{ei})}\right\}\hat{y} \tag{3.20}$$

For segments with -y directed propagation

$$\vec{J}_i = -J_{0i}\left\{e^{\gamma_i(y-Y_{ei})} - \Gamma_i e^{-\gamma_i(y-Y_{ei})}\right\}\hat{y} \tag{3.21}$$

The directions of the magnetic and electric current densities for the rampart line antenna are shown in Fig. 3.5c. These electric and magnetic current densities thus calculated are used next for radiation calculation from various horizontal, vertical and bend sections of the line antenna. Width of the line geometry is first increased to W_e to accommodate the effects of fringing fields [8]. Here effective width W_{ei} for the i^{th} segment is expressed as,

$$W_{ei} = W + 2h \tag{3.22}$$

Here h is the substrate thickness and W is the physical width of the microstrip line.

Geometries of the horizontal and vertical line segments for radiated far field calculation are shown in Fig. 3.6 and Fig. 3.7 respectively. For all further calculations, X_s and Y_s indicate respectively the x and y co-ordinates of the centre point of the starting edge of any segment. This is shown in Fig. 3.6 for a horizontal segment.

3.3.4. RADIATED FAR FIELDS

3.3.4.1. Radiation from Horizontal Line Segments

Electric vector potential ($\vec{F}$):

For the i^{th} *horizontal* segment with +x directed wave propagation shown in Fig. 3.6a, electric vector potentials due to the top and the bottom apertures are calculated from the following integrations,

$$\vec{F}^{Top} = \frac{\varepsilon_0}{4\pi}\frac{e^{-jk_0 r}}{r}\int_{X_s}^{X_e}\int_{-h}^{h}\vec{M}_H^{Top} e^{jk_0\left\{x'\sin\theta\cos\varphi + \left(Y_0 + \frac{W_e}{2}\right)\sin\theta\sin\varphi + z'\cos\theta\right\}} dz' dx' \tag{3.23}$$

$$\vec{F}^{Top} = \frac{\varepsilon_0}{4\pi}\frac{e^{-jk_0 r}}{r}\int_{X_s}^{X_e}\int_{-h}^{h}\vec{M}_H^{Top} e^{jk_0\left\{x'\sin\theta\cos\varphi+\left(Y_0-\frac{W_e}{2}\right)\sin\theta\sin\varphi+z'\cos\theta\right\}}dz'dx' \qquad (3.24)$$

After adding the contributions from both the top and the bottom apertures vectorially, expression for total electric vector potential for the i^{th} horizontal segment with +x directed wave propagation ($\vec{F}_{xi}^{+}$) is,

$$\vec{F}_{xi}^{+} = \frac{\varepsilon_0}{4\pi}\frac{e^{-jk_0 r}}{r}v_i^{+}L_i\left\{e^{\gamma_i X_{ei}}e^{P_{1i}X_{0i}}\frac{\sinh\frac{P_{1i}L_i}{2}}{\frac{P_{1i}L_i}{2}}+\Gamma_i e^{-\gamma_i X_{ei}}e^{P_{2i}X_{0i}}\frac{\sinh\frac{P_{2i}L_i}{2}}{\frac{P_{2i}L_i}{2}}\right\} \qquad (3.25)$$
$$\times\left[2j\sin\left\{k_0\frac{W_{ei}}{2}\sin\theta\sin\varphi\right\}e^{jk_0 Y_{0i}\sin\theta\sin\varphi}\right]\left\{2h\sin c\left(k_0 h\cos\theta\right)\right\}$$

where, $P_{1i} = jk_0\sin\theta\cos\varphi-\gamma_i$ and $P_{2i} = jk_0\sin\theta\cos\varphi+\gamma_i$

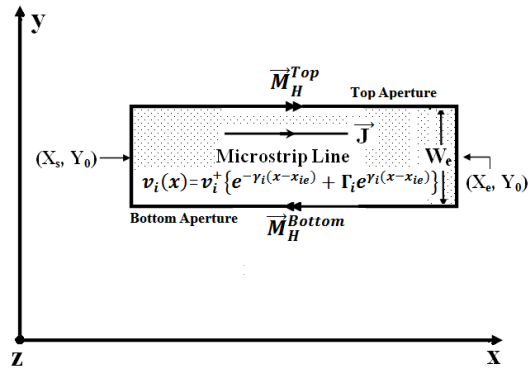

(a)

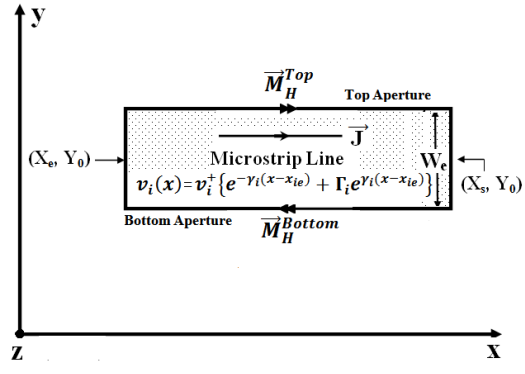

(b)

Fig. 3.6: Top view of the strip with electric current density on strip surface and magnetic current densities on top and bottom apertures for a horizontal line segment with (a) +x directed wave propagation, (b) –x directed wave propagation.

(3.25) is slightly modified for the electric vector potential for a horizontal segment with wave propagation along –x direction ($\vec{F}_{xi}^{-}$) as shown in Fig. 3.6b,

$$\vec{F}_{xi}^{-} = \frac{\varepsilon_0}{4\pi}\frac{e^{-jk_0 r}}{r} v_i^{+} L_i \left\{ e^{-\gamma_i X_{ei}} e^{P_{2i} X_{0i}} \frac{\sinh\frac{P_{2i}L_i}{2}}{\frac{P_{2i}L_i}{2}} + \Gamma_i e^{\gamma_i X_{ei}} e^{P_{1i} X_{0i}} \frac{\sinh\frac{P_{1i}L_i}{2}}{\frac{P_{1i}L_i}{2}} \right\} \times \left[2j\sin\left\{ k_0 \frac{W_{ei}}{2}\sin\theta\sin\varphi \right\} e^{jk_0 Y_{0i}\sin\theta\sin\varphi} \right] \left\{ 2h\sin c\left(k_0 h\cos\theta\right) \right\} \quad (3.26)$$

where, $P_{1i} = jk_0\sin\theta\cos\varphi - \gamma_i$ and $P_{2i} = jk_0\sin\theta\cos\varphi + \gamma_i$

In (3.25) and (3.26), (X_{0i} , Y_{0i}) indicate the co ordinate of centre of the i^{th} horizontal segment.

Magnetic vector potential ($\vec{A}$):

The magnetic vector potential due to the i^{th} horizontal segment with +x directed wave propagation as shown in Fig. 3.6a is calculated using the source integral of electric current density on the strip surface, expressed as

$$\vec{A} = \frac{\mu_0}{4\pi}\frac{e^{-jk_0 r}}{r}\int_{X_s}^{X_e}\int_{Y_0-\frac{W_e}{2}}^{Y_0+\frac{W_e}{2}} \vec{J} e^{jk_0\left\{x'\sin\theta\cos\varphi + y'\sin\theta\sin\varphi + h\cos\theta\right\}} dy' dx' \quad (3.27)$$

On evaluating this integral and multiplying the result with an array factor of the form $2j\sin\left(k_0 h\cos\theta\right)$ to accommodate the effects of the negative image of the horizontal electric current density on the infinite ground plane, expression for the magnetic vector potential for the i^{th} horizontal segment with +x directed wave propagation ($\vec{A}_{xi}^{+}$) is expressed as

$$\vec{A}_{xi}^{+} = \frac{\mu_0}{4\pi}\frac{e^{-jk_0 r}}{r}\frac{v_i^{+}\gamma_i}{j\omega\mu_0 h} L_i \left\{ e^{\gamma_i X_{ei}} e^{P_{1i} X_{0i}} \frac{\sinh\frac{P_{1i}L_i}{2}}{\frac{P_{1i}L_i}{2}} - \Gamma_i e^{-\gamma_i X_{ei}} e^{P_{2i} X_{0i}} \frac{\sinh\frac{P_{2i}L_i}{2}}{\frac{P_{2i}L_i}{2}} \right\} \times \left[W_e \operatorname{sinc}\left\{ k_0 \frac{W_{ei}}{2}\sin\theta\sin\varphi \right\} e^{jk_0 Y_{0i}\sin\theta\sin\varphi} \right] \left\{ 2j\sin\left(k_0 h\cos\theta\right) \right\} \hat{x} \quad (3.28)$$

where, $P_{1i} = jk_0 \sin\theta\cos\varphi - \gamma_i$ and $P_{2i} = jk_0 \sin\theta\cos\varphi + \gamma_i$

The modified expression for electric vector potential due to a horizontal segment with –x directed wave propagation ($\vec{A}_{xi}^{-}$) as shown in Fig. 3.6b is then calculated as,

$$\vec{A}_{xi}^{-} = -\frac{\mu_0}{4\pi}\frac{e^{-jk_0 r}}{r}\frac{v_i^{+}\gamma_i}{j\omega\mu_0 h}L_i\left\{e^{-\gamma_i X_{ei}}e^{P_{2i}X_{0i}}\frac{\sinh\frac{P_{2i}L_i}{2}}{\frac{P_{2i}L_i}{2}} - \Gamma_i e^{\gamma_i X_{ei}}e^{P_{1i}X_{0i}}\frac{\sinh\frac{P_{1i}L_i}{2}}{\frac{P_{1i}L_i}{2}}\right\}\times$$
$$\left[W_e \operatorname{sinc}\left\{k_0\frac{W_{ei}}{2}\sin\theta\sin\varphi\right\}e^{jk_0 Y_{0i}\sin\theta\sin\varphi}\right]\left\{2j\sin\left(k_0 h\cos\theta\right)\right\}\hat{x} \tag{3.29}$$

where, $P_{1i} = jk_0 \sin\theta\cos\varphi - \gamma_i$ and $P_{2i} = jk_0 \sin\theta\cos\varphi + \gamma_i$

3.3.4.2. Radiation from Vertical Line Segments

Electric vector potential:

For the i^{th} *vertical* segment with +y directed wave propagation as shown in Fig. 3.7a, the electric vector potential due to the top aperture is calculated from the following integrations

$$\vec{F}^{Top} = \frac{\varepsilon_0}{4\pi}\frac{e^{-jk_0 r}}{r}\int_{Y_s}^{Y_e}\int_{-h}^{h}\vec{M}_H^{Top}e^{jk_0\left\{\left(X_0+\frac{W_e}{2}\right)\sin\theta\cos\varphi + y'\sin\theta\sin\varphi + z'\cos\theta\right\}}dz'dy' \tag{3.30}$$

$$\vec{F}^{Top} = \frac{\varepsilon_0}{4\pi}\frac{e^{-jk_0 r}}{r}\int_{Y_s}^{Y_e}\int_{-h}^{h}\vec{M}_H^{Bottom}e^{jk_0\left\{\left(X_0-\frac{W_e}{2}\right)\sin\theta\cos\varphi + y'\sin\theta\sin\varphi + z'\cos\theta\right\}}dz'dy' \tag{3.31}$$

After adding the contributions from top and the bottom apertures vectorially, expressions for total electric vector potential for the i^{th} segment with +y directed wave propagation ($\vec{F}_{yi}^{+}$) is found as,

$$\vec{F}_{yi}^{+} = -\frac{\varepsilon_0}{4\pi}\frac{e^{-jk_0 r}}{r} v_i^{+} L_i \left\{ e^{\gamma_i Y_{ei}} e^{Q_{1i} Y_{0i}} \frac{\sinh\frac{Q_{1i}L_i}{2}}{\frac{Q_{1i}L_i}{2}} + \Gamma_i e^{-\gamma_i Y_{ei}} e^{Q_{2i} Y_{0i}} \frac{\sinh\frac{Q_{2i}L_i}{2}}{\frac{Q_{2i}L_i}{2}} \right\}$$
$$\times \left[2j \sin\left\{ k_0 \frac{W_{ei}}{2} \sin\theta\cos\varphi \right\} e^{jk_0 X_{0i} \sin\theta\cos\varphi} \right] \left\{ 2h \sin c\left(k_0 h\cos\theta\right) \right\} \hat{y} \tag{3.32}$$

where, $Q_{1i} = jk_0 \sin\theta\sin\varphi - \gamma_i$ and $Q_{2i} = jk_0 \sin\theta\sin\varphi + \gamma_i$

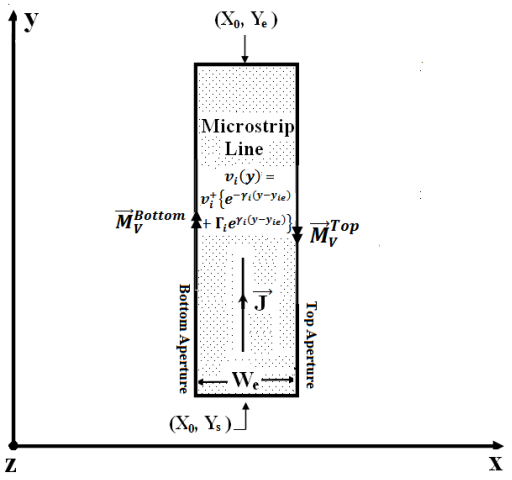

(a)

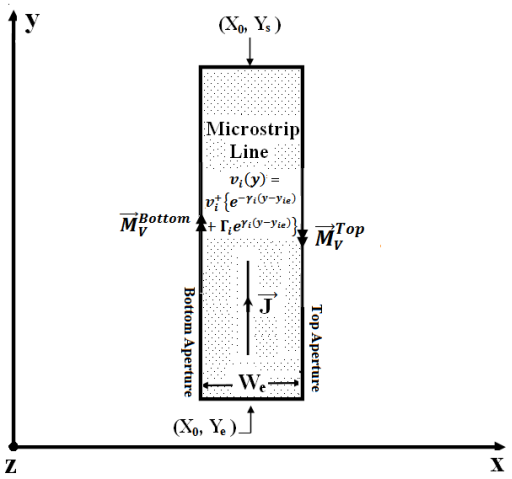

(b)

Fig. 3.7: Top view of the strip with electric current density on the strip surface and magnetic current densities on top and bottom apertures for a vertical line segment with (a) +y directed wave propagation and (b) –y directed wave propagation.

The modified expression for electric vector potential for a vertical segment with wave propagation along –y direction ($\vec{F}_{yi}^{-}$) is expressed as,

$$\vec{F}_{yi}^{-} = -\frac{\varepsilon_0}{4\pi}\frac{e^{-jk_0 r}}{r} v_i^{+} L_i \left\{ e^{-\gamma_i Y_{ei}} e^{Q_{2i} Y_{0i}} \frac{\sinh\frac{Q_{2i}L_i}{2}}{\frac{Q_{2i}L_i}{2}} + \Gamma_i e^{\gamma_i Y_{ei}} e^{Q_{1i} Y_{0i}} \frac{\sinh\frac{Q_{1i}L_i}{2}}{\frac{Q_{1i}L_i}{2}} \right\} \times$$
$$\left[2j \sin\left\{ k_0 \frac{W_{ei}}{2} \sin\theta\cos\varphi \right\} e^{jk_0 X_{0i} \sin\theta\cos\varphi} \right] \left\{ 2h \sin c\left(k_0 h\cos\theta\right) \right\} \hat{y} \tag{3.33}$$

Magnetic vector potential:

The magnetic vector potential due to a vertical segment is calculated using the source integral of electric current density on the strip surface, expressed as

$$\vec{A} = \frac{\mu_0}{4\pi}\frac{e^{-jk_0 r}}{r} \int_{X_s}^{X_e} \int_{Y_0-\frac{W_e}{2}}^{Y_0+\frac{W_e}{2}} \vec{J} e^{jk_0\left\{x' \sin\theta\cos\varphi + y' \sin\theta\sin\varphi + h\cos\theta\right\}} dy' dx' \tag{3.34}$$

On evaluating this integral and multiplying the result with an array factor of the form $2j\sin\left(k_0 h\cos\theta\right)$, expression for the magnetic vector potential for the i^{th} horizontal segment with +y directed wave propagation ($\vec{A}_{yi}^{+}$) is expressed as

$$\vec{A}_{yi}^{+} = \frac{\mu_0}{4\pi}\frac{e^{-jk_0 r}}{r} \frac{v_i^{+}\gamma_i}{j\omega\mu_0 h} L_i \left\{ e^{\gamma_i Y_{ei}} e^{Q_{1i} Y_{0i}} \frac{\sinh\frac{Q_{1i}L_i}{2}}{\frac{Q_{1i}L_i}{2}} - \Gamma_i e^{-\gamma_i Y_{ei}} e^{Q_{2i} Y_{0i}} \frac{\sinh\frac{Q_{2i}L_i}{2}}{\frac{Q_{2i}L_i}{2}} \right\} \times$$
$$\left[W_e \operatorname{sinc}\left\{ k_0 \frac{W_{ei}}{2} \sin\theta\cos\varphi \right\} e^{jk_0 X_{0i} \sin\theta\cos\varphi} \right] \left\{ 2j \sin\left(k_0 h\cos\theta\right) \right\} \hat{y} \tag{3.35}$$

The modified expression for the magnetic vector potential due to a vertical segment with –y directed wave propagation ($\vec{A}_{yi}^{-}$) is expressed as,

$$\vec{A}_{yi}^{-} = -\frac{\mu_0}{4\pi}\frac{e^{-jk_0 r}}{r}\frac{v_i^{+}\gamma_i}{j\omega\mu_0 h}L_i\left\{e^{-\gamma_i Y_{ei}}e^{Q_{2i}Y_{0i}}\frac{\sinh\frac{Q_{2i}L_i}{2}}{\frac{Q_{2i}L_i}{2}} - \Gamma_i e^{-\gamma_i Y_{ei}}e^{Q_{1i}Y_{0i}}\frac{\sinh\frac{Q_{1i}L_i}{2}}{\frac{Q_{1i}L_i}{2}}\right\}$$
$$\times\left[W_e\,\mathrm{sinc}\left\{k_0\frac{W_{ei}}{2}\sin\theta\cos\varphi\right\}e^{jk_0 X_{0i}\sin\theta\cos\varphi}\right]\left\{2j\sin\left(k_0 h\cos\theta\right)\right\}\hat{y} \tag{3.36}$$

3.3.4.3. Radiation from Bends

Electric vector potential

Radiated far fields from microstrip right angled bends may be calculated using various techniques available in the literature. Most widely used of these are - an electric line current approach 11] and a magnetic line current approach [4]. We have used a combination of electric current on the strip surface and magnetic current on the sidewalls along the edges.

For each right angle bend, there are two associated apertures, one in the x-z plane and another in the y-z plane as can be seen in the Fig. 3.8. Center co ordinates for the x-z plane and y-z plane apertures are expressed as ($X_{0B}^{H}, Y_{0B}^{H}, \frac{h}{2}$) and ($X_{0B}^{V}, Y_{0B}^{V}, \frac{h}{2}$) respectively. To maintain compatibility with the bend modeling, aperture illuminations are taken as uniform and the magnitude of the magnetic current flowing through both apertures are calculated as the average of voltage at the end of the preceding segment and that at the front of the succeeding segment. Also, in this analysis, direction of magnetic current on the horizontal and vertical apertures are indicated by s_h and s_v respectively, with s_h or s_v=1 for magnetic current along positive x or y axis and s_h or s_v=-1 for magnetic current along negative x or y axis. Magnetic current on the apertures ($\vec{M}_{bi}$) for the i^{th} segment is thus written as

$$\vec{M}_{bi} = \frac{v_{e(i-1)} + v_{fi}}{2h} s_h \hat{x} \text{ for the horizontal aperture and} \tag{3.37}$$

$$\vec{M}_{bi} = \frac{v_{e(i-1)} + v_{fi}}{2h} s_v \hat{y} \text{ for the vertical aperture} \tag{3.38}$$

Then, magnetic vector potential for the horizontal (x-z plane aperture) and the vertical (y-z plane aperture) apertures indicated as $\vec{F}_h$ and $\vec{F}_v$ respectively, are calculated from

$$\vec{F}_h = \frac{\varepsilon_0}{4\pi} \frac{e^{-jk_0 r}}{r} \int_{X_{0B}^H - \frac{W_e}{2}}^{X_{0B}^H + \frac{W_e}{2}} \int_{-h}^{h} \{ s_h M_b \hat{x} \} e^{jk_0 \{ x' \sin\theta\cos\varphi + Y_{0B}^H \sin\theta\sin\varphi + z' \cos\theta \}} dz' dx' \tag{3.39}$$

$$\vec{F}_v = \frac{\varepsilon_0}{4\pi} \frac{e^{-jk_0 r}}{r} \int_{Y_{0B}^H - \frac{W_e}{2}}^{Y_{0B}^H + \frac{W_e}{2}} \int_{-h}^{h} \{ s_v M_b \hat{y} \} e^{jk_0 \{ X_{0B}^H \sin\theta\cos\varphi + y' \sin\theta\sin\varphi + z' \cos\theta \}} dz' dy' \tag{3.40}$$

Final expressions for $\vec{F}_h$ and $\vec{F}_v$ are as follows

$$\vec{F}_h = \hat{x} F_x = s_h M_{bi} e^{jk_0 \sin\theta \left(X_{0B}^H \cos\varphi + Y_{0B}^H \sin\varphi \right)} W_e \sin c \left(k_0 \frac{W_e}{2} \sin\theta\cos\varphi \right) 2h \sin c \left(k_0 h \cos\theta \right) \tag{3.41}$$

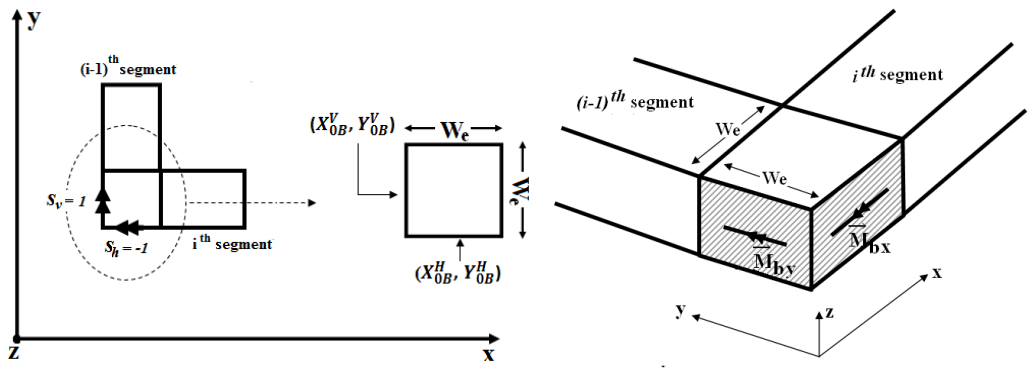

(a) (b)

Fig. 3.8: Magnetic current density on the horizontal and vertical apertures associated with the right angle bend with (a) Top view and (b) Perspective view indicating magnetic currents on the xz plane aperture ($\vec{M}_{bx}$) and the yz plane aperture ($\vec{M}_{by}$).

$$\vec{F}_v = \hat{y}F_y = s_v M_{bi} e^{jk_0 \sin\theta\left(X_{0B}^V \cos\varphi + Y_{0B}^V \sin\varphi\right)} W_e \sin c\left(k_0 \frac{W_e}{2} \sin\theta \sin\varphi\right) 2h \sin c\left(k_0 h \cos\theta\right) \tag{3.42}$$

3.3.4.4. Total radiated fields for the antenna

To get the total electric field radiation in the far-field of the antenna, E_θ and E_φ components of the electric field radiated from the horizontal and vertical segments and from that of the bends are added.

$$E_\theta = \sum E_\theta^{\,horizontal} + \sum E_\theta^{\,vertical} + \sum E_\theta^{\,bends} \tag{3.43}$$

$$E_\varphi = \sum E_\varphi^{\,horizontal} + \sum E_\varphi^{\,vertical} + \sum E_\varphi^{\,bends} \tag{3.44}$$

3.3.5. ITERATIVE CORRECTION

3.3.5.1. Calculation of effective decay constant

The effect of radiation is introduced in the calculation as an equivalent decay constant. Total power lost in the entire line due to this decay constant (α_r) is equal to the total power being from the structure. Power radiated from the antenna is evaluated from the total E_θ and total E_φ in the far-field. This radiated power is then used to find the equivalent decay constant using following steps.

Step I: The effective decay constant due to radiation (α_r) is assumed to be same for all the line segments and is initialized to zero for the 1st iteration. Far fields and total radiated powers (P_r) are calculated from the antenna using formulas derived in previous sections.

Step II: In this step an appropriate value of α_r is calculated so that the total power lost in the antenna due to α_r becomes equal to P_r. Pre-calculated values of v^+ and Γ for each segment is used to calculate the power loss due to α_r

in each segment. Power loss in single segment (i^{th} segment) due to decay constant α_r is

$$P_{ri}^{'} = \frac{|V_i^+|^2}{2Z_0}\left\{\left(e^{2\alpha_r L_i} - 1\right) + |\Gamma_i|^2\left(1 - e^{-2\alpha_r L_i}\right)\right\} \tag{3.45}$$

These losses from individual segments are added to get the total power lost due to α_r alone. This approximate loss is represented by $P_r^{'}$.

$$P_r^{'} = \sum_{i=1}^{N} P_{ri}^{'} \tag{3.46}$$

Quite obviously, $P_r^{'}$ would be different from P_r as initial value of α_r might not be a good guess. Next α_r is increased by a very small amount and $P_r^{'}$ is recalculated. On reaching a predefined level of difference between P_r and $P_r^{'}$ ($|P_r - P_r^{'}|$ within 3% of P_r) this iterative procedure stops, thereby yielding the final value of α_r.

3.3.5.2.Iterative calculation of the radiated power

For the first iteration, total decay constant of the line α is initialized at $\alpha_c + \alpha_d$ where α_c indicates the conductor loss per unit length and α_d indicates the dielectric loss per unit length. (Since α_r is initialized to zero)

Once α_r for the first iteration is found using method described in section 3.3.5.1, the total decay constant of the line is then updated using the initialized value (which indicates the antenna losses) and α_r for the current iteration. S_{11}, input impedance, voltage along the line and the radiated fields are recalculated using this new value of the propagation constant.

Next, α_r for the second iteration is calculated from the total radiated power calculated in the first iteration (as shown in Table 3.1). This process is repeated until the value of α_r saturates, i.e. there is $< 1\%$ relative difference in

α_r in consecutive iterations. In the present work it took 3 iterations for α_r to saturate

TABLE 3.1: Iterative Calculation of the Effective Decay Constant

Iteration	Decay constant (α)		Power (P)	
	Decay constant to accommodate conductor and dielectric losses	Decay constant to accommodate radiation loss	Radiated Power	Total power lost in the antenna
1	$\alpha_c + \alpha_d$	0	$P_r^{(1)}$	$P^{(1)}$
2	$\alpha_c + \alpha_d$	$\alpha_r^{(2)}$	$P_r^{(2)}$	$P^{(2)}$
3	$\alpha_c + \alpha_d$	$\alpha_r^{(3)}$	$P_r^{(3)}$	$P^{(3)}$
.	.	.	.	.
.	.	.	.	.
.	.	.	.	.
$T-1$	$\alpha_c + \alpha_d$	$\alpha_r^{(T-1)}$	$P_r^{(T-1)}$	$P^{(T-1)}$
T	$\alpha_c + \alpha_d$	$\alpha_r^{(T)}$	$P_r^{(T)}$	$P^{(T)}$

3.3.6. RADIATION FROM A CHAMPHERED BEND

Bend based lines are often champhered to reduce stray radiated emission from them. Although this is not likely in a travelling wave antenna, but there are situations where the bends are mitered to get rid of the unwanted reactance. The model presented in the last section can easily be modified to calculate the radiation from a champhered microstrip bend instead of a sharp one.

The total radiated far field in the transmission line model presented above is calculated by considering the contributions from line segments and bends separately. To calculate the radiated far fields from a mitered bend based line, modification in only the bend radiation need to be altered. Rest of the analysis remains essentially the same.

To do this, first a rotated local co-ordinate system (x_{rot}, y_{rot}, z_{rot}) is defined where x_{rot} indicate the co-ordinate along the edge of the champhered bend while y_{rot} indicate the one perpendicular to it. This is shown in Fig. 3.9. The transformation from the original co-ordinate system (x, y, z) to the rotated one (x_{rot}, y_{rot}, z_{rot})) is defined as

$$x_{rot} = x\cos\alpha + y\sin\alpha \tag{3.47a}$$

$$y_{rot} = -x\sin\alpha + y\cos\alpha \tag{3.47b}$$

$$z_{rot} = z \tag{3.47c}$$

where, α is the inclination angle of the champhered edge with respect to the positive x axis. In this coordinate system ($x_{rot}\, y_{rot}$ '), the Cartesian to spherical transformation matrix becomes

$$\begin{bmatrix} r \\ \theta \\ \varphi \end{bmatrix} = \begin{bmatrix} \sin\theta\cos(\varphi-\alpha) & \sin\theta\sin(\varphi-\alpha) & \cos\theta \\ \cos\theta\cos(\varphi-\alpha) & \cos\theta\sin(\varphi-\alpha) & -\sin\theta \\ -\sin(\varphi-\alpha) & \cos(\varphi-\alpha) & 0 \end{bmatrix} \begin{bmatrix} x_{rot} \\ y_{rot} \\ z_{rot} \end{bmatrix} \tag{3.48}$$

It is interesting to note that the inclined edge of the mitered bend in the original (xy) coordinate system has become horizontal in this new coordinate system (x_{rot}, y_{rot}).

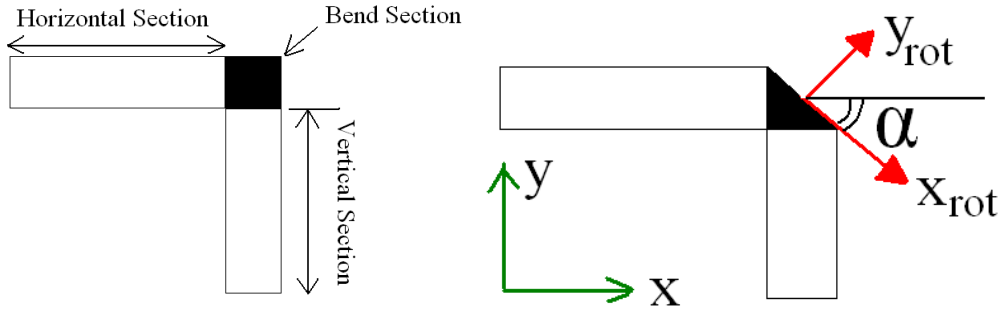

Fig. 3.9: (a) Geometry for the sharp bend and the (b) champhered bend with the original and the rotated co-ordinate system.

Consequently the magnetic ($\vec{A}$) and electric ($\vec{F}$) vector potentials for this inclined edge are calculated by replacing x by x_{rot} and φ by$(\varphi-\alpha)$ in the expressions of (3.41) and (3.42) for right angle bends. Positions of the apertures are included in the analysis after appropriate co-ordinate transformation.

Finally, radiated electric field components E_θ and E_φ are calculated from $A_{x_{rot}}$ and $F_{x_{rot}}$ as

$$E_\theta = -jw\{A_{x_{rot}}\cos\theta\cos(\varphi-\alpha) - \eta_0 F_{x_{rot}}\sin(\varphi-\alpha)\} \tag{3.49}$$

$$E_{\varphi} = -jw\{-A_{x_{rot}} \sin(\varphi - \alpha) - \eta_0 F_{x_{rot}} \cos\theta \cos(\varphi - \alpha)\} \qquad (3.50)$$

This technique is validated using a mitered bend geometry with arm length of 20 mm on either side of the bend shown in Fig. 3.10a. The line has 1.5 mm of width and is simulated on a substrate with thickness of 0.762 mm and permittivity of 4.3. Simulated and calculated normalized radiation patterns shown in Fig. 3.10b indicate good agreement between CST Microwave Studio simulation and the transmission line model.

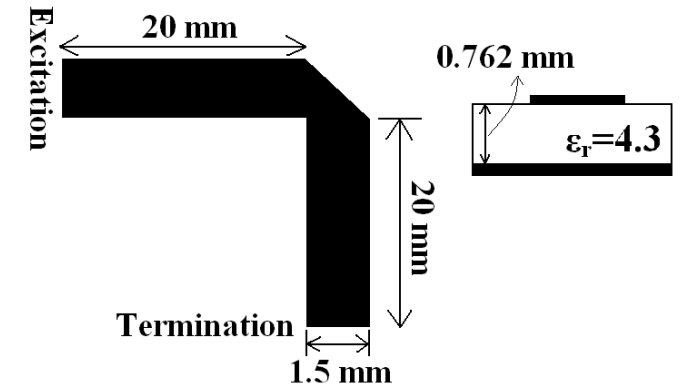

(a)

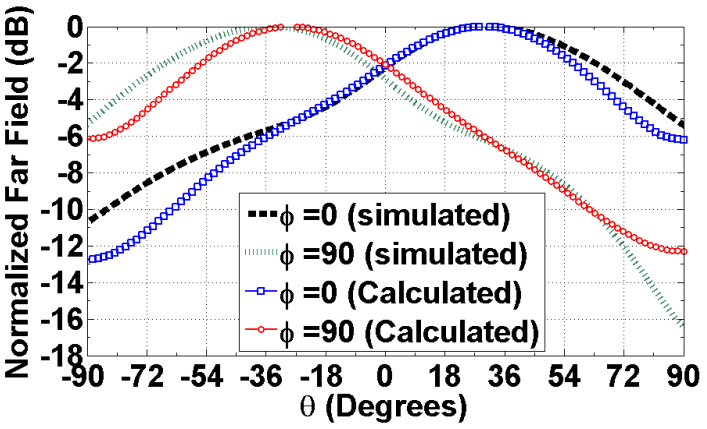

(b)

Fig. 3.10: (a) Simulated geometry for verification of the model and (b) simulated and calculated normalized radiation pattern in the x-z plane and the y-z plane

3.3.7. SIMULATION AND OBSERVATIONS

The analysis technique outlined in the previous sections is applicable to any microstrip line and right angle bend based geometries. In this section the model is applied to analysis of several bend based travelling wave antennas namely Hilbert line, Moore line and Rampart line microstrip configuration. Simulated and calculated S_{11}, Z_{in} are compared. Radiated far fields are also calculated and normalized pattern in two principal planes, gain vs, frequency, efficiency vs, frequency etc are compared with those from full wave simulations. Finally a prototype of the Rampart line having three unit cells is fabricated and results calculated using this transmission line model are compared with those from practical measurement.

3.3.8.1. Straight Line

A simple microstrip line is the building block for most of the bend based travelling wave antennas. It is thus important to calculate and compare the performance of the transmission line model presented in the last section for such a simple straight line first. In this context, a horizontal microstrip line on FR4 substrate (permittivity 4.3 and thickness of 1.6 mm) is simulated in Method of Moment (MoM) based Zeland IE3D software. Results are compared with the transmission line model as well as those predicted from the analytical Green's function based technique of M Leone [11]. Normalized radiated far field in the xz and yz planes from a straight horizontal microstrip lines are shown in Fig. 3.11. The geometry with dimensions is shown in the inset of the figures.

It can be observed that the simple electric and magnetic current based method presented in this work fares well against the standard techniques.

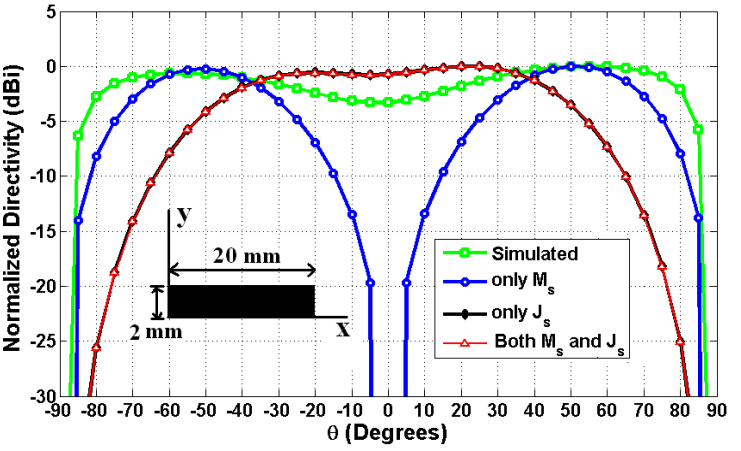

(a)

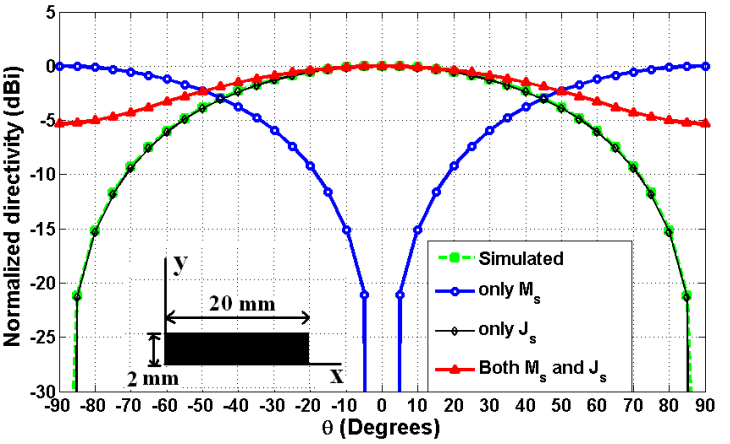

(b)

Fig. 3.11: Normalized directivity for the horizontal microstrip line in the (a) x-z plane and the (b) y-z plane

3.3.8.2. Hilbert Line

The Hilbert line configuration analyzed in this section is shown in Fig. 3.12 with dimensions in mm. Substrate chosen for this structure has a permittivity of 4.3 with a thickness of 0.762 mm (with a loss tangent of 0.002).

Full wave simulation is performed using CST Microwave Studio and Zeland IE3D. Simulated and calculated S_{11}, real and imaginary parts of the input impedance (Z_{in}) are compared and the same are shown in Fig. 3.13. Maximum

realized gain and antenna efficiency with frequency are shown in Fig. 3.14. Radiated far fields in the two principal planes i.e. x-z and y-z planes at the frequencies of 5.4 GHz and 6.3 GHz are plotted in Fig. 3.15. The comparison of terminal and radiation characteristics indicates the effectiveness of the model.

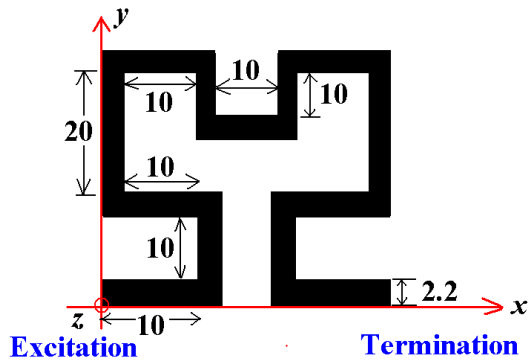

Fig. 3.12: Hilbert line geometry with dimension in mm

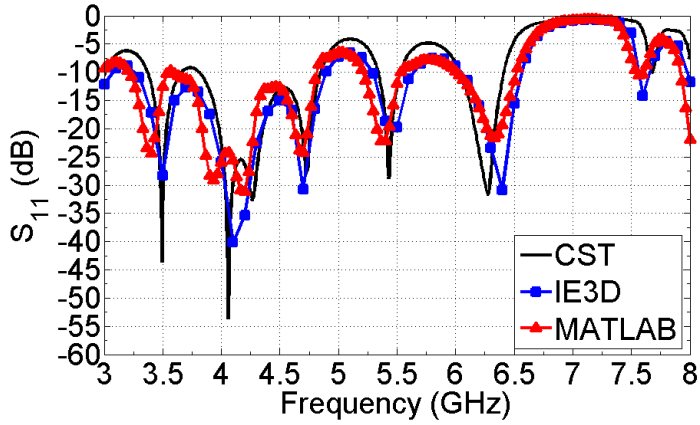

(a)

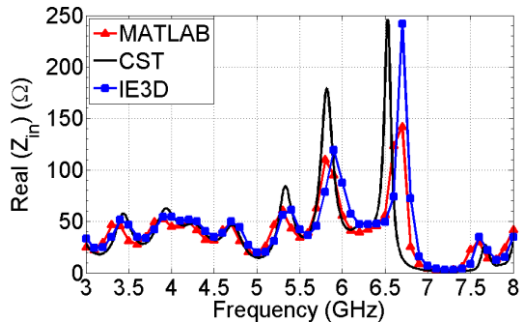

(b)

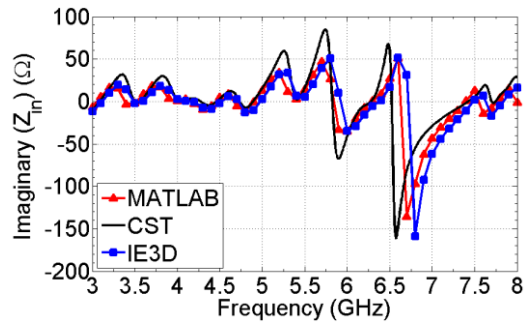

(c)

Fig. 3.13: (a) S_{11} vs. frequency, (b) real and (c) imaginary part of the input impedance with frequency for the Hilbert line

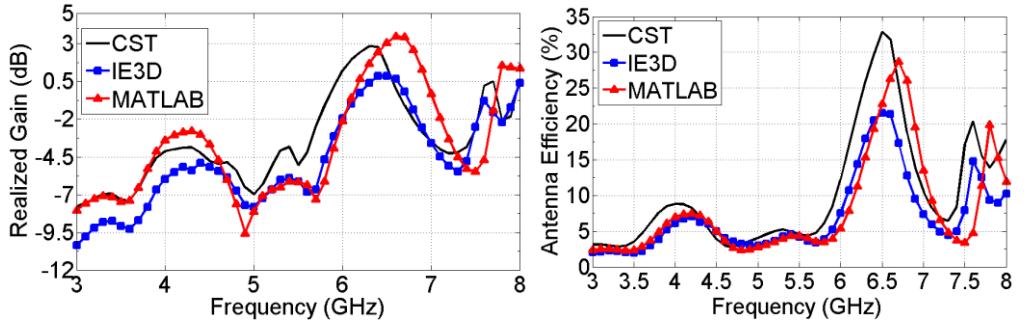

(a) (b)

Fig. 3.14: (a) Maximum realized gain and (b) antenna efficiency with frequency for the Hilbert line.

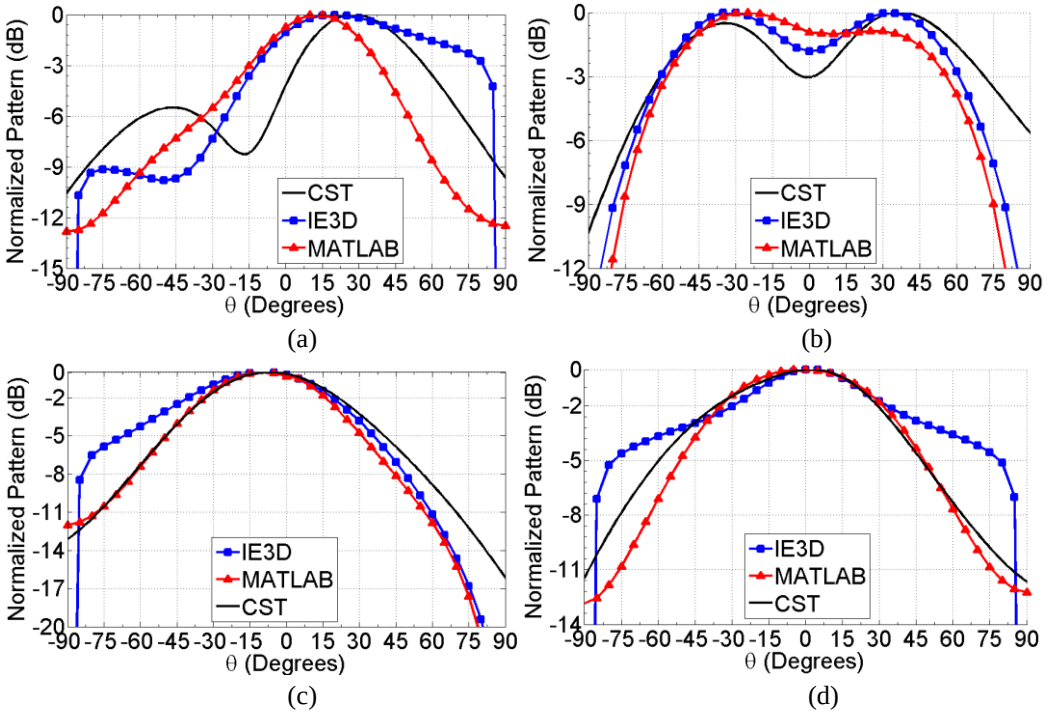

(a) (b)

(c) (d)

Fig. 3.15: Normalized radiated power patterns in the (a) x-z plane at 5.4 GHz, (b) y-z plane at 5.4 GHz, (c) x-z plane at 6.3 GHz and (d) y-z plane at 6.3 GHz for the Hilbert line.

3.3.8.3. Moore Line

The Moore line geometry shown in Fig. 3.16 is taken next for analysis. The substrate used for this geometry has a permittivity of 4 with a thickness of 1.6 mm (loss tangent of 0.02). Dimension of different arms in mm are shown in the figure.

S_{11} and real and imaginary parts of the input impedance for the Moore line are shown in Fig. 3.17. Radiation characteristics in terms of maximum realized gain and antenna efficiency vs. frequency are shown in Fig 3.18. Radiated far fields at two different frequencies in the x-z and y-z plane are shown in Fig. 3.19. Comparison with results obtained from full wave simulators indicates the effectiveness of the model.

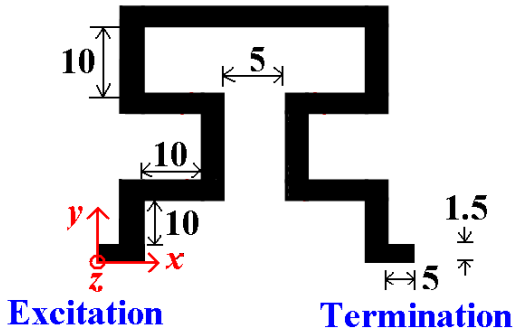

Fig. 3.16: Moore line geometry with dimension in mm

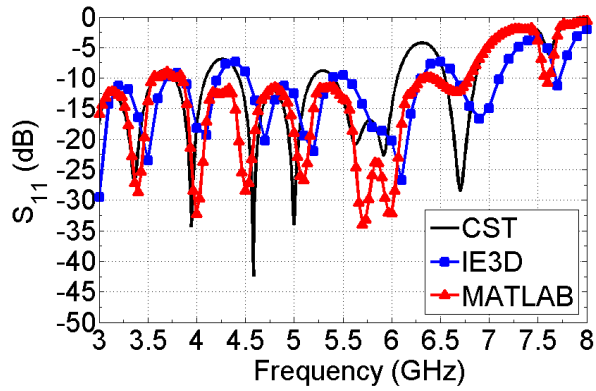

(a)

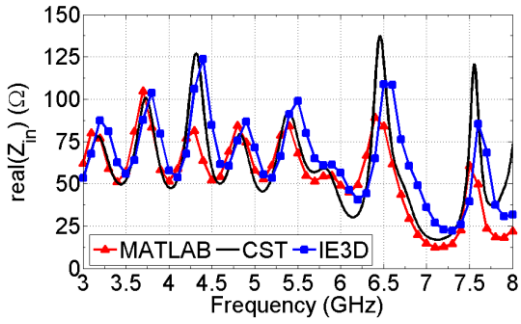

(b)

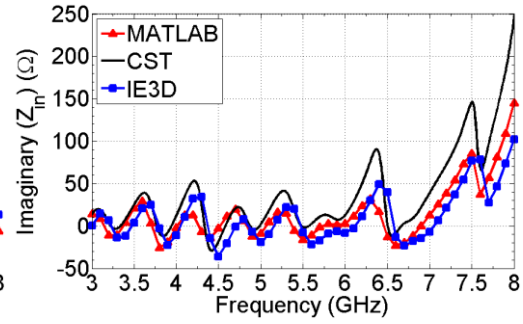

(c)

Fig. 3.17: (a) S_{11} vs. frequency, (b) real and (c) imaginary part of the input impedance with frequency for the Moore line.

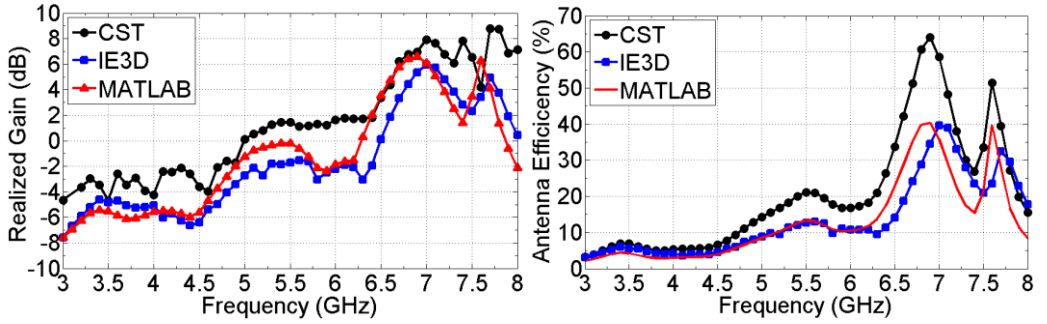

(a) (b)

Fig. 3.18: (a) Maximum realized gain and (b) antenna efficiency with frequency for the Moore line.

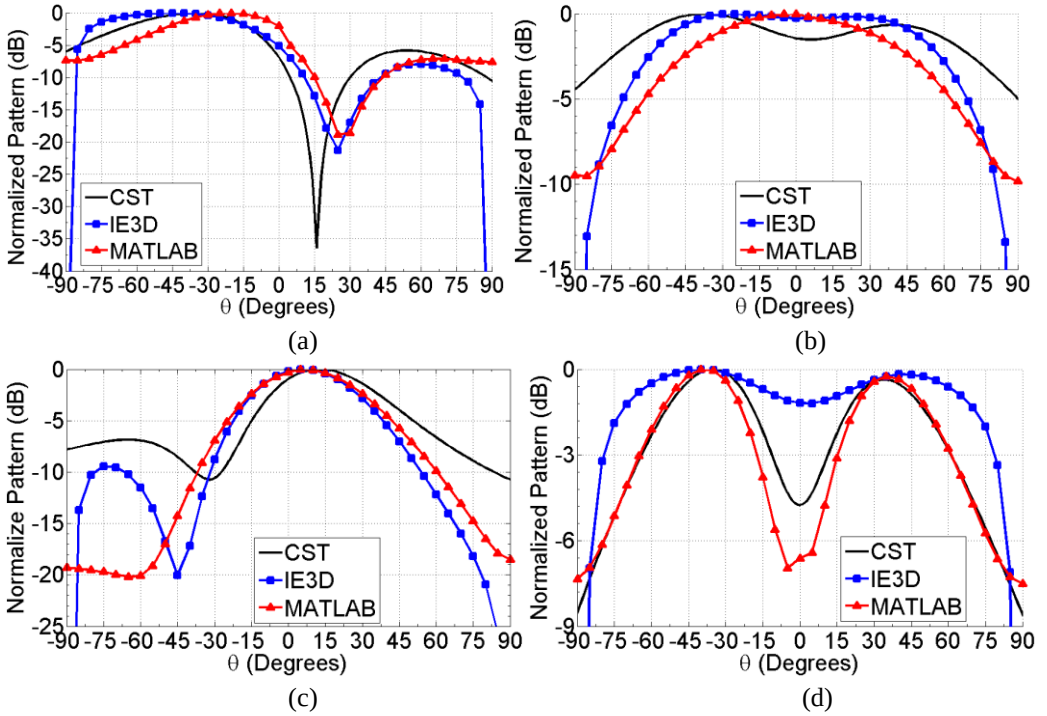

(a) (b)

(c) (d)

Fig. 3.19: Normalized radiated power pattern in the (a) x-z plane at 5 GHz, (b) y-z plane at 5 GHz, (c) x-z plane at 6 GHz and (d) y-z plane at 6 GHz for the Moore line.

3.3.8.4. Rampart Line

Next, a Rampart line with dimensions shown in Fig. 3.20a is analyzed next. Real and imaginary parts of simulated and calculated input impedance are shown in Fig. 3.21a and Fig. 3.21b.

The geometry is fabricated in Rogers RT duroid substrate with permittivity 2.5 a thickness of 0.762 mm (loss tangent 0.002). The fabricated prototype is shown in Fig. 3.20b. Simulated, calculated and measured S_{11} are plotted in Fig. 3.21c.

Fig. 3.22a and Fig. 3.22b shows respectively the maximum realized gain and antenna efficiency. Normalized radiated far fields at 5 GHz, 6 GHz and 7 GHz in the x-z and the y-z plane are plotted in Fig. 3.23a-d.

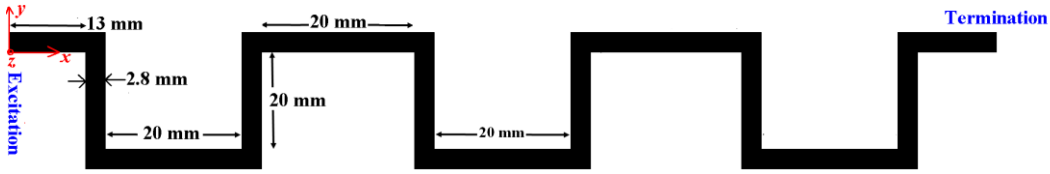

(a)

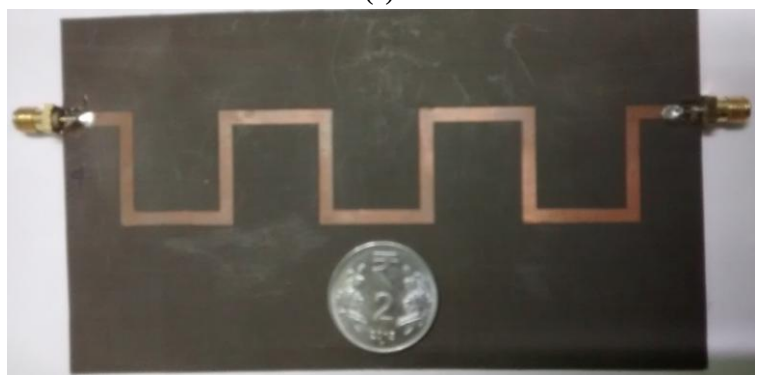

(b)

Fig. 3.20: (a) Rampart line geometry having three unit cells with dimensions in mm and (b) fabricated prototype.

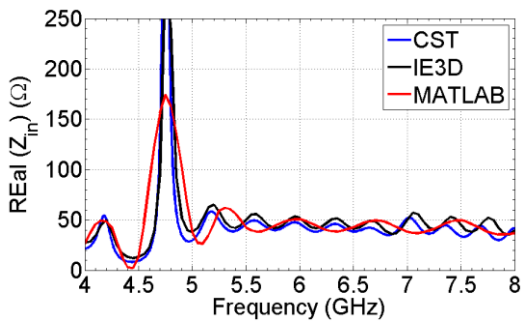

(a)

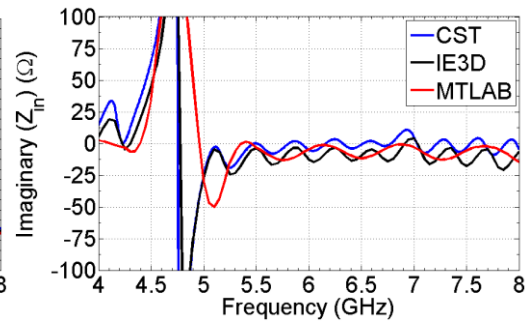

(b)

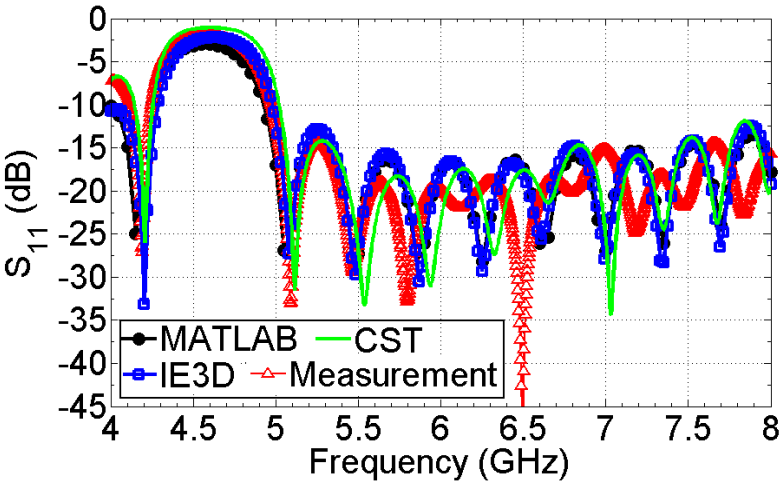

(c)

Fig. 3.21: Simulated and calculated (a) real part and (b) imaginary part of the input impedance and (c) variation of S_{11} with frequency for the Rampart line antenna.

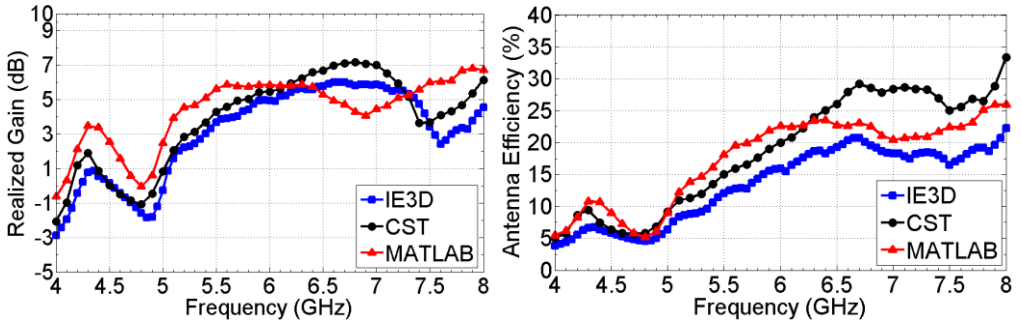

(a) (b)

Fig. 3.22: (a) Maximum realized gain and (b) antenna efficiency with frequency for the Rampart line antenna.

A comparison of simulated, calculated and measured realized gain and antenna efficiency are tabulated in Tables 3.2 and Table 3.3.

Table 3.2: Realized Gain vs. Frequency for the Rampart line antenna

Frequency (GHz)	Simulated Gain (MoM simulation) (dBi)	Simulated Gain (Finite Integration Technique) (dB)	Calculated Gain (Our work) (dB)	Measured Gain (Three Antenna Method) (dB)
5	-0.26	0.82	2.4	0.5
6	4.95	5.47	5.85	4
7	5.88	7	4.44	5.2

Table 3.3: Antenna Efficiency vs. Frequency for the Rampart line antenna

Frequency (GHz)	Simulated Efficiency (MoM simulation) (%)	Simulated Efficiency (Finite Integration Technique) (%)	Calculated Efficiency (Our work) (%)	Measured Efficiency (Wheeler Cap Method) (%)
5	6.36	9.08	9.05	9
6	15.5	20	22.6	21
7	18.3	20.4	28	23

Tabulation of the main lobe direction with frequency shown in Table 3.4 Indicate that the main lobe scans about 28 degrees for frequency changing from 5 GHz to 6 GHz.

Table 3.4: Main lobe direction with frequency for the Rampart line antenna

Frequency (GHz)	Main Lobe direction (Simulation) (Degrees)	Main Lobe Direction (Analysis) (Degrees)	Main Lobe Direction (Measurement) (Degrees)
5	9.72	11.5	12
6	37.41	38.3	40
7 (Dual beam)	0, 69.82	2,65	5,74

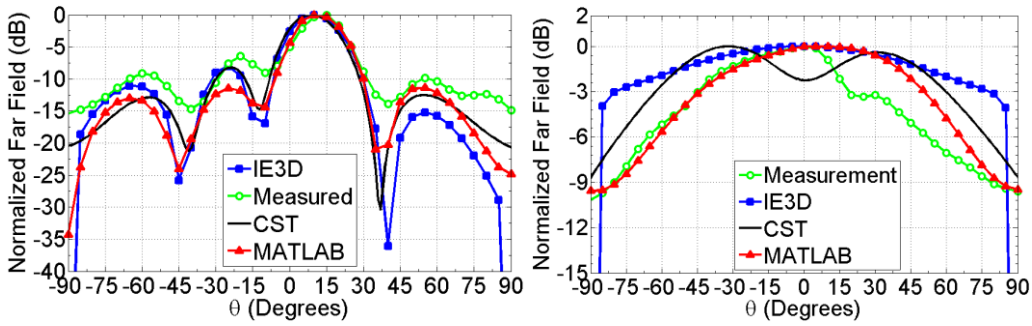

(a) (b)

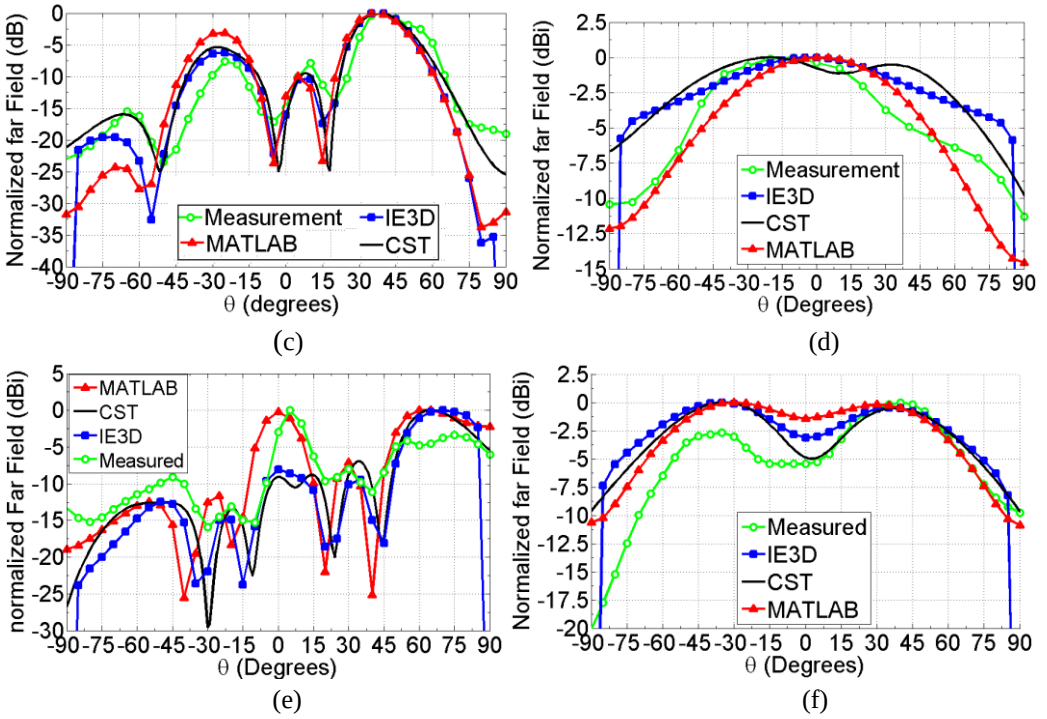

Fig. 3.23: Normalized pattern in the (a) x-z plane, (b) y-z plane at 5 GHz, (c) x-z plane (d) y-z plane at 6 GHz, (a) x-z plane, (b) y-z plane at 7 GHz for the Rampart line.

3.3.8 LIMITATIONS

It is observed from the comparisons of the test cases in the last section with full wave simulations (MoM and Finite integration technique) as well as with practical measurements that the transmission line model is quite effective for travelling wave antennas based on right angle bends. The model however is reliant on the empirical model for the right angle bend and is therefore incapable of analyzing non-right angle bend based geometries (for example square loop antenna, Z-shaped antenna etc.). To alleviate this problem, in the next section we aim to develop a set of empirical formulae for arbitrary microstrip bends (i.e. both acute and obtuse angle bends). This would make the travelling wave antennas based on such bends under the purview of the transmission line model presented herein.

3.4 MODEL FOR ARBITRARY MICROSTRIP BEND

Basic idea used for developing the empirical circuit model for obtuse and acute angle bends is to use the prototype formulae available for right angle bends and introduce parameters which are functions of the bend angle; these steps are discussed in the next sections.

3.4.1. BASIC TECHNIQUE

The lumped T model available for a right angled bend in microstrip line is shown in Fig. 3.24a. Empirical formulae for the series inductance (L_b) and shunt capacitance (C_b) are given by Garg and Bahl [12].

$$L_b = 100h\left\{4\sqrt{\frac{W}{h}} - 4.21\right\} nH \tag{3.51}$$

$$C_b = W\left\{(9.5\varepsilon_r + 1.25)\frac{W}{h} + 5.2\varepsilon_r + 7\right\} pF \text{ for } \frac{W}{h} > 1 \tag{3.52}$$

$$C_b = W\left\{\frac{(14\varepsilon_r + 12.5)\frac{W}{h} - (1.83\varepsilon_r - 2.25)}{\sqrt{\frac{W}{h}}} + \frac{0.02\varepsilon_r}{\frac{W}{h}}\right\} pF \text{ for } \frac{W}{h} < 1 \tag{3.53}$$

Here '*W*' is the width of the microstrip line while '*h*' and 'ε_r' are the thickness and the permittivity of the substrate material respectively. These equations are claimed to be accurate within 5% error for $2.5 \le \varepsilon_r \le 15$ and $0.1 \le W/h \le 5$.

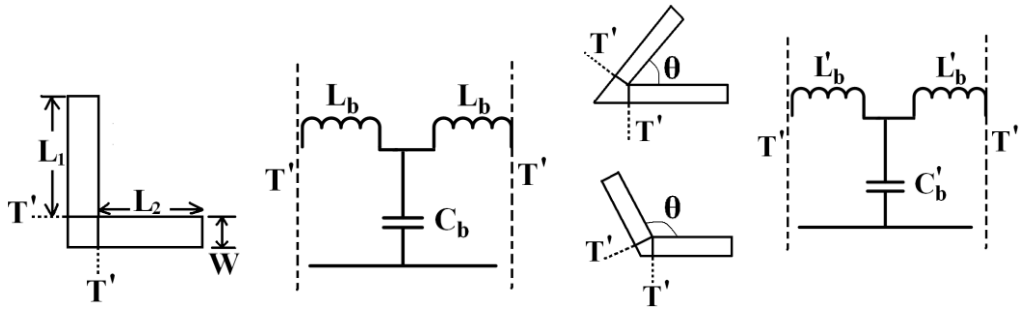

(a) (b)

Fig. 3.24:(a) Right Angle bends geometry and its lumped T circuit model, (b)Acute and Obtuse angle based bend geometries and corresponding lumped T circuit model.

3.4.2. DEVELOPMENT OF THE EMPIRICAL FORMULA

3.4.2.1. Defining an effective width:

Unlike a right angle bend where the bend region is a rectangular section, the bend area for a non-right angle bend (shaded region shown in Fig. 3.25a and Fig. 3.25b) is not a rectangular region. To be able to use the empirical model for right angle bend, first, an effective width is introduced in such a manner that, the total area for a square with side length W_{eff} (shown in Fig. 3.25c) is same as the bend area in the arbitrary bend case with bend angle θ.

So, W_{eff} is defined such that

$$W_{eff}^2 = W^2 \cot\frac{\theta}{2} \tag{3.54}$$

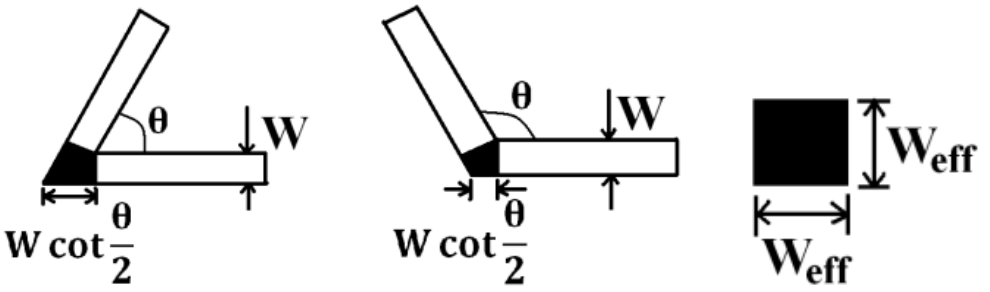

(a) (b) (c)

Fig. 3.25: (a) Acute Angle bends, (b) Obtuse angle bends, and (c) Effective width

which leads to

$$W_{eff} = W\sqrt{\cot\frac{\theta}{2}} \tag{3.55}$$

Next we use (3.51-3.53) with W replaced by $W_{eff.}$

3.4.2.2. Introduction of a Correction factor:

After replacing W by W_{eff} in (3.51-3.53), an empirical factor (c_m') is introduced in the expression of C_b in the following manner.

For W/h>1

$$C_b^{'} = W_{eff}\left\{(9.5\varepsilon_r + 1.25)\frac{W_{eff}}{h} + (5.2 + c_m^{'})\varepsilon_r + 7\right\} pF \tag{3.56}$$

For W/h<1

$$C_b^{'} = W_{eff}\left\{\frac{(14\varepsilon_r + 12.5)\frac{W_{eff}}{h} - ((1.83 + c_m^{'})\varepsilon_r - 2.25)}{\sqrt{\frac{W_{eff}}{h}}} + \frac{0.02\varepsilon_r}{\frac{W_{eff}}{h}}\right\} pF \tag{3.57}$$

Having modified the prototype formulae in such a manner, now, the empirical factor $c_m^{'}$ is evaluated using the following steps.

Step1: Bend geometry of Fig. 3.25a and Fig.3.25b are simulated in a MoM based full wave simulator and S_{11} data is retrieved.

Step 2: Same geometry is modeled as a cascade connection of three ABCD matrices ($ABCD_1 \times ABCD_2 \times ABCD_3$) where $ABCD_1$ and $ABCD_3$ are for the lines on either side of the bend. $ABCD_2$ is the ABCD matrix for the arbitrary bend and is evaluated from the T model for the bend (Fig. 3.24b). From this model, S_{11} is evaluated after considering a matched termination.

Step 3: Root mean square difference between the two S_{11} curves is minimized by varying $c_m^{'}$. To ascertain the range of variation for $c_m^{'}$, as a first order approximation, the normalized difference between bend capacitances of a right angle bend and a bend of angle θ is evaluated in a crude manner.

This gives:

$$\frac{\frac{\varepsilon_r W_{eff}^2}{h} - \frac{\varepsilon_r W^2}{h}}{\frac{\varepsilon_r W^2}{h}} = \cot\frac{\theta}{2} - 1 \tag{3.58}$$

Thus, for each bend of angle θ, $C_m = c_m^{'}\varepsilon_r W_{eff}$ is varied in the range $-\delta$ to δ. Thus an optimal value of $c_m^{'}$ for a particular bend is found from the optimal value of C_m.

Step 4: steps 1 to 3 are repeated for bend angles ranging from 30^0 to 135^0 in the frequency range 1 GHz to 8 GHz. Optimal $c_m^{'}$ values corresponding to each bend angle is noted down as a function of bend angle alone. This process is repeated for different substrate and line parameters (ε_r is chosen as 2.5, 4.4, 6.15 and 9.8 while W/h is varied in the range 0.33 to 3.95). It is observed that the value of $c_m^{'}$ does not vary substantially with the substrate and line parameters and is dependent on the bend angle alone.

3.4.2.3. Curve fitting and final expressions:

Once the data table for $c_m^{'}$ vs. bend angle is created, a curve fitted expression for $c_m^{'}$ is found using MATLAB. The expression is found to be,

For W/h>1:

$$c_m^{'} = 25.21\cot\left(1.145\theta - 0.2281\right) \tag{3.59}$$

For W/h<1:

$c_m^{'}$ is seen to vary linearly with the bend angle (θ) and expressions for these straight lines are calculated as,

Acute Angles: $$c_m^{'} = 25.21 - 25.21\frac{\theta - \frac{\pi}{4}}{\frac{\pi}{4}} \tag{3.60}$$

Obtuse Angles: $$c_m^{'} = 4.55\frac{\theta - \frac{\pi}{2}}{\frac{\pi}{2}} \tag{3.61}$$

These equations are in accordance with the extreme case i.e. for all case, $c_m^{'} \to 0$ as θ approaches $\frac{\pi}{2}$.

3.4.3. SIMULATION AND OBSERVATIONS

Some simulated cases with geometry type shown in Fig. 3.24b having line lengths of 30 mm on either side of the bend are shown in Fig. 3.26. Different substrate configurations and bend configurations are used for validation of the empirical formulae proposed in (3.59)-(3.61). It is observed that proposed formulae for $c_m^{'}$ and corresponding expressions for $C_b^{'}$ and $L_b^{'}$ yield results within 1 dB variation (in both S_{11} and S_{21}) for the bend geometries shown in Fig. 3.25a and Fig. 3.25b, for $2.5 \le \varepsilon_r \le 9.8$, $0.2 \text{ mm} \le W \le 3 \text{ mm}$, h<60 mils in the frequency range $f \le 5$ GHz . Accuracy of the model degrades beyond this range with discrepancies about 5 dB near 8 GHz in some cases.

Also, due to intense mutual coupling between adjacent line sections, performance of the model degrades below bend angle of 45 degrees. However, it should be mentioned at this point that, the range of applicability of the expressions as indicated above, is quite adequate for most interconnect applications as well as applications in line based antennas such as Franklin line, square loop lines, Koch lines etc.

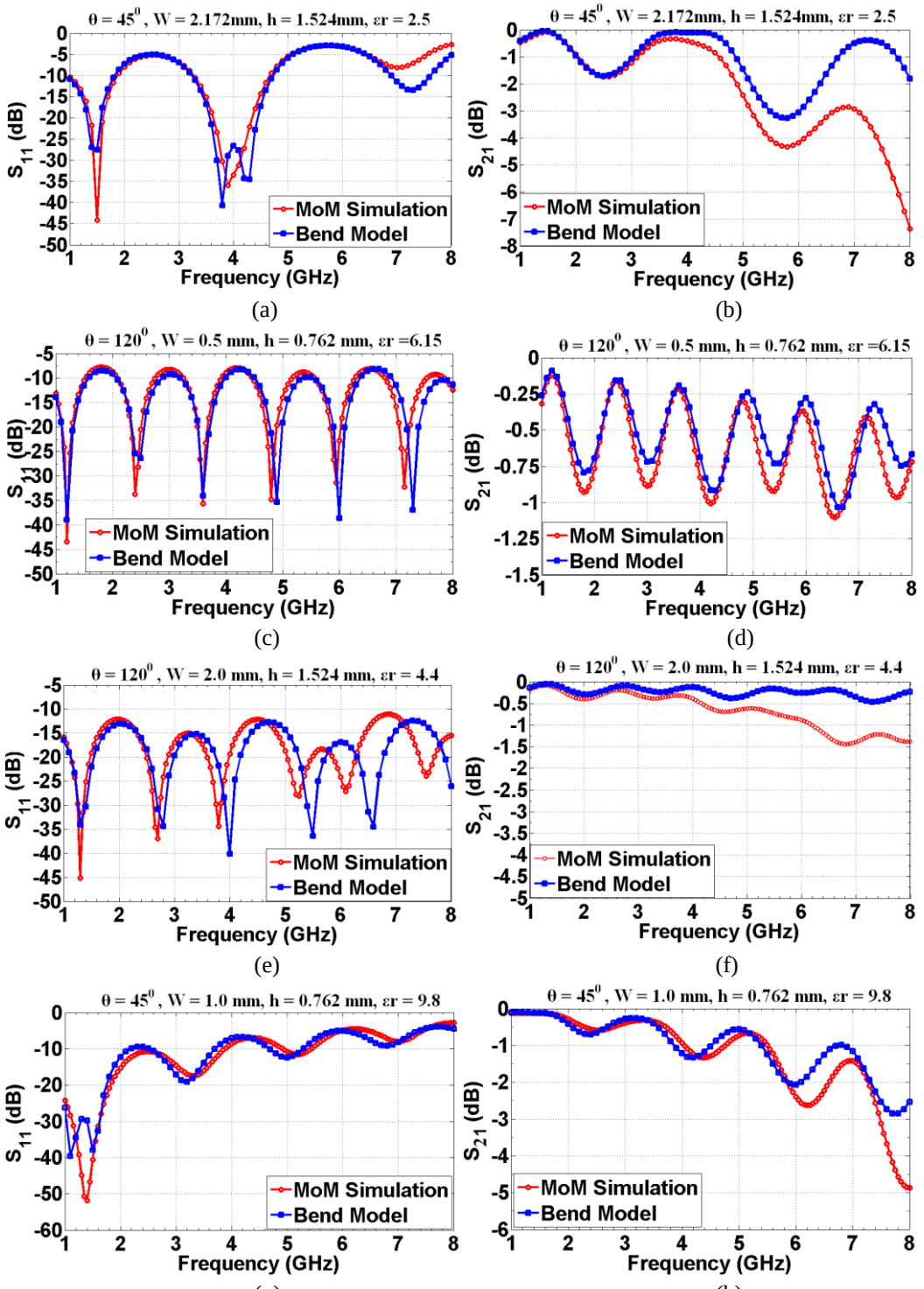

Fig. 3.26: S_{11} and S_{21} for (a) $\theta = 45^0$, W = 2.172mm, h = 1.524mm, $\varepsilon_r = 2$,(b) $\theta = 120^0$, W = 0.5 mm, h = 0.762 mm, $\varepsilon_r = 6.15$, (c) $\theta = 120^0$, W = 2.0 mm, h = 1.524 mm, $\varepsilon_r = 4.4$, (d) $\theta = 45^0$, W = 1.0 mm, h = 0.762 mm, $\varepsilon_r = 9.8$

3.4.4. FABRICATION AND MEASUREMENT

For validation of the model presented here, an acute angle (45^0) and an obtuse angle (120^0) bend based microstrip lines are fabricated on FR_4 substrate with ε_r= 4.4 and h = 60 mils with the geometries presented in Fig. 3.27. The acute angle based geometry has two bends with angle of 45^0 each while the obtuse angle based geometry has two bends with angle of 120^0 each. As shown in Fig. 3.28, results using the bend model presented by us are also compared with results from full wave MoM simulation, using expressions given by Tang et.al. [12] and practical measurements. Measured S_{11} values show good agreement with our model. Incorporation of radiation losses and dispersive nature of loss tangent would allow the empirical formulae to be used over a wider frequency range which we have not taken up presently.

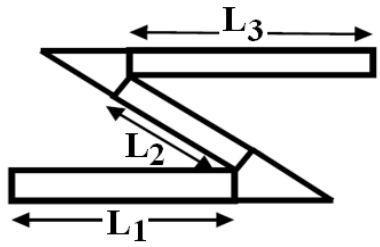

L_1= 44mm , L_2 =20mm, L_3 =44mm , W=2.172 mm

(a)

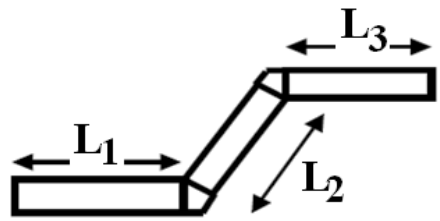

L_1= 32 mm, L_2 =23 mm L_3 =32 mm, W = 2.172 mm

(b)

Fig. 3.27: Fabricated (a) acute angle and (b) obtuse angle based geometries.

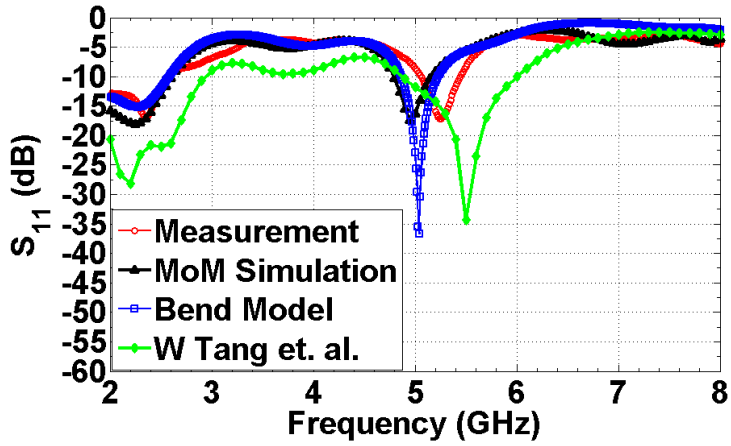

(a)

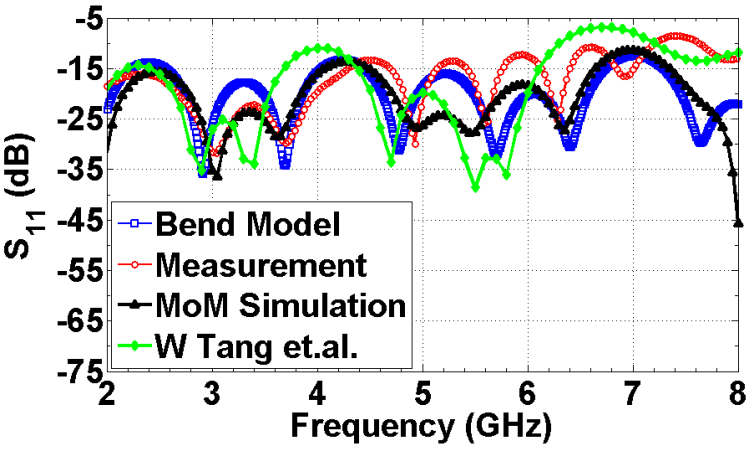

(b)

Fig. 3.28: (a) S_{11} vs. Frequency for the acute angle based geometry, (b) S_{11} vs. Frequency for the obtuse angle based geometry,

3.5 CONCLUSION

A comprehensive transmission line based model for analyzing discrete bends based microstrip travelling wave antennas is presented in this chapter. Input reflection co-efficient and impedances as well as radiation characteristics are evaluated. Effects of internal reflections from the sharp corners and the arbitrary load termination are included in the analysis. Contributions to total radiation from both the electric and magnetic current densities are considered. The model is verified for three different geometries namely the Hilbert line, Moore line and the Rampart line. Comparison of the simulated parameters evaluated using CST Microwave Studio and Zeland IE3D with those from calculation using MATLAB show good agreement. A prototype with three unit cells of the Rampart line is fabricated on RT Duroid substrate and the measured results are compared with those from simulation and calculation with good agreement as well. Next, an empirical circuit model is developed for the reactances of acute/obtuse angle based bends. Curve fitted formulae are presented and the model is verified with simulated as well as practical measurement data for two different fabricated prototypes with acute angle and obtuse angle based lines. Comparison shows good matching of the results. This simple model would thus be able to analyze microstrip travelling wave antennas having any sharp bends for their input as well as radiation characteristics.

REFERENCES:

[1] C. H. Walter, *Traveling wave antennas*. Dover Publications, 1970.

[2] E. Abdo-Sánchez, D. Palacios-Campos, C. Frías-Heras, F. Y. Ng-Molina, T. M. Martín-Guerrero, and C. Camacho-Peñalosa, "Electronically Steerable and Fixed-Beam Frequency-Tunable Planar Traveling-Wave Antenna," IEEE Transactions on Antennas and Propagation, vol. 64, no. 4, pp. 1298-1306, April 2016.

[3] K. Hirose, K. Shinozaki and H. Nakano, "A Comb-Line Antenna Modified for Wideband Circular Polarization," IEEE Antennas and Wireless Propagation Letters, vol. 14, no. , pp. 1113-1116, 2015.

[4] P. S. Hall, "Microstrip Linear Array with Polarization Control", Proc. Inst. Elect. Eng., vol. 130, pt. H, pp. 215-224, Apr. 1983.

[5] Y. Kami and R. Sato, "Analysis of radiation characteristics of a finite-length transmission line using a circuit-concept approach," IEEE Transactions on Electromagnetic Compatibility, vol. 30, no. 2, pp. 114-121, May 1988.

[6] M. I. Aksun and R. Mittra, "Estimation of spurious radiation from microstrip etches using closed-form Green's functions," IEEE Transactions on Microwave Theory and Techniques, vol. 40, no. 11, pp. 2063-2069, Nov 1992.

[7] M. Leone, "Closed-Form Expressions for the Electromagnetic Radiation of Microstrip Signal Traces," IEEE Transactions on Electromagnetic Compatibility, vol. 49, no. 2, pp. 322-328, May 2007.

[8] R. Garg, and I. J. Bahl, "Microstrip Discontinuities," Int. J. Electron., vol. 45, 1978, pp. 81-87

[9] W. Tang, Y.L. Chow and K.F. Tsang, "Different microstrip line discontinuities on a single field-based equivalent circuit model," *IEE Proceedings Microwaves, Antennas and Propagation,* vol.151, no.3, pp.256-262, 21 June 2004

Chapter 4

Arbitrarily Curved Microstrip Lines

Contents

4.1 INTRODUCTION

Advancement in analysis of curved microstrip lines started primarily to study them as a replacement for discrete bends in complex feed networks for microstrip arrays. These rounded off edges confine less amount of electric fields and consequently lead to reduced perturbation on the overall array performance. At the same time these curved bends (mainly circular bends) are proved to be radiating considerable reduced amount of power than their sharper counterparts. Starting with MMIC design, these curved lines were eventually introduced to antenna design as well. They were used in the design of polarization agile microstrip antennas [1], beam steering antennas [2] and in electrically small antennas [3]. Most of the analysis efforts for curved microstrip lines available in the literature have been focused on circular spirals [4] and whenever a sinusoidal or arbitrarily curved lines are considered, it had been in the context of rigorous full wave analysis [5, 6].

This chapter presents two different analysis techniques for arbitrarily curved microstrip lines. Simple transmission line based technique is used for lines with smaller width and curvature while a mode matching technique is developed

for lines with greater width and curvatures. First, curved microstrip lines with smaller curvature and smaller line width supporting the fundamental Quasi TEM mode of propagation is considered. An approximate piecewise linear technique based on simple transmission line theory is formulated in section 4.3. Radiation characteristics are calculated by summing up contributions from individual segments. Next in section 4.4, a Serret-Frenet reference frame based technique is presented in conjunction with the transmission line model to calculate the radiation characteristics quickly. Later in section 4.5, a mode matching based technique is developed to analyze microstrip lines with spatially varying curvature supporting both the fundamental mode and higher order modes as well.

4.2 PROBLEM FORMULATION

The basic problem attempted here is that of analyzing an arbitrarily curved microstrip line. The microstrip line geometry is considered to be based on the central curve y=f(x) having a parametric representation (g(t), h(t)) as shown in Fig. 4.1a. Width of the line built around the central curve is W_0. Top and side views of a prototype arbitrarily curved microstrip line are shown in Fig. 4.1a. The substrate has a permittivity of *'ε_r'* and a thickness of *'d'*. Some of the curved microstrip line geometries dealt with in this chapter are shown in Fig. 4.1b and Fig. 4.1c where a sinusoidal line and a planar microstrip spiral are shown.

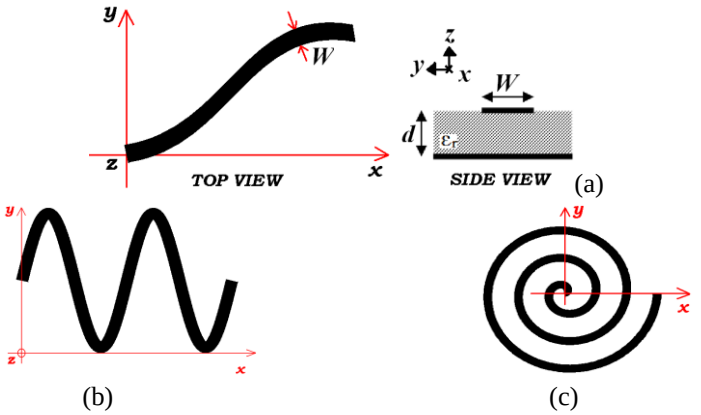

Fig. 4.1: (a) Top and side view of the curved microstrip line geometry, (b) sinusoidally curved microstrip line and (c) planar circular spiral geometry

4.3 PIECEWISE LINEAR MODEL FOR CURVED MICROSTRIP LINES

4.3.1 BASIC TECHNIQUE

The piecewise linear technique begins by discretizing the curved line in finite number of linear segments. Then radiated far fields from each such segment are calculated using a rectilinear transformation of the far-field Green's function and finally the radiated far fields from all such segments are added up to get the total far field. These steps are elaborated in the following sections.

4.3.1.1. Piecewise linear Discretization

The central curve for the arbitrarily curved microstrip line is represented in the parametric form as

$$x = g(\mathrm{t}),\ y = h(\mathrm{t}) \tag{4.1}$$

where 't' varies from T_s to T_e indicating the start and end values of the parameter respectively.

This central curve is now subdivided into N equal segments along the parameter 't'. Adopting a uniform discretizing scheme, the start (X_{sk}, Y_{sk}) and end co-ordinates (X_{ek}, Y_{ek}) for the k^{th} segment are given by

$$X_{sk} = g(\mathrm{t}_k),\ Y_{sk} = h(\mathrm{t}_k) \tag{4.2a}$$

$$X_{ek} = g(\mathrm{t}_{k+1}),\ Y_{ek} = h(\mathrm{t}_{k+1}) \tag{4.2b}$$

where $t_k = T_s + \left(\frac{T_e - T_s}{N}\right)k$ is the starting point value of 't' for the k^{th} segment.

Length of the k^{th} segment (l_k), length of the curve up to the k^{th} (L_k) segment and the total length of the entire line (L_{total}) are calculated as:

$$l_k = \sqrt{\left(X_{sk} - X_{ek}\right)^2 + \left(Y_{sk} - Y_{ek}\right)^2} \tag{4.3}$$

$$L_k = \int_{\zeta=T_s}^{t_k} \sqrt{\left(g'(\zeta)\right)^2 + \left(h'(\zeta)\right)^2}\, d\zeta \tag{4.4}$$

$$L_{total} = \int_{\zeta=T_s}^{T_e} \sqrt{\left(g'(\zeta)\right)^2 + \left(h'(\zeta)\right)^2}\, d\zeta \tag{4.5}$$

Parameters described above are shown in Fig 4.2 for an arbitrary space curve with the parametric representation of $\{g(t) = t,\ h(t) = f(t)\}$ (for example $f(t) = e^{at}$ for an exponential line) Inclination angle and the lengths of individual segments are shown in Fig 4.2.

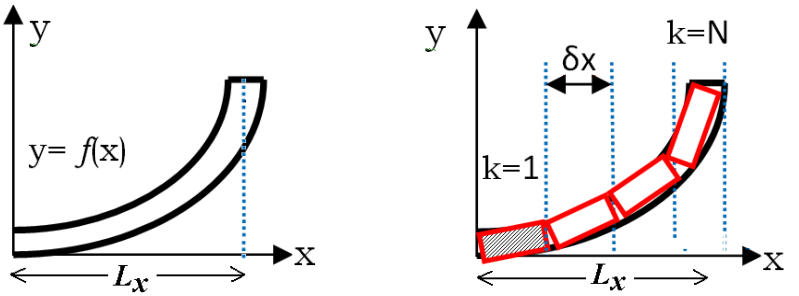

Fig. 4.2: (a) curved microstrip geometry and (b) piecewise discretization of the arbitrary curve

The original arbitrary curved line is thus reduced to N linear segments each with length l_k and inclination angle α_k with its location in space given by the co-ordinates of its starting point (X_{sk}, Y_{sk})

Choice of N here is dependent on the curvature of the line curve (specifically the region of highest curvature) and would increase as the curvature increases. Typically N is chosen so that smallest piecewise line length becomes less than 5% of the guided wavelength, beyond which results do not vary much.

The curvilinear nature of the microstrip line introduces a dispersive nature in the phase constant. The phase constant value can no more be evaluated using standard microstrip line formulae for dispersion. Since we have approximated the

curved line with piecewise linear segments, the phase constant is forcibly assumed to be the same as that of a uniform line with same line width as that of the curved line. Phase constants for a uniform line and a sinusoidally curved microstrip line are plotted in Fig. 4.3. Phase constant of the curved microstrip line is extracted from CST MWS by comparing two port S-parameters from simulation with that of a simple microstrip line. Difference between the phase constants is seen to be within 5% (4.4% at 5 GHz). This validates our approximation of using piecewise linear segments with non dispersive phase constant which holds good for curved microstrip lines with low to moderate curvature.

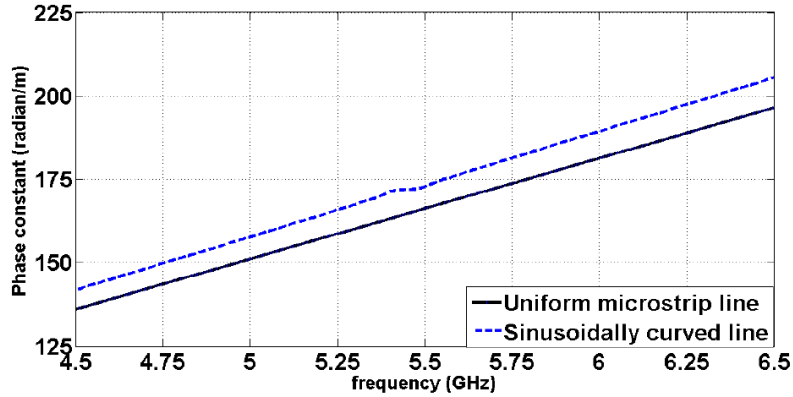

Fig. 4.3: comparison of phase constants between a uniform microstrip line and a sinusoidally curved microstrip line

4.3.1.2. Radiation from an inclined line segment

All the piecewise linear segments in the discretized curved microstrip line have different inclinations dependent on the original curve itself. This requires calculation of radiated far fields from an arbitrarily inclined line segment. To find the radiation from an inclined segment, first the far-fields from a horizontal segment are calculated and then a rotated coordinate system based on the inclined line is defined and all far fields for the inclined line are calculated using a simple mapping.

- *Far Fields for a Horizontal Line*

Radiated far fields from a horizontal '*x*' directed line segment is calculated from the voltage and currents along the line. These voltage and currents may be expressed using transmission line theory as:

$$v = v^{+}\left\{e^{-\gamma(x-l)} + \Gamma_L e^{\gamma(x-l)}\right\} \tag{4.6}$$

$$i = \frac{v^{+}}{Z_0}\left\{e^{-\gamma(x-l)} - \Gamma_L e^{\gamma(x-l)}\right\} \tag{4.7}$$

Here v^{+} is the amplitude of the forward travelling voltage wave, Z_0 is characteristic impedance of the line, γ is complex propagation constant, Γ_L is load reflection coefficient and 'l' is the length of the sgment. This electric current on the strip surface is now used to calculate the radiated far field using a Green's function technique with far field approximations [7] (Fig. 4.4). Closed form expressions for the radiated electric field in the far zone are given by M Leone [8]. These are summarized below:

$$E_\theta = \frac{j\omega\mu_0}{4\pi}\frac{e^{-jk_0 r}}{r}\frac{v^{+}e^{\gamma l}}{Z_0}\left[\frac{e^{(jk_0\sin\theta\cos\varphi-\gamma)l}-1}{(jk_0\sin\theta\cos\varphi-\gamma)} - \Gamma_L e^{-2\gamma l}\frac{e^{(jk_0\sin\theta\cos\varphi+\gamma)l}-1}{(jk_0\sin\theta\cos\varphi+\gamma)}\right] 2jk_0 h\left\{\frac{\sin^2\theta}{\varepsilon_r}-1\right\}\cos\varphi \tag{4.8}$$

$$E_\varphi = \frac{j\omega\mu_0}{4\pi}\frac{e^{-jk_0 r}}{r}\frac{v^{+}e^{\gamma l}}{Z_0}\left[\frac{e^{(jk_0\sin\theta\cos\varphi-\gamma)l}-1}{(jk_0\sin\theta\cos\varphi-\gamma)} - \Gamma_L e^{-2\gamma l}\frac{e^{(jk_0\sin\theta\cos\varphi+\gamma)l}-1}{(jk_0\sin\theta\cos\varphi+\gamma)}\right] 2jk_0 h\cos\theta\sin\varphi \tag{4.9}$$

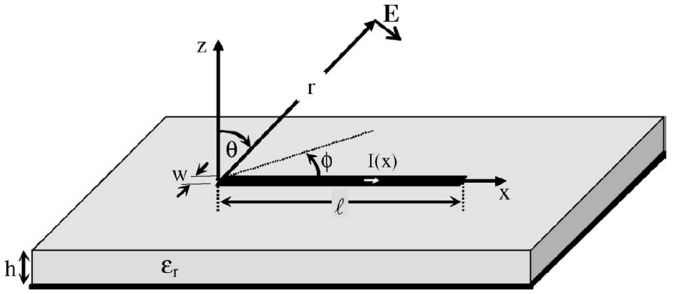

Fig. 4.4: Configuration used in [8] for computing the radiated fields. ©IEEE

- *Far Fields for an Inclined Line*

To calculate the radiated far fields from the inclined line segment shown in Fig. 4.5, the original co-ordinate system is rotated by an angle of 'α' to align the new co-ordinate system with the inclined segment. Thus the rotated coordinate system (x', y', z') is defined with respect to the original co-ordinate system (x, y, z) in the following manner

$$x' = x\cos\alpha + y\sin\alpha \tag{4.10a}$$

$$y' = -x\sin\alpha + y\cos\alpha \tag{4.10b}$$

$$z' = z \tag{4.10c}$$

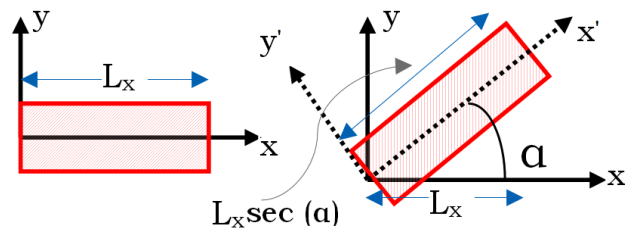

Fig. 4.5: Horizontal segment and corresponding rotated co-ordinate transformation for the inclined segment with an inclination angle of 'α'.

Here, α is the inclination angle of the segment with respect to the positive 'x' axis as shown in Fig. 4.4. In this rotated coordinate system (x', y', z'), the Cartesian to spherical transformation matrix becomes

$$\begin{bmatrix} r \\ \theta \\ \varphi \end{bmatrix} = \begin{bmatrix} \sin\theta\cos(\varphi-\alpha) & \sin\theta\sin(\varphi-\alpha) & \cos\theta \\ \cos\theta\cos(\varphi-\alpha) & \cos\theta\sin(\varphi-\alpha) & -\sin\theta \\ -\sin(\varphi-\alpha) & \cos(\varphi-\alpha) & 0 \end{bmatrix} \begin{bmatrix} x' \\ y' \\ z' \end{bmatrix} \tag{4.11}$$

Since the inclined line in the original (x, y, z) coordinate system has become horizontal (x' directed) in this new coordinate system (x', y', z'), the far-fields radiated by this inclined line segment are found by replacing x by x' and φ by $(\varphi - \alpha)$ in (4.8) and (4.9). This leads to the following expressions for E_θ and E_φ:

$$E_\theta = \frac{j\omega\mu_0}{4\pi}\frac{e^{-jk_0 r}}{r}\frac{v^+ e^{\gamma l}}{Z_0}\left[\frac{e^{\{jk_0\sin\theta\cos(\varphi-\alpha)-\gamma\}l}-1}{\{jk_0\sin\theta\cos(\varphi-\alpha)-\gamma\}} - \frac{\Gamma_L e^{-2\gamma l}e^{\{jk_0\sin\theta\cos(\varphi-\alpha)+\gamma\}l}-1}{\{jk_0\sin\theta\cos(\varphi-\alpha)+\gamma\}}\right] 2jk_0 h\left\{\frac{\sin^2\theta}{\varepsilon_r}-1\right\}\cos(\varphi-\alpha) \tag{4.12}$$

$$E_\varphi = \frac{j\omega\mu_0}{4\pi}\frac{e^{-jk_0 r}}{r}\frac{v^+ e^{\gamma l}}{Z_0}\left[\frac{e^{\{jk_0\sin\theta\cos(\varphi-\alpha)-\gamma\}l}-1}{\{jk_0\sin\theta\cos(\varphi-\alpha)-\gamma\}} - \frac{\Gamma_L e^{-2\gamma l}e^{\{jk_0\sin\theta\cos(\varphi-\alpha)+\gamma\}l}-1}{\{jk_0\sin\theta\cos(\varphi-\alpha)+\gamma\}}\right] 2jk_0 h\cos\theta\sin(\varphi-\alpha) \tag{4.13}$$

4.3.1.3. Total radiated far fields

Once the radiated far fields from an inclined segment with arbitrary inclination 'α' is calculated, total far fields radiated from the entire curved microstrip line are calculated by adding up the radiated fields from individual linear segments ($E_{\theta k}$ and $E_{\varphi k}$) vectorially. There are however two additional factors to be considered in the far field calculation of individual segments. One needs to be aware of the fact that the amplitude of the forward travelling voltage wave (v^+) is different for each segment and secondly the spatial location of individual segments.

Input impedance and the reflection coefficient at the end of each segment (Γ_k) are calculated approximately using the following recursive relation for the kth segment:

$$Z_k = Z_0\frac{Z_{k-1}+Z_0\tanh\{\gamma(L_{total}-L_k)\}}{Z_0+Z_{k-1}\tanh\{\gamma(L_{total}-L_k)\}} \tag{4.14}$$

$$\Gamma_k = \frac{Z_k - Z_0}{Z_k + Z_0} \tag{4.15}$$

where L_k and L_{total} are as given by (4.4) and (4.5).

v^+ is now calculated using the transmission line technique presented in Chapter 3. First, v^+ for the first segment (v_1^+) is calculated using the source voltage (V_s) and the input impedance (Z_{in}) of the entire line:

$$v_1^+ = V_s \frac{Z_{in}}{Z_0 + Z_{in}} \frac{1}{\left\{e^{\gamma l_1} + \Gamma_1 e^{-\gamma l_1}\right\}} \tag{4.16}$$

End voltage of the first segment is calculated as

$$V_{e1} = v_1^+ \left\{1 + \Gamma_1\right\} \tag{4.17}$$

Amplitude of the forward travelling voltage wave and the end voltage of all other segments are calculated in a sequential manner using the following relations

$$v_p^+ = \frac{V_{e(p-1)}}{\left\{e^{\gamma L_p} + \Gamma_p e^{\gamma L_p}\right\}} \tag{4.18}$$

$$V_{e(p-1)} = v_{p-1}^+ \left\{1 + \Gamma_{p-1}\right\} \tag{4.19}$$

v_p^+ and Γ_p thus calculated, can now be used in (4.12)-(4.13);

The spatial positioning factor for the k[th] segment is given by the location of the segment in the rotated co-ordinate system and is given by

$$PF_k = e^{jk_0 \sin\theta\left\{X_{rk}\cos(\varphi-\alpha_k)+Y_{rk}\sin(\varphi-\alpha_k)\right\}} \tag{4.20}$$

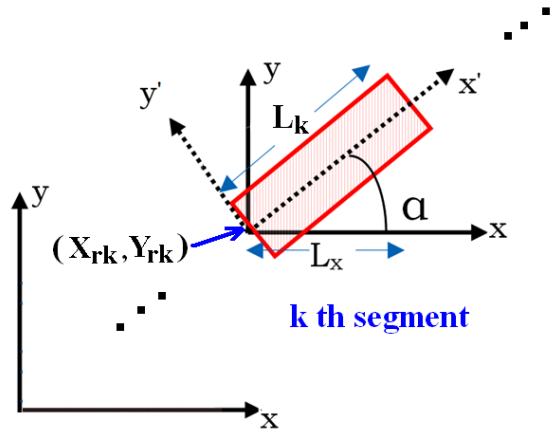

Fig. 4.6: Location of the k[th] linear segment with co-ordinates

where X_{rk} and Y_{rk} are coordinates of the front end of the k[th] segment in the rotated coordinate system and α_k is the inclination angle of that segment. X_{rk} and Y_{rk} are found by transformation from X_{sk} and Y_{sk} which indicate the same point in the original coordinate system. Thus,

$$X_{rk} = X_{sk}\cos\alpha_k + Y_{sk}\sin\alpha_k \tag{4.21}$$

$$Y_{rk} = -X_{sk}\sin\alpha_k + Y_{sk}\cos\alpha_k \tag{4.22}$$

Total E_θ and E_φ radiated from the curved microstrip trace are calculated from

$$E_{\theta strip} = \sum_{k=1}^{N} E_{\theta k} v_{0k} PF_k \tag{4.23}$$

$$E_{\varphi strip} = \sum_{k=1}^{N} E_{\varphi k} v_{0k} PF_k \tag{4.24}$$

In addition to the radiation from the piecewise linear line segments, radiation from the vertical source and load currents are also included in the analysis. In this context, closed form expression for E_θ given by Leone [8] is used:

$$E_{\theta vertical} = \frac{\omega\mu_0}{2\pi}\frac{e^{-jk_0 r}}{r}\, jh\frac{\sin\theta}{\varepsilon_r}\left[\frac{V_{f1}}{Z_{in}} - \frac{V_{eN}}{Z_L}e^{jk_0\sin\theta\{X_L\cos\varphi + Y_L\sin\varphi\}}\right] \tag{4.25}$$

Here $\vec{I}_s\,(=\frac{V_{f1}}{Z_{in}}\hat{z})$ and $\vec{I}_L\,(=\frac{V_{eN}}{Z_L}(-\hat{z}))$ are the source current entering the line and the load current flowing through the terminating impedance into the ground respectively.

Finally, the total radiated far fields (E_θ and E_φ) from the entire structure including contributions from the source and load currents are given by

$$E_{\theta total} = E_{\theta vertical} + \sum_{k=1}^{N} E_{\theta k} v_{0k} PF_k \tag{4.26}$$

$$E_{\varphi total} = \sum_{k=1}^{N} E_{\varphi k} v_{0k} PF_k \tag{4.27}$$

4.3.2 RESULTS

To validate the piecewise linear analysis technique presented in the last sections, a curved microstrip line based on a sinusoidal central curve given by the following equation is analyzed:

$$y = 25\sin\left(\frac{2n\pi}{50}x\right) \tag{4.28}$$

Here '*x*' varies from 0 to 50. Line width is taken as 2.172 mm while the substrate chosen has a permittivity of 2.5 and substrate thickness of 0.762 mm. The line is excited from one end while the other end is terminated in a 50Ω load. The central curve is shown in Fig. 4.7a for *n*=0.5 and 2.

One of the very important parameters in the piecewise linear technique is the number of segments to be taken for discretizing the central curve. Relative change of the input reflection co-efficient (% |dΓ|) in subsequent iterations with increasing number of segments is chosen as the stopping criteria. Fig. 4.7b shows the plot of % |dΓ| against the number of segments at 5GHz and 7 GHz for n=0.5 and n=2. It can be clearly observed that the line with greater curvature (i.e. n=2 case) requires greater number of segments for the piecewise linear analysis to saturate.

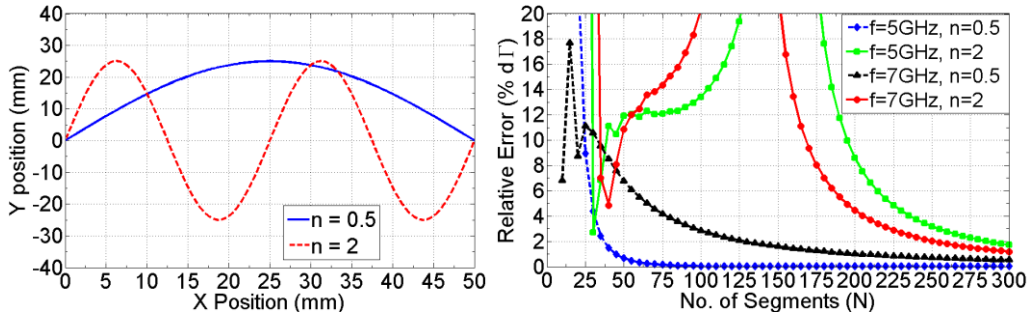

(a) (b)

Fig. 4.7: (a) Central curves for the lines with n=0.5 and n=2 and (b) Relative error with the number of segments taken for the analysis.

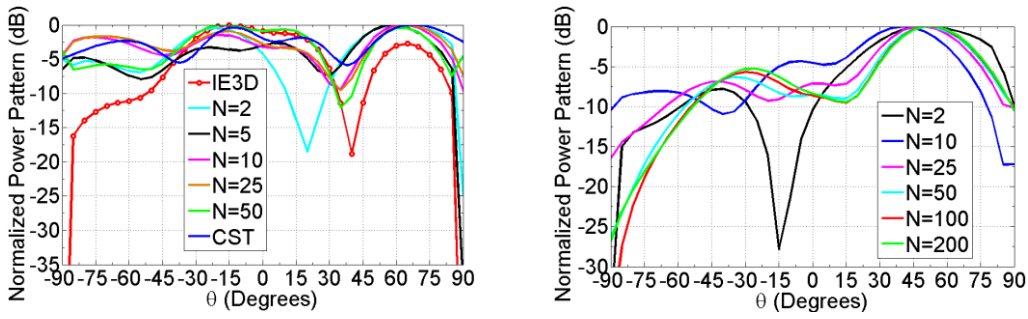

(a) (b)

Fig 4.8: Normalized power pattern in the x-z plane at 7 GHz for (a) n=0.5 and (b) n=1.

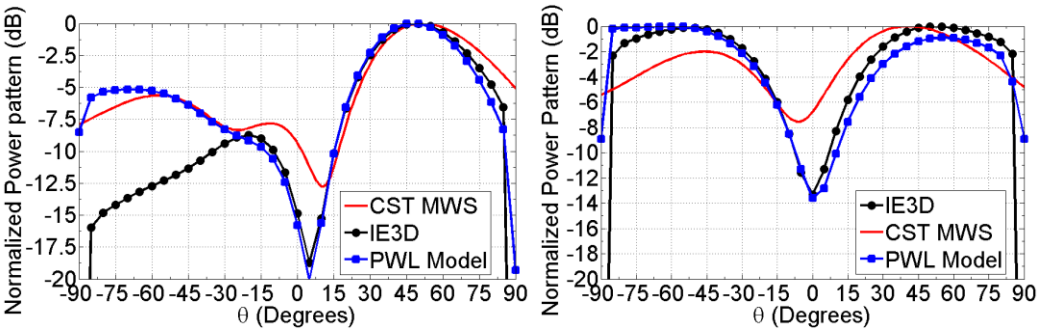

(a) (b)

Fig. 4.9: Normalized radiated power pattern for the sinusoidal line at 5 GHz in the (a) $\varphi=0^0$ plane and the (b) $\varphi=90^0$ plane.

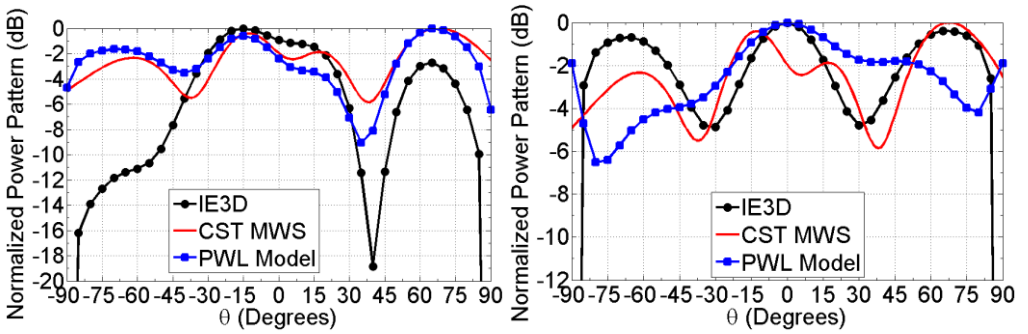

(a) (b)

Fig. 4.10: Normalized radiated power pattern for the sinusoidal line at 7 GHz in the (a) $\varphi=0^0$ plane and the (b) $\varphi=90^0$ plane.

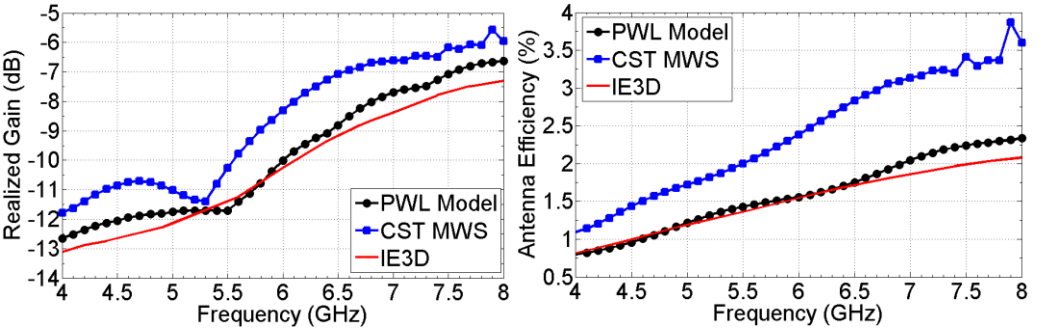

(a) (b)

Fig. 4.11: (a) Realized gain vs. frequency and (b) Antenna efficiency vs. frequency for the sinusoidal line.

Fig. 4.8a shows the radiated far field power pattern at 7 GHz for the geometry given by (4.28) with n=0.5 at $\varphi=0^0$ plane. The pattern is plotted for different number of line segments taken for the analysis. To consolidate the

observation, the $\varphi=0^0$ plane pattern at 7 GHz with n=1 is plotted in Fig. 4.8b for different number of segments.

Radiated far fields from the line at two different frequencies are calculated in the two principal planes ($\varphi=0^0$ and $\varphi=90^0$). These normalized patterns are plotted in Fig. 4.9a, b and Fig. 4.10a, b respectively for 5 GHz and 7 GHz. Radiated far field patterns are seen to be in good agreement with those obtained from simulations using MoM based IE3D as well as CST Microwave Studio. Simulated and calculated realized gain and antenna efficiency of the line are plotted in Fig. 4.11a and 4.11b respectively.

4.3.3 LIMITATIONS

The piecewise linear technique described in the last sections lead to an approximate far field predictions for curved microstrip lines with smaller curvature. However, the piecewise approximation requires a greater number of linear segments for lines with greater curvature. To alleviate this problem to some extent, a Serret-Frenet reference frame based transmission line model is presented in the next section that can calculate the radiated far fields from the line at one go. Moreover, the Green's function technique which is the basis of the piecewise linear technique, is suitable only for microstrip lines supporting the Quasi TEM mode of propagation under a small width, small substrate thickness scenario. A mode matching technique introduced later in this chapter necessitates the utilization of the Serret-Frenet reference frame based radiation calculation for computing the far-fields.

4.4 TRANSMISSION LINE MODEL IN SERRET-FRENET REFERENCE FRAME FOR FAR FIELD CALCULATION

To calculate the radiated far fields from an arbitrarily curved microstrip line, first, a dynamic co-ordinate system based on Serret-Frenet reference frame [9] is defined. Then the internal electric field, magnetic field and consequently the

current densities are expressed in this co ordinate system. Finally, these current densities are used to calculate the vector potentials and the radiated fields thereof. These steps are elaborated in the next few sections.

4.4.1 SERRET-FRENET REFERENCE FRAME

To develop the appropriate co-ordinate system aligned to the arbitrary space curve, we need to parametrically define the two edges as well as the central curve of the curved microstrip line. Unit vectors along and across the line need to be defined (detailed in Appendix I).

The space curve for the central line of the microstrip line is expressed in the parametric form as follows

$$x = g_0(\mathrm{t}), \mathrm{y} = \mathrm{h}_0(\mathrm{t}) \tag{4.29}$$

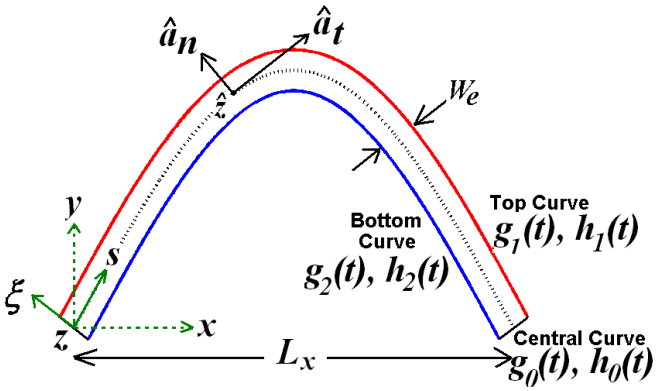

Fig. 4.12: Parametric representation of the microstrip line and the dynamic co -ordinate system

Co-ordinate variables along and across this curve are represented respectively as '*s*' and 'ξ'. Unit vectors along 's' is denoted as $\hat{a}_t$ while the one along 'ξ' is denoted as $\hat{a}_n$. These are shown in Fig. 4.12. Based on this central curve, the top and the bottom curves as indicated in Fig. 4.12 are expressed in the form of curves parallel to (g_0, h_0). Effective with of the microstrip line is considered to be 'W_e' where W_e is calculated from the planar waveguide theory [10].

For the top curve (g_1, h_1) located at a distance of $W_e/2$ from the central curve along ξ :

$$g_1(t) = g_0(t) - \frac{\frac{W_e}{2} h_0'(t)}{\sqrt{g_0'^2(t) + h_0'^2(t)}}, h_1(t) = h_0(t) + \frac{\frac{W_e}{2} g_0'(t)}{\sqrt{g_0'^2(t) + h_0'^2(t)}} \tag{4.30}$$

For the bottom curve (g_2, h_2) located at a distance of $W_e/2$ from the central curve along -ξ :

$$g_2(t) = g_0(t) + \frac{\frac{W_e}{2} h_0'(t)}{\sqrt{g_0'^2(t) + h_0'^2(t)}}, h_2(t) = h_0(t) - \frac{\frac{W_e}{2} g_0'(t)}{\sqrt{g_0'^2(t) + h_0'^2(t)}} \tag{4.31}$$

Then, the tangent ($\hat{a}_t$) and normal vectors ($\hat{a}_n$) along the curves are expressed in terms of g_0 and h_0 as

$$\hat{a}_t = \frac{g_0'(t)\hat{x} + h_0'(t)\hat{y}}{\sqrt{g_0'^2(t) + h_0'^2(t)}} \tag{4.32}$$

$$\hat{a}_n = \frac{-h_0'(t)\hat{x} + g_0'(t)\hat{y}}{\sqrt{g_0'^2(t) + h_0'^2(t)}} \tag{4.33}$$

The parametric length along the curve (s) is written as a function of 't' in the following form

$$s = \int_{\zeta=0}^{t} \sqrt{g_0'^2(\zeta) + h_0'^2(\zeta)}\, d\zeta \tag{4.34}$$

In all the above equations the primed quantities indicate derivatives with respect to 't'.

4.4.2 APPROXIMATE CURRENT DENSITIES

Neglecting all internal reflections and keeping only mismatch losses due to the load termination at the end of the line, transmission line based voltages and current in the line are written as:

$$v = v^{+}\left\{ e^{-\gamma\left(s-\int_{0}^{L_x}\sqrt{g_0'^2(\zeta)+h_0'^2(\zeta)}\,d\zeta\right)} + \Gamma_L e^{\gamma\left(s-\int_{\zeta=0}^{L_x}\sqrt{g_0'^2(\zeta)+h_0'^2(\zeta)}\,d\zeta\right)} \right\} \tag{4.35}$$

$$i = \frac{v^{+}}{Z_0}\left\{ e^{-\gamma\left(s-\int_{\zeta=0}^{L_x}\sqrt{g_0'^2(\zeta)+h_0'^2(\zeta)}\,d\zeta\right)} - \Gamma_L e^{\gamma\left(s-\int_{\zeta=0}^{L_x}\sqrt{g_0'^2(\zeta)+h_0'^2(\zeta)}\,d\zeta\right)} \right\} \tag{4.36}$$

Here 'T' is the extent of the parameter 't' which in case of the sinusoidal line of Fig. 4.12 is equal to the projection of the line on the 'x' axis as shown in Fig. 4.12 and γ is the complex propagation constant which is calculated as:

$$\gamma = \alpha + j\beta(\mathrm{t}) \tag{4.37}$$

Here β is taken as a function of position and is calculated using the curved waveguide model [9].

A Quasi TEM mode of propagation is assumed. Consequently, Electric and magnetic fields are calculated from (4.35) and (4.36) as

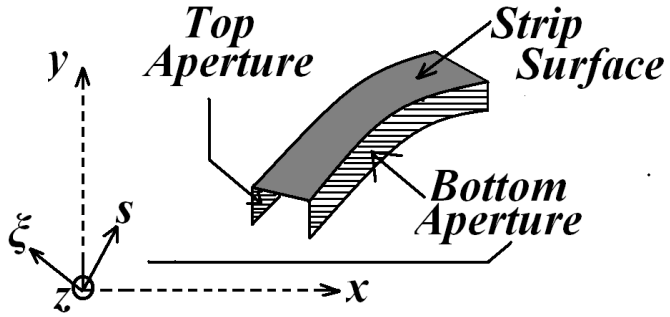

Fig. 4.13: Two side apertures and the strip surface for calculating the vector potentials

$$\vec{E} = -\frac{v}{d}\hat{z} \tag{4.38}$$

$$\vec{H} = \frac{i}{W_e}\hat{\xi} \tag{4.39}$$

Electric current density on the strip surface and magnetic current densities on the two side apertures (namely the top aperture and the bottom aperture) shown in Fig. 4.13 are calculated as

$$\overrightarrow{M}_{top} = E_z \hat{z} \times \hat{a}_n = -E_z \hat{a}_t \tag{4.40}$$

$$\overrightarrow{M}_{bottom} = E_z \hat{z} \times \left(-\hat{a}_n\right) = E_z \hat{a}_t \tag{4.41}$$

$$\vec{J} = -\hat{z} \times H_\xi \hat{a}_n = H_\xi \hat{a}_t \tag{4.42}$$

These electric and magnetic current densities are then used for calculation of the vector potentials.

4.4.3 VECTOR POTENTIALS AND RADIATED FAR-FIELDS

To calculate the radiated far fields from the curved microstrip line geometry, source integration is performed on the magnetic current densities on the side apertures. In addition, contribution from the electric current density on the strip surface is also considered. Electric and magnetic vector potentials are calculated using following equations,

$$\vec{A} = \frac{\mu_0}{4\pi} \int_{t=0}^{L_x} \vec{J}(\mathrm{t})\, \mathrm{W}_0 \frac{e^{-jk_0\left\{r - \vec{r}\,'.\hat{r}\right\}}}{r} \left|\frac{dr'}{dt}\right| dt \tag{4.43}$$

$$\vec{F} = \frac{\varepsilon_0}{4\pi} \int_{t=0}^{L_x} \int_{z=-d}^{d} \overrightarrow{M}(\mathrm{t}) \frac{e^{-jk_0\left\{r - \vec{r}\,'.\hat{r}\right\}}}{r} \left|\frac{dr'}{dt}\right| dt dz \tag{4.44}$$

After substituting $\vec{J}$ in (4.43) from (4.42), the integration along the central curve of the curved line becomes

$$\vec{A} = \frac{\mu_0 \mathrm{W}_0}{4\pi \mathrm{W}_e} \frac{v^+}{Z_0} \frac{e^{-jk_0 r}}{r} \int_{t=0}^{T} \left[\begin{array}{l} \left\{ e^{-\gamma(\mathrm{t})\left(\int_{\zeta=0}^{t} \sqrt{g_0'^2(\zeta)+h_0'^2(\zeta)}\, d\zeta - L_t\right)} - \Gamma_L e^{\gamma(\mathrm{t})\left(\int_{\zeta=0}^{t} \sqrt{g_0'^2(\zeta)+h_0'^2(\zeta)}\, d\zeta - L_t\right)} \right\} \\ \times \left\{ g_0'(\mathrm{t})\hat{x} + h_0'(\mathrm{t})\hat{\mathrm{y}} \right\} e^{jk_0\{g_0(\mathrm{t})\sin\theta\cos\varphi + \mathrm{h}_0(\mathrm{t})\sin\theta\sin\varphi + d\cos\theta\}} \end{array} \right] dt \tag{4.45}$$

After adding the contributions from the negative image of the horizontal electric current density on the infinite ground plane, (4.45) reduces to the following form

$$\vec{A}=\frac{j\mu_0 \mathrm{W}_0}{2\pi \mathrm{W}_e}\frac{v^+}{Z_0}\frac{e^{-jk_0 r}}{r}\sin\left(k_0 d\cos\theta\right)\int_{t=0}^{T}\left[\begin{Bmatrix} e^{-\gamma(\mathrm{t})\left(\int_{\zeta=0}^{t}\sqrt{g_0'^2(\zeta)+h_0'^2(\zeta)}d\zeta-L_t\right)} \\ -\Gamma_L e^{\gamma(\mathrm{t})\left(\int_{\zeta=0}^{t}\sqrt{g_0'^2(\zeta)+h_0'^2(\zeta)}d\zeta-L_t\right)} \end{Bmatrix}\times \left\{g_0'(\mathrm{t})\hat{x}+h_0'(\mathrm{t})\hat{\mathrm{y}}\right\}e^{jk_0\sin\theta\left\{g_0(\mathrm{t})\cos\varphi+\mathrm{h}_0(\mathrm{t})\sin\varphi\right\}}\right]dt \tag{4.46}$$

On the other hand, after substituting $\vec{M}$ in (4.44) from (4.40) and (4.41) we obtain the following expressions for the electric vector potentials due the top and the bottom apertures

$$\vec{F}_{top}=\frac{\varepsilon_0}{4\pi}\frac{e^{-jk_0 r}}{r}\frac{v^+}{d}\int_{t=0}^{T}\int_{z'=-d}^{d}\left[\begin{Bmatrix} e^{-\gamma(\mathrm{t})\left(\int_{\zeta=0}^{t}\sqrt{g_0'^2(\zeta)+h_0'^2(\zeta)}d\zeta-L_t\right)} \\ +\Gamma_L e^{\gamma(\mathrm{t})\left(\int_{\zeta=0}^{t}\sqrt{g_0'^2(\zeta)+h_0'^2(\zeta)}d\zeta-L_t\right)} \end{Bmatrix}\left\{g_1'(\mathrm{t})\hat{x}+h_1'(\mathrm{t})\hat{\mathrm{y}}\right\}\times e^{jk_0\left\{g_1(\mathrm{t})\sin\theta\cos\varphi+\mathrm{h}_1(\mathrm{t})\sin\theta\sin\varphi+z'\cos\theta\right\}}\right]dtdz' \tag{4.47}$$

$$\vec{F}_{bottom}=\frac{-\varepsilon_0}{4\pi}\frac{e^{-jk_0 r}}{r}\frac{v^+}{d}\int_{t=0}^{T}\int_{z'=-d}^{d}\left[\begin{Bmatrix} e^{-\gamma(\mathrm{t})\left(\int_{\zeta=0}^{t}\sqrt{g_0'^2(\zeta)+h_0'^2(\zeta)}d\zeta-L_t\right)} \\ +\Gamma_L e^{\gamma(\mathrm{t})\left(\int_{\zeta=0}^{t}\sqrt{g_0'^2(\zeta)+h_0'^2(\zeta)}d\zeta-L_t\right)} \end{Bmatrix}\left\{g_2'(\mathrm{t})\hat{x}+h_2'(\mathrm{t})\hat{\mathrm{y}}\right\}\times e^{jk_0\left\{g_2(\mathrm{t})\sin\theta\cos\varphi+\mathrm{h}_2(\mathrm{t})\sin\theta\sin\varphi+z'\cos\theta\right\}}\right]dtdz' \tag{4.48}$$

Here primed co-ordinates represent source quantities and unprimed ones indicate co-ordinates in the far field observation region. In (4.46-4.48), L_t is the total curve length of the central curve and is given by

$$L_t=\int_{\zeta=0}^{T}\sqrt{g_0'^2(\zeta)+h_0'^2(\zeta)}d\zeta) \tag{4.49}$$

Radiation from the vertical feed and load currents are also considered in this work. Source (J_{ZS}) and load currents (J_{ZL}) are calculated from the voltages at $s = 0$ and $s = L_t$. These are given by

$$J_{ZS} = V_0 / Z_{in} \tag{4.50}$$

$$J_{ZL} = V_L / Z_L \tag{4.51}$$

Corresponding magnetic vector potentials are calculated by integrating this current from (*-d, d*) due to the positive image of the vertical electric current

$$A_{Zload} = \frac{\mu_0 d}{2\pi\varepsilon_r} \frac{e^{-jk_0 r}}{r} J_{ZL} e^{jk_0\{X_L \sin\theta\cos\varphi + Y_L \sin\theta\sin\varphi\}} \frac{\sin(k_0 d\cos\theta)}{k_0 d\cos\theta} \tag{4.52}$$

$$A_{Zfeed} = \frac{\mu_0 d}{2\pi\varepsilon_r} \frac{e^{-jk_0 r}}{r} J_{ZS} e^{jk_0\{X_S \sin\theta\cos\varphi + Y_S \sin\theta\sin\varphi\}} \frac{\sin(k_0 d\cos\theta)}{k_0 d\cos\theta} \tag{4.53}$$

where (X_s, Y_s) and (X_L, Y_L) are the co-ordinates of the source current and the load current respectively.

Finally, the total radiated far fields are computed from the vector potentials of (4.46-4.48) and (4.52-4.53) using the following expressions

$$E_\theta = -j\omega[\cos\theta\{A_x\cos\varphi + A_y\sin\varphi\} - A_z\sin\theta + \eta_0\{F_y\cos\varphi - F_x\sin\varphi\}] \tag{4.54}$$

$$E_\varphi = -j\omega\left[\{F_y\cos\varphi - F_x\sin\varphi\} - \eta_0\cos\theta\{F_x\cos\varphi + F_y\sin\varphi\}\right] \tag{4.55}$$

4.4.4 RESULTS

The sinusoidal line geometry analyzed in section 4.3 using the piecewise linear model is considered here for analysis. Radiated power patterns in the two principal planes are presented in Fig. 4.14a and Fig. 4.14b for 5 GHz while Fig. 4.15a and 4.15b shows the patterns at 7 GHz. The apparent difference in the patterns calculated using the two techniques are due to the far-field calculation mechanism. While the Green's function technique utilized in the PWL Model is more accurate for calculation of radiation from microstrip traces of smaller widths

in the far zone, the electric and magnetic current based Serret-Frenet model is more generalized in a sense that it can handle microstrip lines with greater widths in both near and far zone by merely altering the integrations.

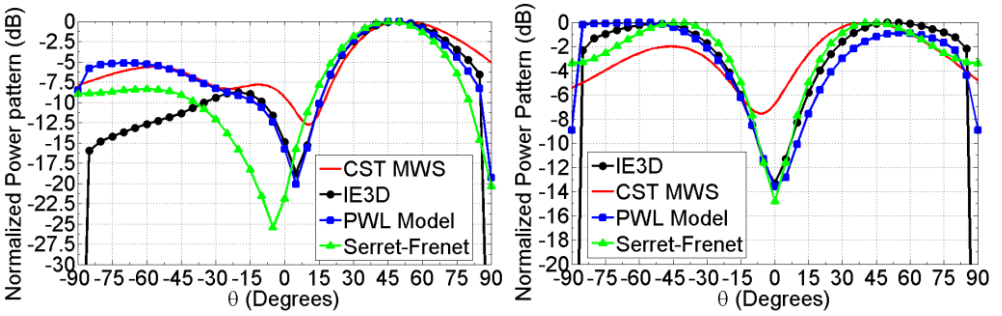

(a) (b)

Fig. 4.14: Normalized power pattern at 5GHz for the sinusoidally curved microstrip line of (4.28) in the (a) x-z plane and (b) y-z plane

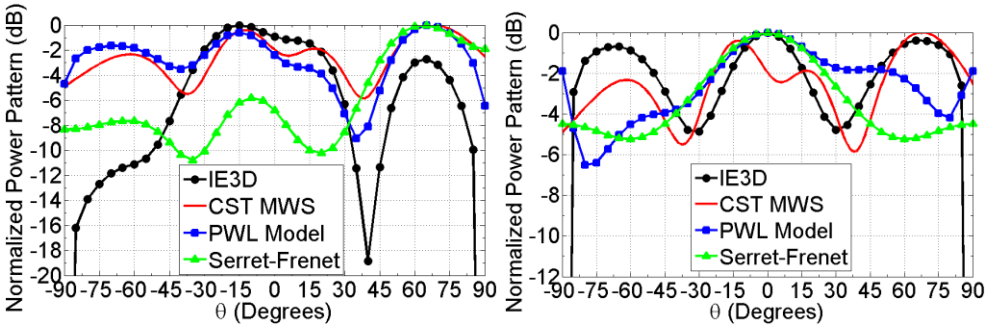

(a) (b)

Fig. 4.15: Normalized power pattern at 7GHz for the sinusoidally curved microstrip line of (4.28) in the (a) x-z plane and (b) y-z plane

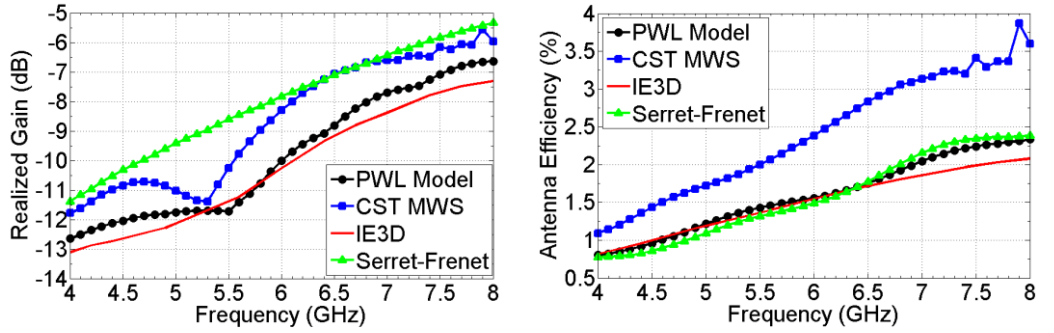

(a) (b)

Fig. 4.16: (a) Realized gain vs. frequency and (b) antenna efficiency vs. frequency for the sinusoidal line using transmission line model in the Serret-Frenet reference frame.

4.5 MODE MATCHING TECHNIQUE BASED ANALYSIS FOR ARBITRARILY CURVED MICROSTRIP LINES

4.5.1 LIMITATIONS OF THE UNIFORM PROPAGATION CONSTANT MODEL

Top and side views of the microstrip line geometry taken for the mode matching analysis are shown in Fig. 4.17. The line is based on a central space curve $y = f(x)$ with a parametric representation $x = g(\mathrm{t}), \mathrm{y} = \mathrm{h}(\mathrm{t})$,'t' being the parameter. Width of the microstrip line is considered to be 'W'.

Position dependent curvature (χ) of this general space curve is calculated from its parametric representation using

$$\chi = \frac{\left| g'(\mathrm{t})\,\mathrm{h}''(\mathrm{t}) - g''(\mathrm{t})\,\mathrm{h}'(\mathrm{t}) \right|}{\left[g'^2(\mathrm{t}) + h'^2(\mathrm{t}) \right]^{\frac{3}{2}}} \tag{4.56}$$

where single and double prime in superscript indicate respectively the first and second derivatives with respect to the independent variable 't'.

The phase constant for the fundamental quasi TEM mode in any curved waveguides/microstrip lines is dependent on the curvature and is calculated using [9]

$$\beta = k_e \sqrt{\left\{ 1 - \frac{W_e^2 \chi^2}{12} \left(1 - \frac{2}{5} k_e^2 W_e^2 \right) \right\}} \tag{4.57}$$

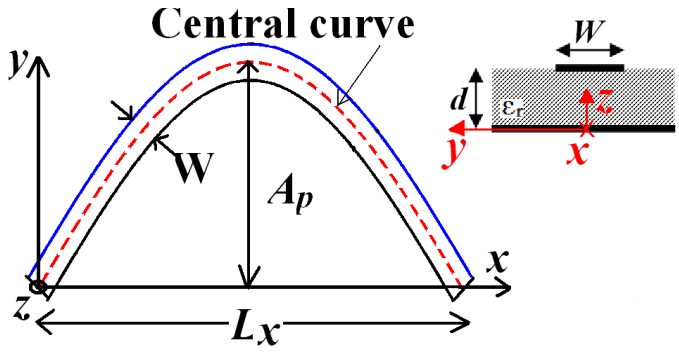

Fig. 4.17: Geometry with co-ordinate system for the mode matching analysis

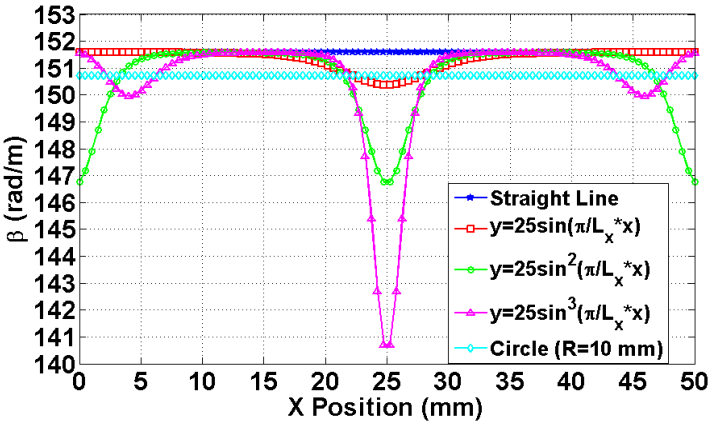

Fig. 4.18: Phase constant vs. position for different curved geometries at 5 GHz

Here, W_e and k_e are the effective line width and the effective wave number respectively, calculated from planar waveguide model.

Fig. 4.18 shows the variation of the phase constant as calculated by (4.57) for different curved microstrip lines. Comparison among a straight line, a circularly curved microstrip line and sinusoidal lines of different curvature profiles are performed. It can be clearly identified that the phase constant has a variation with position and this variation increases near the regions of greater curvature. It thus becomes imperative that curved microstrip lines be analyzed using a technique that is capable of incorporating this variation in phase constant along the line in an appropriate manner for calculation of internal fields as well as radiated far fields from such lines. The mode matching technique presented in the following sections aim to resolve this problem.

4.5.2 BRIEF DESCRIPTTION OF THE TECHNIQUE

The basic formulation of the mode matching technique involves three main steps. First, the curved microstrip line is discretized into several circular segments having constant curvatures and the electric and magnetic fields inside them are expressed in a modal summation of linearly independent functions. Next, electric and magnetic fields are subjected to appropriate source, load and

inter-segment boundary conditions to form a set of simultaneous algebraic equations in the excitation co-efficient of the different modes. Finally, this set of simultaneous equations is solved using standard matrix inversion techniques to calculate the complete solution for the internal fields. These steps are elaborated in the following sections.

4.5.3 DISCRETIZATION OF THE ARBITRARY CURVE

The first step is to fragment the arbitrarily curved microstrip line into N_s circular segments. To this end, the center curve for the microstrip line is first discretized into $2N_s+1$ number of uniformly spaced points along the x axis. Out of these $2N_s+1$ points, three are taken at a time to define a circular segment. Each segment is thus created from the intersection of the arbitrary space curve depicting the microstrip line and a generating circle passing through the three points (x_1,y_1), (x_2,y_2) and (x_3,y_3). This is shown in Fig. 4.19a for a sinusoidally curved line. The circular curve (in red in Fig. 4.19a) thus created is expressed as

$$(\mathrm{x}-\mathrm{x}_0)^2+(y-y_0)^2=a^2 \tag{4.58}$$

where $x_0=-\dfrac{P_2-P_1\dfrac{R_2}{R_1}}{Q_1\dfrac{R_2}{R_1}-Q_2}$,

$$y_0=\frac{P_1}{R_1}+\frac{Q_1}{R_1}\left(\frac{P_2-P_1\dfrac{R_2}{R_1}}{Q_1\dfrac{R_2}{R_1}-Q_2}\right),\ a=\sqrt{\{x_1-x_0\}^2+\{y_1-y_0\}^2}$$

$$P_1=(x_1^2-x_2^2)+(y_1^2-y_2^2), P_2=(x_1^2-x_3^2)+(y_1^2-y_3^2)$$
$$Q_1=2(x_1-x_2), Q_2=2(x_1-x_3), R_1=2(y_1-y_2), R_2=2(y_1-y_3)$$

Here $(\mathrm{x}_0, \mathrm{y}_0)$ and 'a' are respectively the centre coordinate and the radius of the generating circle. In the subsequent analysis, curvature of this circular segment is taken as $\chi=1/a$ As indicated in Fig. 4.19b, an aligned dynamic co-

ordinate system is created [11] with the new co ordinate variables '*s*' along the circular segment, 'ξ' along the cross section and '*z*' along the height. Also, a scaling factor of $(1-\chi\xi)$ is introduced along the '*s*' direction because of the position dependent curvature of the line.

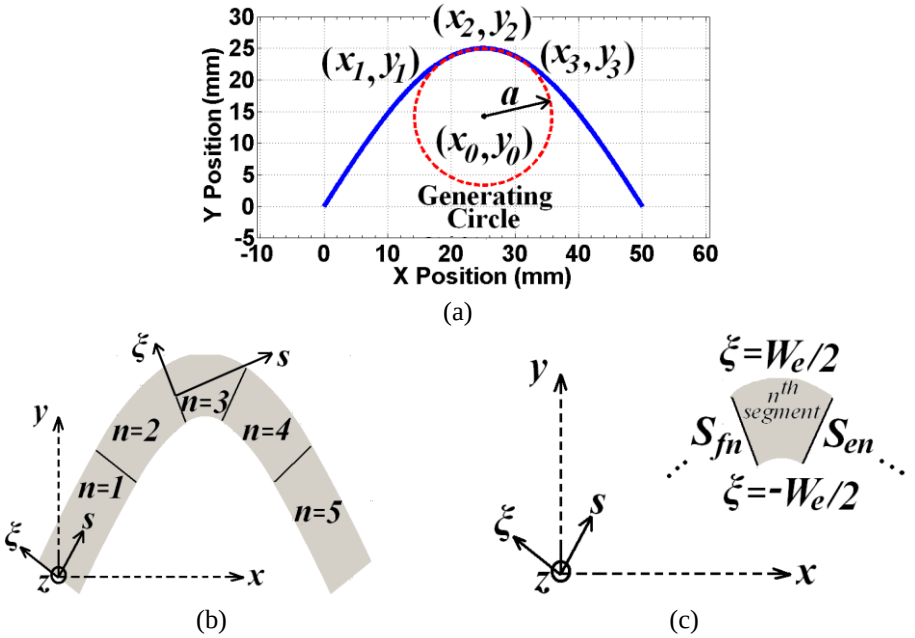

Fig. 4.19: (a) Pictorial representation of a circular segment generated from intersection of the generating circle with the sinusoidal curve, (b) circular segments of the sinusoidal microstrip line (top view) and (c) start and end co-ordinates of the n^{th} circular segment.

4.5.4 FIELD REPRESENTATION AND MODAL PROPERTIES

The discretization procedure generates several circular segments. Electric field underneath each such circular section is variable in along the length as well as the width of the line. These are calculated by assuming a modal propagation along the line and a summation of linearly independent functions weighted by the curvature to approximate the transverse field variation. Linearly independent field solutions for the electric field underneath the n^{th} circular strip in the co-ordinate system as defined in Fig. 4.19b are thus expressed as

$$E_{np} = e^{-j\beta_{np}s}\psi_{np} \tag{4.59}$$

$$\psi_{np} = \phi_{0p} + \chi_n\phi_{1p} + \chi_n^2\phi_{2p} + \ldots \tag{4.60}$$

Here '*n*' is the segment number, '*p*' is the mode number, '*s*' is the co-ordinate variable along the curve, χ_n is the curvature of the n^{th} circular segment and the phase constant (β_{np}) is given by [9]

$$\beta_{np} = \begin{cases} k_e\sqrt{\left\{1-\dfrac{W_e^2\chi_n^2}{12}\left(1-\dfrac{2}{5}k_e^2W_e^2\right)\right\}} & \text{for p=0} \\ \sqrt{k_e^2\left(1-\dfrac{p^2\pi^2}{k_e^2W_e^2}\right)+\dfrac{\pi^2\chi_n^2}{6}\left[p^2+\dfrac{12-p^2\pi^2}{2p^2\pi^4}k_e^2W_e^2-\dfrac{21+p^2\pi^2}{2p^4\pi^6}k_e^4W_e^4\right]} & \text{for p>0} \end{cases} \tag{4.61}$$

$\phi_{ip}(i=0,1,2,\cdots)$ are functions of transverse co-ordinate variable 'ξ' and are given in [11] for different '*i*' and '*p*'. These are reproduced here with appropriate modifications in the co-ordinate variables.

$$\phi_{0p} = \cos\left[\frac{p\pi}{W_e}\left(\xi-\frac{W_e}{2}\right)\right] \tag{4.62}$$

$$\phi_{1p} = \begin{cases} -k_e^2\xi\left(\dfrac{W_e^2}{4}-\dfrac{\xi^2}{3}\right) & for\ p=0 \\ \dfrac{W_e^2}{2p^2\pi^2}\left\{\dfrac{d\phi_{0p}}{d\xi}\left[\beta_p^2\left(\xi^2-\dfrac{W_e^2}{4}\right)-\dfrac{k^2W_e^2}{p^2\pi^2}\right]+k_e^2p\phi_{0p}\right\} & for\ p>0 \end{cases} \tag{4.63}$$

$$\phi_{2p} = \begin{cases} \dfrac{k_e^2\xi^2}{6}\left[2\xi^2-W_e^2+\dfrac{k_e^2}{60}\left(6W_e^4-15\xi^2W_e^2+8\xi^4\right)\right] & \text{for } p=0 \\ L_p(\xi)\phi_{0p}+M_p(\xi)\dfrac{d\phi_{0p}}{d\xi} & \text{for } p>0 \end{cases} \tag{4.64}$$

where

$$L_p = \frac{W_e^2 \xi^2}{8n^2\pi^2}\left[k_e^2\left(\frac{7k_e^2 W_e^2}{n^2\pi^2} - 4 \right) + \beta_p^4 \left(\frac{W_e^2}{2} - \xi^2 \right) \right] \tag{4.65}$$

$$M_p = \frac{-W_e^4 \xi}{48 p^4 \pi^4}\left[12k_e^2\left(\frac{7k_e^2 W_e^2}{p^2\pi^2} - 4 \right) + \beta_p^2 \left(W_e^2 - 4\xi^2 \right)\left(9k_e^2 - 4\beta_p^2 \right) \right] \tag{4.66}$$

These linearly independent solutions for electric field in the n^{th} segment (E_{np}) are converted to an orthogonal set by defining an appropriate weighted orthogonalization [12] procedure as follows

$$\int_{-W_e/2}^{W_e/2} E_{np} E_{nq} \left(1 - \chi_n \xi\right)^{-1} d\xi = 0 \quad \text{for p} \neq q \tag{4.67}$$

Using (4.60) and (4.67), this condition reduces to the following,

$$\int_{-W_e/2}^{W_e/2} \psi_{np} \psi_{nq} \left(1 - \chi_n \xi\right)^{-1} d\xi = 0 \quad \text{for p} \neq q \tag{4.68}$$

4.5.5 MODE MATCHING PRE-PROCESSING

Following the discretization procedure described in the previous section, we have N_s circular segments with known phase constants and cross sectional field variations. These N_s segments are in a sequentially cascaded connection. In this section we use a sequential mode matching procedure to find a complete solution to the internal electric field inside the arbitrarily curved line.

Firstly, the electric field in the n^{th} circular segment is written as a summation of modal wave functions in the following manner [11].

$$E_z = \sum_{p=0}^{\infty} \left[c_{np}^a \cos\beta_{np}\left(s - s_{fn} \right) + c_{np}^b \cos\beta_{np}\left(s - s_{en} \right) \right] \psi_{np} \tag{4.69}$$

Here c_{np}^a and c_{np}^b are unknown modal amplitudes for the p^{th} mode inside the n^{th} segment which shall be calculated using the mode matching procedure. S_{fn}

and S_{en} are consecutively the front and end position of the nth segment as shown in Fig. 4.19c.

Internal magnetic field is calculated from the electric field using Maxwell's equation as,

$$\overrightarrow{H} = \frac{1}{j\omega\mu_0}\left[\frac{1}{1-\chi_n\xi}\frac{\partial E_z}{\partial s}\hat{\xi} - \frac{\partial E_z}{\partial \xi}\hat{s}\right] \tag{4.70}$$

Only H_ξ is considered for subsequent calculations as this component yields longitudinal currents on the strip and contribute to power flow along the line. Consequently, H_ξ is calculated as

$$H_\xi = \frac{-1}{j\omega\mu_0(1-\chi\xi)}\sum_{p=0}^{\infty}\beta_{np}\left[c_{np}^a \sin\beta_{np}(s-s_{fn}) + c_{np}^b \sin\beta_{np}(s-s_{en})\right]\psi_{np} \tag{4.71}$$

The microstrip line is considered to be excited by a surface current J_0 A/m as indicated in Fig. 4.20b and is terminated in a lumped load Z_l shown in Fig. 4.22b. Boundary conditions and the sequential mode matching procedure are described next.

4.5.6 MODE MATCHING PROCEDURE

4.5.6.1. Feed boundary condition

The excitation to the microstrip line in this thesis is modeled as a vertical strip of current having a height equal to the thickness of the substrate (*d*) and width W_f. The width is chosen to emulate an SMA (Sub miniature type A) connector as feeding arrangement. Boundary condition at the excitation strip is then expressed as follows,

$$H_{\xi 1}(s = s_{f1}) = \begin{cases} J_z & \text{for } \xi_0 \le \xi \le \xi_0 + W_f \\ 0 & \text{elsewhere} \end{cases} \tag{4.72}$$

Here ξ_0 indicates the offset feed position. For example, ξ_0 is 0 (i.e. fed at the center of the strip edge) for the fundamental mode and (W_e/2-W$_f$/2) for the first higher order mode in the microstrip line (since the first higher order mode has a odd symmetry along the width of the line, there is a null at the center of the strip edge). This feed position is chosen according to the electric field maximum for the microstrip line mode under consideration.

Application of (4.32) on the magnetic field of the first segment defined earlier leads to,

$$\frac{1}{j\omega\mu_0\left(1-\chi_1\xi\right)}\sum_{p=0}^{\infty}-\beta_{1p}\left[-c_{1p}^{b}\sin\beta_{1p}L_1\right]\psi_{1p}=\begin{cases}J_z & \text{for } \xi_0\le\xi\le\xi_0+W_f\\ 0 & \text{elsewhere}\end{cases} \qquad (4.73)$$

Now, multiplying both side by ψ_{1q} and integrating with respect to ξ from $-W_e/2$ to $W_e/2$, we obtain

$$c_{1q}^{b}=\frac{j\omega\mu_0}{I_1\beta_{1q}\sin\beta_{1q}L_1}\int_{\xi_0}^{\xi_0+W_f}J_z\psi_{1q}d\xi \quad \text{for } q=0,\,1\ldots\infty \qquad (4.74)$$

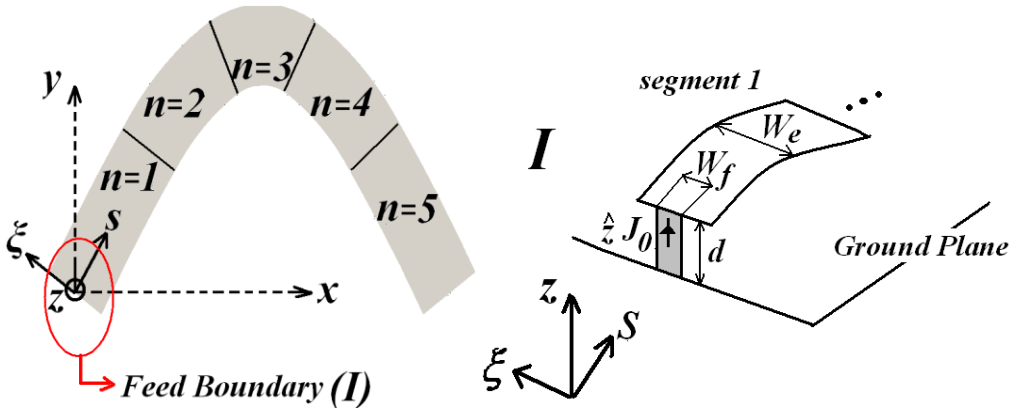

Fig. 4.20: (a) Feed boundary on the curved line geometry and (b) the vertical current strip model for the source

4.5.6.2. Inter-segment boundary condition

Continuity of the tangential electric and magnetic fields along the interface between the n-1th and the nth segment (shown in Fig. 4.21b) gives the following two boundary conditions.

$$H_{\xi\,n-1}(s = s_{en-1}) = H_{\xi n}(s = s_{fn}) \tag{4.75}$$

$$E_{z\,n-1}(s = s_{en-1}) = E_{zn}(s = s_{fn}) \tag{4.76}$$

Application of (4.75) gives,

$$\frac{1}{j\omega\mu_0(1-\chi_{n-1}\xi)}\sum_{p=0}^{\infty}-\beta_{n-1p}\left[c^a_{n-1p}\sin\beta_{n-1p}L_{n-1}\right]\psi_{n-1p} = \frac{1}{j\omega\mu_0(1-\chi_n\xi)}\sum_{m=0}^{\infty}-\beta_{nm}\left[-c^b_{nm}\sin\beta_{nm}L_n\right]\psi_{nm} \tag{4.77}$$

where L_q is the length of the q^{th} segment.

Now, multiplying both sides by ψ_{nq} and integrating with respect to ξ from $-W_e/2$ to $W_e/2$, we obtain

$$c^b_{nq} = \frac{1}{I_1\beta_{nq}\sin\beta_{nq}L_n}\sum_{p=0}^{\infty}-I_2\beta_{n-1p}c^a_{n-1p}\sin\beta_{n-1p}L_{n-1} \qquad q = 0, 1\ldots\infty \tag{4.78}$$

Here $I_1 = \int_{-W_e/2}^{W_e/2}\psi^2_{nq}(1-\chi_n\xi)^{-1}d\xi$ and $I_2 = \int_{-W_e/2}^{W_e/2}\psi_{n-1p}\psi_{nq}(1-\chi_n\xi)^{-1}d\xi$

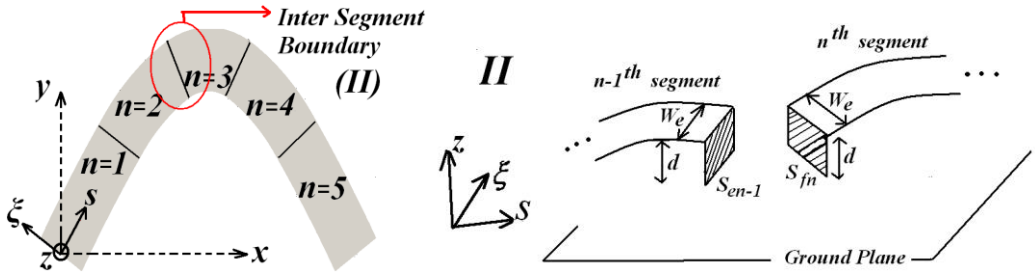

(a) (b)

Fig. 4.21: (a) Inter-segment boundary on the curved line geometry and (b) the interface of the two consecutive segments.

Application of (4.76) on the other hand leads to

$$\sum_{p=0}^{\infty}\left[c_{n-1p}^{a}\cos\beta_{n-1p}L_{n-1}+c_{n-1p}^{b}\right]\psi_{n-1p}=\sum_{t=0}^{\infty}\left[c_{nt}^{a}+c_{nt}^{b}\cos\beta_{nt}L_{n}\right]\psi_{nt} \tag{4.79}$$

Now, multiplying both sides by $\psi_{nq}(1-\chi_n\xi)^{-1}$ and integrating with respect to ξ from (-W_e/2 to W_e/2) we obtain

$$\begin{aligned}&\sum_{p=0}^{\infty}\left[c_{n-1p}^{a}\cos\beta_{n-1}^{p}L_{n-1}+c_{n-1p}^{b}\right]\int_{-W_e/2}^{W_e/2}\psi_{n-1p}\psi_{nq}(1-\chi_n\xi)^{-1}d\xi=\\&\sum_{t=0}^{\infty}\left[c_{nt}^{a}+c_{nt}^{b}\cos\beta_{nt}L_{n}\right]\int_{-W_e/2}^{W_e/2}\psi_{nt}\psi_{nq}(1-\chi_n\xi)^{-1}d\xi\end{aligned} \tag{4.80}$$

Enforcing the orthogonal properties of ψ_{nt} and ψ_{nq} , we obtain the following form after some simplification,

$$c_{nq}^{a}=\sum_{p=0}^{\infty}c_{n-1p}^{a}\left[\cos\beta_{n-1p}L_{n-1}\frac{I_3}{I_1}+\frac{\beta_{n-1p}\sin\beta_{n-1p}L_{n-1}}{\beta_{nq}\tan\beta_{nq}L_{n}}\frac{I_2}{I_1}\right]+c_{n-1p}^{b}\frac{I_3}{I_1}\quad\text{for } q=0,\,1,\,...\infty \tag{4.81}$$

Here $I_3=\int_{-W_e/2}^{W_e/2}\psi_{n-1p}\psi_{nq}(1-\chi_n\xi)^{-1}d\xi$

4.5.6.3. Load boundary condition

The microstrip line is terminated in a general complex load (Z_L). Boundary condition used for this load is expressed as follows,

$$\frac{E_{zN_s}(\mathrm{s}=\mathrm{s}_{eN_s},\xi=0)}{H_{\xi N_s}(\mathrm{s}=\mathrm{s}_{eN_s},\xi=0)}=-\frac{W_e}{d}Z_L \tag{4.82}$$

where '*d*' is the substrate thickness. This leads to the following form after substituting E and H from (4.69) and (4.71) and subsequent simplification,

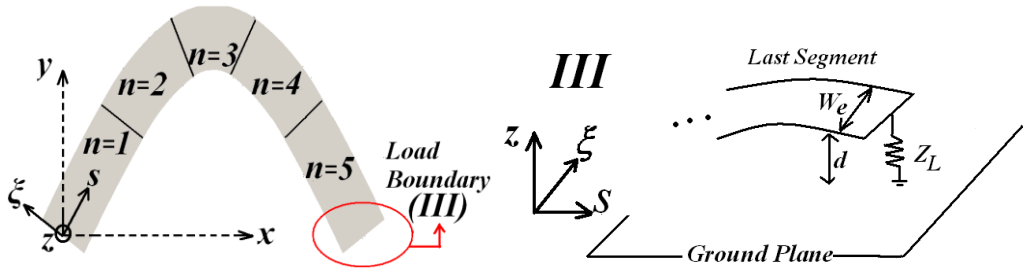

(a) (b)

Fig. 4.22: (a) Load boundary on the curved line geometry and (b) the vertical localized impedance model for the load.

$$\sum_{q=0}^{\infty}\left[c_{N_sq}^{a}\left(\cos\beta_{N_sq}L_{N_s}-\frac{W_e}{d}Z_L\frac{\beta_{N_sq}\sin\beta_{N_sq}L_{N_s}}{j\omega\mu_0}\right)+c_{N_sq}^{b}\right]\psi_{N_sq}\Big|_{\xi=0}=0 \qquad (4.83)$$

$$q=0,\ 1..\infty$$

From the linear independence property of ψ_{N_sq}, it can be inferred that,

$$c_{N_sq}^{a}\left(\cos\beta_{N_sq}L_{N_s}-\frac{W_e}{d}Z_L\frac{\beta_{N_sq}\sin\beta_{N_sq}L_{N_s}}{j\omega\mu_0}\right)+c_{N_sq}^{b}=0 \qquad (4.84)$$

$$q=0,\ 1..\infty$$

For the sake of numerical computation, we have reduced the infinite number of modes in all the modal summations to N_m finite number of modes. Consequently, 'q' varies from 0 to N_m-1 for all the equations above.

Now, we have $2N_sN_m$ number of unknowns and equations. c_{nq}^{a} and c_{nq}^{b} are the unknown quantities. To solve these $2N_sN_m$ number of simultaneous equations, we have represented the set of equations as

$$[Q][c]=[b_e] \qquad (4.85)$$

Here [c] indicates the column vector containing the unknown variables c_{nq}^{a} and c_{nq}^{b}, $[b_e]$ indicates the excitation vector on the first segment and [Q] indicates the co efficient matrix seeded using (4.74),(4.78), (4.81) and (4.84).

4.5.7 CALCULATION OF RADIATED FAR FIELDS

Total radiated far-fields from the curved microstrip line is calculated after evaluating and adding contributions from electric and magnetic surface current densities in the Serret-Frenet reference frame described in section 4.3. Basic steps for the procedure are described below:

The electric and the magnetic fields solved inside the piecewise circular segments are represented by

$$E_{zn}(\mathrm{s},\xi),\ H_{\xi n}(\mathrm{s},\xi) \tag{4.86}$$

These are in general functions of the parametric position along the curve and the transversal co-ordinate (ξ). The parametric position along the curve in turn depends on the spatial representation of the original curve itself i.e. the parameter '*t*' in the representation g(*t*) and h(*t*). Thus the first step undertaken is representation of the fields in terms of '*t*'. The '*s*' to '*t*' mapping in the present work is done using Matlab curve fitting tool (spline fitting).

Next, the two edges and the central curve of the microstrip line are represented as

$$\begin{aligned} &\textit{Top Curve}: g_1(\mathrm{t}), \mathrm{h}_1(\mathrm{t}) \\ &\textit{Bottom Curve}: g_2(\mathrm{t}), \mathrm{h}_2 \\ &\textit{Central Curve}: g_0(\mathrm{t}), \mathrm{h}_0(\mathrm{t}) \end{aligned} \tag{4.87}$$

Here $g_i(t)$ and $h_i(t)$ are represented in the same manner as was done in (4.30) and (4.31).

Next, the radiated vector potentials are calculated using the standard source integrals in the following form:

$$\vec{A} = \frac{\mu_0}{4\pi} \int_{\xi=-\frac{W_e}{2}}^{\frac{W_e}{2}} \int_{t=0}^{L_x} \left(\hat{z} \times \vec{H}_\xi\right) \frac{e^{-jk_0\left\{r - \vec{r}'.\hat{r}\right\}}}{r} \left|\frac{dr'}{dt}\right| dt \; d\xi \tag{4.88}$$

$$\vec{F}_{top} = \frac{\varepsilon_0}{4\pi} \int_{t=0}^{L_x} \int_{z=-d}^{d} \left(\vec{E}_z \times \hat{a}_n\right) \frac{e^{-jk_0\left\{r - \vec{r}'.\hat{r}\right\}}}{r} \left|\frac{dr'}{dt}\right| dtdz \tag{4.89}$$

$$\vec{F}_{bottom} = \frac{\varepsilon_0}{4\pi} \int_{t=0}^{L_x} \int_{z=-d}^{d} \left(\vec{E}_z \times -\hat{a}_n\right) \frac{e^{-jk_0\left\{r - \vec{r}'.\hat{r}\right\}}}{r} \left|\frac{dr'}{dt}\right| dtdz \tag{4.90}$$

Radiated far-fields are subsequently calculated from these vector potentials.

4.5.8 RESULTS AND OBSERVATIONS

First the sinusoidal microstrip line described by (4.28) is analyzed using the mode matching technique. There are two very important notions associated with the mode matching technique presented in this work. These are convergence with respect to the number of segments and convergence with respect to the number of modes. Number of segments taken while plotting Fig. 4.23b had been 50.

Fig. 4.23 shows the variation of relative change in the input reflection co-efficient of the line at 7 GHz as the number of segments and the number of modes increase respectively.

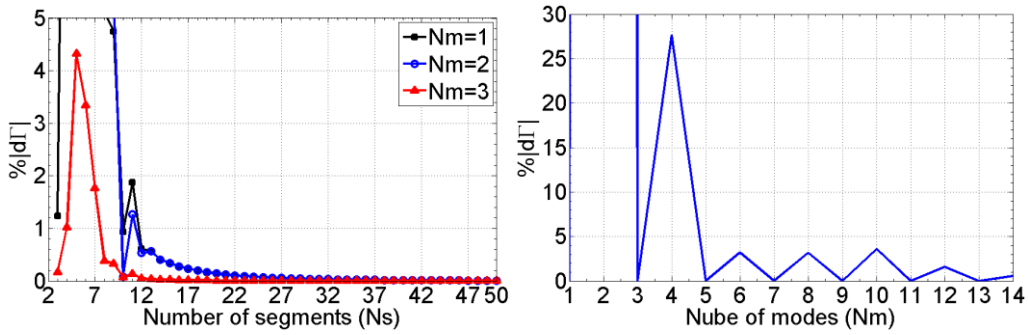

(a) (b)

Fig. 4.23: (a) Convergence with respect to the number of segments and (b) convergence with respect to the number of modes

Radiated far fields at 5 GHz and 7 GHz in the two principal planes are plotted in Fig. 4.24a, b and Fig. 4.24c, d respectively. Variation of the realized gain and antenna efficiency with frequency are shown in Fig. 4.25. Distribution of the internal electric field (E_z) along the line plotted in Fig. 4.26 clearly indicates the perturbation of the Quasi TEM mode of propagation in the regions closer to the curvature of the sinusoidal line.

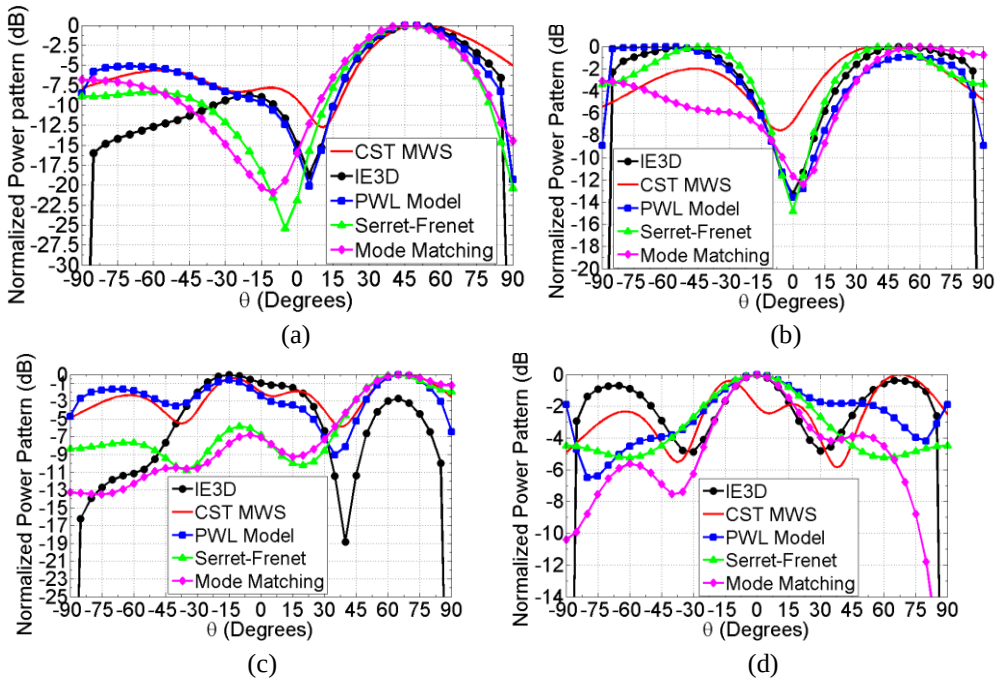

Fig. 4.24: Normalized power pattern in the (a) x-z plane, (b) y-z plane at 5 GHz and (c) x-z plane and (d) y-z plane at 7 GHz

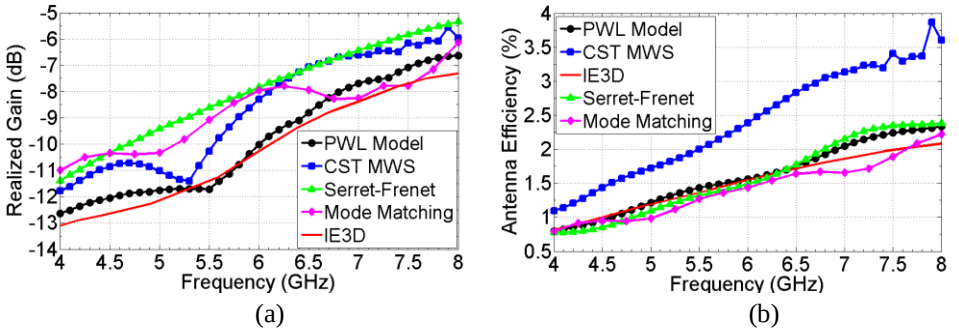

Fig. 4.25: Variation of (a) realized gain and (b) antenna efficiency with frequency.

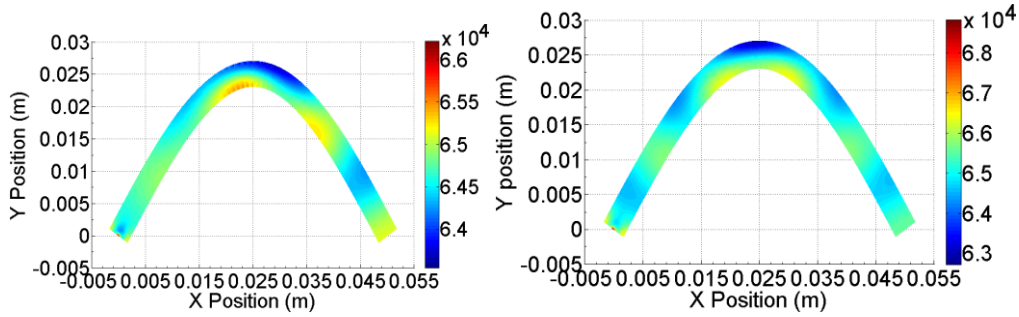

(a) (b)

Fig. 4.26: Calculated magnitude of the internal electric field (|Ez|) inside the curved microstrip line at (a) 5 GHz and (b) 7 GHz

4.6 FABRICATION AND MEASUEMENTS

Last few sections of this chapter discuss in detail different models appropriate for analyzing arbitrarily curve microstrip lines. A comparison of the results obtained using these models with practical measurements of a fabricated prototype are presented in this section. The fabricated prototype of the sinusoidal line shown in Fig. 4.27 is based on the following central curve:

$$y = 25\sin\left(\frac{2n\pi}{50}x\right) \tag{4.92}$$

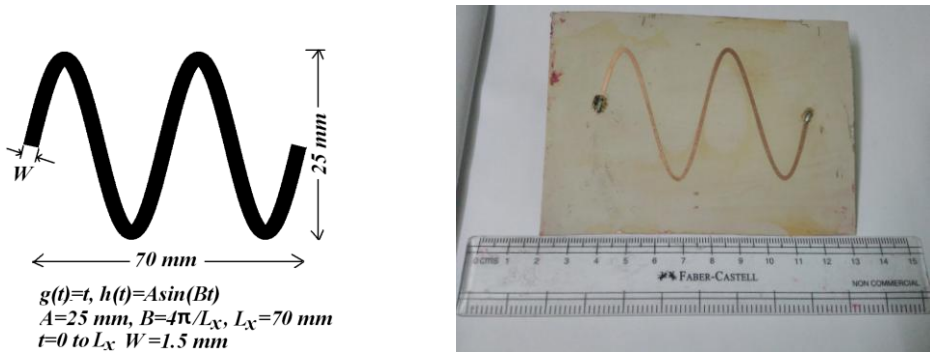

(a) (b)

Fig. 4.27: (a) Final design of the sinusoidal line with dimensions and (b) Fabricated prototype.

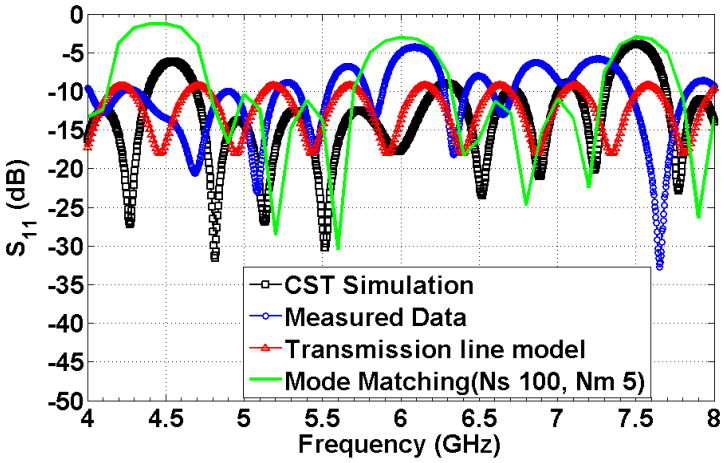

(a)

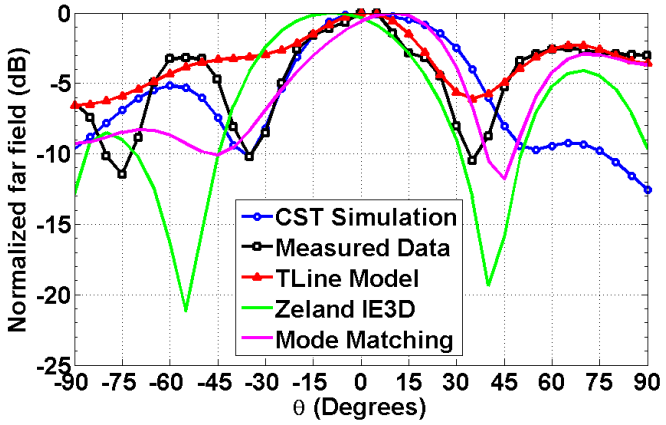

(b)

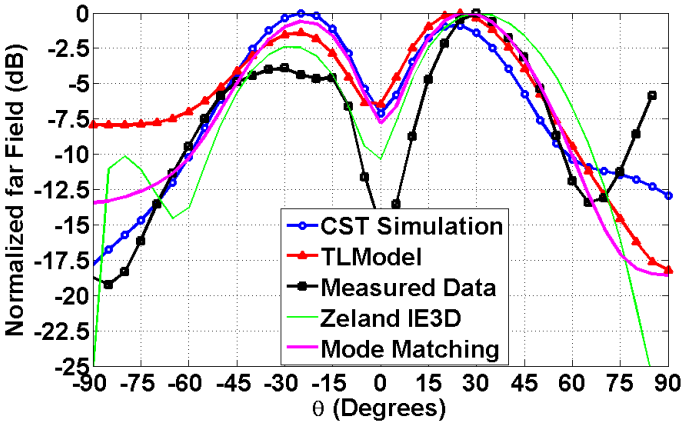

(c)

Fig. 4.28: Simulated, calculated and measured (a) S_{11} vs. frequency, (b) Radiation pattern in the x-z plane and (c) radiation pattern in the y-z plane.

Simulated, calculated and measured S_{11} for the sinusoidal line is shown in Fig. 4.28a. Radiated far fields in the x-z plane and y-z plane are shown in Fig. 4.28b and Fig. 4.28c respectively. Comparison of the results indicates that the models presented in this chapter are effective in predicting the characteristics of curved microstrip lines.

4.7 CONCLUSION

This chapter deals with the analysis of curved microstrip antennas. Internal fields and radiation characteristics are evaluated. Three different models are presented for lines with various amounts of curvatures. For microstrip lines with small to moderate degree of curvature, the piecewise linear model proves to be simple and effective in predicting the radiation characteristics. However increasing curvature necessitates subsequent increase in the number of segments required in the piecewise linear analysis which in turn would lead to increase in simulation time. To alleviate this problem a transmission line based model is presented in the Serret-Frenet reference frame. This model is capable of incorporating the changes in the phase constant of the line due to curvature and the radiation characteristics are calculated with contributions from both electric and magnetic currents. Both these models however depend on the basic transmission line analogy. This restricts the applicability of these models only to lines with smaller amount of width. With increasing line width the transverse field variations can no longer be negligible. A sequential mode matching based technique is presented to solve this predicament. This second order mode matching based technique is capable of describing the two dimensional internal field variations inside the line with reasonable accuracy.

However, it must be pointed out that the mode matching technique, although quite generalized, is limited in application as envisaged here by the fact that the number of transverse modal terms is restricted to two and for line with greater width variations or greater curvature would require subsequent increment in the number of terms in the transverse field expansion.

REFERENCES:

[1] C. Wood, "Curved microstrip lines as compact wideband circularly polarised antennas," in *IEE Journal on Microwaves, Optics and Acoustics*, vol. 3, no. 1, pp. 5-13, January 1979.

[2] X. Gao and Z. Shen, "UHF/UWB Tag Antenna of Circular Polarization," in *IEEE Transactions on Antennas and Propagation*, vol. 64, no. 9, pp. 3794-3802, Sept. 2016.

[3] C. G. Kakoyiannis and P. Constantinou, "Radiation properties and ground-dependent response of compact printed sinusoidal antennas and arrays," in *IET Microwaves, Antennas & Propagation*, vol. 4, no. 5, pp. 629-642, May 2010.

[4] D. Jaisson, "Quasi-static model for circular transmission lines," *Proceedings of 1995 SBMO/IEEE MTT-S International Microwave and Optoelectronics Conference*, Rio de Janeiro, Brazil, 1995, pp. 825-828 vol.2.

[5] S. K. Khamas and G. G. Cook, "Moment-method analysis of printed wire spirals using curved piecewise sinusoidal subdomain basis and testing functions," in *IEEE Transactions on Antennas and Propagation*, vol. 45, no. 6, pp. 1016-1022, June 1997.

[6] Rong-Lin Li and H. Nakano, "Numerical analysis of arbitrarily shaped probe-excited single-arm printed wire antennas," in *IEEE Transactions on Antennas and Propagation*, vol. 46, no. 9, pp. 1307-1317, Sept. 1998.

[7] D. A. Hill, D. G. Camell, K. H. Cavcey, and G. H. Koepke, “Radiated emissions and immunity of microstrip transmission lines: Theory and reverberation chamber measurements,” IEEE Trans. Electromagn. Compat., vol. 38, no. 2, pp. 165–172, May 1996.

[8] M. Leone, "Closed-Form Expressions for the Electromagnetic Radiation of Microstrip Signal Traces," IEEE Transactions on Electromagnetic Compatibility, vol. 49, no. 2, pp. 322-328, May 2007.

[9] L. Lewin, Electromagnetic Waves and Curved Structures, New York:IEEE Press, 1977, pp. 36.

[10] G. Kompa and R. Mehran, "Planar waveguide model for calculating microstrip components," in *Electronics Letters*, vol. 11, no. 19, pp. 459-460, 18 September 1975.

[1] A. Weisshaar and V. K. Tripathi, "Perturbation analysis and modeling of curved microstrip bends," in *IEEE Transactions on Microwave Theory and Techniques*, vol. 38, no. 10, pp. 1449-1454, Oct. 1990.

[11] R. F. Harrington, "The method of moments in electromagnetics," *Journal of Electromagnetic waves and Applications*, *1*(3), pp.181-200, 1987.

Chapter 5

Non-Uniform Microstrip Lines

Contents

5.1 INTRODUCTION

Non uniform microstrip lines have been an inseparable design component in MMIC circuits for a long time. These lines have been extensively used in designing band pass [1] or band stop filters [2] for higher order spurious mode suppression, coupled wideband power dividers [3] and in analog signal processing units [4]. Leaky wave antennas with beam focusing in the near field [5] have also been achieved using periodic versions of these non uniform microstrip lines. In this context, it becomes very important to analyze these arbitrarily non uniform microstrip lines for their internal field distribution, terminal properties (S parameters) as well as estimate the fields radiated from them.

This chapter presents two different approximate techniques for analyzing arbitrarily non uniform microstrip lines. First a Fourier series based technique is developed for solving the one dimensional (1D) second order differential equation with variable co-efficients corresponding to a non uniform line. This model is valid for lines supporting the fundamental quasi TEM mode alone and fails to depict the internal fields accurately as the line width increases which tends to introduce higher order microstrip line modes. To alleviate this problem, a mode

matching based technique is developed for lines with greater amount of non uniformity. This model is capable of handling higher order modes in the non uniform microstrip line.

The chapter is organized in four sections. First, the canonical problem of non uniform microstrip line along with the co-ordinate system chosen is described. Next, the Fourier series technique and mode matching techniques are introduced. Finally, conclusions are drawn after presenting relevant observations.

5.2 PROBLEM FORMULATION

The side view and top view of the non-uniform microstrip line considered for analysis is shown in Fig. 5.1a and Fig. 5.1b respectively. The top edge of the line follows an arbitrary curve *y=f(x)* which for the sake of analysis is taken as follows

$$y = f(x) = W_0 + W_p \left\{1 + \sin\left(\frac{2m\pi x}{L}\right)\right\} \qquad (5.1)$$

where W_0, W_p, L are the base width, peak non uniformity and the length of the whole line respectively. These parameters are indicated in Fig. 5.1. The line width as seen in Fig. 5.1a is given by *W=f(x)*. Co-ordinate system and generic symbols adopted are shown in Fig. 5.1. Substrate chosen is primarily Arlon AD430 with dielectric constant (ε_r) of 4.3 and thickness (h) of 0.762 mm (loss tangent 0.003).

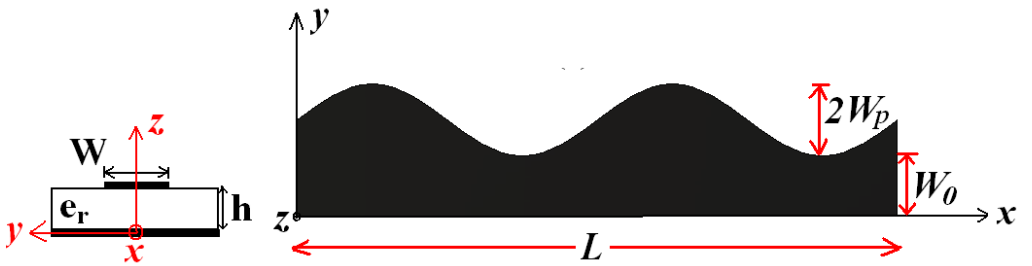

(a) (b)

Fig. 5.1: (a) Side view and (b) top view of the non uniform microstrip line geometry.

5.3 FOURIER SERIES BASED TECHNIQUE FOR MILD NON-UNIFORMITIES

5.3.1 BASIC TECHNIQUE

To develop the second order voltage differential equation for the non uniform line shown in Fig. 5.1b, we start with the coupled voltage-current equations below [6],

$$\frac{dv}{dx} = -Zi \tag{5.2}$$

$$\frac{di}{dx} = -Yv \tag{5.3}$$

where 'v' and 'i' are respectively the spatial voltage and current on the line and 'Z' and 'Y' are the per unit length impedance and admittances of the line.

These per unit length parameters are constant quantities for uniform microstrip lines but in the present case, for a non uniform microstrip line these become spatial functions with dependence on the varying line width. 'Z' and 'Y' are related to the characteristic impedances (Z_0) and propagation constant (γ) of the line through the following relationship

$$Z = Z_0\gamma \tag{5.4}$$

$$Y = \frac{Z_0}{\gamma} \tag{5.5}$$

Z_0 and γ are pre-calculated [7] using the position dependent line width of the non uniform line. Consequently, Z_0, γ and in turn Z and Y are now functions of 'x' in our case.

Writing (5.2) in the form $\frac{1}{Z}\frac{dv}{dx} = -i$ and differentiating both sides with respect to 'x' we obtain after using (5.3) to substitute $\frac{di}{dx}$, the following differential equation for spatial voltage ('v') along the non uniform microstrip line

$$\frac{d^2v}{dx^2} + P(x)\frac{dv}{dx} + Q(x)v = 0 \tag{5.6}$$

where $P(x) = -\frac{1}{Z}\frac{dZ}{dx}$, $Q(x) = -ZY$ with $Z = Z_0\gamma$, $Y = \frac{Z_0}{\gamma}$

Now, *P(x)* and *Q(x)* are expanded in a Fourier series as

$$P(\mathrm{x}) = \sum_{m=-\infty}^{\infty} p_m e^{-jm\frac{2\pi}{L}x} \tag{5.7}$$

$$Q(\mathrm{x}) = \sum_{n=-\infty}^{\infty} q_n e^{-jn\frac{2\pi}{L}x} \tag{5.8}$$

where $p_m = \frac{1}{L}\int_0^L P(\mathrm{x})\,\mathrm{e}^{jm\frac{2\pi}{L}x}dx$ and $q_n = \frac{1}{L}\int_0^L Q(\mathrm{x})\,\mathrm{e}^{jn\frac{2\pi}{L}x}dx$

Next, the unknown voltage (*v*) is expressed in Fourier series in the following form

$$v = \sum_{t=-\infty}^{\infty}\left\{v_t^+ e^{-\gamma_0 x} + v_t^- e^{\gamma_0 x}\right\}e^{-jt\frac{2\pi}{L}x} = \sum_{t=-\infty}^{\infty}\left\{v_t^+ e^{a_t x} + v_t^- e^{b_t x}\right\} \tag{5.9}$$

Here $a_t = -\gamma_0 - j\frac{2\pi}{L}\mathrm{t}$, $b_t = \gamma_0 - j\frac{2\pi}{L}t$ and γ_0 is the unknown propagation constant along the non uniform microstrip line. It is to be noted that γ_0 is not a spatial function; rather it is a constant throughout the line.

The corresponding first and second derivatives of '*v*' with respect to *x* are defined as

$$\frac{dv}{dx} = \sum_{t=-\infty}^{\infty}\left\{a_t v_t^+ e^{a_t x} + b_t v_t^- e^{b_t x}\right\} \tag{5.10}$$

$$\frac{d^2v}{dx^2} = \sum_{t=-\infty}^{\infty}\left\{a_t^2 v_t^+ e^{a_t x} + b_t^2 v_t^- e^{b_t x}\right\} \tag{5.11}$$

Putting (5.9), (5.10) and (5.11) in (5.6) we obtain,

$$\begin{aligned}&\sum_{t=-\infty}^{\infty}\left\{a_t^2 v_t^+ e^{a_t x} + b_t^2 v_t^- e^{b_t x}\right\} + \sum_{m=-\infty}^{\infty}\sum_{t=-\infty}^{\infty} p_m e^{-jm\frac{2\pi}{L}x}\left\{a_t v_t^+ e^{a_t x} + b_t v_t^- e^{b_t x}\right\} + \\ &\sum_{n=-\infty}^{\infty}\sum_{t=-\infty}^{\infty} q_n e^{-jn\frac{2\pi}{L}x}\left\{v_t^+ e^{a_t x} + v_t^- e^{b_t x}\right\} = 0\end{aligned} \tag{5.12}$$

which upon simplification leads to,

$$\sum_{t=-\infty}^{\infty}\left\{a_t^2 v_t^+ e^{a_t x}+b_t^2 v_t^- e^{b_t x}\right\}+\sum_{n=-\infty}^{\infty}\sum_{t=-\infty}^{\infty} q_n\left\{v_t^+ e^{a_{t+n} x}+v_t^- e^{b_{t+n} x}\right\} + \sum_{m=-\infty}^{\infty}\sum_{t=-\infty}^{\infty} p_m\left\{a_t v_t^+ e^{a_{t+m} x}+b_t v_t^- e^{b_{t+m} x}\right\}=0 \tag{5.13}$$

Now, equating the co-efficient of $e^{a_k x}$ on both sides we obtain after limiting the infinite sums within (-N, N),

$$a_k^2 v_k^+ + \sum_{l=l_1}^{l_2} v_l^+\left(p_{k-l} a_l + q_{k-l}\right)=0 \text{ for } k=-N...N \tag{5.14}$$

which can be expressed as $[A_1][\ v^+]=0$.

Similarly, equating the co-efficient of $e^{b_k x}$ on both sides we obtain,

$$b_k^2 v_k^- + \sum_{l=l_1}^{l_2} v_l^-\left(p_{k-l} b_l + q_{k-l}\right)=0 \text{ for } k=-N...N \tag{5.15}$$

Here $l_1=-N+k\left\{k/|k|+1\right\}/2,\ l_2=N-k\left\{k/|k|-1\right\}/2$

(5.15) can be expressed as $[A_2][\ v^-]=0$.

Next, these two sets of (2N+1) equations formed by (5.14) and (5.15) are combined and arranged as

$$[A]_{(4N+2)\times(4N+2)}[v]_{(4N+2)\times 1}=0 \tag{5.16}$$

where $[A]=\begin{bmatrix}[A_1] & [0]\\ [0] & [A_2]\end{bmatrix}$ and $[v]=\begin{bmatrix}[v^+]\\ [v^-]\end{bmatrix}$.

A non trivial solution of (5.16) (i.e. v≠0) would be available only if [A] is singular. Now, the only unknown quantity in [A] is the propagation constant of the line (γ_0 (=$j\beta$)). So, we solve for the singularity of [A] by maximizing the conditioning factor of A (a matrix with conditioning factor greater than 10^{15} is considered as singular) or by solving for |[A(β))]|=0 [8]. We have used a simple Bisection technique for solving abovementioned transcendental equation. This involves varying the unknown quantity (β) in a range and looking to maximize the absolute value of the conditioning factor of A (|cond(A(β))|). Alternatively, we

could look for the zero crossings of the determinant of [A] as well. The range of variation for β is chosen as $\omega\sqrt{\varepsilon_{mean}}/c-100$ to $\omega\sqrt{\varepsilon_{mean}}/c+100$ where ε_{mean} is the mean effective dielectric constant of the substrate and $c=3\times10^8$ m/s. The singularity condition is also cross verified with the rank of the matrix which, at the point of singularity, has a value lesser than the dimension of the matrix [A] thereby rendering the matrix [A] to be singular.

Once γ_0 is calculated from the singularity condition mentioned above, we find the null space of the matrix [A] using singular value decomposition (SVD) in Matlab. It is observed that the rank of [A] is 4N while its dimension is (4N+2) × (4N+2). This leads to a null space with nullity of 2. This null space of the matrix 'A' ($N([\mathrm{A}])$) is now represented as the span of all the null space vectors

$$N([\mathrm{A}]) = span\left\{[v_a]_{(4\mathrm{N}+2)\times1}, [v_b]_{(4\mathrm{N}+2)\times1}\right\} \tag{5.17}$$

Next, solution of the original boundary value problem (BVP) i.e. solution to (5.6) is represented as a linear combination of the null space vectors

$$[v]_{(4\mathrm{N}+2)\times1} = \alpha_a[\mathrm{v}_a]_{(4\mathrm{N}+2)\times1} + \alpha_b[\mathrm{v}_b]_{(4\mathrm{N}+2)\times1} \tag{5.18}$$

Here α_a and α_b are unknown linear combination factors to be evaluated from the source and load boundary conditions discussed next.

5.3.2 SOURCE AND LOAD BOUNDARY CONDITIONS

To solve for the unknown weight factors α_a and α_b in (5.18), two additional boundary conditions are needed. These boundary conditions are formulated from the *v-i* relationship of the transmission line as indicated in (5.2)

$$-\frac{dv}{dx} = Zi \tag{5.19}$$

Now, putting *'dv/dx'* from (5.10) we obtain '*i*' as

$$i = -\frac{1}{Z}\sum_{t=-\infty}^{\infty}\left\{a_t v_t^{+} e^{a_t x} + b_t v_t^{-} e^{b_t x}\right\} \tag{5.20}$$

The excitation condition adopted in this work is that of a voltage source (v_s) with series internal impedance of 'Z_s'. This condition is expressed as

$$v_s - Z_s i_0 = v_0 \tag{5.21}$$

where 'v_0' and 'i_0' represent the voltage and current on the line at x=0.

Now, putting (5.9) and (5.20) in (5.21), we obtain after some simplification,

$$\sum_t v_t^+ \left(1 - \frac{Z_s}{Z(\mathrm{x}=0)} a_t\right) + v_t^- \left(1 - \frac{Z_s}{Z(\mathrm{x}=0)} b_t\right) = v_s \tag{5.22}$$

Here Z(0) is Z at x=0.

On the other hand, we use the load boundary condition as

$$\frac{v(\mathrm{x}=\mathrm{L})}{i(\mathrm{x}=\mathrm{L})} = \frac{\sum_{t=-\infty}^{\infty} \left\{v_t^+ e^{a_t L} + v_t^- e^{b_t L}\right\}}{-\frac{1}{Z(\mathrm{x}=\mathrm{L})} \sum_{t=-\infty}^{\infty} \left\{a_t v_t^+ e^{a_t L} + b_t v_t^- e^{b_t L}\right\}} = Z_L \tag{5.23}$$

Here Z_L is the load impedance. Putting (5.9) and (5.20) in (5.23), with further simplification we get,

$$\sum_t v_t^+ e^{a_t L} \left(1 + \frac{Z_L}{Z(\mathrm{L})} a_t\right) + v_t^- e^{b_t L} \left(1 + \frac{Z_L}{Z(\mathrm{L})} b_t\right) = 0 \tag{5.24}$$

(5.22) and (5.24) are now expressed respectively as

$$[Q]_{1\times(4N+2)} [v]_{(4N+2)\times 1} = v_s \tag{5.25}$$

$$[R]_{1\times(4N+2)} [v]_{(4N+2)\times 1} = 0 \tag{5.26}$$

Substituting [v] in (5.25) and (5.26) from (5.18) and simplifying we obtain

$$\begin{bmatrix} [Q][V_a] & [Q][V_b] \\ [R][V_a] & [R][V_b] \end{bmatrix} \begin{bmatrix} \alpha_a \\ \alpha_a \end{bmatrix} = \begin{bmatrix} v_s \\ 0 \end{bmatrix} \tag{5.27}$$

Once α_a and α_a are solved from (5.27), solution to the original BVP is calculated using (5.18).

5.3.3 INPUT IMPEDANCE CALCULATION

The input impedance for the non uniform microstrip line is calculated from terminal voltage and currents as below

$$Z_{in} = \frac{v(\mathrm{x}=0)}{i(\mathrm{x}=0)} = \frac{\sum_{t=-N}^{N} \left\{ v_t^+ + v_t^- \right\}}{-\frac{1}{Z(0)} \sum_{t=-N}^{N} \left\{ a_t v_t^+ + b_t v_t^- \right\}} \tag{5.28}$$

Here $Z(0)$ is 'Z' evaluated at x=0 i.e. at the input terminal. Input reflection co-efficient (S_{11}) is calculated from this input impedance.

5.3.4 CALCULATION OF RADIATED FAR FIELDS

Radiated far-field from the non uniform microstrip line is calculated using the voltage and currents along the line calculated in the last sections. The quasi TEM mode assumption underneath the line dictates that the only non-zero electric field quantity is E_z and the corresponding magnetic field is H_y. Consequently, radiation is considered from magnetic currents on the two sidewall apertures and the electric surface current on the strip surface. These apertures along with the current densities are shown in Fig. 5.2.

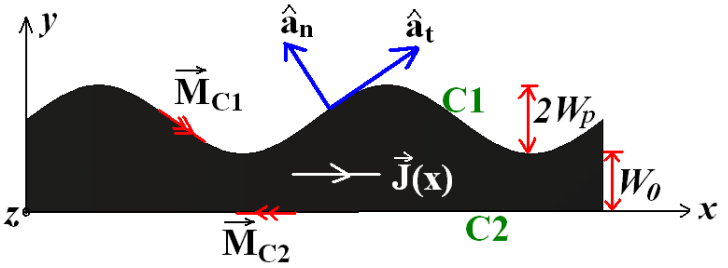

Fig. 5.2: Magnetic and electric current densities on the radiating sidewall apertures and the strip surface for radiated far field calculation

To quantify the current densities and calculate the radiated vector potentials, a planar form of Serret-Frenet reference [9] frame ($\hat{a}_t, \hat{a}_n, \hat{z}$) is now defined for a generalized planar curve. The planar curve is represented in parametric form as ($g(t)$, $h(t)$, z) and any position on the curve is represented as

$$\vec{R} = g(\mathrm{t})\,\hat{\mathrm{x}} + \mathrm{h}(\mathrm{t})\,\hat{\mathrm{y}} \tag{5.29}$$

Corresponding tangent ($\hat{a}_t$) and normal ($\hat{a}_n$) vectors are defined as

$$\hat{a}_t = \frac{g'(\mathrm{t})\hat{x} + h'(\mathrm{t})\,\hat{\mathrm{y}}}{\sqrt{\left\{g'(\mathrm{t})\right\}^2 + \left\{h'(\mathrm{t})\right\}^2}} \tag{5.30}$$

$$\hat{a}_n = \frac{-h'(\mathrm{t})\hat{x} + g'(\mathrm{t})\,\hat{\mathrm{y}}}{\sqrt{\left\{g'(\mathrm{t})\right\}^2 + \left\{h'(\mathrm{t})\right\}^2}} \tag{531}$$

In the present case, i.e. for the general space curve y=f(x) the parametric representations become g(t)=x, y(t)=f(x) and the orthogonal unit vectors of (5.30) and (5.31) are calculated accordingly. $g'(\mathrm{t})$ and $h'(\mathrm{t})$ are the derivatives of *g* and *h* with respect to '*t*'

Magnetic currents on the sidewalls are now calculated using the internal electric field in this newly defined co-ordinate system as

$$\begin{aligned}\vec{M}_{C1}(\mathrm{x}, \mathrm{y} = \mathrm{f}(\mathrm{x})) &= E_z(\mathrm{x}, \mathrm{f}(\mathrm{x}))\,\hat{\mathrm{z}} \times \hat{a}_n \\ &= -E_z(\mathrm{x}, \mathrm{f}(\mathrm{x}))\hat{a}_t \\ &= \frac{v(\mathrm{x}, \mathrm{f}(\mathrm{x}))}{h}\,\hat{a}_t\end{aligned} \tag{5.32}$$

$$\begin{aligned}\vec{M}_{C2}(\mathrm{x}, \mathrm{y} = 0) &= E_z(\mathrm{x}, \mathrm{y} = 0)\hat{z} \times (-\hat{\mathrm{y}}) \\ &= E_z(\mathrm{x}, \mathrm{y} = 0)\hat{x} \\ &= -\frac{v(\mathrm{x}, \mathrm{y} = 0)}{h}\,\hat{x}\end{aligned} \tag{5.33}$$

Here 'C1' and 'C2' in the subscript indicate the two sidewall edges of the microstrip line as shown in Fig. 5.2. After substituting '*v*' in (5.32) and (5.33) from (5.9) we obtain

$$\vec{M}_{C1} = \frac{1}{h}\sum_{t=-\infty}^{\infty}\left\{v_t^+ e^{-\gamma_0 x} + v_t^- e^{\gamma_0 x}\right\} e^{-jt\frac{2\pi}{L}x}\,\frac{\hat{x} + \dfrac{df}{dx}\,\hat{\mathrm{y}}}{\sqrt{1 + \left(\dfrac{df}{dx}\right)^2}} \tag{5.34}$$

$$\vec{M}_{C2} = -\frac{1}{h}\sum_{t=-\infty}^{\infty}\left\{v_t^{+}e^{-\gamma_0 x} + v_t^{-}e^{\gamma_0 x}\right\}e^{-jt\frac{2\pi}{L}x}\hat{x} \tag{5.35}$$

Electric current density on the strip surface is expressed as

$$\vec{J}(x) = \frac{I(x)}{W_e(x)}\hat{x} \tag{5.36}$$

Here W_e is the effective width of the line given by $W_e = W + 2h$.

Using the magnetic current densities in (5.34) and (5.35), electric vector potentials from the edge marked 'C1' (F_{C1}) and edge marked 'C2' (F_{C2}) in Fig. 5.2 are calculated as

$$\vec{F}_{C1} = \frac{\varepsilon_0}{4\pi}\frac{e^{-jk_0 r}}{r}\int_{x'=0}^{L}\int_{z'=-h}^{h}\vec{M}_{C1}e^{jk_0\{x'\sin\theta\cos\varphi + f(x')\sin\theta\sin\varphi + z'\cos\theta\}}\sqrt{1+\left(\frac{df}{dx'}\right)^2}\,dz'dx' \tag{5.37}$$

$$\vec{F}_{C2} = \frac{\varepsilon_0}{4\pi}\frac{e^{-jk_0 r}}{r}\int_{x'=0}^{L}\int_{z'=-h}^{h}\vec{M}_{C2}e^{jk_0\{x'\sin\theta\cos\varphi + f(x')\sin\theta\sin\varphi + z'\cos\theta\}}dz'dx' \tag{5.38}$$

On the other hand, magnetic vector potential due to the electric current density on the strip surface is expressed as

$$\vec{A} = \frac{\mu_0}{4\pi}\frac{e^{-jk_0 r}}{r}\left\{2j\sin\left(k_0 h\cos\theta\right)\right\}\int_{x'=0}^{L}\int_{y'=0}^{W(x')}\vec{J}(x')e^{jk_0\{x'\sin\theta\cos\varphi + y'\sin\theta\sin\varphi\}}dy'dx' \tag{5.39}$$

In both (5.38) and (5.39), the primed quantities indicate the source co-ordinates.

5.3.5 ITERATIVE CORRECTION OF RESULTS

The radiated far fields i.e. E_θ and E_φ are calculated from these three vector potentials. After calculating the total radiated power (P_{rad}) from the structure using the standard 2D integral over the upper hemisphere using (5.37)-(5.39), we aim to calculate an equivalent attenuation constant (α_r) to introduce radiation losses in the analysis.

In this regard it is observed that the power lost in the line due to a non-zero α_r is given by [10]

$$P_{loss} = 0.5\,\mathrm{Re}\left[v(0)i^*(0) - v(L)i^*(L)\right] \tag{5.40}$$

where v and i are as calculated from (5.6) and (5.17) respectively. α_r is now calculated by minimizing $|P_{rad}\text{-}P_{loss}|$.

5.3.6 RESULTS AND DISCUSSION

Validation of the analysis technique presented in the last sections is performed on a non uniform microstrip line fabricated with the following equation for $f(x)$ and a length of 50 mm

$$y = f(\mathrm{x}) = 1.5 + W_p\left\{1 + \sin\left(0.08\pi x\right)\right\} mm \tag{5.41}$$

Arlon AD430 with 30 mils of thickness and a relative permittivity of 4.3 is used as substrate. The geometry is terminated with 50 Ω impedance. Initially, the characteristic impedance and phase constant of the line as calculated using the standard dispersion relations are plotted in Fig. 5.3a and Fig. 5.3b respectively. Spatial variation of 'Z' using (5.4) is shown in Fig. 5.4a.

The parameters P_x and Q_x as defined in (5.6) are expanded in Fourier series representation. Variation of P_x and Q_x with position along the line at 7 GHz are plotted in Fig. 5.4a and Fig. 5.4b respectively. The line being considered lossless, both P_x and Q_x become purely real quantities.

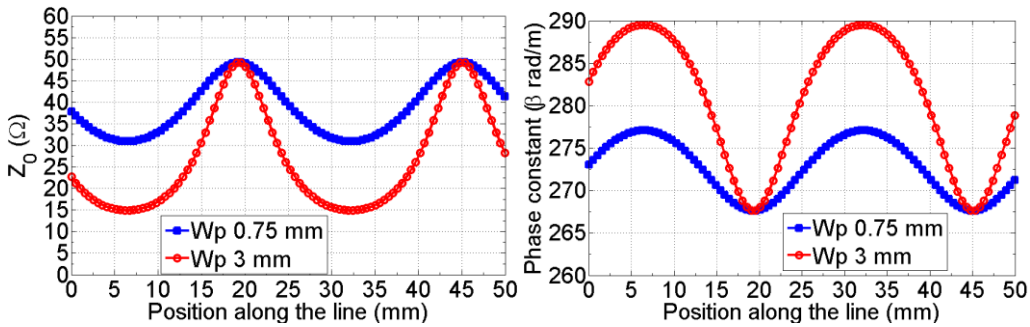

(a) (b)

Fig. 5.3: Spatial variation of the line parameters along the line at 7 GHz, (a) characteristic impedance vs. position along the line and (b) phase constant along the line vs. position along the line.

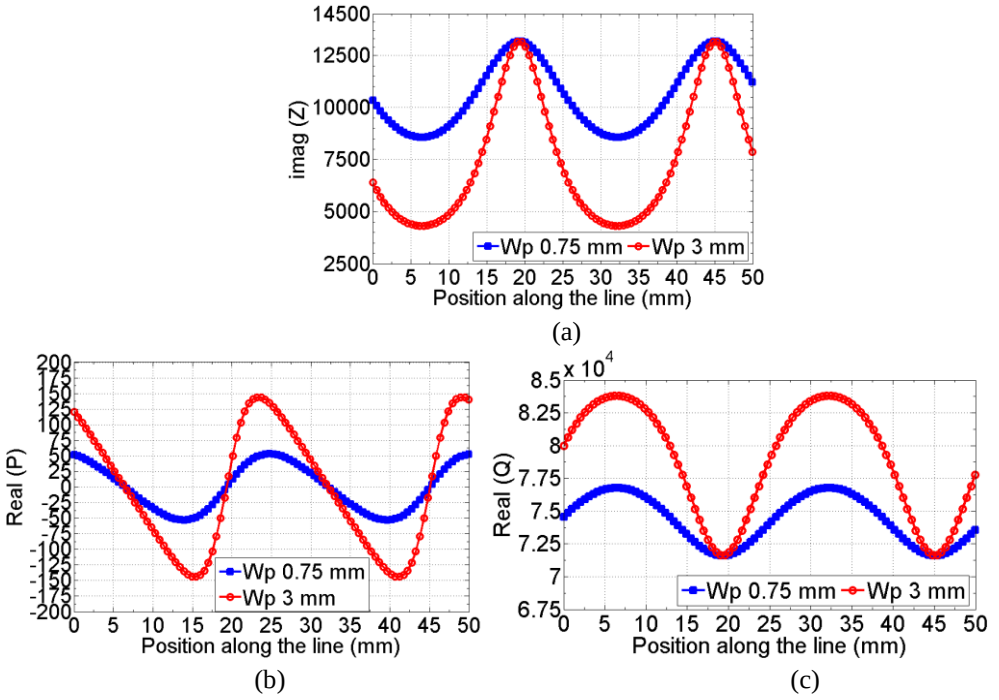

Fig. 5.4: Derived line parameters at 7 GHz with (a) imaginary part of Z vs. frequency, (b) real part of P and (c) real part of Q.

After the Fourier expansions of (5.7) and (5.8) real and imaginary parts of the coefficients of the Fourier series terms (p_m, q_m) are evaluated and the same are plotted at 7 GHz in Fig. 5.5a and Fig. 5.5b for p_m and Fig. 5.5c, Fig. 5.5d for q_m respectively.

Once the line parameters and their Fourier representations are calculated, the homogenous set of (5.16) is formulated. To test for the singularity of [A], its conditioning factor is evaluated and the same is plotted in Fig. 5.6a with respect to β for the two lines (W_p 0.75 and W_p 1.5) at 5.5 GHz and 7 GHz. Corresponding plots for the determinant of the co-efficient matrix (|A|) are also plotted in Fig. 5.6b for reference. The determinant of the matrix has been normalized with respect to its maximum value as the order of the determinant was turning out to be as high as 10^{111}.

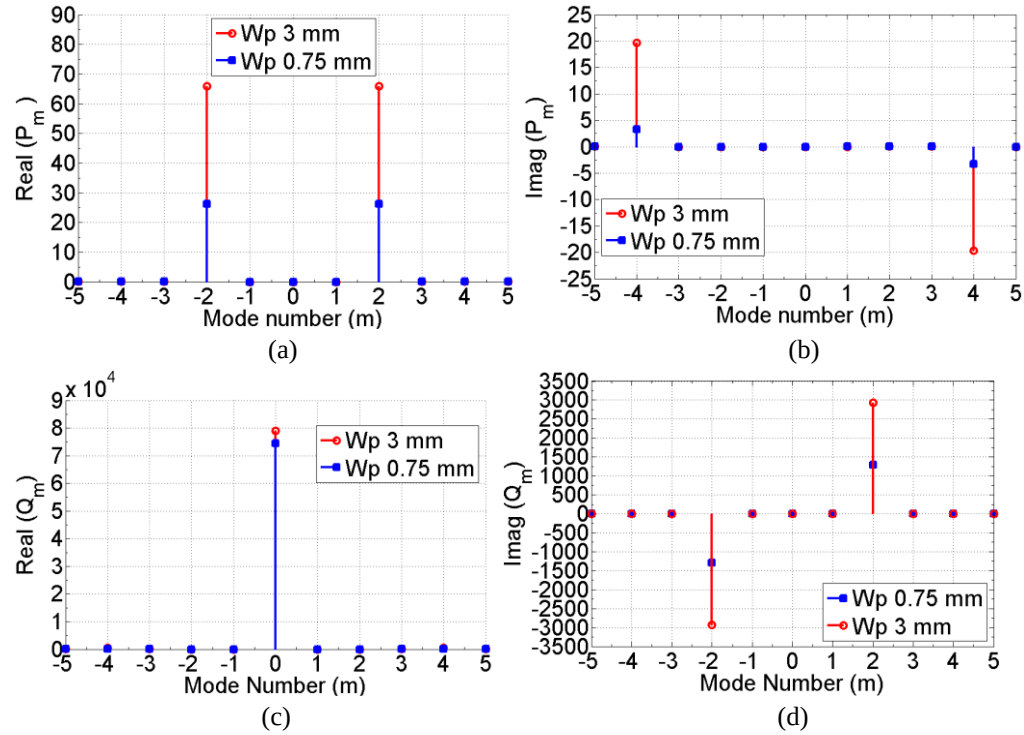

Fig. 5.5: (a) Real and (b) imaginary part of Fourier co-efficient for P (p_m) and (c) real and (d) imaginary parts of the Fourier co-efficient for Q (q_m).

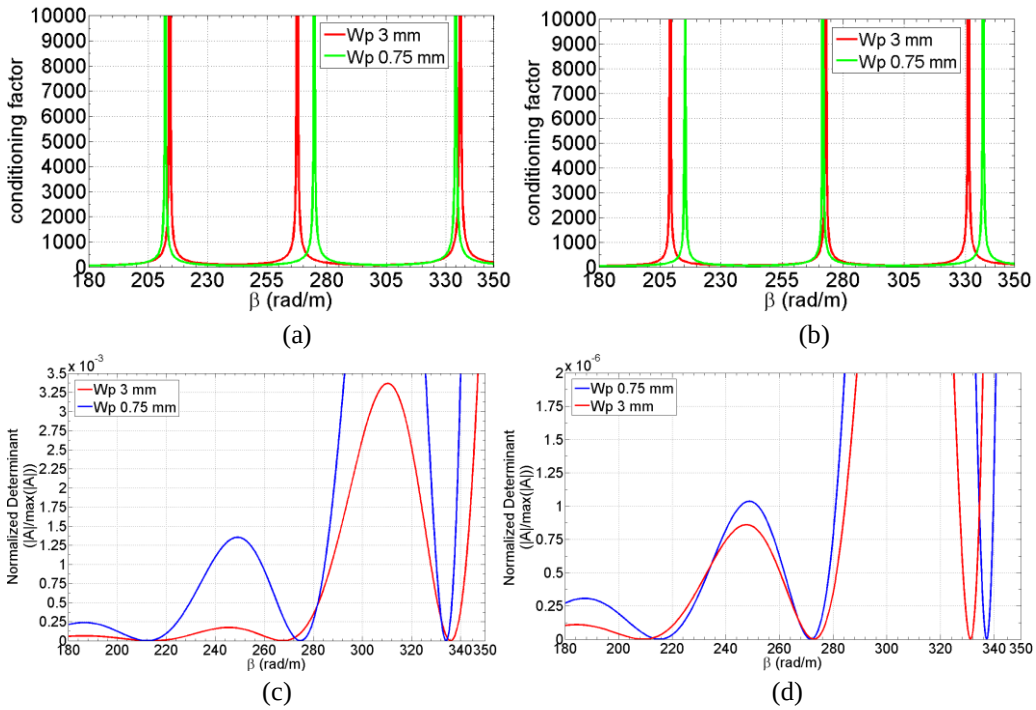

Fig. 5.6: Conditioning factor vs. phase constant at (a) 5.5 GHz, (b) 7 GHz and determinant of [A] vs. phase constant at (c) 5.5 GHz and (d) 7 GHz.

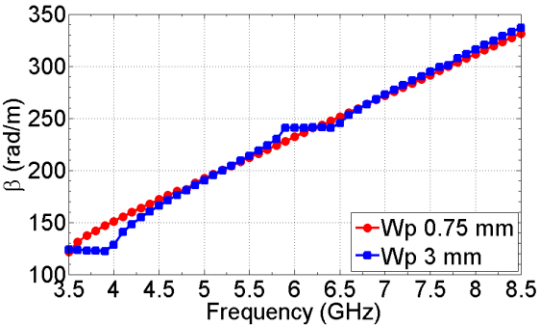

Fig. 5.7: Evaluated phase constant of the non uniform line with frequency

It can be observed that there are multiple possible roots available for the characteristic equation under consideration (cond(A) maximum or |A|=0). This is to be expected since the solution form anticipated is of the Fourier series nature which in turn is periodic itself. However, for the sake of analysis we have tracked the fundamental Floquet mode which conforms to the quasi-static solution available for uniform lines at lower frequencies and has a non-negative slope (positive group velocity) all along. A plot of the phase constant calculated in this manner with frequency is shown in Fig. 5.7.

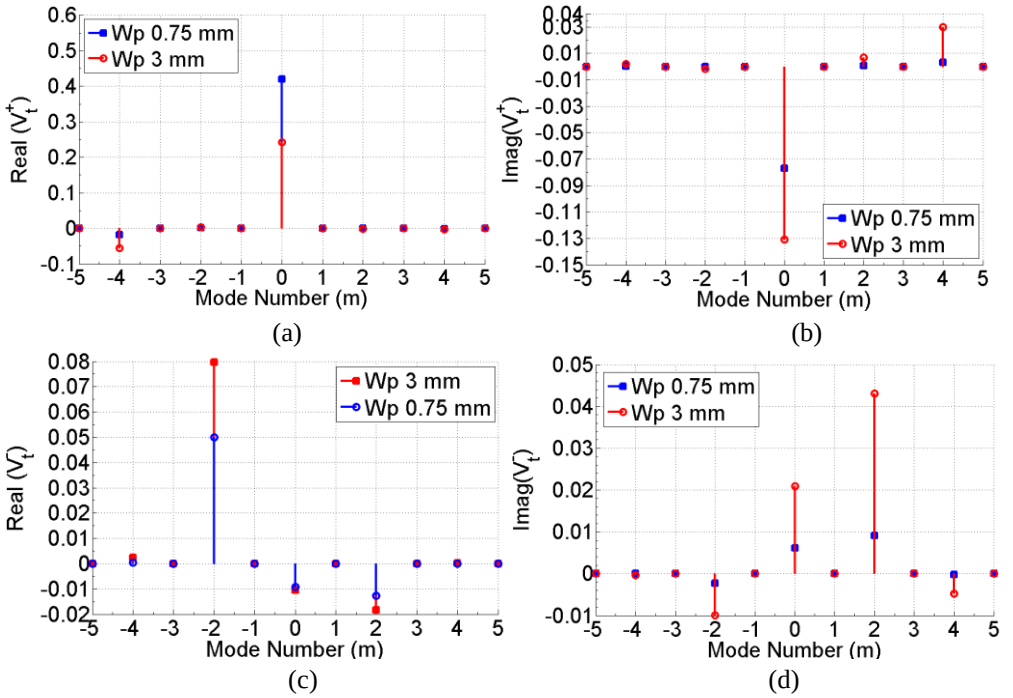

Fig. 5.8: (a) Real and (b) imaginary part of v_t^+, (c) real and (d) imaginary part of v_t^- after evaluating the Fourier co-efficients using source and load boundary conditions.

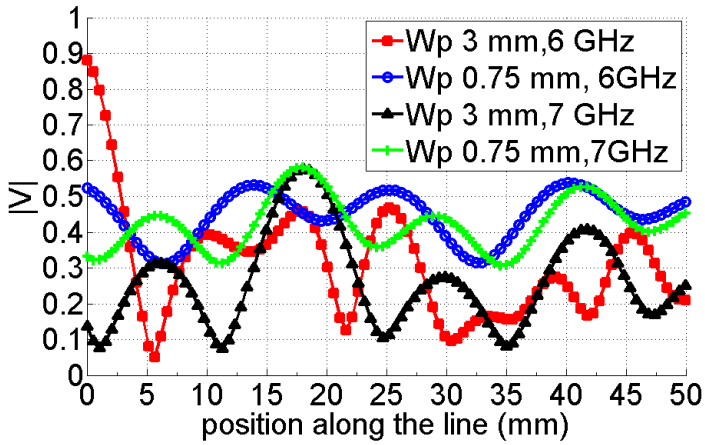

Fig. 5.9: Voltage along the line at 6 GHz and 7 GHz for W_p 0.75 mm and 3 mm

Next, the null space is calculated using MATLAB and after applying the source and load boundary conditions, final values for the Fourier coefficients in the expansion of the line voltage (v_t^+, v_t^-) as expressed in (5.9) are calculated. A plot of the amplitude and phase of the Fourier coefficients for the two lines are shown in Fig. 5.8. Variation of the voltage amplitude along the line at two different frequencies is plotted in Fig. 5.9.

One of the very important factors in this expansion based techniques is the number of coefficients (N) to be taken for the analysis. A plot of the percentage error in the input reflection co-efficient (% $|d\Gamma|$) with increasing number of terms (N) at a frequency of 5.5 GHz and 7 GHz are shown in Fig. 5.10a and Fig. 5.10b respectively.

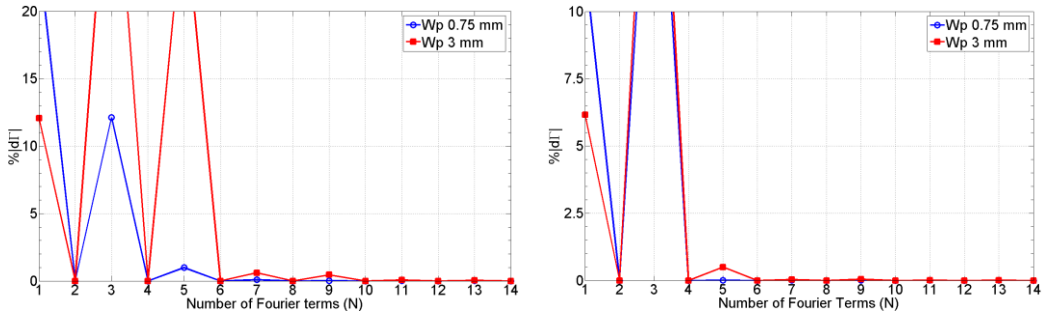

(a) (b)

Fig. 5.10: Convergence of the percentage error in the input reflection co-efficient with increasing number of terms in the Fourier analysis.

Simulated and calculated S_{11} for the sinuous line with Wp 3 mm is shown in Fig. 5.11. Radiated far fields at 4.9 GHz in the x-z plane ($\varphi=0^0$ plane) and the y-z ($\varphi=90^0$) plane for the line with Wp 3 mm are also calculated and the same are plotted in Fig. 5.12a and 5.12b respectively. N is taken as 5 for computing all these antenna characteristics.

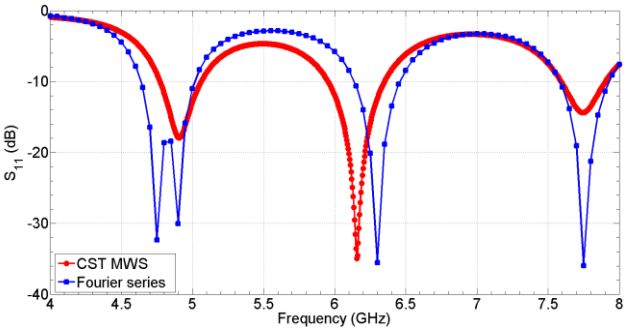

Fig. 5.11: simulated and computed S_{11} vs. frequency for the line with peak non-uniformity (W_p) of 3mm

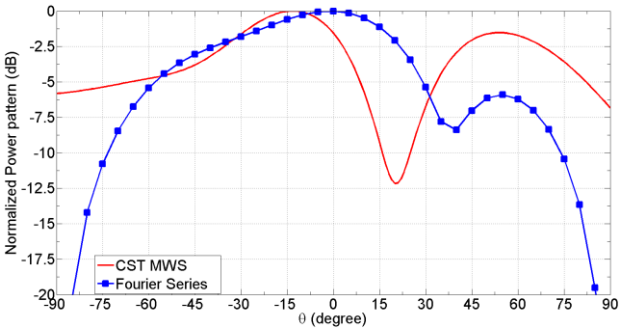

(a)

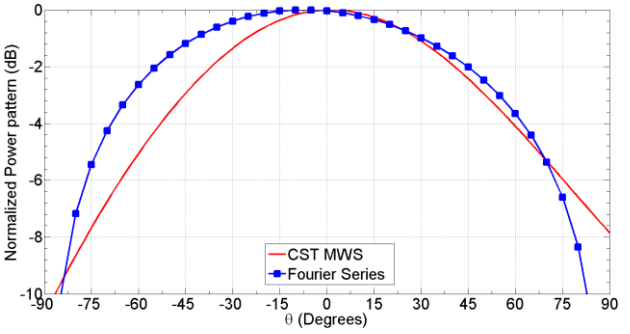

(b)

Fig. 5.12: Normalized power pattern for the W_p=3 mm sinuous line in the (a) x-z plane and the (b) y-z plane

5.4 MODE MATCHING BASED TECHNIQUE FOR ARBITRARY NON-UNIFORMITIES

The Fourier series based technique described in the last sections is based primarily on a solution of the 1D telegrapher's equation on voltage (Equation 5.6). This solution thus ignores any cross-sectional internal field variations i.e. field variations along the line width. It indeed is a very suitable model for microstrip lines with smaller W_0 and/or mild non-uniformities. However, with increasing 'W_0' or increasing width modulation (W_p) the cross-sectional field variation is no longer negligible and it rather plays an important role in internal fields as well as radiated far field calculation. As an example, a sinusoidal line with W_0 of 15 mm and W_p of 3 mm following (5.41) has a maximum electrical width of about $0.78\lambda_g$ at 6 GHz where λ_g is the guided wave length underneath the strip at that frequency. This is a considerable length and field variations across it can no longer be neglected. This situation thus necessitates the use of a more elegant technique capable of handling 2D field variations underneath the strip. The solution we have aimed at is a mode matching technique capable of describing both longitudinal and transverse field variations.

In this section thus, we attempt to analyze a non uniform microstrip line with arbitrary amount of width modulation, arbitrary base width and termination using a sequential mode matching based method. This technique is described next in the context of a non uniform microstrip line shown in Fig 5.1. The basic mode matching technique is divided in three steps. First, the non uniform line is discretized into 'M' uniform rectangular line segments. Next, mode matching procedure is applied to the interface of these uniform line segments. Modal description of the excitation and termination conditions is incorporated. Finally the coefficient vector is evaluated by standard matrix inversion routines. These steps are elaborated next.

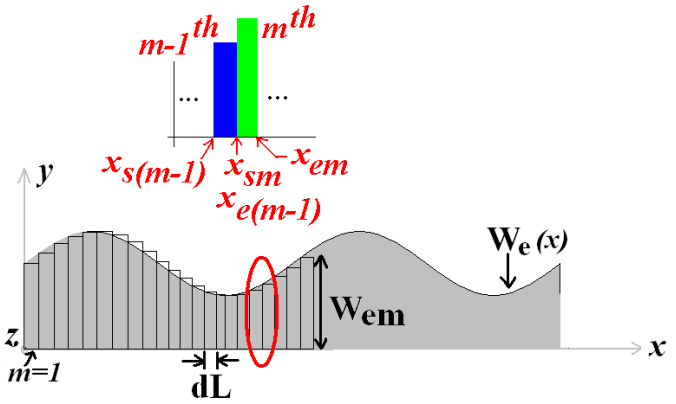

Fig. 5.13: Uniform Discretization of the non uniform microstrip line for the mode matching analysis

5.4.1 DISCRETIZATION OF THE NON-UNIFORM LINE

The non uniform microstrip line is first uniformly segmented into '*M*' uniform line segments of different widths. The Discretization scheme is as shown in Fig. 5.13. The mth linear segment has a length and effective width of dL (=L/M) and W_{em} respectively. (Length of the mth segment is taken as L_m in general for the analysis to follow. L_m=dL for the uniform Discretization scheme).

5.4.2 MODE MATCHING PREPROCESSING

Electric field inside the mth line segment is expressed as a combination of 'N' modes and is expressed as

$$E_{zm}(\mathrm{x},\mathrm{y}) = \sum_{n=0}^{N} \left\{ a_{mn} \cos\beta_{mn}\left(x - x_{sm}\right) + b_{mn} \cos\beta_{mn}\left(x - x_{em}\right) \right\} \cos\left(k_{mn} y\right) \qquad (5.42)$$

where $k_{mn} = \dfrac{n\pi}{W_{em}}$, $\beta_{mn} = \sqrt{k_m^2 - k_{mn}}$ with $k_m = \dfrac{\omega\sqrt{\varepsilon_{em}}}{c}$

Here, W_{em} and ε_{em} are respectively the effective width and effective dielectric constant of the mth uniform segment. x_{sm} and x_{em} are the start and end x-coordinate of the mth segment as shown in Fig. 5.13. Corresponding magnetic field inside the mth uniform line segment is calculated using the Maxwell's equation as

$$\nabla \times \overrightarrow{E_m} = -j\omega\mu_0 \overrightarrow{H_m} \tag{5.43}$$

$$\overrightarrow{H_m} = \frac{1}{-j\omega\mu_0} \begin{vmatrix} \hat{x} & \hat{y} & \hat{z} \\ \frac{\partial}{\partial x} & \frac{\partial}{\partial y} & \frac{\partial}{\partial z} \\ 0 & 0 & E_{zm} \end{vmatrix} \tag{5.44}$$

From this, different components of H_m are calculated as

$$H_{mx}(\mathrm{x},\mathrm{y}) = \frac{1}{j\omega\mu_0} \sum_{n=0}^{N} k_{mn} \begin{Bmatrix} a_{mn} \cos\beta_{mn}\left(x - x_{sm}\right) + \\ b_{mn} \cos\beta_{mn}\left(x - x_{em}\right) \end{Bmatrix} \sin\left(k_{mn} y\right) \tag{5.45}$$

$$H_{my}(\mathrm{x},\mathrm{y}) = \frac{1}{j\omega\mu_0} \sum_{n=0}^{N} -\beta_{mn} \begin{Bmatrix} a_{mn} \sin\beta_{mn}\left(x - x_{sm}\right) + \\ b_{mn} \sin\beta_{mn}\left(x - x_{em}\right) \end{Bmatrix} \cos\left(k_{mn} y\right) \tag{5.46}$$

Here H_{mx} and H_{my} are respectively the *'x'* and *'y'* components of the magnetic field underneath the m^{th} line segment. The electric and magnetic fields expressed in (5.42), (5.45)-(5.46) are now subjected to the boundary conditions discussed next.

5.4.3 MODE MATCHING PROCEDURE

5.4.3.1 Source Boundary Condition

Excitation for the microstrip line is modelled as a vertical current strip of width W_f as shown in Fig. 5.14. The current density is taken as $J_0=1/W_f$. This excitation is included in the analysis through the following boundary condition

$$\begin{aligned} \hat{x} \times H_{1y} \hat{y} &= J_0 \hat{z} \text{ for } y_0 \le y \le y_0 + W_f,\ x = x_{s1} \\ &= 0 \text{ otherwise at } x = x_{s1} \end{aligned} \tag{5.47}$$

Here H_{1y} is the y-component of the magnetic field in the 1^{st} segment. Using the magnetic field expressed in (5.46) to substitute H_{1y} in (5.47) we obtain,

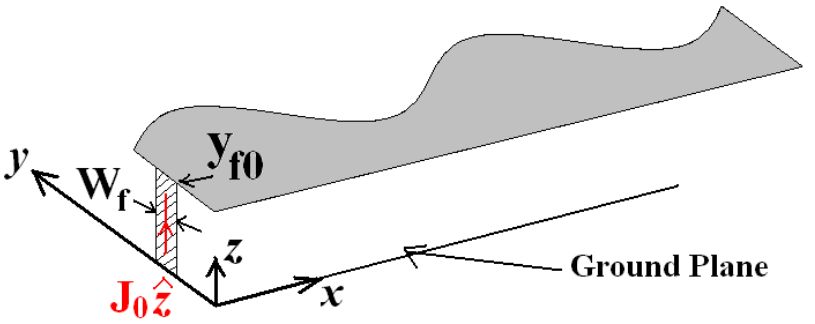

Fig. 5.14: The source modeled as a vertical strip of electric current density with a magnitude of J_0 and width of W_f

$$\frac{-1}{j\omega\mu_0}\sum_n \beta_{1n}\cos(k_{1n}y)\left\{b_{1n}\sin(\beta_{1n}L_1)\right\} = J_0 \text{ for } y_0 \le y \le y_0 + W_f \\ = 0 \text{ otherwise} \tag{5.48}$$

Now, multiplying both sides by $\cos(k_{1t}y)$ and integrating in (0, W_1), we obtain after some simplification,

$$b_{1t} = \frac{j\omega\mu_0}{\beta_{1t}\sin(\beta_{1t}L_1)} \frac{\int_{y_0}^{y_0+W_f} J_0\cos(k_{1t}y)\,dy}{\sigma(1,t)} \quad \text{for } t = 0,1\ldots N \tag{5.49}$$

$$\text{Here } \sigma(q,t) = \int_0^{W_{qe}} \cos(k_{qn}y)\cos(k_{qt}y)\,dy = W_{qe}/2 \text{ if t=n} \neq 0 \\ = W_{qe} \quad \text{if t=n=0} \tag{5.50}$$

5.4.3.2 *Inter-Segment Boundary Condition*

There are two types of interfaces between the mth and the (m+1)th segment. We designate these case I ($W_m > W_{m+1}$) and case II ($W_m < W_{m+1}$) where W_m is the width of the m^{th} segment and W_{m+1} is the width of the $(m+1)^{th}$ segment.

For case I ($W_m > W_{m+1}$) shown in Fig. 5.15a, continuity of tangential electric field at the interface between the m^{th} and the $(m+1)^{th}$ segment is expressed as

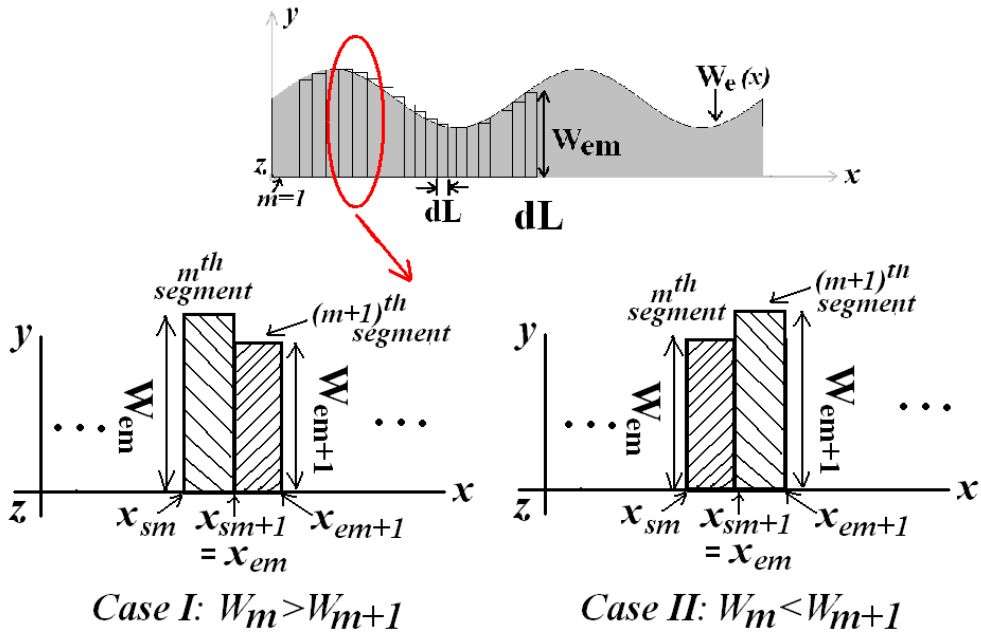

(a) (b)

Fig. 5.15: The two types of inter-segment boundary conditions with (a) case I ($W_m > W_{m+1}$) and (b) case II ($W_m < W_{m+1}$)

$$E_{zm}(\mathrm{x} = \mathrm{x}_{em}, 0 \le \mathrm{y} \le \mathrm{W}_{em+1}) = E_{zm+1}(\mathrm{x} = \mathrm{x}_{sm+1}, 0 \le \mathrm{y} \le \mathrm{W}_{em+1}) \quad (5.51)$$

Continuity of tangential magnetic field at the interface between the m^{th} and the $(m+1)^{\text{th}}$ segment is expressed as

$$\begin{aligned} H_{ym}(\mathrm{x} = \mathrm{x}_{em}) = H_{ym+1}(\mathrm{x} = \mathrm{x}_{sm+1}) \quad & \text{for } 0 \le \mathrm{y} \le \mathrm{W}_{em+1} \\ = 0 \quad & \text{for } \mathrm{W}_{em+1} < \mathrm{y} \le \mathrm{W}_{em} \end{aligned} \quad (5.52)$$

This leads to the following condition.

$$\begin{aligned} & \frac{1}{j\omega\mu_0}\sum_{n=0}^{N} -\beta_{mn}\left\{a_{mn}\sin\beta_{mn}L_m\right\}\cos\left(k_{mn}y\right) \\ & = \frac{1}{j\omega\mu_0}\sum_{p=0}^{N} -\beta_{m+1p}\left\{-b_{m+1p}\sin\beta_{m+1p}L_{m+1}\right\}\cos\left(k_{m+1p}y\right) \quad \text{for } 0 \le y \le W_{em+1} \\ & = 0 \quad \text{for } W_{em+1} \le y \le W_{em} \end{aligned} \quad (5.53)$$

Multiplying both sides by $\cos\left(k_{mt}y\right)$ and integrating in the range (0, W_m),

we obtain after some simplification,

$$a_{mt} = \frac{1}{\sigma(\mathrm{m,t})\beta_{mt}\sin\left(\beta_{mt}L_m\right)}\sum_{n=0}^{N} -\beta_{m+1n}b_{m+1n}\sin\left(\beta_{m+1n}L_{m+1}\right) \times \int_{0}^{W_{em+1}} \cos\left(k_{m+1n}y\right)\cos\left(k_{mt}y\right)dy \quad \text{for t=0,1...N} \tag{5.54}$$

On the other hand, continuity condition of the tangential electric field using (5.51) leads to,

$$\sum_{n=0}^{N}\left\{a_{mn}\cos\beta_{mn}L_m + b_{mn}\right\}\cos\left(k_{mn}y\right) = \sum_{p=0}^{N}\left\{a_{m+1p} + b_{m+1p}\cos\beta_{m+1p}L_{m+1}\right\}\cos\left(k_{m+1p}y\right) \tag{5.55}$$

Now, multiplying both sides by $\cos\left(k_{m+1t}y\right)$ and integrating in the range (0, W_{m+1}), we obtain, after some simplification,

$$\left\{a_{m+1t} + b_{m+1t}\cos\left(\beta_{m+1t}L_{m+1}\right)\right\}\sigma(\mathrm{m+1,t}) = \sum_{n=0}^{N}\left\{a_{mn}\cos\left(\beta_{mn}L_m\right) + b_{mn}\right\} \times \int_{0}^{W_{em+1}} \cos\left(k_{mn}y\right)\cos\left(k_{m+1t}y\right)dy \text{ for t=0,1...N} \tag{5.56}$$

For <u>case II</u> shown in Fig. 5.15b, Continuity of tangential electric field at the interface between the m^{th} and the $(m+1)^{\text{th}}$ segment leads to

$$E_{zm}(\mathrm{x} = \mathrm{x}_{em}, 0 \le \mathrm{y} \le \mathrm{W}_{em}) = E_{zm+1}(\mathrm{x} = \mathrm{x}_{sm+1}, 0 \le \mathrm{y} \le \mathrm{W}_{em}) \tag{5.57}$$

On the other hand, continuity of tangential magnetic field at the interface between the m^{th} and the $(m+1)^{\text{th}}$ segment leads to

$$\begin{aligned} H_{ym+1}(\mathrm{x} = \mathrm{x}_{sm+1}) = H_{ym}(\mathrm{x} = \mathrm{x}_{em}) \quad & \text{for } 0 \le \mathrm{y} \le \mathrm{W}_{em} \\ =0 \quad & \text{for } \mathrm{W}_{em} \le \mathrm{y} \le \mathrm{W}_{em+1} \end{aligned} \tag{5.58}$$

We obtain from this continuity of the tangential magnetic field,

$$\begin{aligned}&\frac{1}{j\omega\mu_0}\sum_{n=0}^{N}-\beta_{m+1n}\left\{-b_{m+1n}\sin\beta_{m+1n}L_{m+1}\right\}\cos\left(k_{m+1n}y\right)\\&=\frac{1}{j\omega\mu_0}\sum_{p=0}^{N}-\beta_{mp}\left\{a_{mp}\sin\beta_{mp}L_m\right\}\cos\left(k_{mp}y\right)\ \text{ for } 0\le y\le W_{em}\\&=0\qquad\qquad\qquad\qquad\qquad\qquad\text{for } W_{em}\le y\le W_{em+1}\end{aligned}\tag{5.59}$$

Multiplying both sides by $\cos\left(k_{m+1t}y\right)$ and integrating in the range (0, W_{m+1}), we obtain after some simplification,

$$b_{m+1t}=\frac{1}{\sigma(\mathrm{m+1,t})\beta_{m+1t}\sin\left(\beta_{m+1t}L_{m+1}\right)}\sum_{n=0}^{N}-\beta_{mn}a_{mn}\sin\left(\beta_{mn}L_m\right)\ \times\int_0^{W_{em}}\cos\left(k_{mn}y\right)\cos\left(k_{m+1t}y\right)dy\ \text{for t=0,1...N}\tag{5.60}$$

On the other hand, continuity of tangential electric field using (5.57) yields

$$\sum_{n=0}^{N}\left\{a_{mn}\cos\beta_{mn}L_m+b_{mn}\right\}\cos\left(k_{mn}y\right)=\sum_{p=0}^{N}\left\{a_{m+1p}+b_{m+1p}\cos\beta_{m+1p}L_{m+1}\right\}\cos\left(k_{m+1p}y\right)\tag{5.61}$$

Now, multiplying both sides by $\cos\left(k_{mt}y\right)$ and integrating in the range (0, W_m), we obtain, after some simplification,

$$\left\{a_{mt}\cos\left(\beta_{mt}L_m\right)+b_{mt}\right\}\sigma(\mathrm{m,t})=\sum_{n=0}^{N}\left\{a_{m+1n}\cos\left(\beta_{m+1n}L_{m+1}\right)+b_{m+1n}\right\}\times\int_0^{W_{em}}\cos\left(k_{m+1n}y\right)\cos\left(k_{mt}y\right)dy\ \text{for t=0,1...N}\tag{5.62}$$

5.4.3.3 Load Boundary Condition

Interfacing the lumped load with the mode matching procedure requires additional modelling of the load impedance. The terminating impedance (Z_l) is replaced by a microstrip line of width W_l, such that its characteristic impedance is equal to Z_l (shown in Fig. 5.16). This turns out to be approximately 1.5 mm for

the substrate chosen (AD430 30 mils). Boundary conditions are applied in the interface between sections I and II shown in Fig. 5.16. Electric and magnetic fields in section I are expressed using (5.42) and (5.46) with m=M while those in section II are expressed as follows

$$E_{zl} = \sum_{n=0}^{N} c_n e^{-j\beta_{\ln}(\mathrm{x}-x_{eM})} \cos\{k_{\ln}(y - y_l)\} \tag{5.63}$$

$$H_{yl} = \frac{1}{j\omega\mu_0} \sum_{n=0}^{N} -j\beta_{\ln} c_n e^{-j\beta_{\ln}(\mathrm{x}-x_{eM})} \cos\{k_{\ln}(y - y_l)\} \tag{5.64}$$

Boundary condition at the interface of the Mth segment (section I in Fig. 5.16) and the equivalent microstrip line (section II in Fig. 5.16) are now expressed as:

$$E_{zM}(\mathrm{x} = \mathrm{x}_{eM}, y_l \le \mathrm{y} \le \mathrm{y}_l + \mathrm{W}_l) = E_{zl}(\mathrm{x} = \mathrm{x}_{eM}) \tag{5.65}$$

$$\begin{aligned} H_{yM} &= H_{yl} \quad \text{for} \quad \mathrm{x} = \mathrm{x}_{eM},\ y_l \le \mathrm{y} \le \mathrm{y}_l + \mathrm{W}_l \\ &= 0 \qquad \text{for} \quad \mathrm{x} = \mathrm{x}_{eM},\ y_l > \mathrm{y} \ \text{ and } \ \mathrm{y}_l + \mathrm{W}_l < \mathrm{y} \le \mathrm{W}_M \end{aligned} \tag{5.66}$$

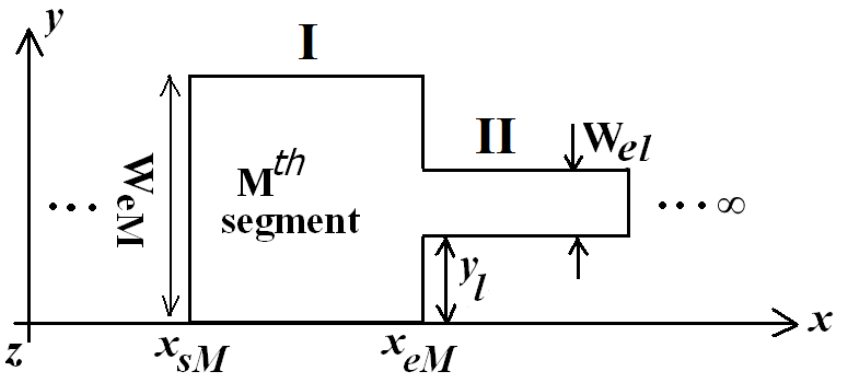

Fig. 5.16: The load boundary condition and the equivalent modeled strip in region II to replace the arbitrary load impedance.

Using the continuity of tangential magnetic field as expressed in (5.66) we obtain,

$$\frac{1}{j\omega\mu_0} \sum_{n=0}^{N} -\beta_{Mn} a_{Mn} \sin(\beta_{Mn} L_M) \cos(k_{Mn} y) = \frac{1}{j\omega\mu_0} \sum_{p=0}^{N} -j\beta_{lp} c_p \cos\{k_{lp}(y - y_l)\} \tag{5.67}$$

Multiplying both sides by $\cos(k_{Mt}y)$ and integrating in the range (0, W_{eM}), we obtain after some simplification,

$$-\beta_{Mt}a_{Mt}\sin(\beta_{Mt}L_M)\sigma(M,t)=\sum_{p=0}^{N}-j\beta_{lp}c_p\int_{y_l}^{y_l+W_l}\cos\{k_{lp}(y-y_l)\}\cos(k_{Mt}y)\,dy$$

for t=0,1...N

(5.68)

Using the continuity condition of (5.65) for tangential electric field at the interface of the Mth segment and the modelled termination we obtain in $y_l \leq y \leq y_l + W_l$,

$$\sum_{n=0}^{N}\left[a_{Mn}\cos(\beta_{Mn}L_M)+b_{Mn}\right]\cos(k_{Mn}y)=\sum_{p=0}^{N}c_p\cos\{k_{lp}(y-y_l)\} \qquad (5.69)$$

Multiplying both sides by $\cos(k_{lt}(y-y_l))$ and integrating in (y_l, y_l+W_l) we obtain after some simplification

$$c_t\sigma_l=\sum_n\begin{Bmatrix}a_{Mn}\cos(\beta_{Mn}L_M)\\+b_{Mn}\end{Bmatrix}\int_{y_l}^{y_l+W_l}\cos(k_{Mn}y)\cos\{k_{\ln}(y-y_l)\}\,dy \text{ for t=0,1...N}$$

(5.70)

$$\text{where } \sigma_l(t)=\int_0^{W_l}\cos\{k_{ln}(y-y_l)\}\cos\{k_{lt}(y-y_l)\}\,dy = W_l/2 \text{ if t=n} \neq 0 \qquad (5.71)$$

$$= W_l \quad \text{if t=n=0}$$

Abovementioned steps lead to (2NM+N) equations in (2NM+N) unknowns. These are arranged in a matrix equation and standard matrix inversion techniques are used for solving the unknown coefficient vector.

5.4.4 CALCULATION OF INPUT IMPEDANCE

Input impedance and S_{11} for the non uniform microstrip line is calculated from the electric and magnetic fields at the point of excitation assuming unit current excitation. This leads to the following expression

$$Z_{in} = -h\sum_{n=0}^{N_m}\left\{a_{1n} + b_{1n}\cos\left(\beta_{1n}\Delta L\right)\right\}\cos\left(k_{1n}y_{f0}\right) \tag{5.72}$$

5.4.5 CALCULATION OF RADIATED FIELDS

Radiated far-field from the line is calculated in a piecewise manner. Contributions from individual subsections are considered and finally added to get the total radiated far field.

Electric and magnetic current densities considered in the m[th] segment are shown in Fig. 5.17. They are calculated using the following relations

$$\vec{M}_{m1} = E_{zm}(\mathrm{y} = \mathrm{W}_e, \mathrm{z} = \mathrm{h})\,\hat{\mathrm{z}}\times\hat{\mathrm{y}} \tag{5.73}$$

$$\vec{M}_{m2} = E_{zm}(\mathrm{y} = 0, z = h)\,\hat{\mathrm{z}}\times(-\hat{\mathrm{y}}) \tag{5.74}$$

$$\vec{\mathrm{J}}_m = -\hat{\mathrm{z}}\times\left\{\mathrm{H}_{xm}(\mathrm{z} = \mathrm{h})\hat{x} + \mathrm{H}_{ym}(\mathrm{z} = \mathrm{h})\hat{y}\right\} \tag{5.75}$$

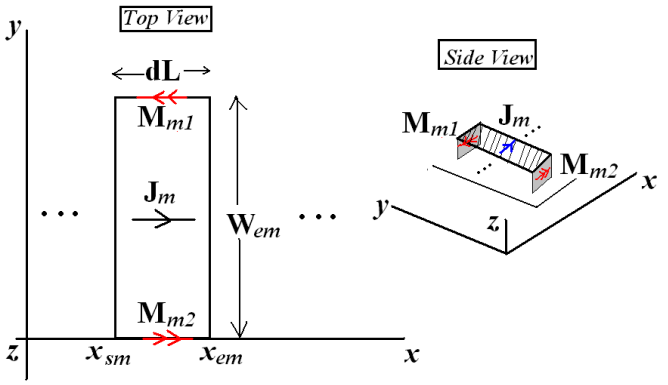

Fig. 5.17: Radiating apertures and corresponding electric and magnetic current densities for calculation of radiated far fields.

Electric and magnetic potentials radiated in the far-field from these sources are calculated using the following integrals

$$\vec{F}_{m1} = \frac{\varepsilon_0}{4\pi}\frac{e^{-jk_0 r}}{r}\int_{x'=0}^{L}\int_{z'=-h}^{h}\vec{M}_{m1}e^{jk_0\{x'\sin\theta\cos\varphi + W_{em}\sin\theta\sin\varphi + z'\cos\theta\}}dz'dx' \tag{5.76}$$

$$\vec{F}_{m2} = \frac{\varepsilon_0}{4\pi}\frac{e^{-jk_0 r}}{r}\int_{x'=0}^{L}\int_{z'=-h}^{h}\vec{M}_{m2}e^{jk_0\{x'\sin\theta\cos\varphi+z'\cos\theta\}}dz'dx' \tag{5.77}$$

$$\vec{A}_m = \frac{\mu_0}{4\pi}\frac{e^{-jk_0 r}}{r}\left\{2j\sin\left(k_0 h\cos\theta\right)\right\}\int_{x'=0}^{L}\int_{y'=0}^{W_{em}}\vec{J}_m\, e^{jk_0\{x'\sin\theta\cos\varphi+y'\sin\theta\sin\varphi\}}dy'dx' \tag{5.78}$$

After some calculations and simplification we obtain the following expressions for the vector potentials

$$F_{xm1} = -\frac{\varepsilon_0}{4\pi}\frac{e^{-jk_0 r}}{r}2h\sin c\left(k_0 h\cos\theta\right)e^{jk_0 W_{em}\sin\theta\sin\varphi}\times \sum_{n=0}^{N_m}\left[\cos\left(k_{mn}W_{em}\right)\left\{\frac{Q_{1mn}}{\lambda_{1mn}}\left(e^{j\lambda_{1mn}x_{em}}-e^{j\lambda_{1mn}x_{sm}}\right)+\frac{Q_{2mn}}{\lambda_{2mn}}\left(e^{j\lambda_{2mn}x_{em}}-e^{j\lambda_{2mn}x_{sm}}\right)\right\}\right] \tag{5.79}$$

$$F_{xm2} = \frac{\varepsilon_0}{4\pi}\frac{e^{-jk_0 r}}{r}2h\sin c\left(k_0 h\cos\theta\right)\sum_{n=0}^{N_m}\left[\left\{\begin{array}{l}\frac{Q_{1mn}}{\lambda_{1mn}}\left(e^{j\lambda_{1mn}x_{em}}-e^{j\lambda_{1mn}x_{sm}}\right)\\ +\frac{Q_{2mn}}{\lambda_{2mn}}\left(e^{j\lambda_{2mn}x_{em}}-e^{j\lambda_{2mn}x_{sm}}\right)\end{array}\right\}\right] \tag{5.80}$$

$$A_{xm} = \frac{\mu_0}{4\pi}\frac{e^{-jk_0 r}}{r}\sum_{n=0}^{N_m}-\beta_{mn}\left[\frac{W_{em}}{2}\left\{e^{j\frac{\lambda_3 W_{em}}{2}}\sin c\left(\frac{\lambda_3 W_{em}}{2}\right)+e^{j\frac{\lambda_4 W_{em}}{2}}\sin c\left(\frac{\lambda_4 W_{em}}{2}\right)\right\}\times \left\{2j\sin\left(k_0 h\cos\theta\right)\right\}\frac{1}{j\omega\mu_0}\left\{\frac{Q_{1mn}}{j\lambda_{1mn}}\left(e^{j\lambda_{1mn}x_{em}}-e^{j\lambda_{1mn}x_{sm}}\right)+\frac{Q_{2mn}}{j\lambda_{2mn}}\left(e^{j\lambda_{2mn}x_{em}}-e^{j\lambda_{2mn}x_{sm}}\right)\right\}\right] \tag{5.81}$$

$$A_{ym} = \frac{\mu_0}{4\pi}\frac{e^{-jk_0 r}}{r}\sum_{n=0}^{N_m}-k_{mn}\left[\frac{W_{em}}{2j}\left\{e^{j\frac{\lambda_3 W_{em}}{2}}\sin c\left(\frac{\lambda_3 W_{em}}{2}\right)-e^{j\frac{\lambda_4 W_{em}}{2}}\sin c\left(\frac{\lambda_4 W_{em}}{2}\right)\right\}\times \left\{2j\sin\left(k_0 h\cos\theta\right)\right\}\frac{1}{j\omega\mu_0}\left\{\frac{Q_{1mn}}{j\lambda_{1mn}}\left(e^{j\lambda_{1mn}x_{em}}-e^{j\lambda_{1mn}x_{sm}}\right)+\frac{Q_{2mn}}{j\lambda_{2mn}}\left(e^{j\lambda_{2mn}x_{em}}-e^{j\lambda_{2mn}x_{sm}}\right)\right\}\right] \tag{5.82}$$

Here $\lambda_{1mn} = \beta_{mn} + k_0\sin\theta\cos\varphi,\ \lambda_{2mn} = -\beta_{mn} + k_0\sin\theta\cos\varphi$

$$\lambda_{3mn} = k_{mn} + k_0 \sin\theta \sin\varphi,\ \lambda_{4mn} = -k_{mn} + k_0 \sin\theta \sin\varphi$$

$$Q_{1mn} = \frac{a_{mn}}{2} e^{-j\beta_{mn} x_{sm}} + \frac{b_{mn}}{2} e^{-j\beta_{mn} x_{em}},$$

$$Q_{2mn} = \frac{a_{mn}}{2} e^{j\beta_{mn} x_{sm}} + \frac{b_{mn}}{2} e^{j\beta_{mn} x_{em}}$$

Feed and termination model used in this analysis is that of vertical electric current. Radiation from these vertical electric currents can be taken into account whenever necessary in the following manner,

$$A_z = \frac{\mu_0 h}{2\pi\varepsilon_r} \frac{e^{-jk_0 r}}{r} \left[\begin{array}{l} I_{zs} \left\{ e^{jk_0 \sin\theta (X_s \cos\varphi + Y_s \sin\varphi)} \right\} \sin c\left(k_0 h \cos\theta\right) - \\ I_{zl} \left\{ e^{jk_0 \sin\theta (X_l \cos\varphi + Y_l \sin\varphi)} \right\} \sin c\left(k_0 h \cos\theta\right) \end{array} \right] \tag{5.83}$$

where I_{zs} and I_{zl} are the vertical electric current at the source and load terminals respectively. X_s, Y_s, X_l, Y_l are respectively the X and Y co-ordinates for the excitation and termination. Total radiated far field (E_θ and E_φ) from the entire line is calculated by summing up contributions from all the segments and consequently,

$$E_\theta = -j\omega \sum_{m=1}^{N_s} \left\{ A_{xm} \cos\theta \cos\varphi - A_z \sin\theta + \eta (F_{xm1} + F_{xm2}) \cos\theta \sin\varphi \right\} \tag{5.84}$$

$$E_\varphi = -j\omega \sum_{m=1}^{N_s} \left\{ -A_{xm} \sin\varphi - \eta (F_{xm1} + F_{xm2}) \cos\theta \cos\varphi \right\} \tag{5.85}$$

5.4.6 RESULTS AND DISCUSSIONS

To validate the effectiveness of the mode matching based technique described in the last sections, a non uniform microstrip line following the Fig. 5.1 and (5.1) with W_0 15 mm and W_p 3 mm and n=2, is simulated and the antenna characteristics are compared with those obtained using full wave simulation.

Modal convergence is the most important parameter to observe in case of any mode matching technique. Variation of the percentage change in the input

reflection co-efficient with inceasing number of modes is plotted in Fig. 5.18 at three different frequencies. It can be observed that increasing the number of segments does not have a remarkable effect on convergence but as the number of modes increase the analysis goes toward convergence. Stopping criteria for the technique is set at maximum 3% change of the input reflection co-efficient for at least three subsequent iterations.

Fig. 5.19 shows the post convergence plot of S_{11} vs. frequency. Normalized radiation patterns at 4.5 GHz in the two principal planes (x-z plane and y-z plane) are plotted in Fig. 5.20a and Fig. 5.20b respectively.

Internal electric field inside the non uniform line is in general a function of both the length along the line as well as the width. Magnitude of the internal electric field for the line under consideration at 6 GHz is shown in Fig. 5.21a while the same plot extracted from full wave simulation is shown in Fig. 5.21b.

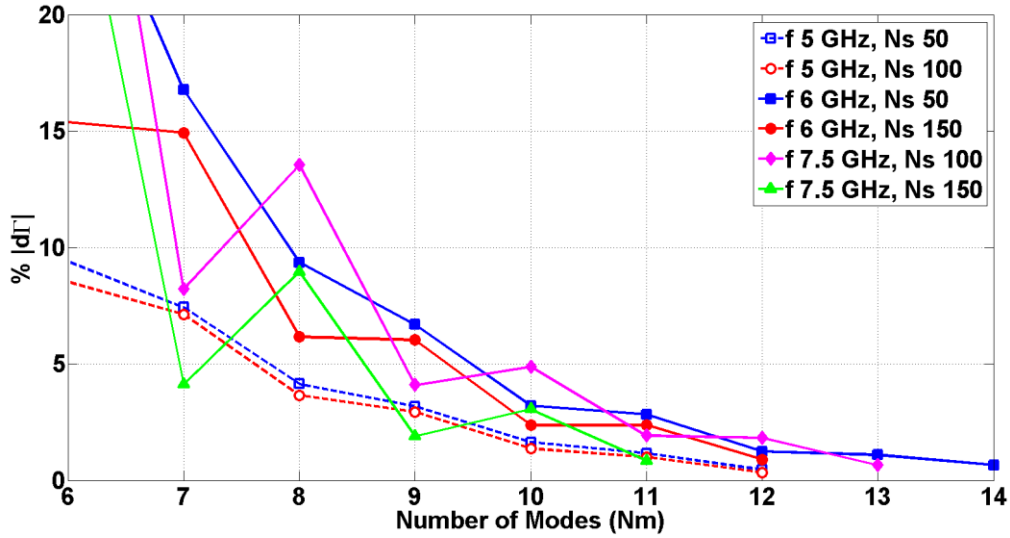

Fig. 5.18: Convergence study, plot of %|dΓ| with increasing number modes for different number of segments at three different frequencies

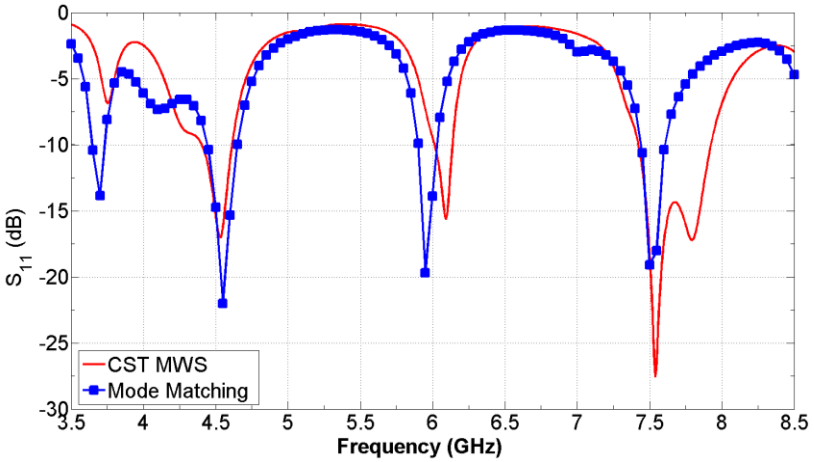

Fig. 5.19: Simulated and calculated S_{11} vs. frequency

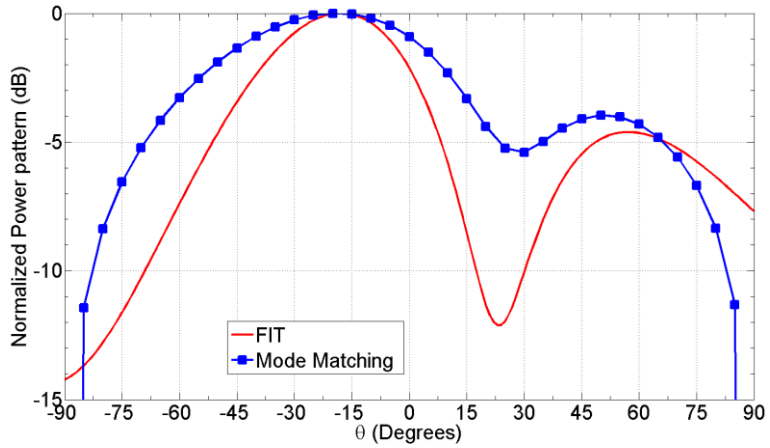

(a)

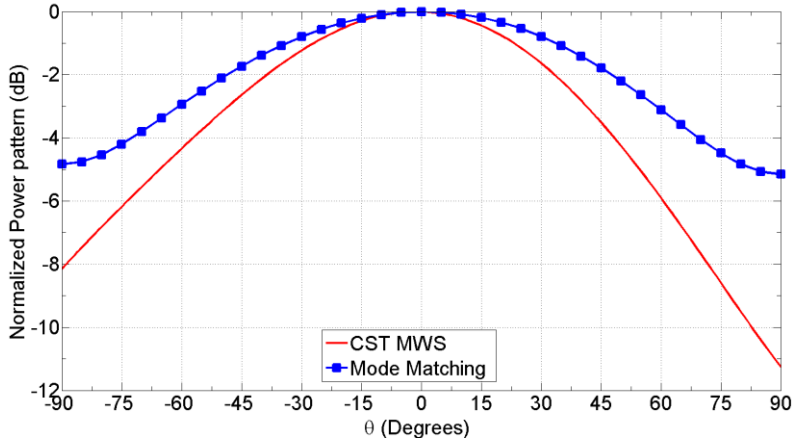

(b)

Fig. 5.20: Normalized radiated power pattern at 4.5 GHz in the (a) x-z plane and (b) y-z plane

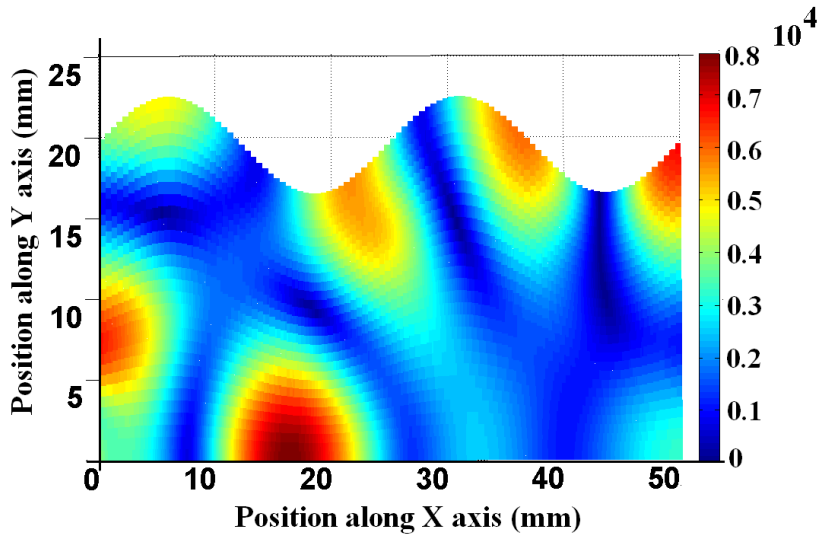

(a)

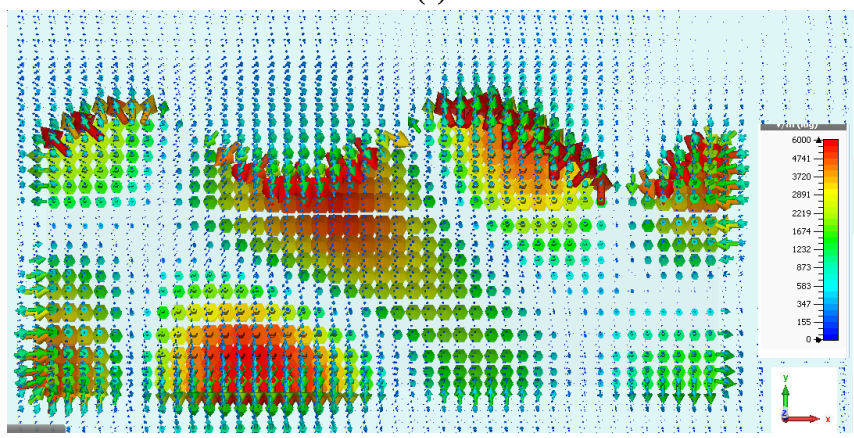

(b)

Fig. 5.21: (a) Calculated and (b) simulated plot of magnitude of the internal electric field inside the line at 6 GHz

5.5 PRACTICAL MEASUREMENTS

To validate the simulation techniques presented in this chapter and compare the obtained results with practical measurements, two different prototypes of the non uniform microstrip line are fabricated on Arlon AD430 substrate with thickness of 30 mils and permittivity of 4.3 (loss tangent 0.003). These fabricated prototypes are shown in Fig. 5.22a and 5.22b respectively.

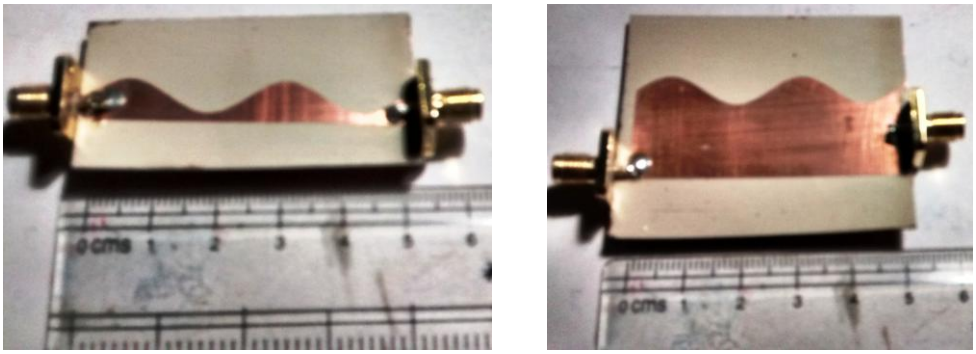

(a) (b)

Fig. 5.22: Fabricated prototypes with (a) W_0 1.5 mm, W_p 3 mm and length of 50 mm, (b) W_0 15 mm, W_p 3mm, length 50mm

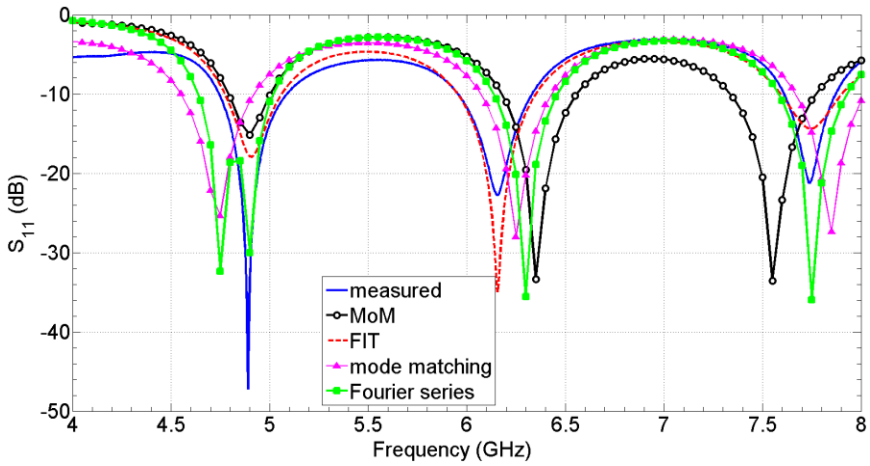

(a)

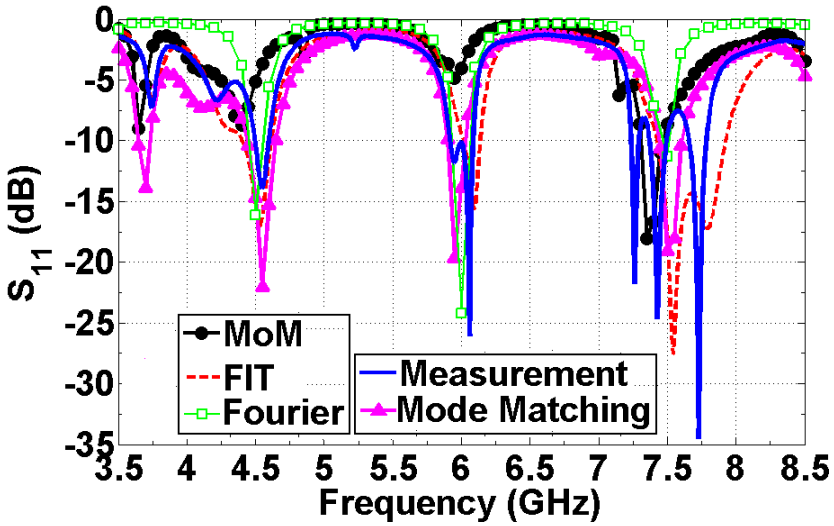

(b)

Fig. 5.23: Simulated, calculated and measured S_{11} with frequency for the lines of Fig. 5.24 (a) W_0 1.5 mm and (b) W_0 15 mm.

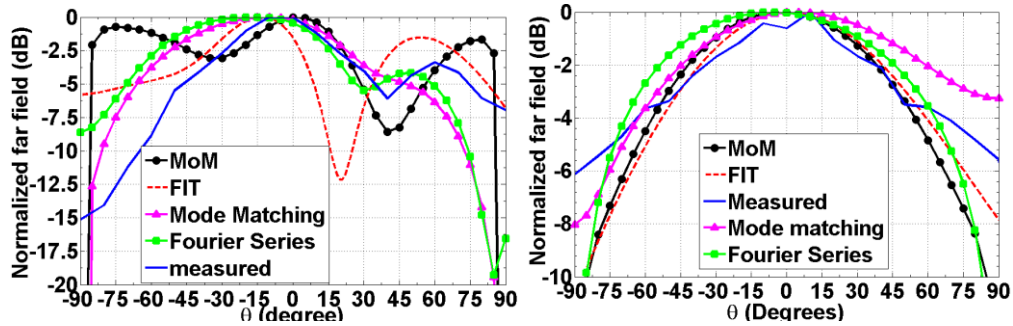

(a) (b)

Fig. 5.24: Normalized power pattern in the far zone at 4.9 GHz in the (a) x-z plane and (b) y-z plane.

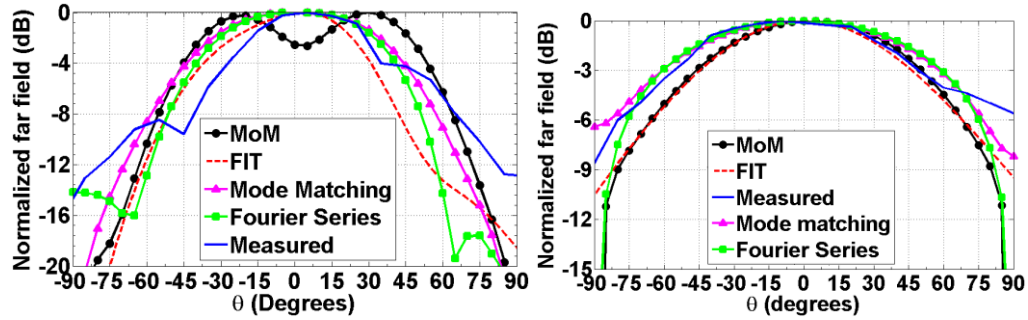

(a) (b)\

Fig. 5.25: Normalized power pattern in the far zone at 6.2 GHz in the (a) x-z plane and (b) y-z plane.

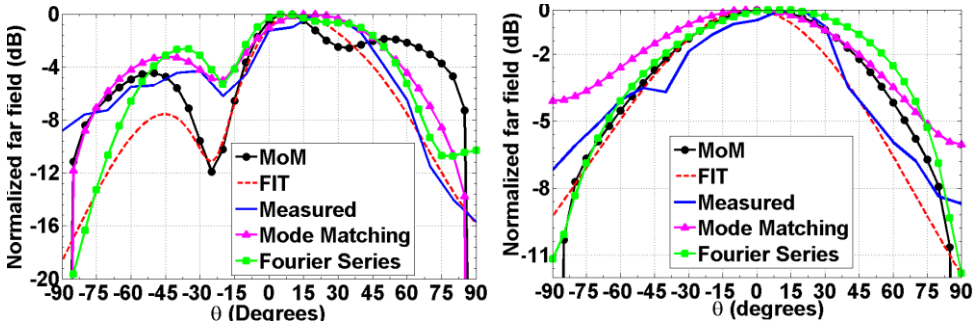

(a) (b)

Fig. 5.26: Normalized power pattern in the far zone at 7.8 GHz in the (a) x-z plane and (b) y-z plane.

These two geometries are analyzed using the Fourier series technique as well as the mode matching technique. Additionally, simulated results using MoM based Zeland IE3D and FIT based CST Microwave Studio have also been used. Results are compared with those from practical measurement.

Simulated, calculated and measured S_{11} with frquency for the two lines are shown in Fig. 5.23a and Fig. 5.23b respectively for W_0 1.5 mm and W_0 15 mm.

Comparison of the normalized radiated power patterns from the line with W_0 1.5 mm in the x-z plane and the y-z plane are shown in Fig. 5.24, Fig. 5.25 and Fig. 5.26 respectively for the operating frequencies of 4.9 GHz, 6.2 GHz and 7.8 GHz.

On the other hand, normalized radiated power patterns for the line with W_0 15 mm at 4.5 GHz, 6 GHz and 7 GHz in the two principal planes are shown in Fig. 5.27 Fig. 5.28 and Fig. 5.29 respectively.

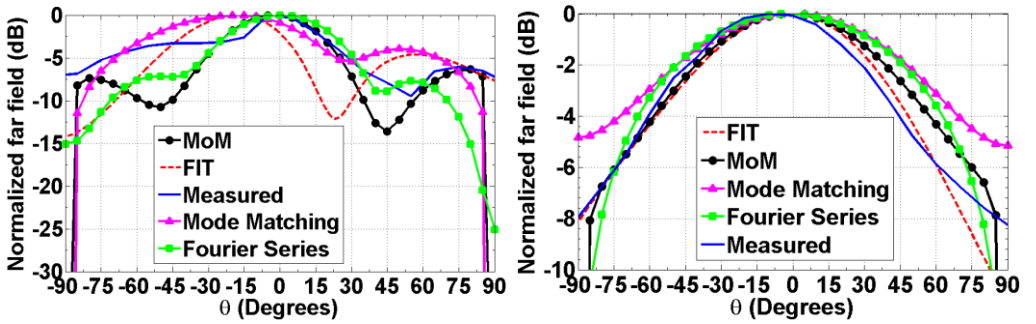

(a) (b)

Fig. 5.27: Normalized power pattern in the far zone at 4.5 GHz in the (a) x-z plane and (b) y-z plane for the line with W_0 15 mm.

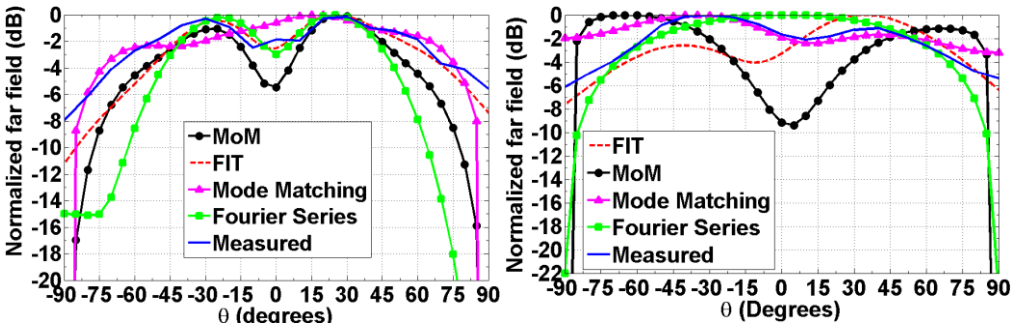

(a) (b)

Fig. 5.28: Normalized power pattern in the far zone at 6.2 GHz in the (a) x-z plane and (b) y-z plane for the line with W_0 15 mm.

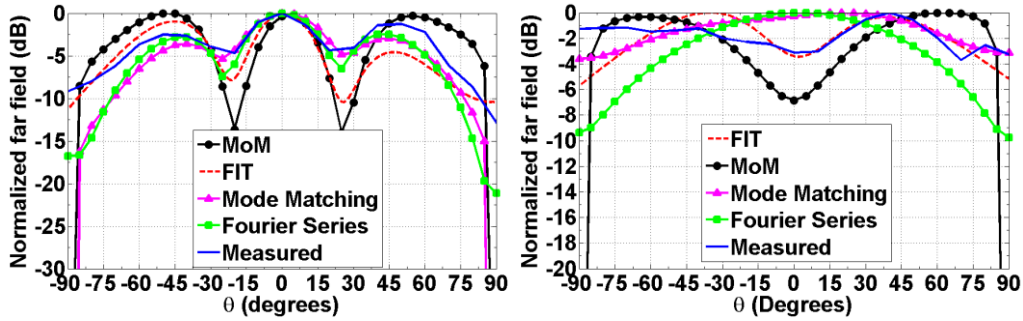

(a) (b)

Fig. 5.29: Normalized power pattern in the far zone at 7.5 GHz in the (a) x-z plane and (b) y-z plane for the line with W_0 15 mm.

5.6 CONCLUSION

An attempt to generally analyze non uniform microstrip lines has been made in this chapter. Microstrip lines with smaller line width or smaller amount of non uniformity supports the Quasi TEM mode of propagation with negligible transverse field variation. This principle is utilized to develop a Fourier series based technique for lines with small to moderate non uniformity. Spatial voltage and currents are solved using a Fourier series expansion. Modified phase constant of the line is calculated in the process. Far fields radiated by such lines are calculated using a Serret-Frenet reference frame based dynamic co-ordinate system. This model however fails to depict the internal fields when the line width is higher and cross-sectional field variation is non-negligible. To alleviate such problems, a mode matching based technique is presented for lines with arbitrary non uniformity. Internal electric and magnetic fields are represented using a two dimensional modal function and appropriate boundary conditions are applied. Radiated far fields are calculated by vectorially adding the contributions from electric and magnetic current densities in all the linear segments. Terminal properties and radiated far fields calculated using these models are compared with those obtained using commercial full wave simulators as well as practical measurement.

REFERENCES:

[1] D. Nesic, and B. Kolundzija, "Band-stop filter with suppression of requested number of spurious stopbands," *International Journal of Microwave and Wireless Technologies*, *9*(5), 995-1002, 2017.

[2] K. A. Shamaileh, M. Almalkawi, V. K. Devabhaktuni, N. I. Dib, B. Henin, and A. M. Abbosh, "Non-uniform transmission line ultra-wideband wilkinson power divider," *Progress In Electromagnetics Research C*, Vol. 44, 1-11, 2013.

[3] M. S. Liang, B. Z. Wang, Z. M. Zhang and S. Ding, "Simplified Pulse Shaping Network for Microwave Signal Focusing Based on Time Reversal," in *IEEE Antennas and Wireless Propagation Letters*, vol. 14, pp. 225-228, 2015.

[4] A. J. Martinez-Ros, J. L. Gómez-Tornero, V. Losada, F. Mesa and F. Medina, "Non-Uniform Sinusoidally Modulated Half-Mode Leaky-Wave Lines for Near-Field Focusing Pattern Synthesis," in *IEEE Transactions on Antennas and Propagation*, vol. 63, no. 3, pp. 1022-1031, March 2015.

[5] Electromagnetic Wave and Radiating Systems. By E C Jordan and K G Balmain.PHI learning Pvt. Ltd. 2009.

[6] A. T. Starr, "The Nonuniform Transmission Line," in *Proceedings of the Institute of Radio Engineers*, vol. 20, no. 6, pp. 1052-1063, June 1932

[7] R. Garg, I. Bahl and M. Bozzi, *Microstrip lines and slotlines*. Artech house. 2013.

[8] T. Itoh and R. Mittra, "Spectral-Domain Approach for Calculating the Dispersion Characteristics of Microstrip Lines (Short Papers)," in IEEE Transactions on Microwave Theory and Techniques, vol. 21, no. 7, pp. 496-499, Jul 1973.

[9] Electromagnetic Waves and curved structures. Lewin L, Chang. David C, and Edward F Kuester. Peter Peregrinus.1977

[10] R. E. Collin. *Foundations for microwave engineering*. John Wiley & Sons, 2007.

Chapter 6

Higher Order Leaky Modes in Microstrip Lines

Contents

6.1 INTRODUCTION

The fundamental Quasi TEM mode in microstrip lines is a mode bound to the structure which radiates very little power. Introduction of discontinuities can give rise to local current imbalance and higher order modes thus generated might increase the amount of power radiated. However, to substantiate the amount of radiation a considerable amount of length is necessary. An alternative to this low radiation Quasi TEM mode had been found by Menzel [1] in the form of a leaky wave antenna although he did not coin the term. These planar leaky wave antennas can be classified into two categories, namely the uniform leaky wave antennas and the periodic leaky wave antennas. In the case of uniform leaky wave antennas, a higher order mode (typically TE_{01} [2] or TE_{02} [3] with respect to the direction of propagation) is excited in the microstrip line. Near the cut-off of such modes at frequencies for which the phase constant of the propagating mode (β) becomes smaller that the free space phase constant (k_0), the mode becomes fast and consequently leak power all along the line without necessitating any discontinuity [4]. On the other hand, periodic leaky wave antennas in most cases

are constituted of a host microstrip line supporting the fundamental Quasi TEM mode. Introduction of periodic loads on this host line gives rise to numerous Floquet modes. Some of these Floquet modes (typically the n= -1 or the n= -2 modes [5]) become fast in the frequency range of interest and contribute to the total radiation from the structure.

In this chapter, techniques available for analyzing the dispersion characteristics of uniform and periodic leaky microstrip antenna are discussed and two examples of such antennas are simulated to compare the effectiveness of the models. These models are used in later chapters for analyzing specific designs of leaky wave antennas. It needs to be pointed out that the basic analysis techniques presented in this chapter are well established ones and it is outlined here for maintaining continuity with the analysis and simulations to be presented in later chapters.

6.2 PROBLEM FORMULATION

Two specific different problems are attempted in this chapter. First, a microstrip line supporting the first higher order mode (TE_{01}) is considered. Shown in Fig. 6.1a, this microstrip line is assumed to have a width of 'W_0' and a length of 'L'. In the second part of the chapter, the periodic leaky wave antenna shown in Fig. 6.1b is analyzed and its characteristics are observed. Symbols used in rest of the chapter are shown in Figs. 6.1a and b.

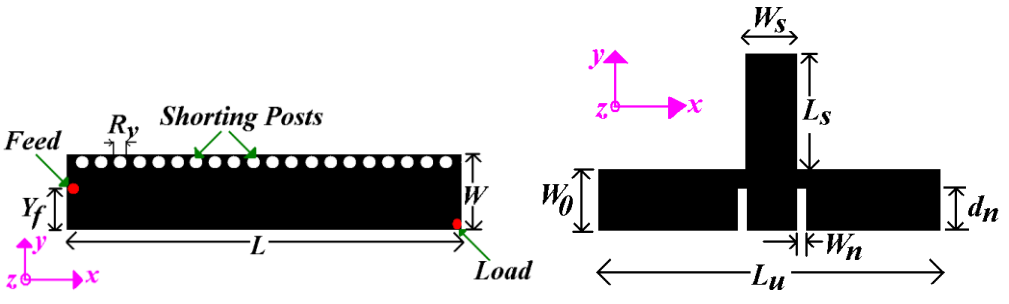

(a) (b)

Fig. 6.1: Geometry types considered in this work with the (a) uniform leaky wave antenna and (b) unit cell for the periodic leaky wave antenna.

6.3 UNIFORM LEAKY WAVE ANTENNAS

6.3.1 SIMPLIFIED MODELS AND THEIR COMPARISON

6.3.1.1. Closed Form Expressions For the First Higher Order Mode

Liu and Long have developed a set of closed form expressions [6] for calculating the attenuation constant (α) and the phase constant (β) of the first higher order mode in microstrip line. Their expressions are based on an equivalent complex line width (W_e) and generic propagation constant from waveguide theory. These formulae are summarized below.

$$k = \beta - j\alpha = \sqrt{k_0^2 \varepsilon_{eff} - \frac{\pi^2}{W_e^2}} \tag{6.1}$$

$$W_e = W + 2(\Delta W - jb) \tag{6.2}$$

$$\Delta W = h\left[1 + 0.8874\left(\frac{1}{\varepsilon_r + 0.375}\right)\left(\frac{\frac{W}{h} - 11}{\frac{W}{h} + 20.26}\right)\right] \tag{6.3}$$

$$b = \frac{h}{2\varepsilon_{eff}} \tag{6.4}$$

These formulae are claimed to be accurate within an error of 10% for $W/h \geq 5.5$ and $\varepsilon_r \leq 12$.

6.3.1.2. Planar Waveguide Model

Menzel used a simple planar waveguide model. The microstrip line he chose, supported the first higher order mode (TE_{01}). This model is more appropriate for calculating the propagation constants for higher order modes. The phase constant of the n^{th} higher order mode in the microstrip line is given by:

$$k = \beta - j\alpha = \sqrt{k_0^2 \varepsilon_{eff} - \frac{n^2 \pi^2}{W_e^2}} \tag{6.5}$$

where we have considered W_e to be an average of the effective widths given by the planar waveguide model [7] (PWG Model) and the one obtained from length extension formula of a microstrip patch [8]. Consequently, W_e is expressed as

$$W_{e1} = \frac{377h}{Z_0 \sqrt{\varepsilon_{eff}}} \tag{6.6}$$

$$W_{e2} = W + 0.814h \left(\frac{\varepsilon_{eff} + 0.3}{\varepsilon_{eff} - 0.258} \right) \left(\frac{\frac{W}{h} + 0.264}{\frac{W}{h} + 0.8} \right) \tag{6.7}$$

$$W_e = \frac{W_{e1} + W_{e2}}{2} \tag{6.8}$$

The attenuation constant was ignored by Menzel and the same cannot be calculated in a straightforward manner. However one can approximate the attenuation constant by calculating the total radiated power from the structure and evaluating an effective decay constant to accommodate it into the analysis.

To observe and justify the use of the average effective line width of (6.6), two different microstrip lines are analyzed for the propagation constant of the first higher order mode using (6.1) and (6.5). These are plotted in Fig. 6.2a and Fig. 6.2b respectively for ε_r *=2.2, h= 0.762, W=12*mm and ε_r *=4, h= 1.6, W=12mm*. the phase constant in case of the planar waveguide model are calculated using $W=W_{e1}$, $W=W_{e2}$ and $W=W_e$. It is observed that the latter case (W_e) predicts the value of β with reasonable accuracy.

The planar waveguide model is more suitable for the analysis to follow the latter chapters of this thesis. In cases of periodic structures where the first higher order mode is perturbed by introduction of distributed loads, the circuit model and the simple ABCD matrix based technique fails to evaluate the dispersion characteristics and a more generalized technique is necessitated.

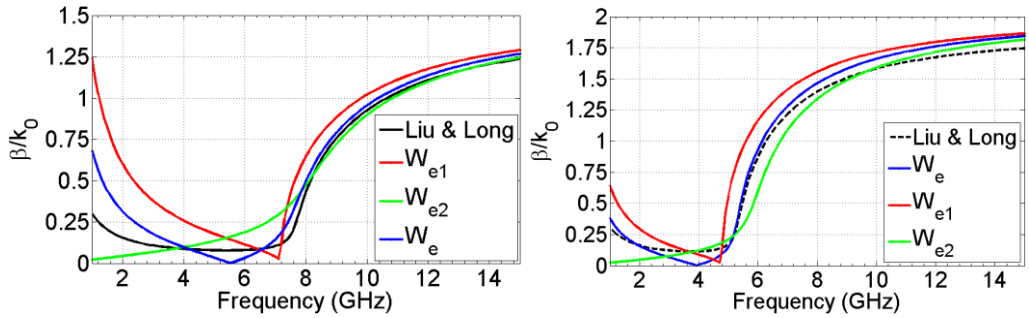

Fig. 6.2: β/k_0 for microstrip line with (a) ε_r =2.2, h= 0.762, W=12mm and (b) ε_r =4, h=1.6, W=12mm

6.3.1.3. Leaky region and the main beam direction

Once the dispersion characteristics for the first higher order mode are calculated and plotted, the leaky region where the structure radiates substantially, is isolated. The simple principle is to make the propagating wave fast in nature with its phase velocity greater than that of speed of light in free space. This is readily calculated as the region where β/k_0 <1. This region is shaded in green in Fig. 6.3a and Fig. 6.3b for the two cases considered in the last sections.

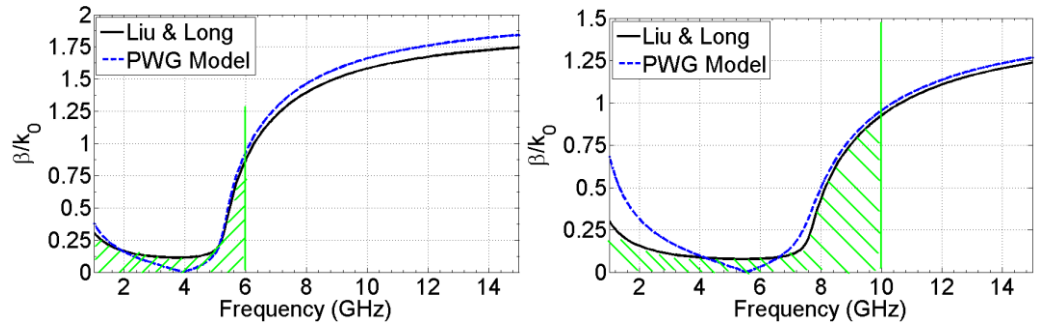

Fig. 6.3: Leaky region shaded in green for microstrip line with (a) ε_r =2.2, h= 0.762, W=12mm and (b) ε_r =4, h=1.6, W=12mm

However, on meticulous observation, it has been found that the leaky region is in actuality just below the surface wave dispersion characteristics. As the dispersion characteristic of any higher order mode crosses the characteristic of the first

higher order surface wave mode in the structure (TM_1^z in thin microstrip geometries), it tend to become leaky by nature. This is primarily because of the introduction of a branch cut singularity that contributes to the total radiation just below that frequency.

Once the radiation zone is established from the dispersion characteristics, the direction of main beam can easily be estimated using the very standard relationship valid for any travelling wave type structures [5]:

$$\theta_{\max} = \sin^{-1}\left(\frac{\beta}{k_0}\right) \tag{6.9}$$

6.3.1.4. Equivalent Transmission Line Model for Calculation of Terminal Properties

Both the techniques discussed above yields the propagation constant and attenuation constant of the higher order mode propagating in the microstrip line. To calculate the input reflection co-efficient of a microstrip line supporting such a mode and terminated in matched impedance, an equivalent transmission line model is presented in this section.

First the wave impedance of the TE mode is calculated using the standard relationship [9]

$$Z_{TE_{01}} = 377\frac{k_0}{\beta} \tag{6.10}$$

The characteristic impedance of the line to be used in the transmission line model is calculated using:

$$Z_0 = Z_{TE_{01}}\frac{h}{W_e} \tag{6.11}$$

Now, with β defined in (6.1) or (6.5) and Z_0 defined in (6.10), ABCD matrix for the microstrip line in the first higher order mode is given by

$$[\mathrm{T}] = \begin{bmatrix} \cosh(\gamma L) & Z_0 \sinh(\gamma L) \\ (1/\mathrm{Z}_0)\sinh(\gamma L) & \cosh(\gamma L) \end{bmatrix} \tag{6.12}$$

Input impedance and the input reflection co-efficient are calculated from this ABCD matrix after considering the structure to be terminated in a load impedance of Z_l which in most cases is either a matched termination for the system impedance of 50Ω. This model is applied in the sections to follow.

6.3.2 EXCITATION OF THE TE_{01} MODE AND ITS PROPERTIES

In this section, a microstrip line harboring the leaky first higher order mode is designed and its terminal as well as radiation characteristics are observed. Exploiting the transversal odd symmetry of the first higher order mode, a half width microstrip line [10] is considered by placing shorting posts along the longitudinal axis of the microstrip line. One edge of the line is shorted to the ground plane using vertical shorting posts. This in turn, eliminates the fundamental Quasi TEM mode and excites the first higher order mode alone.

A half width microstrip leaky wave antenna is designed on Arlon Ad430 substrate with permittivity 4.3 and substrate thickness of 0.762 mm (loss tangent 0.003). Line width (W) is kept at 6.5 mm. This is supposed to place the first higher order mode of the microstrip line near 6 GHz. However, minor deviation is expected because of the insertion of cylindrical metallic shorting posts for shorting. The geometry simulated in CST Microwave Studio is the one shown in Fig. 6.1a with L=50mm, W = 6.5 mm, along with the co-ordinate system and dimensions. Length of the line (L) is kept fixed at 50 mm. The line is terminated in 50 Ω impedance.

To obtain optimum matching, feed position of the coaxial probe feeding is parametrically optimized. It is observed that having a feed position (Y_f in Fig. 6.1a) of about 3.1 mm yields an optimal impedance bandwidth. Corresponding S_{11} is shown in Fig. 6.4. The same figure also shows the S_{11} for lines with different widths.

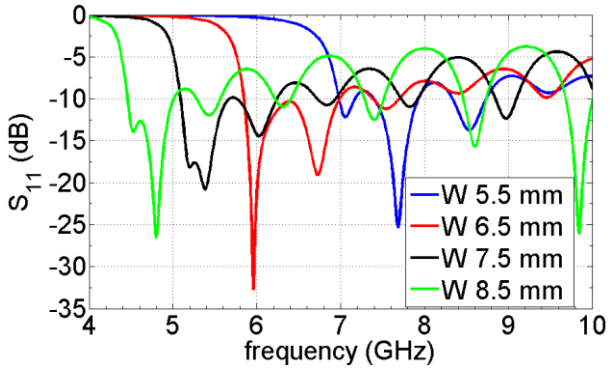

Fig. 6.4: S_{11} vs. frequency for different line widths

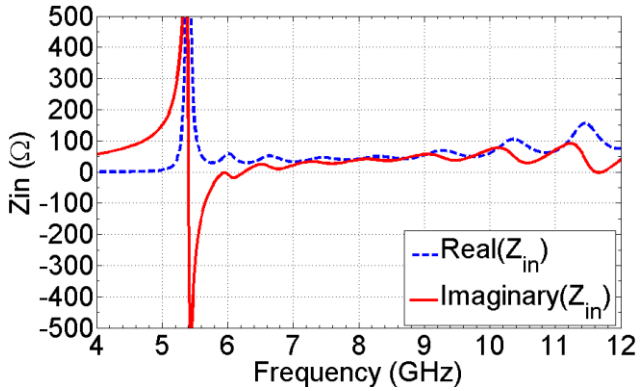

Fig. 6.5: Input impedance vs. frequency for line width of 6.5 mm.

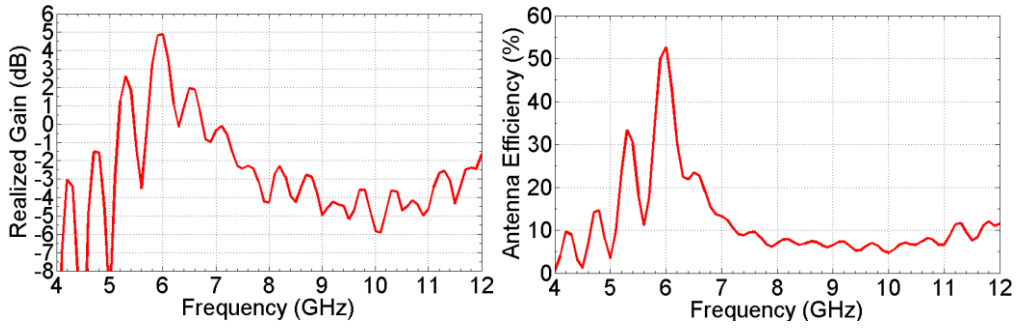

(a) (b)

Fig. 6.6: Variation of (a) realized gain and (b) antenna efficiency with frequency.

We have proceeded with the rest of the section considering the line width as 6.5 mm. Nature of input impedance is shown in Fig. 6.5 where a clear resonance can be observed just below 5.5 GHz. Simulated realized gain and antenna efficiency shown in Fig. 6.6 indicate that the structure radiates substantial amount of power at the onset of the first higher order mode.

Plot of internal electric field inside the microstrip line at 6 GHz is shown in Fig. 6.7. The occurrence of the first higher order mode along the cross-section of the line is evident.

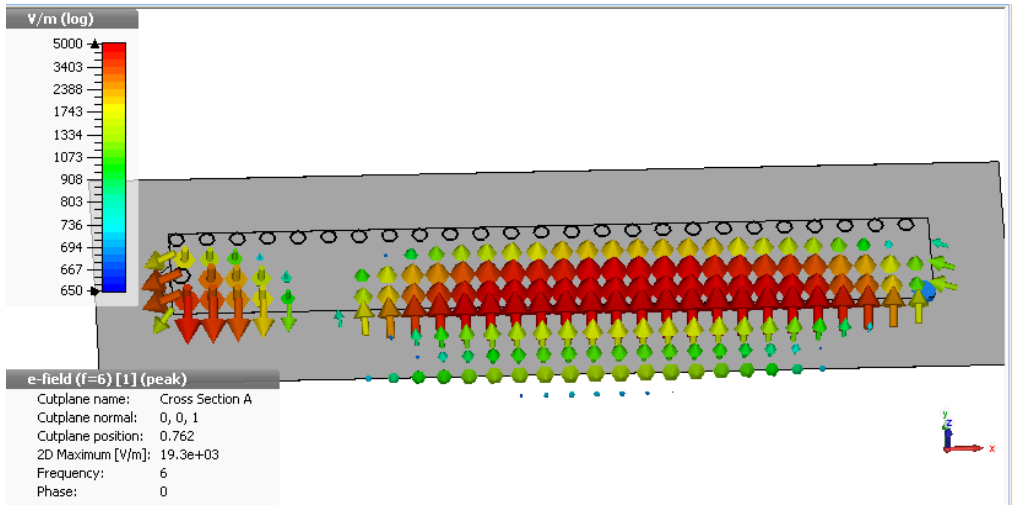

Fig. 6.7: Internal electric field inside the structure at 6 GHz.

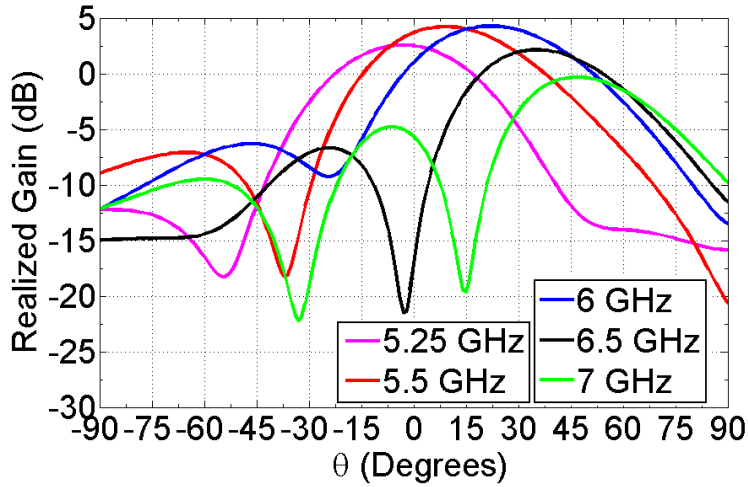

Fig. 6.8: Radiated far field in the x-z plane at 5.25 GHz, 5.5 GHz, 6 GHz, 6.5 GHz and 7 GHz.

Realized gain for the structure over a frequency range of 5.25 GHz to 7 GHz is shown in Fig. 6.8. It clearly indicates that the beam scanning with frequency. Main lobe direction, maximum realized gain and antenna efficiency with frequency are tabulated in Table I.

Table 6.1: Radiation Characteristics at Different Frequencies

Frequency (GHz)	Direction of Main Lobe (^{0})	Maximum realized gain (dB)	Antenna efficiency (%)
5.25	-3	2.57	31
5.5	9	4.23	47
5.75	13	0.32	32
6	22	4.27	47
6.25	30	2	28
6.5	35	2.14	23
6.75	43	0.86	17
7	47	-0.3	13
7.25	52	-1.3	11

Effects of number of shorting posts used for suppressing the fundamental as well as higher order even modes have been extensively studied by Liu *et.al.* [6] However, the use of such shorting posts along the edge is always subject to fabrication difficulty. Instead a solid shorting wall using a copper tape can be used. This scheme is shown in Fig. 6.9.

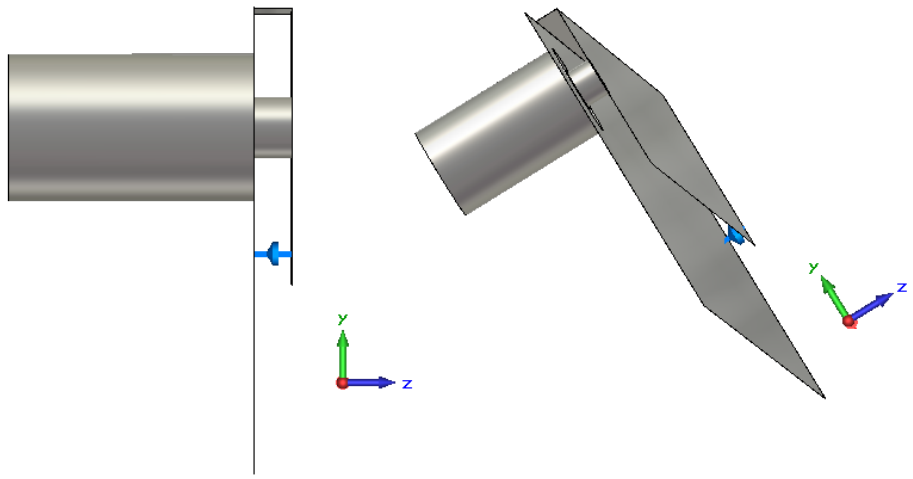

Fig. 6.9: Side view and the perspective view for the geometry with continuous edge shorting

As expected, in the case of continuous shorting shown in Fig. 6.9, the line width for similar band of operation is slightly different. The optimal line width is found to be 5.625 mm with the continuous shorting. Simulated input reflection co-efficient, gain and efficiencies for the solid edge shorting are shown in Fig. 6.10 and 6.11 respectively. Radiation patterns in the two principal planes at the three frequencies mentioned are also compared and plotted in Fig. 6.12. It is noted that except for slight reduction in the realized gain, there are no substantial alterations in terms of antenna performance.

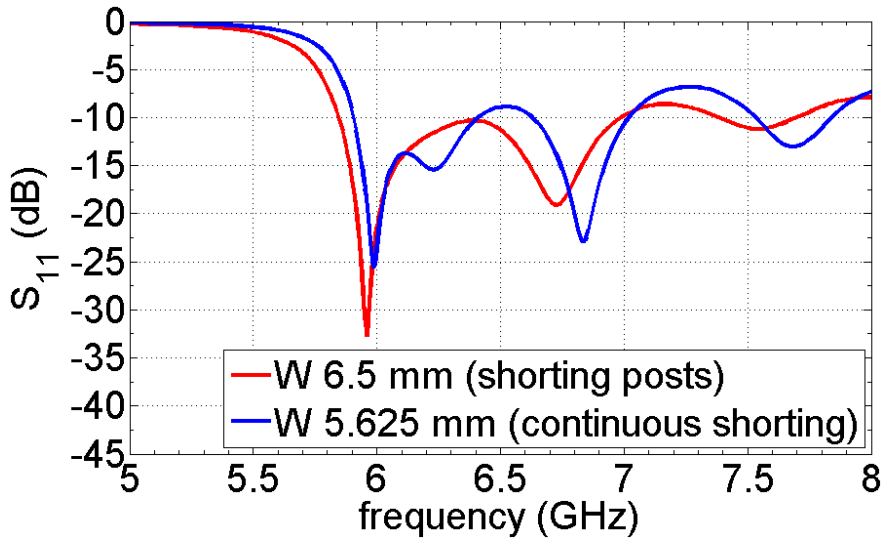

Fig. 6.10: S_{11} vs. frequency plot for the half width microstrip leaky wave antenna with shorting posts and continuous shorting.

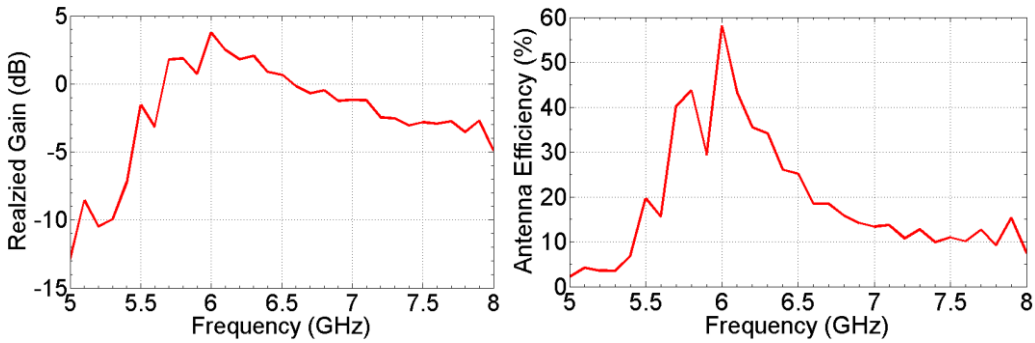

(a) (b)

Fig. 6.11: Variation of (a) realized gain and (b) antenna efficiency with frequency.

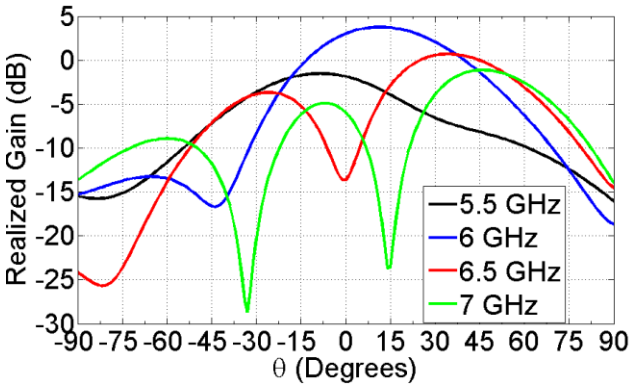

Fig. 6.12: Radiated far field in the x-z plane for the continuous edge shorting case at (a) 5.5 GHz, (b) 6 GHz, (c) 6.5 GHz and (d) 7 GHz.

6.4 PERIODIC LEAKY WAVE ANTENNAS

In case of a periodically loaded microstrip line antenna, some of the higher order Floquet modes tend to enter a fast wave zone thereby contributing to total radiation substantially. The basic analysis technique along with the identification and properties of the leaky higher order Floquet modes are discussed in the section to follow in the context of a microstrip line loaded periodically with an open stub and two notches from the edge on either side of the stub.

6.4.1 CALCULATION OF DISPERSION CHARACTERISTICS WITH THE LEAKY REGION

The stub and notch loaded microstrip line antenna taken for analysis is shown in Fig.6.1b. Model of the effective load is shown in Fig. 6.13 where the notches are modeled as series inductance (L_n) and the stub is modeled as a shunt capacitor of capacitance C_s .

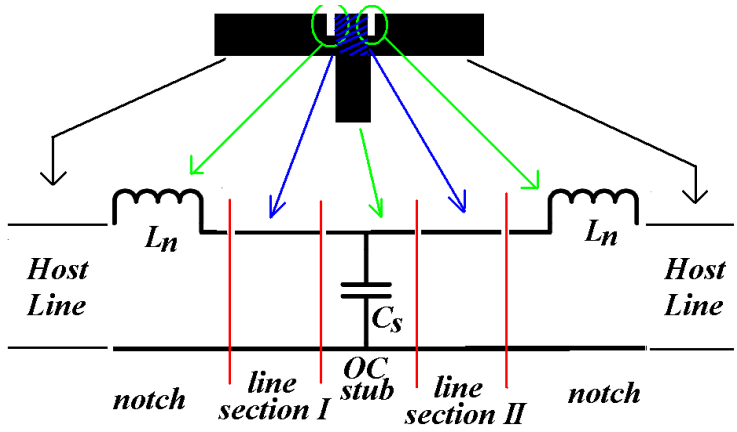

Fig. 6.13: Equivalent model of the periodic load.

L_n and C_s are given by

$$L_n = 2h\left(1-\frac{Z_0\sqrt{\varepsilon_{re}}}{Z'_0\sqrt{\varepsilon'_{re}}}\right)^2 \quad nH \tag{6.13}$$

$$C_s = \frac{\tanh(\gamma L_s)}{j\omega Z_0}\, pF \tag{6.14}$$

where ε_{re} and ε'_{re} are the effective dielectric constants for microstrip lines with widths W and W-W_n respectively and Z_0 and Z'_0 are the corresponding characteristic impedances. In (6.14), Z_0, L_s and γ are respectively the characteristic impedance, length and the complex propagation constant of the stub.

With the series inductance and the shunt capacitances defined in (6.13) and (6.14), the ABCD matrix for the effective load of the host microstrip line is calculated by cascading the series inductor, small line section of length $W_s/2$, the stub admittance, another line of length $W_s/2$ and the series inductor again. This leads to

$$ABCD_{disc} = \begin{bmatrix} 1 & j\omega L_n \\ 0 & 1 \end{bmatrix} \begin{bmatrix} \cosh\left(\gamma_1 \frac{W_s}{2}\right) & Z_{01}\sinh\left(\gamma_1 \frac{W_s}{2}\right) \\ \left(\frac{1}{Z_{01}}\right)\sinh\left(\gamma_1 \frac{W_s}{2}\right) & \cosh\left(\gamma_1 \frac{W_s}{2}\right) \end{bmatrix} \begin{bmatrix} 1 & 0 \\ j\omega C_s & 1 \end{bmatrix} \times \begin{bmatrix} \cosh\left(\gamma_1 \frac{W_s}{2}\right) & Z_{01}\sinh\left(\gamma_1 \frac{W_s}{2}\right) \\ \left(\frac{1}{Z_{01}}\right)\sinh\left(\gamma_1 \frac{W_s}{2}\right) & \cosh\left(\gamma_1 \frac{W_s}{2}\right) \end{bmatrix} \begin{bmatrix} 1 & j\omega L_n \\ 0 & 1 \end{bmatrix} \quad (6.15)$$

Here ω is the angular frequency while $\gamma_1$is the complex propagation constant of the unloaded line.

ABCD matrix for the unit cell can now be expressed as

$$ABCD_f = \begin{bmatrix} A_f & B_f \\ C_f & D_f \end{bmatrix} = ABCD_L \times ABCD_{disc} \times ABCD_L \quad (6.16)$$

Here $ABCD_L$ is the ABCD matrix for the line sections 1 and 2, while subscripts 'disc' and 'f' are indicative of ABCD matrices for the discontinuity and final unit cell respectively. After utilizing the periodicity property and reciprocity condition for the unit cell matrix [20], we arrive at the following equation,

$$\cosh\left(\gamma_m l_u\right) = \frac{A_f + D_f}{2} \quad (6.17)$$

Here, γ_m is the complex propagation constant for the periodic structure. γ_m can be written as $\gamma_m = \alpha_m + j\beta_m$,where α_m and β_m respectively the attenuation constant and the phase constant of the periodic line. From (6.17) α_m and β_m are calculated as

$$\alpha_m = \text{Real}\left[\frac{1}{l_u}\cosh^{-1}\left(\frac{A_f + D_f}{2}\right)\right] \quad (6.18)$$

$$\beta_m = \text{Imaginary}\left[\frac{1}{l_u}\cosh^{-1}\left(\frac{A_f + D_f}{2}\right)\right] \quad (6.19)$$

Bloch Impedance (Z_B) for the periodic structure is calculated from the following equation

$$Z_B^{\pm} = \frac{\pm B_f}{\sqrt{A_f^2 - 1}} \tag{6.20}$$

Since the unit cell under consideration is symmetric by nature, $|Z_B^+| = |Z_B^-| = |Z_B|$.

To find the input reflection co-efficient of the structure, the geometry is modeled as a microstrip line with propagation constant γ_m, characteristic impedance Z_B and total line length of Nl_u where N is the number of unit cells.

To validate the model presented above, geometry with the following specifications is simulated using both MATLAB and MoM based full wave simulator Zeland IE3D. Arlon AD430 substrate with permittivity 4.3 and substrate thickness of 0.762 mm is used.

The simulated geometry as seen in Fig. 6.1b, has dimensions of: W_0 = 2.5 mm, L_u = 25 mm, L_s = 3.18 mm, W_s = 1.65 mm, W_n = 0.7 mm and d_n = 2 mm. Five unit cells are cascaded to form the antenna structure. Port 1 is excited with a 1V voltage source with 50 ohm internal impedance and port 2 is terminated in 50 ohm impedance. Calculated and simulated S_{11} vs. frequency are plotted in Fig. 6.14.

The phase constant within the principal value range (0 to π/l_u) and attenuation constant for the line is shown in Fig. 6.15. Two distinct stop band around 3 GHz and 8.5 GHz are visible.

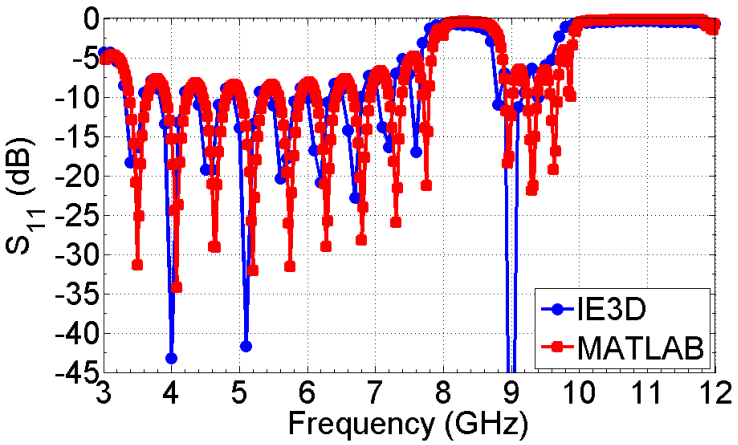

Fig. 6.14: S_{11} vs. frequency for the notch and stub loaded microstrip line with five unit cells

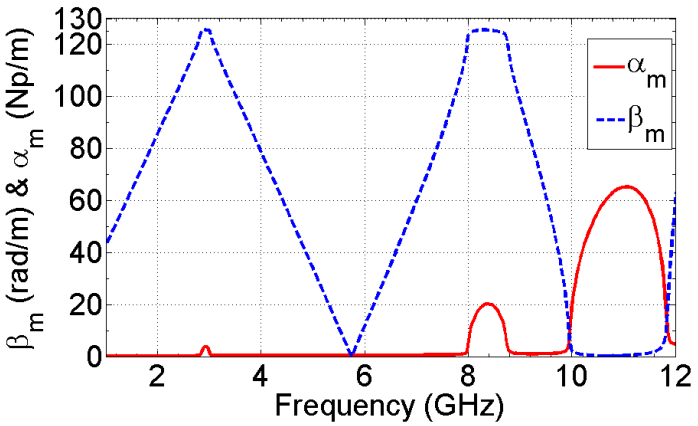

Fig. 6.15: Phase constant and attenuation constant for the notch and stub loaded microstrip line

6.4.2 LEAKY FLOQUET MODES AND THEIR CHARACTERITICS

Complete dispersion characteristics along with all the higher order Floquet modes for the notch and stub loaded microstrip line are shown in Fig. 6.16. This is calculated by simply shifting the principle value solution of (6.17) using the following relation:

$$\beta = \pm\beta_0 + \frac{2n\pi}{l_u}; \quad n = 0, \pm 1, \pm 2 \qquad (6.18)$$

The leaky fast wave region is shaded in green in Fig. 6.16. It can be observed that the n= -1 mode with positive group velocity i.e. the n= -1^{+} mode enters the leaky region near 4 GHz (region shaded in green). Consequently, this mode starts radiating beyond this frequency. As the frequency increase, the phase velocity for this radiating Floquet mode increases monotonically up to the next stop band. This is reflected in the radiation pattern in terms of main beam scanning with frequency. Simulated radiated far fields in the x-z plane in the frequency range 4 GHz to 7.5 GHz plotted in Fig. 6.17a clearly show the main beam scanning with frequency.

Reverting back to the dispersion characteristics of Fig. 6.16 once again, we can observe that near the frequency of 7.8 GHz (region shaded in magenta), there is another Floquet mode apart from the n= -1^{+}, that enter the leaky region. It is the n= -2^{+} mode. This gives rise to an interesting property in the radiation characteristics. The two radiating leaky modes lead to the existence of two distinct main lobes in the radiation pattern and with increasing frequency both of these lobes tend to shift. Simulated radiation patterns at four different frequencies (8 GHz, 8.5 GHz, 9 GHz and 9.5 GHz) near in the x-z plane shown in Fig. 6.17b indicate this property clearly.

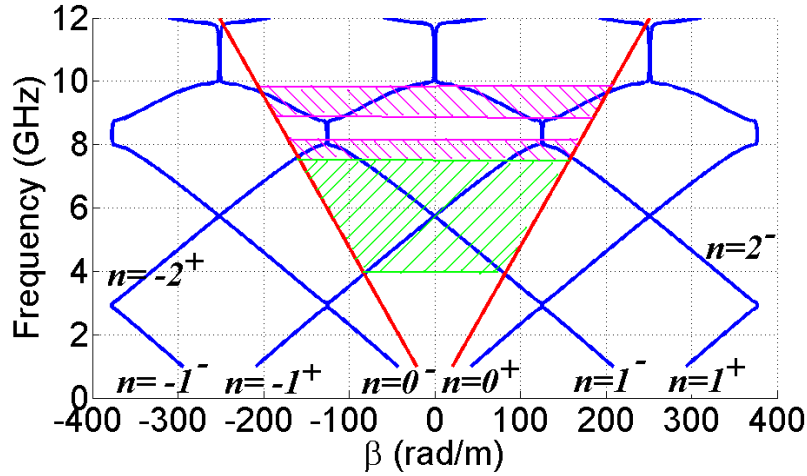

Fig. 6.16: Dispersion characteristics showing higher order Floquet modes and indicating the leaky region in shading for the notch and stub loaded microstrip line.

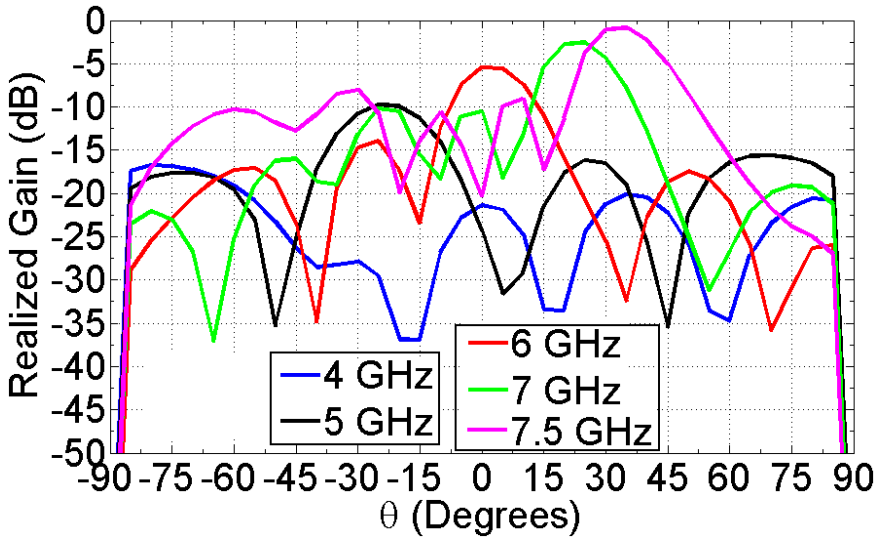

(a)

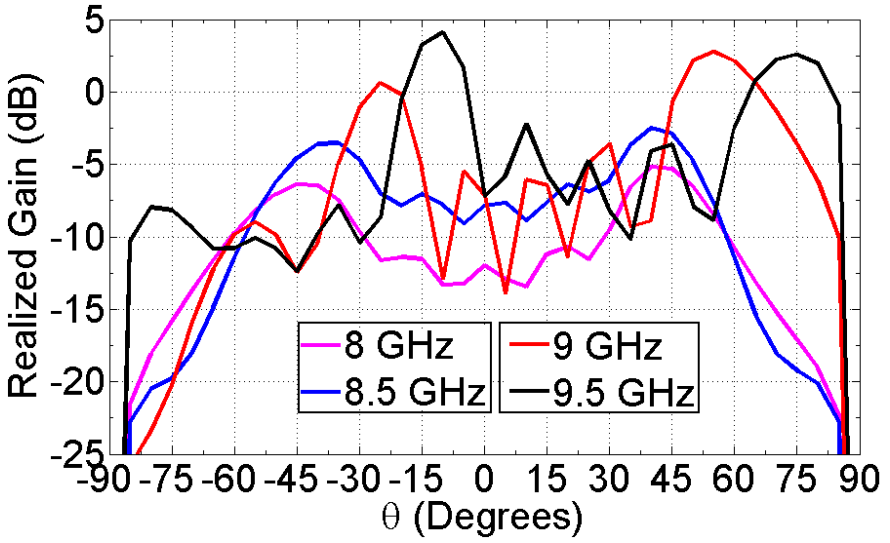

(b)

Fig. 6.17: Radiated far field for the notch and stub loaded microstrip line with five unit cells in the x-z plane for (a) 4 GHz to 7.5 GHz and (b) 8 GHz to 9.5 GHz

6.5 CONCLUSION

Standard techniques based on planar waveguide model are explored for calculating the dispersion characteristics as well as terminal properties of a microstrip line supporting higher order modes. Comparison with closed form

expression for the 1st higher order mode shows the effectiveness of the model. A half width microstrip leaky wave antenna is designed and performance of the antenna using cylindrical metallic posts and continuous shorting wall are compared. A periodic leaky wave antenna using a combination of stub and two notches as load is considered next. Dispersion characteristics are evaluated and the leaky region is observed. Beam scanning with frequency is observed in both the cases. Techniques presented in this chapter is to be used in chapters 7 and 8 in the context of periodic leaky wave antennas perturbing the fundamental Quasi TEM and the first higher order mode as well.

REFERENCES:

[1] W. Menzel, "A New Travelling Wave Antenna in Microstrip," *1978 8th European Microwave Conference*, Paris, France, 1978, pp. 302-306.

[2] D. Xie, L. Zhu and X. Zhang, "An EH_0-Mode Microstrip Leaky-Wave Antenna With Periodical Loading of Shorting Pins," in *IEEE Transactions on Antennas and Propagation*, vol. 65, no. 7, pp. 3419-3426, July 2017.

[3] D. Xie, L. Zhu, X. Zhang and N. Liu, "Gain-enhanced EH_1 mode microstrip leaky-wave antenna with periodical loading of shorting pins," in *IET Microwaves, Antennas & Propagation*, vol. 12, no. 2, pp. 230-236, 7 2 2018.

[4] A. A. Oliner and R. C. Johnson, Leaky-wave antennas, antenna engineering handbook. 1993.

[5] A. A. Oliner, "Radiating periodic structure: analysis in terms of k vs. β diagrams", in *Short Course on Microwave Field and Network Techniques*, Polytechnic Institute of Brooklyn, New York, 1963

[6] J. Liu and Y. Long, "Formulas for complex propagation constant of first higher mode of microstrip line," in *Electronics Letters*, vol. 44, no. 4, pp. 261-262, 14 February 2008.

[7] G. Kompa and R. Mehran, "Planar waveguide model for calculating microstrip components," in *Electronics Letters*, vol. 11, no. 19, pp. 459-460, 18 September 1975.

[8] A. B. Constantine, Antenna theory: analysis and design. *MICROSTRIP ANTENNAS, third edition, John Wiley & sons*. 2005.

[9] R. E. Collin, Foundations for Microwave Engineering, 2nd ed. NewYork: McGraw-Hill, 1992, ch. 8.

[10] G. M. Zelinski, G. A. Thiele, M. L. Hastriter, M. J. Havrilla, and A. J. Terzuoli, "Half width leaky wave antennas," *IET Microwaves, Antennas & Propagation*, *1*(2), pp.341-348, 2007.

[11] Zeland IE3D v10.

[12] CST Microwave Studio. CST corp. 2017

Chapter 7

Higher Order Floquet Modes in Periodic Microstrip Lines: Analysis

Contents

7.1 INTRODUCTION

Microstrip lines periodically loaded with perturbations of lumped (inductors/capacitors) or distributed (stubs/notches/slots) nature have been analyzed traditionally using an ABCD matrix technique [1]. This technique, while being quite simple in nature, can be applied only in cases where the line supports a Quasi TEM mode and the periodic loading can be approximated by some circuit model or equivalent networks [2]. The cascaded ABCD matrix model can forcibly be applied to line supporting higher order modes only if the propagation constant and the Bloch characteristic impedances are known beforehand. This in turn involves rigorous full wave analysis [3]. With the advent of microstrip leaky wave antennas [4] it has been necessitated to evaluate the dispersion characteristics of periodically loaded microstrip lines when a higher order mode instead of the fundamental Quasi TEM mode is perturbed [5]. Our work in this chapter concerns with this particular problem.

The chapter starts with brief description of the problem and the geometry types considered. Microstrip lines supporting the fundamental and higher order modes and loaded with open and shorted stubs are analyzed first for their dispersion characteristics. Next, loaded SIW type lines are considered where both the edges along the length of the line are shorted to the ground using cylindrical shorting posts. Finally conclusions are drawn after presenting data from practical measurement.

7.2 PROBLEM FORMULATION

Geometry types for analysis considered in this work is primarily stub loaded microstrip lines. Four categories of the unit cell geometries are considered. Simple microstrip line geometry with open or shorted stub loading (shown in Fig. 7.1a) is considered first. This geometry is supposed to support both the fundamental Quasi TEM mode and higher order modes (TE_{01}^{x}, TE_{02}^{x}) and their corresponding spatial harmonics. Next, an edge shorted half width microstrip line shown in Fig. 7.1b is taken up to excite selectively the first higher order mode alone. A Substrate Integrated Waveguide (SIW) type microstrip line with both

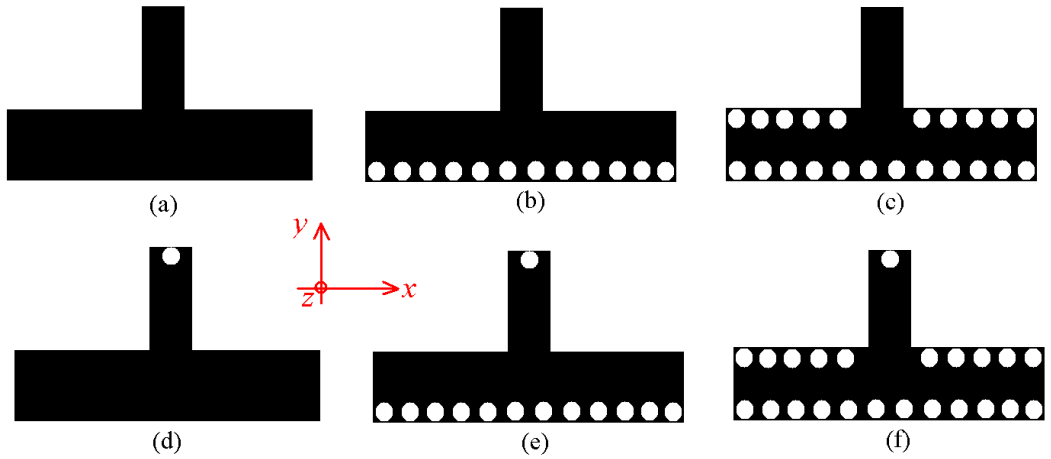

Fig. 7.1: Geometry types considered in this chapter with open stub loaded (a) microstrip line, (b) half width microstrip line, (c) SIW type line, shorted stub loaded (d) microstrip line, (e) half width microstrip line, (f) SIW type line

edges shorted shown in Fig. 7.1c is considered next. Loading of this geometry with open or shorted stubs introduces spatial harmonics as expected. Unit cell length, the host line width, stub length and width in all the subsequent analysis are taken in general as L_u, W_l, L_s and W_s respectively while the substrate permittivity and the thickness are taken as ε_r and h respectively.

7.3 ANALYSIS OF NON-SIW TYPE GEOMETRIES

The unit cell geometry for the stub loaded microstrip line is first divided in two regions as shown in Fig. 7.2. The cylindrical posts shown in Fig. 7.2 are considered approximately as a continuous shorting edge. This approximation is valid when the number of shorting posts is large and the inter-post gap is quite small with respect to the guided wavelength of the structure. As a rule of thumb we have taken an inter-post gap of 1.5 mm which is almost $0.08\lambda_g$ at 8GHz.

Electric field inside the two regions (namely region I and region II) is expressed in Fourier series representation. After imposition of boundary conditions pertaining to the magnetic walls and continuity of tangential electric and magnetic fields, mode matching procedure is applied to calculate the dispersion characteristics of the unit cell geometry. These steps are elaborated next.

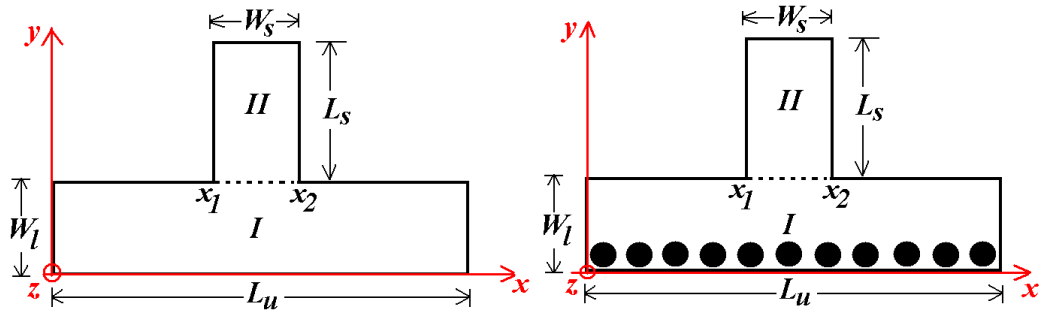

Fig. 7.2: Unit cell geometry with dimensions and symbols for (a) open stub loaded microstrip line and (b) open stub loaded half width microstrip line with suppresses even modes.

7.3.1 PREPROCESSING AND FIELD REPRESENTATION

Electric field in region I (E_z^I) is first expressed as a modal summation of different Floquet modes with non zero transverse variation as

$$E_z^I = \sum_{m=-\infty}^{\infty} A_m \cos\left\{\beta_{ym}^{(l)} y - \delta_0\right\} e^{-\gamma_m x} \tag{7.1}$$

This representation of E_z^I is general for both cases shown in Fig. 7.2a and Fig. 7.2b. Depending on whether there is a magnetic wall or an electric wall at y=0, δ_0 in (7.1) is chosen as either 0 or π/2 respectively. δ_0 essentially identifies the nature of the boundary at *y*=0 and in turn makes the analysis generalized for both a full width and half width microstrip line.

It should be noted that the transversal wave number ($\beta_{ym}^{(l)}$) is not solely dependent on the transverse dimension (as is custom in microstrip cavity type problems where the wave number takes the form: $m\pi / W_l$ with W_1 being the length of the cavity along the concerned dimension). This is because of the existence of the stub on one side of the line which makes such discrete mode matching difficult [6]. Keeping the phase constant unknown allows the provisions for mode matching.

In (7.1) A_m are the unknown modal coefficients to be calculated from the mode matching procedure and $\beta_{ym}^{(l)}$, γ_m are respectively the phase constant and the complex propagation constants along '*y*' and '*x*' direction inside the line for the m^{th} Floquet mode. These are given by the following relations

$$\gamma_m = \gamma_0 + j\frac{2m\pi}{L_u};\ \gamma_0 = \alpha_0 + j\beta_0 \tag{7.2}$$

$$\beta_{ym}^{(l)} = \sqrt{k_l^2 + \gamma_m^2}\ ;\ k_l = k_0\sqrt{\varepsilon_{eff\_l}} \tag{7.3}$$

where γ_0 is the propagation constant for the spatial harmonic corresponding to m=0 i.e. the fundamental Floquet mode, k_l is the phase constant inside the substrate region underneath the host line.

On the other hand, electric field inside the region II (E_z^{II}) is expressed as a modal summation of normal microstrip cavity modes as

$$E_z^{II} = \sum_{n=0}^{\infty} \cos\left\{\beta_{xn}^{(s)}(\mathrm{x}-\mathrm{x}_1)\right\}\left[B_n e^{-j\beta_{yn}^{(s)}(\mathrm{y}-\mathrm{W}_l)} + C_n e^{j\beta_{yn}^{(s)}(\mathrm{y}-\mathrm{W}_l)} \right] \tag{7.4}$$

Here $\beta_{xn}^{(s)}$ and $\beta_{yn}^{(s)}$ are respectively the phase constants along the 'x' and 'y' directions inside the stub region (region II) and are given by

$$\beta_{xn}^{(s)} = \frac{n\pi}{W_s} \tag{7.5}$$

$$\beta_{yn}^{(s)} = \sqrt{k_s^2 - \beta_{xn}^{(s)2}} \; ; k_s = k_0\sqrt{\varepsilon_{eff\_s}} \tag{7.6}$$

B_n and C_n are the unknown modal excitation coefficients to be solved.

Corresponding magnetic fields inside the regions I and II are calculated from (7.1) and (7.4) using Maxwell's equation in the following manner

$$\vec{H} = \frac{j}{\omega\mu}\begin{vmatrix} \hat{x} & \hat{y} & \hat{z} \\ \frac{\partial}{\partial x} & \frac{\partial}{\partial y} & 0 \\ 0 & 0 & E_z \end{vmatrix} = \frac{j}{\omega\mu}\left\{ \hat{x}\frac{\partial E_z}{\partial y} - \hat{y}\frac{\partial E_z}{\partial x} \right\} \tag{7.7}$$

Consequently, the 'x' and 'y' directed magnetic fields in the two regions (H_x^I, H_y^I, H_x^{II} and H_y^{II}) are calculated using (7.1), (7.4) and (7.7). These are calculated as follows

$$H_x^I = \frac{j}{\omega\mu}\frac{\partial E_z}{\partial y} = -\frac{j}{\omega\mu}\sum_{m=-\infty}^{\infty} \beta_{ym}^{(l)} A_m \sin\left\{\beta_{ym}^{(l)} y - \delta_0\right\} e^{-\gamma_m x} \tag{7.8}$$

$$H_y^I = -\frac{j}{\omega\mu}\frac{\partial E_z}{\partial x} = \frac{j}{\omega\mu}\sum_{m=-\infty}^{\infty} \gamma_m A_m \cos\left\{\beta_{ym}^{(l)} y - \delta_0\right\} e^{-\gamma_m x} \tag{7.9}$$

$$H_x^{II} = -\frac{j}{\omega\mu}\sum_{n=0}^{\infty} j\beta_{yn}^{(s)} \cos\left\{\beta_{xn}^{(s)}(\mathrm{x}-\mathrm{x}_1)\right\}\left[\begin{matrix} B_n e^{-j\beta_{yn}^{(s)}(\mathrm{y}-\mathrm{W}_l)} - \\ C_n e^{j\beta_{yn}^{(s)}(\mathrm{y}-\mathrm{W}_l)} \end{matrix}\right] \tag{7.10}$$

$$H_y^{II} = \frac{j}{\omega\mu}\sum_{n=0}^{\infty} \beta_{xn}^{(s)} \sin\left\{\beta_{xn}^{(s)}(\mathrm{x}-\mathrm{x}_1)\right\}\left[\begin{matrix} B_n e^{-j\beta_{yn}^{(s)}(\mathrm{y}-\mathrm{W}_l)} + \\ C_n e^{j\beta_{yn}^{(s)}(\mathrm{y}-\mathrm{W}_l)} \end{matrix}\right] \tag{7.11}$$

7.3.2 MODE MATCHING PROCEDURE

Electric and magnetic fields in the two regions expressed in the last section are now subjected to appropriate boundary conditions at the geometry interfaces. As indicated before, a cavity model type formulation is used presently. These boundary conditions are discussed next.

1. Using the magnetic or electric wall approximation at the far end of the stub (*i.e.* at $y=W_l+L_s$)

   (a) $H_x^{II} = 0$ for $x_1 \le x \le x2,\ y = W_l + L_s$ for an open circuited stub (7.12)

   (b) $E_z^{II} = 0$ for $x_1 \le x \le x_2,\ y = W_l + L_s$ for a short circuited stub (7.13)

2. Using the continuity of tangential electric field (E_z) at the interface between the stub and the host line,

   $$E_z^I = E_z^{II} \text{ for } x_1 \le x \le x_2,\ y = W_l \tag{7.14}$$

3. Using the magnetic wall at $y=W_l$, and continuity of the tangential magnetic field (H_x) at the stub-line interface,

   $$H_x^I = \begin{cases} 0 & \text{for } x < x_1 \ \&\ x > x_2, y = W_l \\ H_x^{II} & \text{for } x_1 \le x \le x_2,\ y = W_l \end{cases} \tag{7.15}$$

These boundary conditions are now applied to the electric and magnetic fields expressed in (7.1), (7.4) and (7.8)-(7.11). These are elaborated below:

1. (a) $H_x^{II} = 0$ for $x_1 \le x \le x_2$, $y = W_l + L_s$ for an open circuited stub

After putting H_x^{II} from (7.9) we obtain

$$\sum_{n=0}^{\infty} j\beta_{yn}^{(s)} \cos\left\{\beta_{xn}^{(s)}(\mathrm{x}-\mathrm{x}_1)\right\}\left[B_n e^{-j\beta_{yn}^{(s)}L_s} - C_n e^{j\beta_{yn}^{(s)}L_s} \right] = 0 \qquad (7.16)$$

Multiplying both sides by $\cos\left\{\beta_{xp}^{(s)}(\mathrm{x}-\mathrm{x}_1)\right\}$ and integrating in (x_1, x_2) we obtain,

$$\sum_{n=0}^{\infty} j\beta_{yn}^{(s)}\left[B_n e^{-j\beta_{yn}^{(s)}L_s} - C_n e^{j\beta_{yn}^{(s)}L_s} \right]\int_{x_1}^{x_2} \cos\left\{\beta_{xn}^{(s)}(\mathrm{x}-\mathrm{x}_1)\right\}\cos\left\{\beta_{xp}^{(s)}(\mathrm{x}-\mathrm{x}_1)\right\} dx = 0 \qquad (7.17)$$

After using the following orthogonality relationship,

$$\int_{x_1}^{x_2} \cos\left\{\beta_{xn}^{(s)}(\mathrm{x}-\mathrm{x}_1)\right\}\cos\left\{\beta_{xp}^{(s)}(\mathrm{x}-\mathrm{x}_1)\right\} dx = \begin{cases} 0 \text{ for } n \neq p \\ \dfrac{W_s}{2} \text{ for } n = p \neq 0 \\ W_s \text{ for } n = p = 0 \end{cases} \qquad (7.18)$$

We obtain the following set of equations

$$\beta_{yp}^{(s)}\left[B_p e^{-j\beta_{yp}^{(s)}L_s} - C_n e^{j\beta_{yp}^{(s)}L_s} \right] = 0 \text{ for p=0,1,...}\infty \qquad (7.19)$$

which is readily reduced to the following form

$$C_p = B_p e^{-2j\beta_{yp}^{(s)}L_s} \text{ for p=0,1,...}\infty \qquad (7.20)$$

1. (b) $E_z^{II} = 0$ for $x_1 \le x \le x_2$, $y = W_l + L_s$ for a short circuited stub

After putting E_z^{II} from (7.4) we obtain

$$\sum_{n=0}^{\infty} \cos\left\{\beta_{xn}^{(s)}(\mathrm{x}-\mathrm{x}_1)\right\}\left[B_n e^{-j\beta_{yn}^{(s)}(\mathrm{y}-\mathrm{W}_l)} + C_n e^{j\beta_{yn}^{(s)}(\mathrm{y}-\mathrm{W}_l)}\right] = 0 \qquad (7.21)$$

Multiplying both sides by $\cos\left\{\beta_{xp}^{(s)}(\mathrm{x}-\mathrm{x}_1)\right\}$ and integrating in (x_1, x_2) we obtain,

$$\sum_{n=0}^{\infty}\left[B_n e^{-j\beta_{yn}^{(s)}L_s} + C_n e^{j\beta_{yn}^{(s)}L_s}\right]\int_{x_1}^{x_2} \cos\left\{\beta_{xn}^{(s)}(\mathrm{x}-\mathrm{x}_1)\right\}\cos\left\{\beta_{xp}^{(s)}(\mathrm{x}-\mathrm{x}_1)\right\}dx = 0 \qquad (7.22)$$

After using the orthogonality relationship expressed in (7.18), we obtain the following set of equations

$$\left[B_p e^{-j\beta_{yp}^{(s)}L_s} + C_n e^{j\beta_{yp}^{(s)}L_s}\right] = 0 \text{ for p=0,1,...}\infty \qquad (7.23)$$

which is readily reduced to the following form

$$C_p = B_p e^{-2j\beta_{yp}^{(s)}L_s} \text{ for p=0,1,...}\infty \qquad (7.24)$$

For brevity, boundary conditions derived in (7.20) and (7.24) are now expressed in a generalized form as

$$C_p = sB_p e^{-2j\beta_{yp}^{(s)}L_s} \text{ for p=0,1,...}\infty \qquad (7.25)$$

where s=1 for open ended stubs and s= -1 for short circuited stubs.

2. $E_z^I = E_z^{II}$ for $x_1 \le x \le x_2$, $y = W_l$

After putting E_z^I and E_z^{II} from (7.1) and (7.4) respectively we obtain

$$\sum_{m=-\infty}^{\infty} A_m \cos\left\{\beta_{ym}^{(l)}W_l - \delta_0\right\}e^{-\gamma_m x} = \sum_{n=0}^{\infty}\cos\left\{\beta_{xn}^{(s)}(\mathrm{x}-\mathrm{x}_1)\right\}\left[B_n + C_n\right] \qquad (7.26)$$

Multiplying both sides by $\cos\left\{\beta_{xp}^{(s)}(\mathrm{x}-\mathrm{x}_1)\right\}$ and integrating in (x_1, x_2) we obtain,

$$\sum_{n=0}^{\infty}\left[B_n+C_n\right]\int_{x_1}^{x_2}\cos\left\{\beta_{xn}^{(s)}(\mathrm{x}-\mathrm{x}_1)\right\}\cos\left\{\beta_{xp}^{(s)}(\mathrm{x}-\mathrm{x}_1)\right\}dx=$$
$$\sum_{m=-\infty}^{\infty}A_m\cos\left\{\beta_{ym}^{(l)}W_l-\delta_0\right\}\int_{x_1}^{x_2}e^{-\gamma_m x}\cos\left\{\beta_{xp}^{(s)}(\mathrm{x}-\mathrm{x}_1)\right\}dx \tag{7.27}$$

Orthogonality condition of (7.18) together with (7.25) reduces the abovementioned relationship to the following form,

$$B_p=\frac{\eta_p}{W_s\left(1+e^{-2j\beta_{yp}^{(s)}L_s}\right)}\sum_{m=-\infty}^{\infty}A_m\cos\left(\beta_{ym}^{l}W_l-\delta_0\right)I_1(p,m)\qquad \text{for p=0,1,...}\infty \tag{7.28}$$

Here

$$I_1(p,m)=\int_{x_1}^{x_2}e^{-\gamma_m x}\cos\left\{\beta_{xp}^{(s)}(\mathrm{x}-\mathrm{x}_1)\right\}dx$$
$$=\left[e^{\left\{\gamma^{+}x_0-j\beta_{xp}^{(s)}x_1\right\}}\frac{\sinh\left(\gamma^{+}\frac{W_s}{2}\right)}{\gamma^{+}}+e^{\left\{\gamma^{-}x_0+j\beta_{xp}^{(s)}x_1\right\}}\frac{\sinh\left(\gamma^{-}\frac{W_s}{2}\right)}{\gamma^{-}}\right] \tag{7.29}$$

where

$$\gamma^{\pm}=-\gamma_m\pm j\beta_{xp}^{(s)},\ x_0=x_1+\frac{W_s}{2}$$

(7.28) is now expressed in following form for brevity,

$$B_p=\sum_{m=-\infty}^{\infty}S_{mp}A_m\ \text{ for p=0,...}\infty \tag{7.30}$$

where

$$S_{mp} = \frac{\eta_p \cos\left(\beta_{ym}^{l} W_l - \delta_0\right) I_1(p,m)}{W_s\left(1+e^{-2j\beta_{yp}^{(s)} L_s}\right)} \tag{7.31}$$

3. $$H_x^I = \begin{cases} 0 & \text{for } x < x_1 \ \& \ x > x_2, y = W_l \\ H_x^{II} & \text{for } x_1 \le x \le x_2,\ y = W_l \end{cases}$$

After putting H_x^I and H_x^{II} from (7.8) and (7.10) respectively, we obtain

$$-\frac{j}{\omega\mu}\sum_{m=-\infty}^{\infty}\beta_{ym}^{(l)} A_m \sin\left\{\beta_{ym}^{(l)} W_l - \delta_0\right\} e^{-\gamma_m x} = X \tag{7.32}$$

where

$$X = \begin{cases} 0 \text{ for } x < x_1 \text{ and } x > x_2 \\ -\frac{j}{\omega\mu}\sum_{n=0}^{\infty} j\beta_{yn}^{(s)} \cos\left\{\beta_{xn}^{(s)}(\mathrm{x}-\mathrm{x}_1)\right\}\left[B_n - C_n\right] \text{ for } x_1 \le x \le x_2 \end{cases} \tag{7.33}$$

Multiplying both sides by $e^{\gamma_p x}$ and integrating in (0, L_u) we obtain

$$\sum_{m=-\infty}^{\infty}\beta_{ym}^{(l)} A_m \sin\left\{\beta_{ym}^{(l)} W_l - \delta_0\right\}\int_0^{L_u} e^{-\gamma_m x} e^{\gamma_p x} dx =$$
$$\sum_{n=0}^{\infty} j\beta_{yn}^{(s)}\left[B_n - C_n\right]\int_{x_1}^{x_2}\cos\left\{\beta_{xn}^{(s)}(\mathrm{x}-\mathrm{x}_1)\right\} e^{\gamma_p x} dx \tag{7.34}$$

After using the following orthogonality condition,

$$\int_0^{L_u} e^{-\gamma_m x} e^{\gamma_p x} dx = \begin{cases} 0 & \text{for } p \ne m \\ L_u & \text{for } p = m \end{cases} \tag{7.35}$$

(7.34) is reduced to the following form

$$\beta_{yp}^{(l)} A_p \sin\left\{\beta_{yp}^{(l)} W_l - \delta_0\right\} L_u = \sum_{n=0}^{\infty} j\beta_{yn}^{(s)}\left[B_n - C_n\right] I_1(n,-p) \quad \text{for } p = 0,1,...\infty$$

(7.36)

Here I_1 is as defined in (7.29). Now, using (7.25) to substitute C_n and subsequently using (7.28) to replace B_n with A_n we obtain after some simplification

$$-L_p A_p + \sum_{m=-\infty}^{\infty} R_{pm} A_m = 0 \text{ for } p = -\infty,...\infty \tag{7.37}$$

Here,

$$L_p = \beta_{yp}^{(l)} \sin\left\{\beta_{yp}^{(l)} W_l - \delta_0\right\} L_u \tag{7.38}$$

$$R_{pm} = \sum_{n=0}^{\infty} Y_{np} S_{mn} \tag{7.39}$$

$$Y_{np} = X_n I_1(n,-p) \tag{7.40}$$

$$X_n = j\beta_{yn}^{(s)}\left(1 - e^{-2j\beta_{yn}^{(s)} L_s}\right) \tag{7.41}$$

(7.37) is the final set of equations to be solved. To solve for the unknown co-efficients A_m, (7.37) now expressed in the matrix form as

$$\begin{bmatrix} -L_{-M} + R_{(-M)(-M)} & \cdots & R_{(-M)(0)} & \cdots & R_{(-M)(M)} \\ \vdots & \ddots & \vdots & & \vdots \\ R_{(0)(-M)} & \cdots & -L_0 + R_{(0)(0)} & \cdots & R_{(0)(\mathrm{M})} \\ \vdots & & \vdots & \ddots & \vdots \\ R_{(\mathrm{M})(-\mathrm{M})} & \cdots & R_{(\mathrm{M})(0)} & \cdots & -L_M + R_{(\mathrm{M})(\mathrm{M})} \end{bmatrix} \begin{bmatrix} A_{-M} \\ \vdots \\ A_0 \\ \vdots \\ A_M \end{bmatrix} = 0 \tag{7.42}$$

It is obvious that the inclusion of higher order Floquet modes into the analysis would in turn lead to modes with huge and imaginary values for $\beta_{ym}^{(l)}$ in (7.3). This quantity is related to the internal fields through sin and cosine arguments. As $\beta_{ym}^{(l)}$ grows largely imaginary, these sin and cosine terms tend to become huge and very difficult to handle by any computational software like

MATLAB. To alleviate this problem, as suggested by W C Chew [6], we have solved for $A_m^{'}$ and $B_m^{'}$ instead of A_m and B_m. These are related by the following relationship

$$A_m^{'} = A_m \cos\left(\beta_{ym}^{(l)} W_l - \delta_0\right) \tag{7.43}$$

$$B_m^{'} = B_m \left(1 + e^{-2j\beta_{ym}^{(l)} l_s}\right) \tag{7.44}$$

The null space problem of (7.42) is solved after necessary substitutions and alteration due to (7.43) and (7.44).

7.3.3 PROPAGATION CONSTANT CALCULATION

The matrix equation shown in (7.42) is of the form

$$[\Lambda]_{(2M+1)\times(2M+1)} \; [A]_{(2M+1)\times 1} = 0 \tag{7.45}$$

It is evident that any non trivial solution of (7.45) would necessitate singularity of $[\Lambda]$. Thus we look for possible singularities of [Λ]. Only unknown quantity in [Λ] being γ_0, this is done by varying the imaginary part of the unknown propagation constant of the fundamental Floquet mode ($\gamma_0=\alpha_0+j\beta_0$). The real part is kept constant at zero as we have primarily assumed a lossless scenario.

β_0 is obtained when the conditioning factor of [Λ] becomes very large (or the determinant becomes close to zero) and the matrix is rendered ill conditioned. It is observed that the matrix [Λ] has multiple singularities. After extracting the phase constants corresponding to these singularities by varying β_0 and using a simple root finding algorithm (bisection method), it is observed that these multiple singularities correspond to different spatial harmonics of the fundamental and higher order microstrip line modes. The dispersion characteristics with harmonic numbers are discussed later.

As expected, there would be frequencies where no perceivable solution for

β_0 can be found from (7.45). These are the stop-band frequencies for the structure. The stop-band attenuation at these frequencies can be calculated by making β_0=0 and varying α_0 in the same manner as before.

Once the propagation constants for all the Floquet modes are calculated, the null space of [Λ] from (7.45) yields the generic modal amplitudes of the different Floquet modes. The null space of [Λ] is calculated using the singular value decomposition method (SVD) in Matlab. This yields the modal amplitudes of the Floquet modes. A complete solution of the fields inside the periodic structure would necessitate analysis of the entire structure involving the boundary conditions at the inter-unit cell interfaces as well as at the load and source terminals. This would in turn deprive us of the whole advantage of the Floquet theory based analysis. Specific excitation or termination conditions are excluded at this time to keep the simplicity of the technique described.

7.3.4 SIMULATION AND OBSERVATIONS

To validate the analysis technique presented in this work, some of the geometries shown in Fig. 7.1 are analyzed for their dispersion characteristics. These are discussed next.

7.3.4.1. Stub loaded microstrip line supporting Quasi TEM modes

The open stub loaded microstrip line shown in Fig. 7.1a is analyzed first. The line is simulated on a substrate with permittivity 4.0 and substrate thickness of 1.6 mm. Host line parameters are taken as: L_u = 20 mm and W_l = 3.3 mm. Physical stub lengths are varied as L_s=1mm and 3 mm while keeping the stub width constant at 2 mm.

First, nature of the conditioning factor is plotted in Fig. 7.3 for the 3 mm stub at 5.5 GHz and 6.5 GHz. Multiple singularities of the co-efficient matrix correspond to the phase constants of various Floquet spatial harmonics.

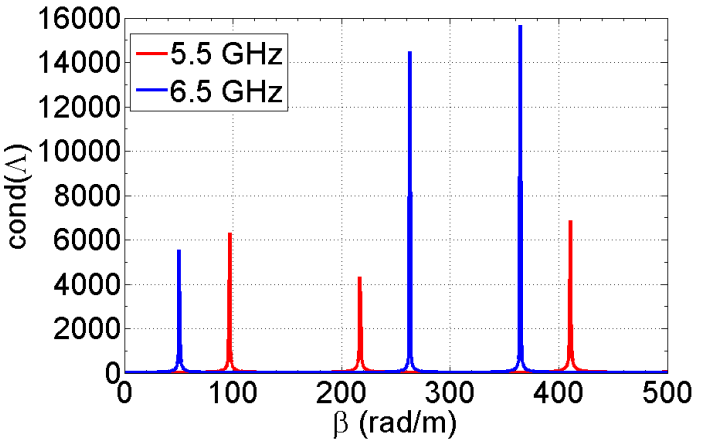

Fig. 7.3: Nature of the conditioning factor with β for a stub length of 3 mm

A study of the effects of the number of modes on the host line as well as that in the stub is made. Calculated values of β_0 at 6 GHz for the two stubs with M and N are shown in Table 7.1 for stubs of different lengths.

Table 7.1: Values of β_0 for different M and N values

L_s=1 mm			**L_s=3 mm**		
β_0	**M**	**N**	**β_0**	**M**	**N**
85.32	1	1	76.22	1	1
85.08	2	1	75.03	2	1
84.9	3	1	74.3	3	1
84.8	4	1	73.83	4	1
85.1	2	2	75.08	2	2
84.99	3	3	74.44	3	3
84.87	4	4	74.05	4	4

Dispersion characteristics are calculated using the technique outlined in the last sections. Phase constants of different Floquet modes are shown in Fig. 7.3b and Fig. 7.3c respectively for two different stub lengths. Curves shown in red and magenta are the ones calculated using the mode matching technique where the red ones indicate the dispersion curve inside the principal value region (β within 0 and π/l_u) while the magenta ones are the dispersion curves for higher order Floquet modes. Dispersion curves as calculated using the conventional

ABCD matrix method are also plotted in the same graph for comparison. These are shown in black. Free space dispersion characteristics are plotted in blue to indicate the leaky region. The pass bands and stop bands are distinctly visible. In all the cases, the number of modes inside the region I (*M*) and inside the region II (*N*) are considered as *M*=3 and *N*=3.

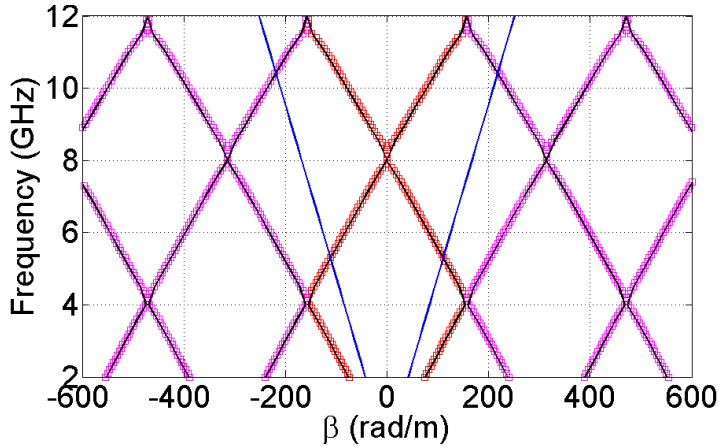

(b)

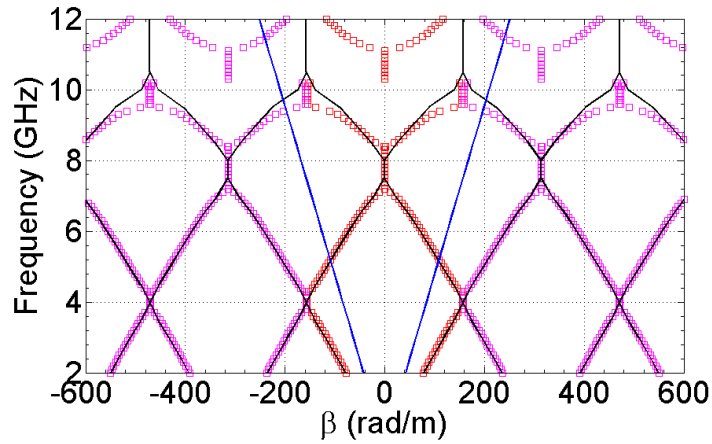

(b)

Fig. 7.4: Dispersion characteristics calculated using the mode matching technique (shown in red and magenta) and calculated using the ABCD matrix technique (shown in black) along with the free space dispersion curves (shown in blue) for (a) stub length of 1 mm and (b) stub length of 3 mm

At the stop bands of the structure, the attenuation constant is calculated using technique described earlier. Nature of this stop band is shown in Fig. 7.5 for the two stub lengths.

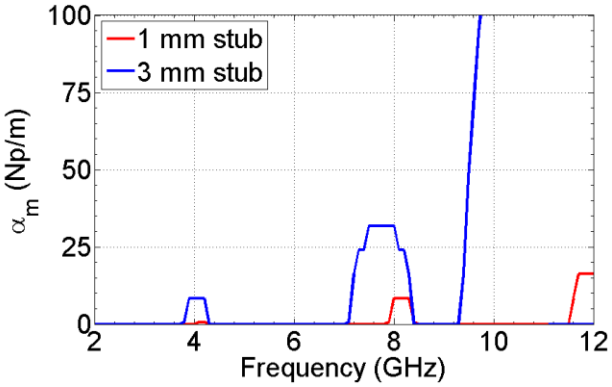

Fig. 7.5: Attenuation constant at the stop bands of the structure.

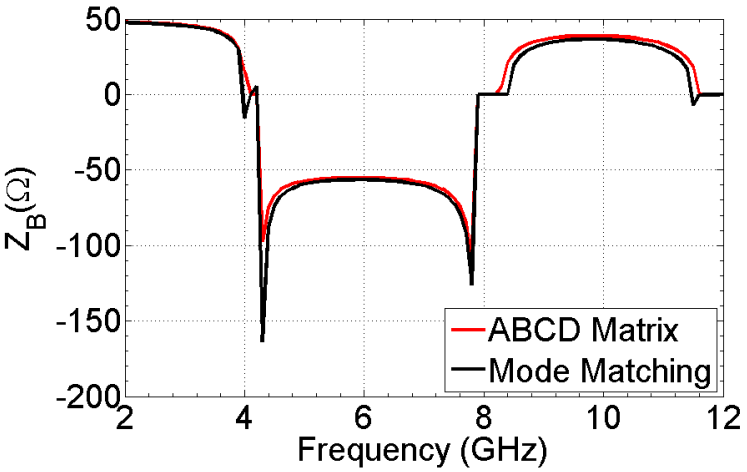

(a)

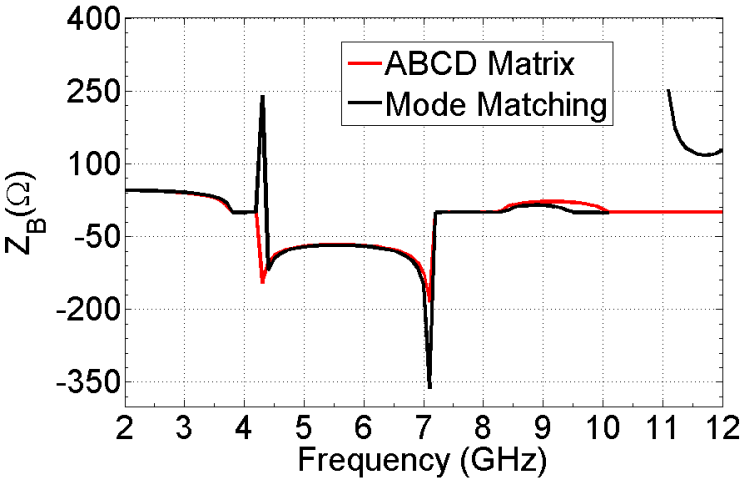

(b)

Fig. 7.6: Bloch impedance calculated using equivalent circuit based ABCD matrix method and the mode \matching techniques for the (a) Ls = 1mm and (b) Ls=3 mm.

Bloch impedance and input reflection co-efficient for the structure with 11 unit cells is calculated using both ABCD matrix technique and the mode matching procedure. They are plotted in Fig. 7.6 and Fig. 7.7 respectively.

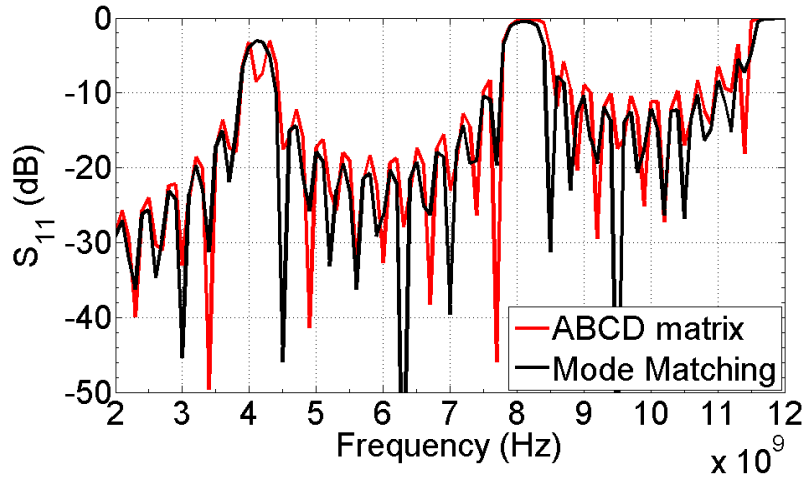

(a)

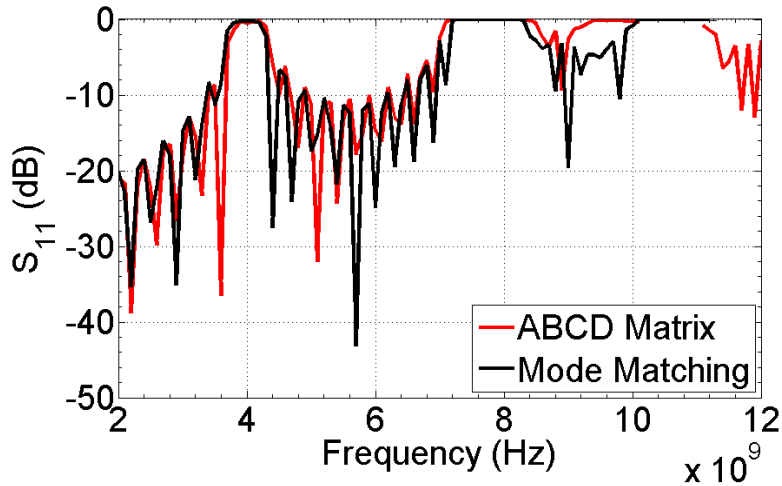

(b)

Fig. 7.7: S_{11} vs. frequency for the (a) 1 mm long stub loaded microstrip line and (b) 3 mm long stub loaded line.

After obtaining β_0, the null space for [Λ] is calculated. Although we have not solved the complete boundary value problem inclusive of the entire structure along with the source and load, the null space evaluated here indicates to some extent, the excitation co-efficients for different Floquet modes. The amplitudes of

different Floquet modes are plotted in Fig. 7.8a, Fig. 7.8b and Fig. 7.8c respectively for frequencies of 3 GHz, 6 GHz and 11.5 GHz. It is clear that at 3 GHz, the m=0 mode is excited and it remains outside the leaky region. At 6 GHz however the m= -1 mode is excited properly and it is within the leaky region contributing substantially to the total radiation. At frequencies even higher i.e. at

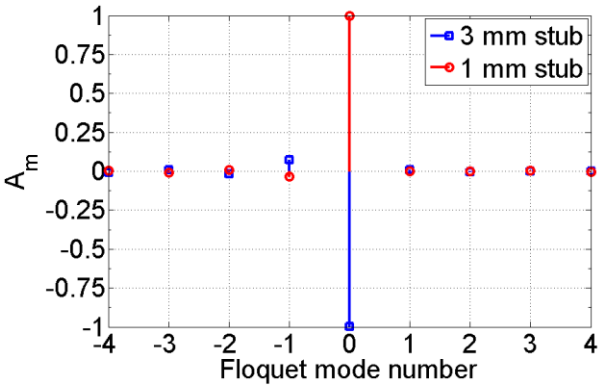

(a)

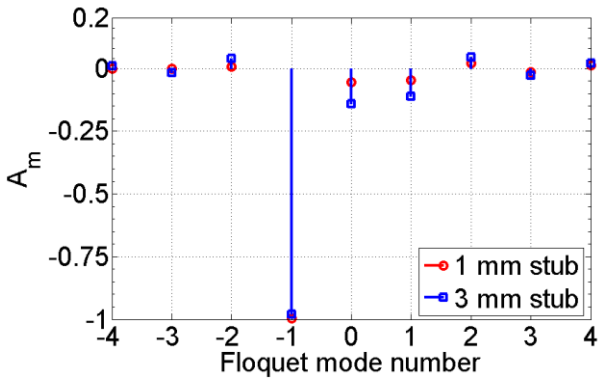

(b)

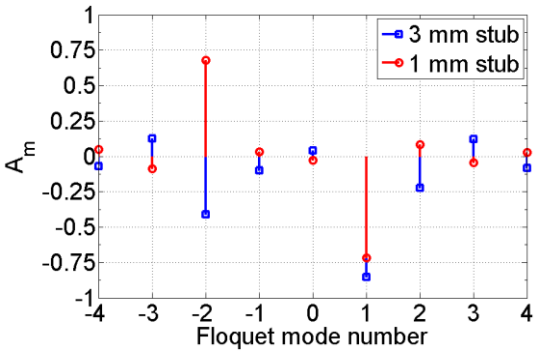

(c)

Fig. 7.8: Modal excitation co-efficients calculated from the null space of [Λ] for different stub lengths at (a) 3 GHz, (b) 6 GHz and (c) 11.5 GHz

11.5 GHz, apart from the m= -1 modes, the m= -2 mode is also excited and enters the leaky region thereby inciting a dual beam nature in the radiation pattern of the antenna.

7.3.4.2. Stub loaded microstrip line supporting the first higher order mode

To validate the analysis technique for microstrip lines supporting higher order modes, the geometry of Fig. 7.2b is now analyzed. Dimensions chosen are as follows: l_u=25 mm, W_l = 6.5 mm. First, the line without any perturbation is analyzed. The dispersion characteristics are shown in Fig. 7.5a and 7.5b respectively for stub lengths of 0 mm and 5 mm.

It can be observed from Fig. 7.9 that the higher order mode of the microstrip line is inside the leaky fast wave region right after its cut-off. Consequently, radiation would occur without any leaky Floquet modes. In case of the stub loaded line (dispersion characteristics shown in Fig.7.10), stop bands are introduced - this would suppress the radiation from the higher order mode.

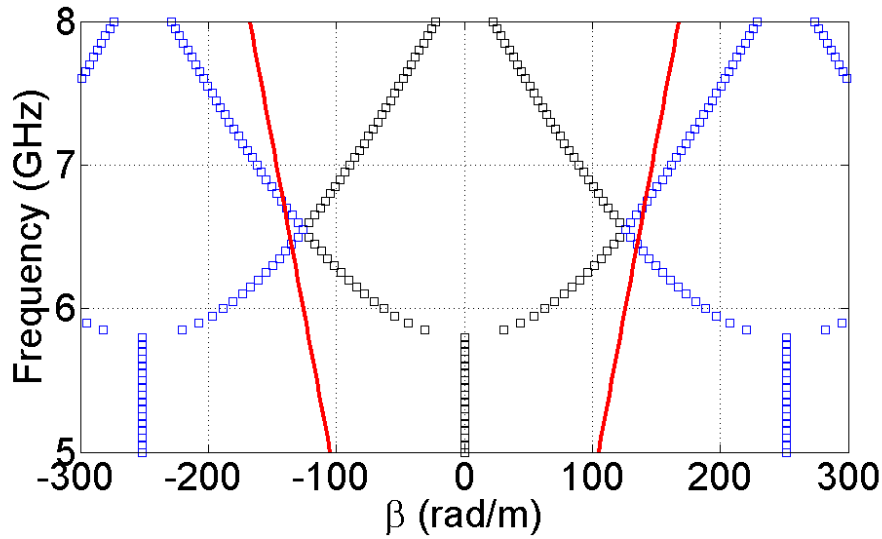

Fig. 7.9: Dispersion characteristics for the microstrip line with higher order mode without stub loading

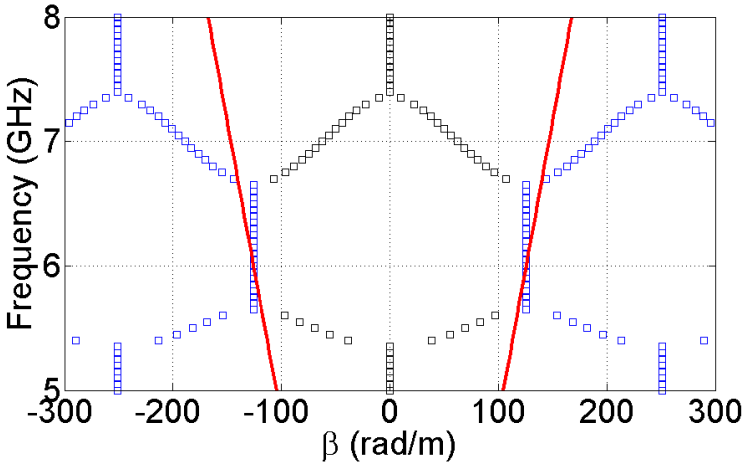

Fig. 7.10: Dispersion characteristics for the microstrip line with higher order mode with stub loading

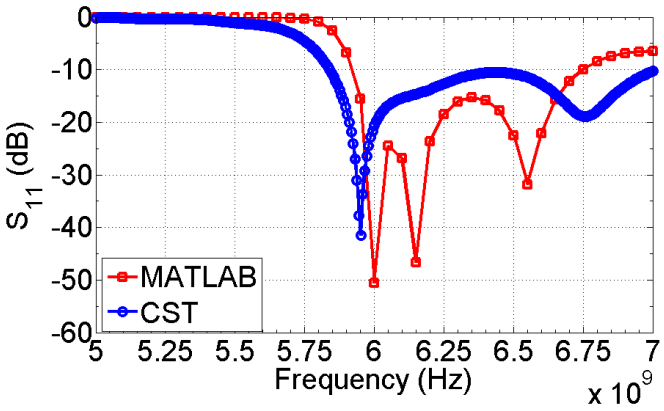

(a)

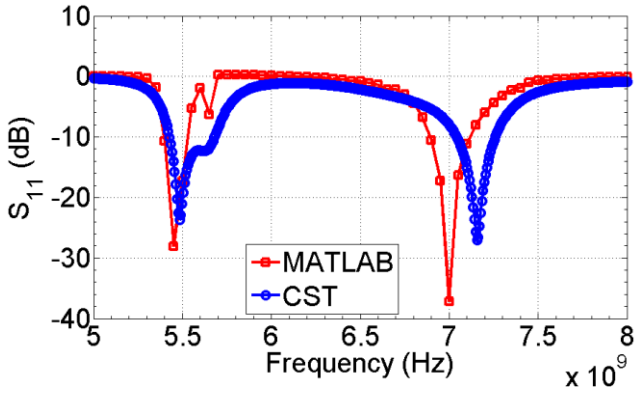

(b)

Fig. 7.11: S_{11} vs. frequency for (a) uniform microstrip line and (b) stub loaded microstrip line supporting higher order modes.

7.4 ANALYSIS OF SIW TYPE GEOMETRIES

We now consider the geometry types shown in Fig. 7.12. The edges for the host microstrip line are shorted using cylindrical metallic vias as in planar Substrate Integrated Waveguide (SIW) lines. In this work we have simplified this problem by assuming a continuous shorting wall instead of periodic metallic vias. However, it is argued that for sufficiently small inter-via distance, this assumption of a continuous shorting wall along the length of the line is quite accurate. This had already been observed in the context of a leaky wave antenna design in chapter 6. There two microstrip lines with shorted edges were simulated. Results for shorting using metallic posts and continuous shorting wall were observed to be equivalent.

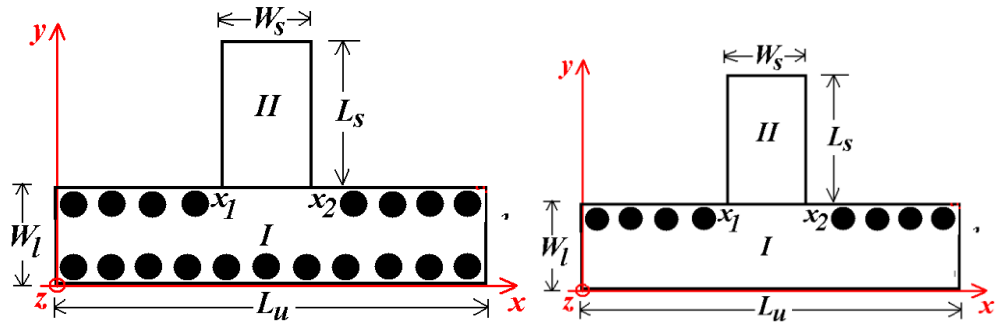

Fig. 7.12: The two types of SIW type geometry considered for the analysis

7.4.1 PREPROCESSING AND FIELD REPRESENTATION

Expressions for the electric and magnetic fields are essentially kept same as in the last case i.e. the expressions in (7.1), (7.4) for electric field and (7.8)-(7.11) for the magnetic field are used. These are not repeated in this section.

Only the boundary condition at $y=W_l$ is changed from a magnetic wall in case of the non-SIW type geometries case to an electric wall in this case. Both the

geometry types shown in Fig. 7.8 are considered in this section. These are characterized by $\delta_0 = \pi/2$ for case I and $\delta_0 = 0$ for case II as shown in Fig.7.8.

7.4.2 MODE MATCHING PROCEDURE

Electric and magnetic fields in the two regions shown in Fig. 7.8 are now subjected to appropriate boundary conditions at the geometry interfaces. These boundary conditions and subsequent analysis are discussed next.

1. Using the magnetic or electric wall approximation at the far end of the stub,

   (a) $H_x^{II} = 0$ for $x_1 \le x \le x_2,\ y = W_l + L_s$ for an open circuited stub (7.46)

   (b) $E_z^{II} = 0$ for $x_1 \le x \le x_2,\ y = W_l + L_s$ for a short circuited stub (7.47)

2. Using the continuity of tangential magnetic field (H_x) at the interface between the stub and the host line,

   $$H_x^I = H_x^{II} \text{ for } x_1 \le x \le x_2,\ y = W_l \tag{7.48}$$

3. Using the electric wall at $y=W_l$, and continuity of the tangential electric field (E_z) at the stub-line interface,

   $$E_z^I = \begin{cases} 0 & \text{for } x < x_1 \ \&\ x > x_2, y = W_l \\ E_z^{II} & \text{for } x_1 \le x \le x_2,\ y = W_l \end{cases} \tag{7.49}$$

These boundary conditions are now applied to the electric and magnetic fields expressed in (7.1), (7.4) and (7.8)-(7.11).

1. The two boundary conditions at the edge of the stub for open and shorted stubs remained same as in the case of non SIW type geometry discussed in section 7.3. Consequently, these conditions are summarized in the following form

$$C_p = sB_p e^{-2j\beta_{yp}^{(s)}L_s} \text{ for p=0,1,...}\infty \tag{7.50}$$

where s=1 for open ended stubs and s=-1 for short circuited stubs.

2. $H_x^I = H_x^{II}$ for $x_1 \le x \le x_2,\ y = W_l$

After putting H_x^I and H_x^{II} from (7.8) and (7.10) respectively we obtain

$$\sum_{m=-\infty}^{\infty} \beta_{ym}^{(l)} A_m \sin\left\{\beta_{ym}^{(l)} W_l - \delta_0\right\} e^{-\gamma_m x} = \sum_{n=0}^{\infty} j\beta_{yn}^{(s)} \cos\left\{\beta_{xn}^{(s)}(\mathrm{x}-\mathrm{x}_1)\right\}\left[B_n - C_n\right] \tag{7.51}$$

Multiplying both sides by $\cos\left\{\beta_{xp}^{(s)}(\mathrm{x}-\mathrm{x}_1)\right\}$ and integrating in (x_1, x_2) we obtain,

$$\begin{aligned}&\sum_{n=0}^{\infty} j\beta_{yn}^{(s)}\left[B_n - C_n\right]\int_{x_1}^{x_2} \cos\left\{\beta_{xn}^{(s)}(\mathrm{x}-\mathrm{x}_1)\right\}\cos\left\{\beta_{xp}^{(s)}(\mathrm{x}-\mathrm{x}_1)\right\}dx = \\ &\sum_{m=-\infty}^{\infty} \beta_{ym}^{(l)} A_m \sin\left\{\beta_{ym}^{(l)} W_l - \delta_0\right\}\int_{x_1}^{x_2} e^{-\gamma_m x}\cos\left\{\beta_{xp}^{(s)}(\mathrm{x}-\mathrm{x}_1)\right\}dx\end{aligned} \tag{7.52}$$

Orthogonality condition of (7.18) together with (7.50) reduces the abovementioned relationship to the following form,

$$B_p = \frac{\eta_p}{j\beta_{yp}^{(s)} W_s\left(1 - se^{-2j\beta_{yp}^{(s)}L_s}\right)}\sum_{m=-\infty}^{\infty} A_m \beta_{ym}^{l}\cos\left(\beta_{ym}^{l} W_l - \delta_0\right) I_1(p,m) \tag{7.53}$$

for p=0,1,...∞

Here

$$I_1(p,m)=\int_{x_1}^{x_2} e^{-\gamma_m x}\cos\left\{\beta_{xp}^{(s)}(\mathrm{x}-\mathrm{x}_1)\right\}dx$$

$$=\left[e^{\left\{\gamma^+ x_0-j\beta_{xp}^{(s)}x_1\right\}}\frac{\sinh\left(\gamma^+\frac{W_s}{2}\right)}{\gamma^+}+e^{\left\{\gamma^- x_0+j\beta_{xp}^{(s)}x_1\right\}}\frac{\sinh\left(\gamma^-\frac{W_s}{2}\right)}{\gamma^-}\right] \quad (7.54)$$

where $\gamma^{\pm}=-\gamma_m\pm j\beta_{xp}^{(s)}, x_0=x_1+\frac{W_s}{2}$

(7.53) is expressed in following form for brevity,

$$B_p=\sum_{m=-\infty}^{\infty} S_{mp}A_m \text{ for p=0,...}\infty \quad (7.55)$$

where

$$S_{mp}=\frac{\eta_p\beta_{ym}^l\cos\left(\beta_{ym}^l W_l-\delta_0\right)I_1(p,m)}{j\beta_{yp}^{(s)}W_s\left(1-se^{-2j\beta_{yp}^{(s)}L_s}\right)} \quad (7.56)$$

3. $E_z^I=\begin{cases}0 & \text{for } x<x_1 \ \&\ x>x_2, y=W_l\\ E_z^{II} & \text{for } x_1\le x\le x_2,\ y=W_l\end{cases}$

After putting E_z^I and E_z^{II} from (7.1) and (7.4) respectively, we obtain

$$E_z^I=\sum_{m=-\infty}^{\infty} A_m\cos\left\{\beta_{ym}^{(l)}W_l-\delta_0\right\}e^{-\gamma_m x}=X \quad (7.57)$$

where $X=\begin{cases}0 \text{ for } x<x_1 \text{ and } x>x_2\\ \sum_{n=0}^{\infty}\cos\left\{\beta_{xn}^{(s)}(\mathrm{x}-\mathrm{x}_1)\right\}\left[B_n+C_n\right] \text{ for } x_1\le x\le x_2\end{cases}$ (7.58)

Multiplying both sides by $e^{\gamma_p x}$ and integrating in (*0*, L_u) we obtain

$$\sum_{m=-\infty}^{\infty} A_m \cos\left\{\beta_{ym}^{(l)} W_l - \delta_0\right\} \int_0^{L_u} e^{-\gamma_m x} e^{\gamma_p x} dx =$$
$$\sum_{n=0}^{\infty} \left[B_n + C_n\right] \int_{x_1}^{x_2} \cos\left\{\beta_{xn}^{(s)} (\mathrm{x} - \mathrm{x}_1)\right\} e^{\gamma_p x} dx \qquad (7.59)$$
$$\text{for } p = 0,1...\infty$$

After using the following orthogonality condition,

$$\int_0^{L_u} e^{-\gamma_m x} e^{\gamma_p x} dx = \begin{cases} 0 & \text{for } p \neq m \\ L_u & \text{for } p = m \end{cases} \qquad (7.60)$$

(7.59) is reduced to the following form

$$\sum_{m=-\infty}^{\infty} A_m \cos\left\{\beta_{ym}^{(l)} W_l - \delta_0\right\} \int_0^{L_u} e^{-\gamma_m x} e^{\gamma_p x} dx = \sum_{n=0}^{\infty} \left[B_n + C_n\right] I_1(n, -p) \qquad (7.61)$$
$$\text{for } p = 0,1...\infty$$

Here I_1 is as defined in (7.54). Now, using (7.50) to substitute C_n and subsequently using (7.53) to replace B_n with A_n we obtain after some simplification

$$-L_p A_p + \sum_{m=-\infty}^{\infty} R_{pm} A_m = 0 \text{ for } p = -\infty,...\infty \qquad (7.62)$$

Here,

$$L_p = L_u \cos\left\{\beta_{yp}^{(l)} W_l - \delta_0\right\} \qquad (7.63)$$

$$R_{pm} = \sum_{n=0}^{\infty} Y_{np} S_{mn} \qquad (7.64)$$

$$Y_{np} = \left(1 + s e^{-2j\beta_{yn}^{(s)} L_s}\right) I_1(n, -p) \qquad (7.65)$$

(7.62) is now expressed in the matrix form as

$$\begin{bmatrix} -L_{-M}+R_{(-M)(-M)} & \dots & R_{(-M)(0)} & \dots & R_{(-M)(M)} \\ \vdots & \ddots & \vdots & & \vdots \\ R_{(0)(-M)} & \dots & -L_0+R_{(0)(0)} & \dots & R_{(0)(\mathrm{M})} \\ \vdots & & \vdots & \ddots & \vdots \\ R_{(\mathrm{M})(-\mathrm{M})} & \dots & R_{(\mathrm{M})(0)} & \dots & -L_M+R_{(\mathrm{M})(\mathrm{M})} \end{bmatrix} \begin{bmatrix} A_{-M} \\ \vdots \\ A_0 \\ \vdots \\ A_M \end{bmatrix} = 0 \qquad (7.66)$$

As was justified in the last case for the non SIW type unit cells, we solve for $A_m^{'}$ and $B_m^{'}$ instead of A_m and B_m. The relationship between these quantities are now defined as,

$$A_m^{'} = A_m \sin\left(\beta_{ym}^{(l)} W_l - \delta_0\right) \qquad (7.67)$$

$$B_m^{'} = B_m \left(1 - e^{-2j\beta_{ym}^{(l)} l_s}\right) \qquad (7.68)$$

Proceeding in a manner similar to the case of non SIW type geometries, we calculate the dispersion curves for the geometry of Fig. 7.1c with W_l =12mm, L_u=25 mm with open stubs of 5 mm length and width of 3 mm. (Substrate chosen is FR4 with permittivity of 4.3 and thickness of 0.762 mm). The calculated dispersion characteristics and simulated input reflections co-efficient are plotted together in Fig. 7.13.

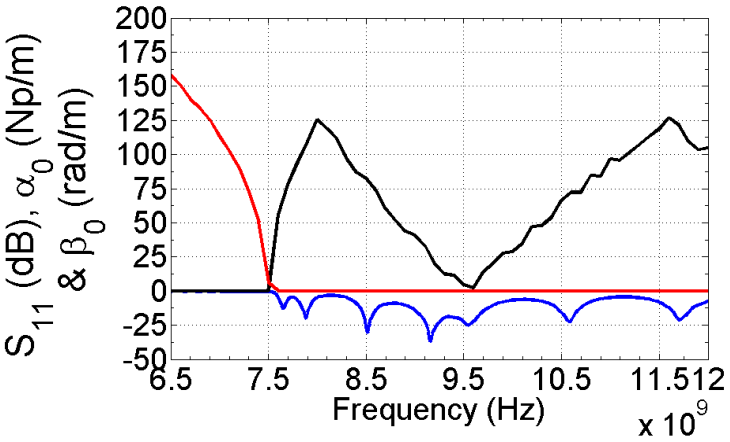

Fig. 7.13: Calculated dispersion characteristics and simulated S_{11} for the SIW based geometry

7.5 PRACTICAL MEASUREMENTS

To validate the analysis presented in this chapter, a stub loaded microstrip line geometry is fabricated in FR_4 substrate (permittivity 4.0 and thickness 1.6 mm). Geometry with 11 units of the cell shown in Fig. 7.14 is fabricated. Simulated, measured and calculated S_{11} are show in Fig. 7.16. Fig. 7.17a shows the dispersion characteristics computed using the theory presented here while Fig. 7.17b show the simulated and measured radiation patterns in the range of 5.5 GHz to 7 GHz. It is clear from the dispersion characteristics that the structure enters the leaky region near 5 GHz and radiated in the second quadrant thereafter. Beam scanning can be noticed from the eradiation pattern in the x-z plane.

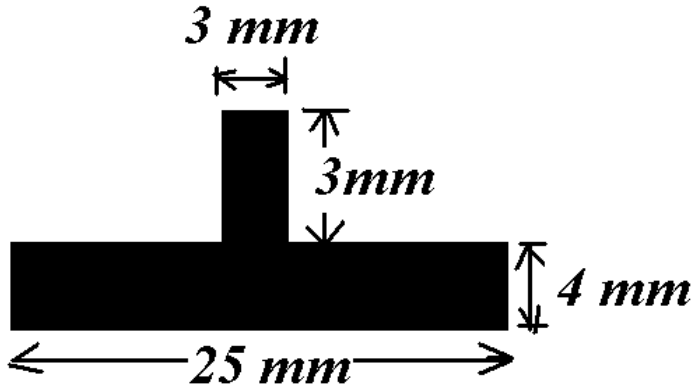

Fig. 7.14: Schematic diagram of the fabricated geometry

Fig. 7.15: Photograph of the fabricated prototype

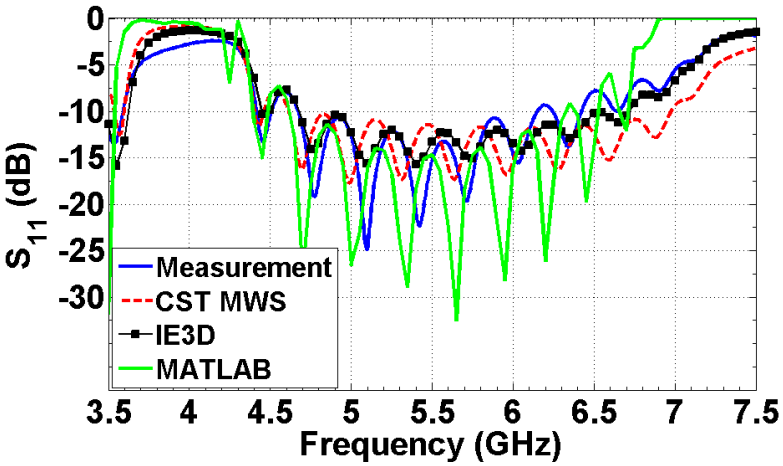

Fig. 7.16: Simulated, computed and measured S_{11} for the geometry of Fig. 7.10.

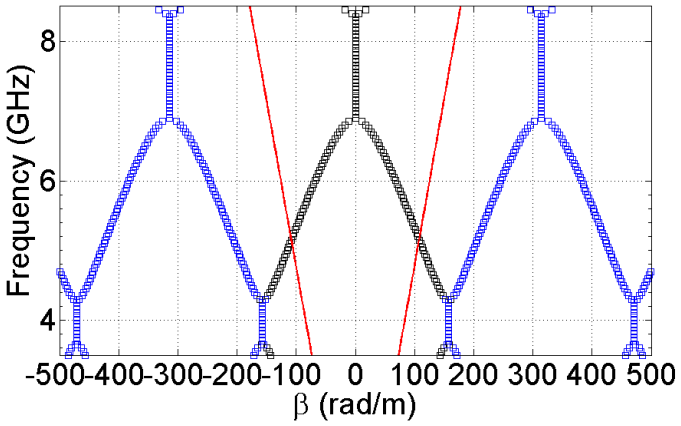

(a)

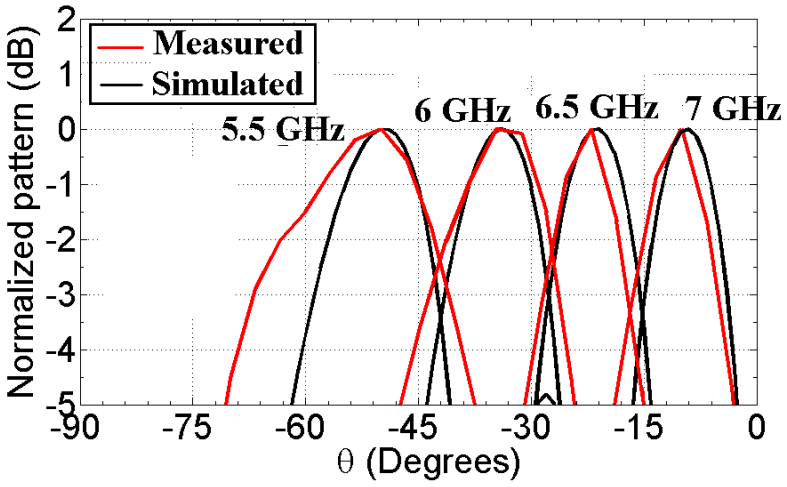

(b)

Fig. 7.17: (a) Calculated dispersion characteristics and (b) simulated and measured radiation pattern in the x-z plane at 5.5 GHz, 6 GHz, 6.5 GHz and 7 GHz.

7.6 CONCLUSION

A Floquet theory and mode matching based analysis technique is presented for microstrip lines with periodic loading. Microstrip line supporting both fundamental mode and higher order modes can be analyzed using this model. Three different cases are investigated. Quasi TEM mode based microstrip line with stub loading, first higher order mode based microstrip line with stub loading and SIW type line with both the edges along the line shorted to the ground. The quasi TEM mode based line is fabricated and practical measurements are taken indicating good agreement with the theory presented.

REFERENCES:

[1] Collin, R.E., 2007. *Foundations for microwave engineering*. John Wiley & Sons

[2] A. F. Harvey, Periodic and Guiding Structures at Microwave Frequencies, IRE Trans. Microw. Theory Tech., vol. 8, no. 1, pp. 30-61, January 1960.

[3] P. Baccarelli, C. Di Nallo, S. Paulotto and D. R. Jackson, "A full-wave numerical approach for modal analysis of 1-D periodic microstrip structures," in *IEEE Transactions on Microwave Theory and Techniques*, vol. 54, no. 4, pp. 1350-1362, June 2006.

[4] P. Baccarelli, S. Paulotto, D. R. Jackson and A. A. Oliner, "A New Brillouin Dispersion Diagram for 1-D Periodic Printed Structures," in *IEEE Transactions on Microwave Theory and Techniques*, vol. 55, no. 7, pp. 1484-1495, July 2007.

[5] D. K. Karmokar, Y. J. Guo, P. Qin, K. P. Esselle and T. S. Bird, "Forward and Backward Beam-Scanning Tri-Band Leaky-Wave Antenna," in *IEEE Antennas and Wireless Propagation Letters*, vol. 16, pp. 1891-1894, 2017.

[6] W. C. Chew, 2012. Lectures on theory of microwave and optical waveguides. *University of Illinois Lecture*.

Chapter 8

Periodic Leaky Wave Antennas: Observations and Applications

Contents

8.1 INTRODUCTION

In the last few years research on periodic leaky wave antennas has become intensified primarily due to their characteristics in terms of beam scanning with frequency and simplified excitation [1, 2]. In most of the periodic leaky wave antennas, either the n= -1[3] or the n= -2 [4] Floquet modes are made to enter the leaky fast wave region of the dispersion characteristics. The excitation of these higher order modes and their nature depend extensively on the periodicity and the nature of loading. In this context slots [5-6] or stubs [7-8] on microstrip line have become very popular choices.

In this chapter our intention is twofold. Firstly, several different lumped and distributed loads for microstrip line are considered and their dispersion characteristics as well as nature of the leaky region are observed. Some cases are simulated using conventional full wave simulator to obtain the radiation characteristics of leaky wave antennas comprising them. Next, one of the cases i.e. the dual stub (open and shorted stub loaded) loaded microstrip line is analyzed

in detail to outline systematic design guidelines for developing single and dual wideband leaky wave antennas. Some simple guidelines are outlined for designing multi-beam antennas as well. Two different prototypes are fabricated and results are discussed.

8.2 PROBLEM FORMULATION

The basic problem considered in this chapter is that of a periodically loaded microstrip line. The host line is considered to have a width of 'W_0' in general. Some of the cases considered in this chapter are shown in Fig. 8.1. The specific geometry of the dual stub loading is shown in Fig. 8.1b. Unless otherwise specified, the substrate chosen is Arlon AD430 with 30 mils of substrate thickness and a permittivity of 4.3.

(a) (b) (c)

Fig. 8.1 :(a) Dual stub loaded microstrip line, (b) stub and notch loaded microstrip line and (c) width modulated microstrip lines considered in this chapter.

8.3 COMPARISON OF DIFFERENT TYPES OF LOADS

A simple technique to determine the leaky fast wave region where the periodic structure radiates considerable amount of power, had been discussed in chapter 6. Here the same technique is utilized to consider and observe the behavior of several different types of loads on microstrip line. In this section, loading effects of different types of loads for microstrip lines in both lumped and

distributed nature are considered for their dispersion characteristics and nature of the leaky regions.

8.3.1. LUMPED LOADS

Dispersion characteristics of microstrip lines periodically loaded with lumped loads [9] are discussed first. They constitute the basic prototype for several other distributed load cases. For all the following cases, L_0, C_0 are load inductance and capacitances respectively and l_u is the length of the unit cell. l_u is chosen to be 20 mm throughout for all simulations. Unless otherwise specified, Arlon AD430 with permittivity of 4.3 and substrate thickness 30 mils (loss tangent 0.003) is used as substrate and the host microstrip line is considered to have a width of 2.172 mm which has approximately 30 Ω of characteristic impedance. In all the cases to follow, the host line characteristic impedance can be tuned to optimize pass band matching.

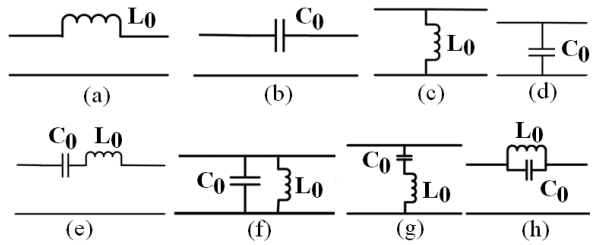

Fig. 8.2: Different prototype lumped loads for microstrip line

8.3.1.1. Simple reactance loading

As L_0 increases for the series inductor (L_0) (shown in Fig. 8.2a), stopband widths increase toward the lower frequencies with a fixed upper limit. Consequently the passbands also shift toward the lower frequencies. Stopband attenuation also increases with increasing L_0 (shown in Fig. 8.3a). As L_0 increases, real part of the Bloch impedance (Z_b) moves away from characteristic impedance of the unloaded line (Z_0) (shown in Fig. 8.3c). Consequently impedance matching degrades even in the passband.

In case of the series capacitor (C_0) (shown in Fig. 8.2b), as C_0 increases, stopband widths decrease toward the lower frequencies with a fixed lower bound. Consequently the passbands also shift and widen toward the lower frequencies. Stopband attenuation decreases with increasing C_0 (Fig. 8.3b). As C_0 increases real part of Z_b comes more toward Z_0 (Fig. 8.3d) and consequently impedance matching gets better even in the stopband. S_{11} plot leans toward a wideband behavior with increasing C_0 as the stopband width becomes negligible.

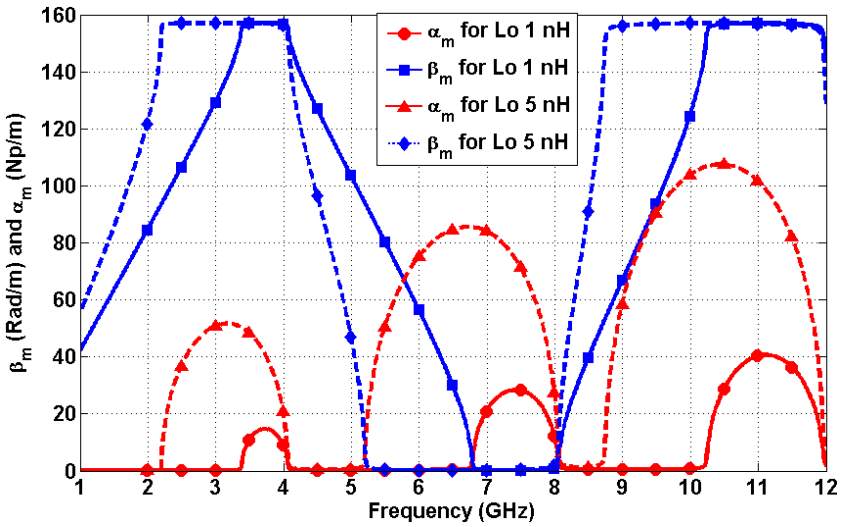

(a)

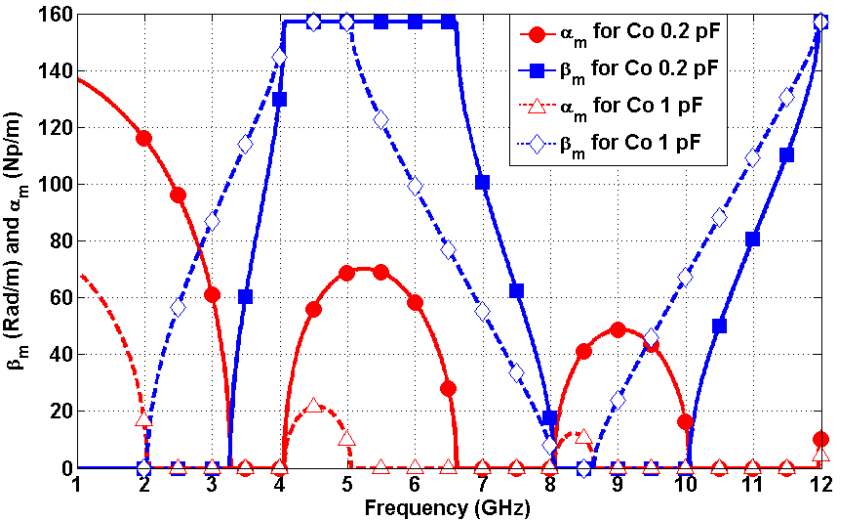

(b)

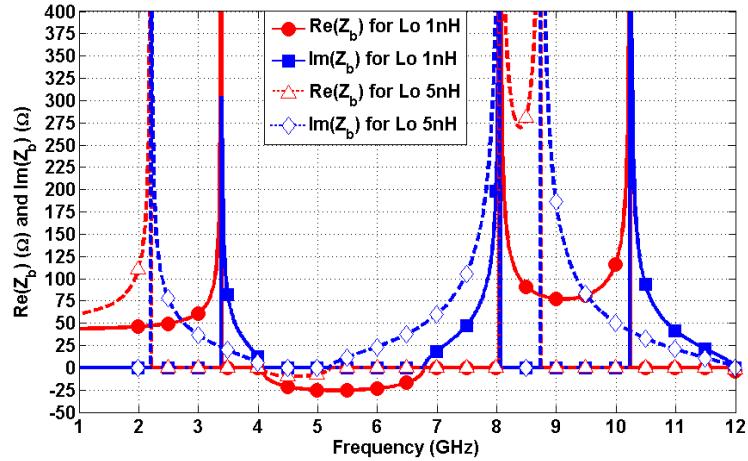

(c)

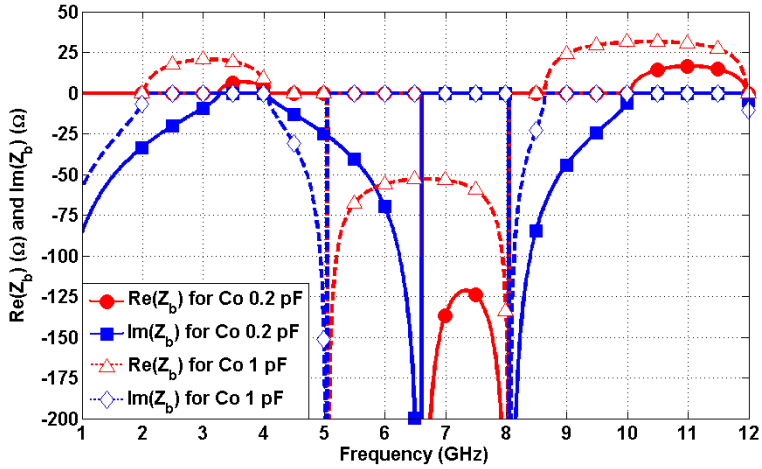

(d)

Fig. 8.3: Phase constant, attenuation constant for (a) series inductor load, (b) series capacitor load and real, imaginary part of Bloch impedance for (c) series inductor load, (d) series capacitor load.

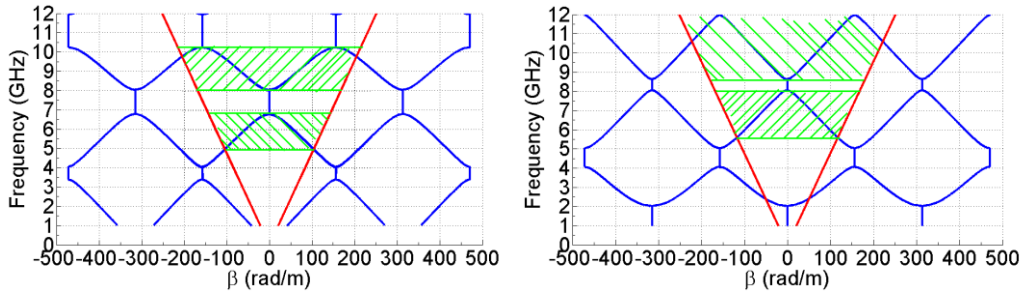

(a) (b)

Fig. 8.4: Dispersion characteristics indicating the leaky region shaded in green for (a) 1 nH series inductor loaded line and (b) 1 pF series capacitor loaded line.

Dispersion characteristics of the microstrip line loaded with a 1 nH inductor and a 1 pF capacitor inclusive of all the higher order Floquet modes is shown in Fig.8.4a and Fig. 8.4b respectively. The leaky fast wave regions are shaded green in the two figures.

8.3.1.2. Resonant network loading

Series LC in series arm:

Near the resonant frequency (f_0) of the series LC load (Fig. 8.2e) stopband width and attenuation is minimum. Both of these increase for stopbands on either side of f_0. This effect can be utilized to obtain a wideband behavior by placing f_0 near a stopband (indicated by Bragg frequency (f_B) or its multiples) to merge adjacent passbands. (Fig. 8.5a). Near f_0, real part of Z_B (Bloch impedance) has values close to Z_0 (Fig. 8.5b) and is removed farther from Z_0 on either side of f_0. This also explains the wideband behavior near f_0. As L_0 decreases and C_0 increases, real part of Z_B in all the pass bands comes closer to the Z_0. Consequently, the S_{11} performance gets better and we have a very wide band behavior. Dispersion characteristics corresponding to a series LC loaded line are calculated. Resonant frequency of the LC network is chosen to be 8.08 GHz with L_0=1nH and C_0=0.388 pF. The microstrip line chosen here has the Bragg frequency at about 4.04 GHz. Thus, the choice of f_0 here, is at $2f_B$ and evidently the stopband near 8.08 GHz is eliminated (Fig.8.5a).

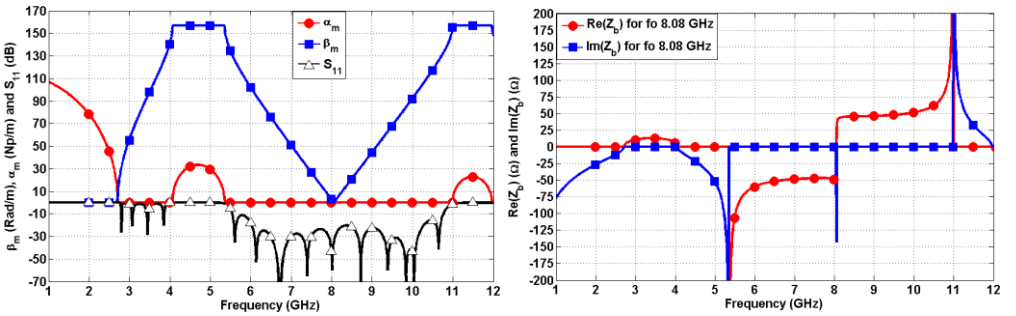

Fig. 8.5: (a) Phase constant and attenuation constant and (b) real and imaginary parts of the Bloch impedance for a microstrip line periodically loaded with series LC network in the series arm with f_0 at 8.08 GHz

Parallel LC in series arm:

There is a distinct stopband with highest attenuation and bandwidth (Fig. 8.6a) near resonant frequency (f_0) of the parallel LC network (Fig. 8.2h). Stop band width as well as attenuation decrease away from f_0 for stopbands on either side of f_0. As L_0 increases or C_0 decreases, stopband near f_0 widens and matching in nearby passbands degrade. The real part of Z_B moves away from Z_0 as we move toward f_0 (Fig. 8.6b). Consequently, impedance matching near f_0 is worst.

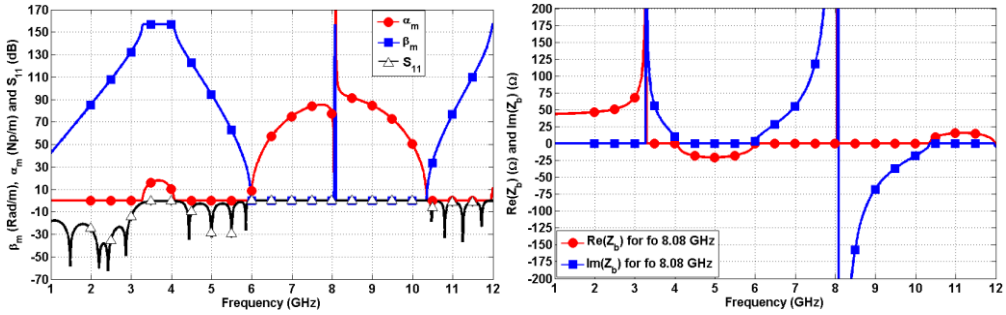

(a) (b)

Fig. 8.6: Phase constant and attenuation constant and (b) real and imaginary parts of the Bloch impedance for a microstrip line periodically loaded with parallel LC network in the series arm

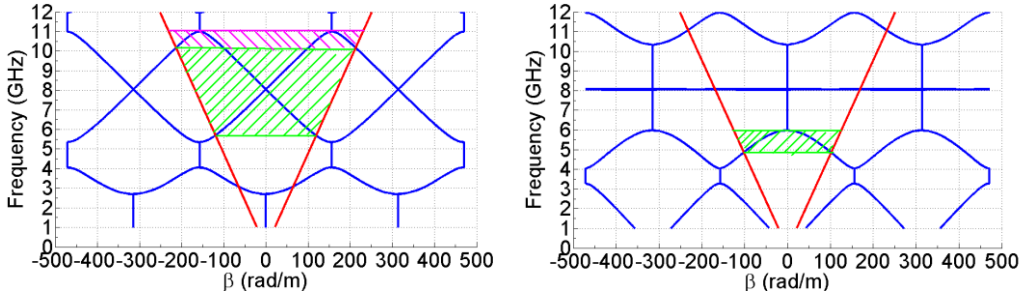

(a) (b)

Fig. 8.7: (a) Dispersion characteristics with all higher order Floquet modes indicating the leaky fast wave region for microstrip line periodically loaded with the (a) series LC network in series arm and (b) shunt LC network in series arm.

Dispersion characteristics corresponding to a parallel LC loaded line is then calculated (Fig. 8.6). Resonant frequency and values of L_0 and C_0 are same as was in the case of the series LC load. It is evident from Fig. 8.6a that the resonant frequency of the parallel LC load near 8.08 GHz has widened the stopband near

that frequency. The sharp change in dispersion characteristics near the second Bragg frequency (8.08 GHz) is due to the existence of closely spaced zero introduced by $\sin(\beta l_u)$ and a pole due to the ant resonant frequency of the lumped load.

Complete dispersion characteristics with all the Floquet modes and the leaky region for the two cases considered above are shown in Fig. 8.7. In both cases the region shaded in green harbors the n= -1 mode as the only fast one while in Fig. 8.7a, the region in pink has both the n= -1 and the n= -2 mode inside the leaky region leading to a dual beam nature in the radiation pattern.

Other two configurations of Fig. 8.2 namely series LC in shunt (Fig. 8.2g) and parallel LC in series (Fig. 8.2h) configurations are duals of the two discussed here and would exhibit similar dispersion behavior.

8.3.1.3. Loading with a T circuit

The T equivalent circuit shown in Fig. 8.8a is analyzed in this section. ABCD matrix for this T circuit can be expressed in the following form [10]

$$\begin{bmatrix} 1-\omega^2 L_0 C_0 & j\omega L_0\left(2-\omega^2 L_0 C_0\right) \\ j\omega C_0 & 1-\omega^2 L_0 C_0 \end{bmatrix} \tag{8.1}$$

Upon comparing this ABCD matrix with those for a series inductor and a series capacitor it is clear that the behavior of the microstrip line loaded with this ABCD matrix is different in different frequency ranges. Basic behaviors of any inductive or capacitive circuits are controlled by the term |B| of the corresponding ABCD matrices. For an inductor this term is monotonically increasing while for a capacitor it is monotonically decreasing.

For the present case however, behavior of the said expression (|B|= $j\omega L_0\left(2-\omega^2 L_0 C_0\right)$) is not monotonic. Rather, it increases upto a frequency (f_1

say) and then starts to decrease to reach to zero at f_2 after which it monotonically increases. So, effectively the T circuit behaves like a series inductor below f_1, like a series capacitor between f_1 and f_2 and again like a series inductor beyond f_2. This leads to an interesting property in the dispersion characteristics. Stopband attenuation increases upto f_1 then it starts decreasing to reach a minimum value before f_2 and attenuation again increases beyond f_2. Consequently, it is possible to completely eliminate a stopband by placing f_2 near a stopband. Fig. 8.8a shows the dispersion characteristics for a microstrip line (width of 2.172 mm in Arlon AD430 substrate with permittivity of 4.3 and substrate thickness 0.762 mm)

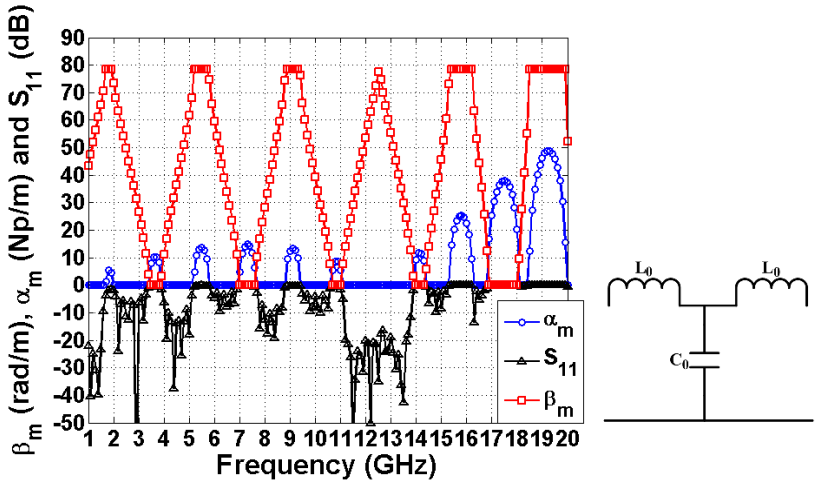

(a) (b)

Fig. 8.8: (a) phase constant, attenuation constant and S_{11} for a specific T network and (b) the lumped T network

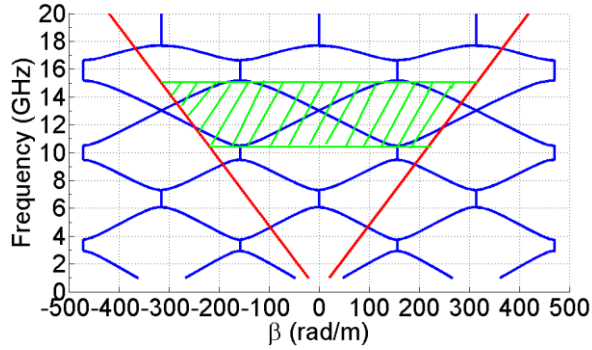

Fig. 8.9: Dual beam leaky region for the T circuit with n= -1 and n= -2 Floquet mode in the fast zone.

thickness 0.762 mm) loaded with a T circuit having L_0=1 nH and C_0=0.245 pF. Corresponding S_{11} for five unit cells terminated in 50 Ω are shown in the same figure. Evidently from Fig. 8.8a, for frequencies upto 8.1 GHz, the circuit behaves like a series inductor, between 8.1 GHz and 14 GHz it behaves like a series capacitor and beyond 14 GHz again like a series inductor. As described earlier, the stopband near 12.5 GHz is eliminated and adjacent pass bands merge to yield a wide pass band between 10 GHz and 14 GHz. Fig. 8.9 shows the complete dispersion characteristics indicative of the leaky region shaded in green.

This T equivalent circuit analysis would prove to be very effective in designing and analyzing microstrip lines loaded with similar distributed networks as well. This is discussed in the context of a stub and slot loaded microstrip line in a later section in this chapter.

8.3.2. STUBS ON MICROSTRIP LINE

8.3.2.1. Open and Shorted stubs

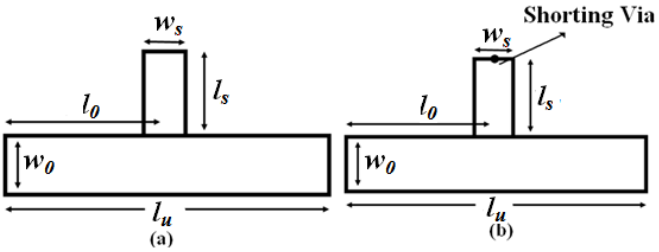

Fig. 8.10: Unit cell geometry of the stub loaded microstrip line with (a) OC stub and (b) SC stub as load

Open circuited and short circuited stubs on microstrip line behave in a similar fashion to different lumped L and C circuits discussed in the last section. To begin with, positions of various stopbands are calculated using the Bragg frequency and their multiples at

$$f_{sB} = mf_B = \frac{mc}{2L_u\sqrt{\varepsilon_{eff}}} \tag{8.2}$$

Here f_{SB} are stopband frequencies, f_B the Bragg frequency, c=3×10^{11}mm/s, L_u is the unit cell length and ε_{eff} is the effective dielectric constant of the microstrip line.

Input impedance of a stub (OC/SC) is expressed as

$$Z_{in\_oc} = Z_{0s} \tanh\left(\gamma_s L_s\right) \tag{8.3}$$

$$Z_{in\_sc} = Z_{0s} \coth\left(\gamma_s L_s\right) \tag{8.4}$$

TABLE 8.1: NATURE OF EQUIVALENT LUMPED MODEL FOR OC STUB AND SC STUB FOR VARIOUS STUB LENGTHS

Stub length range	Behavior of the OC Stub	Behavior of the SC Stub
$2m\frac{\lambda_g}{4} < l_s < (2m+1)\frac{\lambda_g}{4}$ m=0,1,2…	Shunt capacitor $C_{OC} = \frac{\tanh\gamma_S l_s}{j\omega Z_{0S}}$	Shunt inductor $L_{SC} = \frac{Z_{0S}\tanh\gamma_S l_s}{j\omega}$
$(2m+1)\frac{\lambda_g}{4} < l_s < (2m+2)\frac{\lambda_g}{4}$ m=0,1,2…	Shunt inductor $L_{OC} = \frac{Z_{0S}\coth\gamma_S l_s}{j\omega}$	Shunt capacitor $C_{SC} = \frac{\coth\gamma_S l_s}{j\omega Z_{0S}}$

For the open circuit stub case, complex propagation constant γ_m for a lossless microstrip line can be calculated from,

$$\cosh\left(\gamma_m L_u\right) = \cos\left(\beta L_u\right) - \frac{Z_0}{2Z_{0s}}\tan\left(\beta_s L_s\right)\sin\left(\beta L_u\right) \tag{8.5}$$

Here, β, β_S are the phase constants of the unloaded microstrip line and the stub respectively with Z_0 and Z_{0S} being the corresponding characteristic impedances.

An interesting observation is made near $l_S=\lambda_g/2$ and $l_S=\lambda_g/4$. The frequency at which the OC stub length is an odd multiple of $\lambda g/4$ (odd multiples of 4 GHz in Fig. 8.11a) there is a distinct stopband with highest attenuation and

widest bandwidth. On the other hand frequencies at which stub length is a multiple of of $\lambda_g/2$ (even multiples of 4 GHz in Fig. 8.11a) yield stopband with minimum almost zero attenuation, thereby merging the two nearby passbands and giving a passband of wide bandwidth. The observation is reversed for SC stubs with a wide passband for $l_S=\lambda_g/4$ and a distinct stopband for $l_S=\lambda_g/2$ (Fig. 8.11b). Attenuation profile on either side of $l_S=\lambda_g/4$ can easily be correlated to the behavior of a shunt capacitor or a shunt inductor.

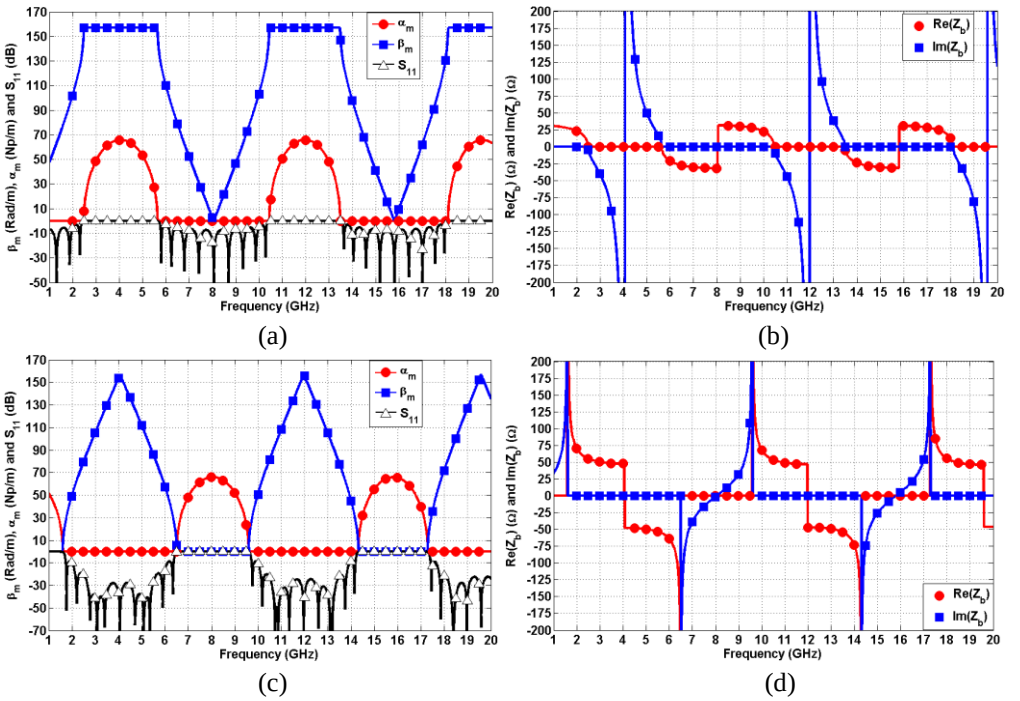

Fig. 8.11: (a) β_m , α_m and S_{11} vs. frequency, (b) real and imaginary parts of Bloch impedance for periodic OC stubs of length 10 mm. $l_S= \lambda_g/4$ near first bragg frequency at 4 GHz, (c) and (d) real and imaginary parts of Bloch impedance for periodic SC stubs of length 10 mm. $l_S= \lambda_g/4$ near first Bragg frequency at 4 GHz

Fig. 8.12 demonstrates the dispersion property (Fig. 8.11a, 8.11c) and nature of Bloch characteristic impedance (Fig. 8.11b, 8.11d) of OC and SC stub loaded microstrip line (l_u chosen as 20 mm). Stub lengths for both cases are chosen as 10 mm. Consequently, $l_S= \lambda_g/4$ is placed near the first Bragg frequency at 4 GHz. This widens the stopband near that frequency for the OC stub case (Fig.

8.11a) while completely suppressing the stopband for the SC stub case (Fig. 8.11c).

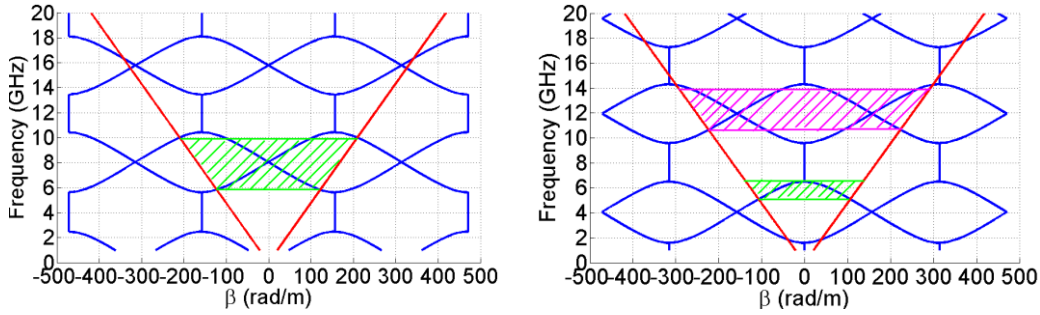

Fig. 8.12: Dispersion characteristics with the leaky fast wave region for (a) 10 mm open stub loaded line and (b) 10 mm shorted stub loaded line.

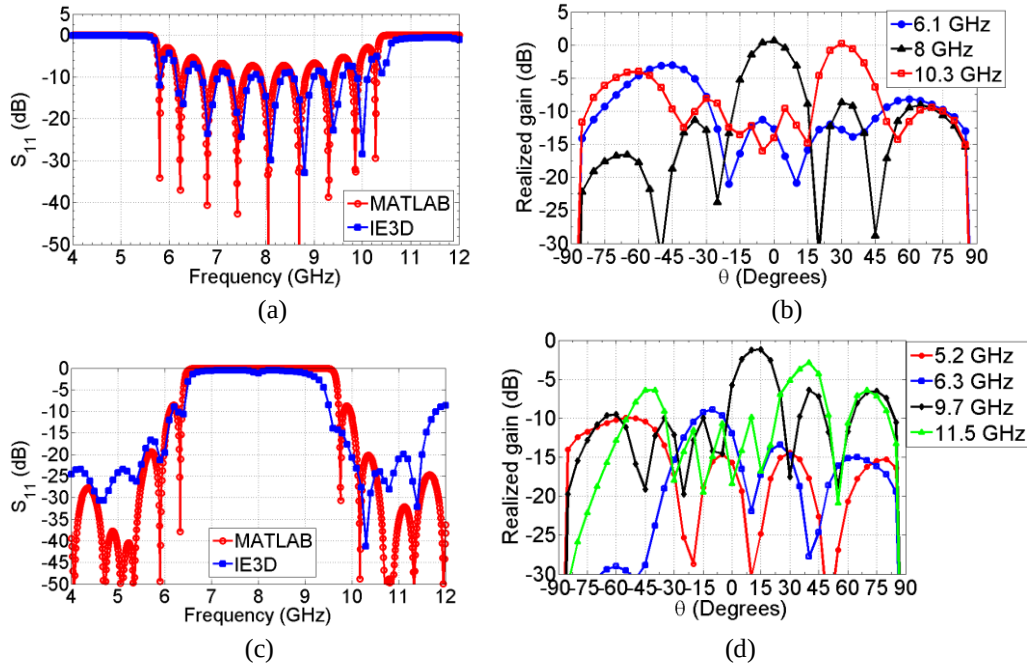

Fig. 8.13: (a) S_{11} vs. frequency and (b) Radiation pattern for the 10 mm open stub and (c) S_{11} vs. frequency and (d) radiation pattern for the 10 mm shorted stub.

Calculated dispersion characteristics of Fig. 8.12 indicate clearly the entrance of the stub loaded structure into the leaky fast wave region near 6 GHz for the open stub case and 5.5 GHz for the shorted stub case. In case of the OC stub loading the leaky n= -1 Floquet mode radiates upto 10 GHz. On the other hand, the region shaded in pink for the shorted stub case has both the n= -1 and

the n= -2 mode inside the leaky region. This leads to dual beam nature in the radiation pattern which is evident from the pattern plotted in Fig. 8.13d at 11.5 GHz

8.3.2.2. Multiple stub loading

From the observations made on the behavior of open and short circuited stubs in last section, it is evident that on using both SC and OC stubs on the same unit cell it is possible to have a repetitive resonant behavior in the loading. Also, since both stubs are in shunt, stopbands due to both (all multiples of $l_S=\lambda_g/4$) are visible in the dispersion characteristics (Fig. 8.14).

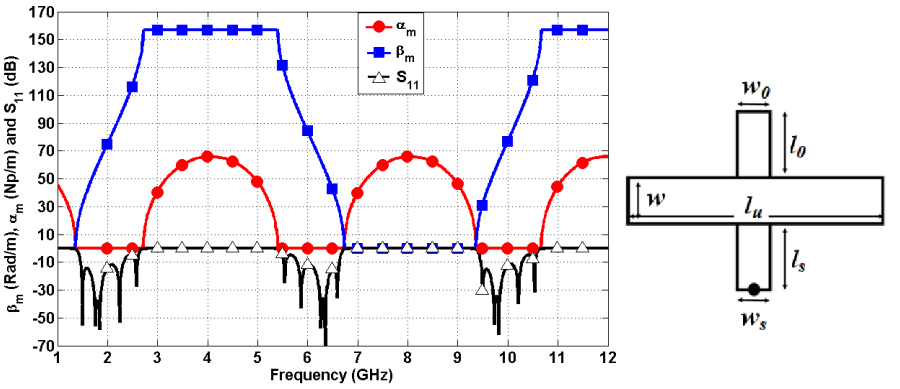

Fig. 8.14: β_m ,α_m S_{11} vs. frequency for microstrip line loaded periodically with both SC and OC stubs in the same unit cell

For observing the nature of the dispersion characteristics, the frequency range is divided into two sections, namely Region I with frequency up to f_c and Region II with frequency beyond f_c. Here f_c is the frequency at which either the OC or SC stub length is $\lambda_g/4$ whichever occurs first.

Region I ($f<f_c$):

From Table 8.1, it is clear that below f_c the OC stub can be modeled as a shunt capacitor (C_{OC}) and the SC stub can be modeled as a shunt inductor (L_{SC}). Thus, this arrangement acts like a parallel LC network placed in shunt to the microstrip line. From analysis of prototype lumped circuit as in section 8.3.1.1, we know that

there would arise a wide passband near the resonant frequency (f_0) of this equivalent LC network. Resonant frequency is given by the transcendental equation

$$f_0 = \frac{1}{2\pi\sqrt{L_{sc}C_{oc}}} \tag{8.6}$$

which can be simplified to

$$1+\frac{Z_{0\_OC}}{Z_{0\_SC}}\tanh\left(\gamma_s L_s\right)\tanh\left(\gamma_o L_o\right)=0 \tag{8.7}$$

Here Z_{0sc}, Z_{0oc} are the characteristic impedances and γ_S, γ_O are the complex propagation constants of the shorted stub line and the open stub line respectively. Corresponding stub lengths are L_0 and L_s. In the case where the stub lengths are chosen to be of equal length, i.e. $L_0 = L_S$ (=L say), and both the stubs have identical characteristic impedance, above equation is simplifies to

$$f_0 = \frac{c}{8L\sqrt{\varepsilon_{eff}}} \tag{8.8}$$

As is expected, stopbands near resonant frequency (f_0) have minimum attenuation and the nearby passbands merge to yield a wideband behavior. This is evident from Fig. 8.15a where a combination of SC and OC stubs (length of both are chosen as 2.5 mm) are used to obtain a fundamental resonant frequency of about 8 GHz. This frequency is chosen near $2f_B$ so that the stopband nearby is suppressed and we obtain a wide passband. Center frequency and bandwidth of this passband can be controlled by varying L_0 and L_s.

Region II ($f>f_c$):

For the frequency range beyond f_c, stopbands for both the SC stub as well as the OC stub are visible. Consequently, passbands in between become smaller and matching degrades. To forcibly obtain a better passband behavior in this region, L_0 and L_s must be made different, thereby pushing the stopband due to the SC stub to higher frequencies and making more room for the passband in between the two

distinct stopbands. Fig. 8.15b demonstrates this effect where OC stub length is kept constant at 10 mm ($\lambda_g/4$ for OC stub near 4 GHz). SC stub length is changed first to 8 mm and then to 5 mm. Evidently, as SC stub length decreases, the first stopband due to SC stub is shifted to 10.17 GHz and 16.27 GHz respectively. Consequently matching is improved in the passband in between near 7.5 GHz.

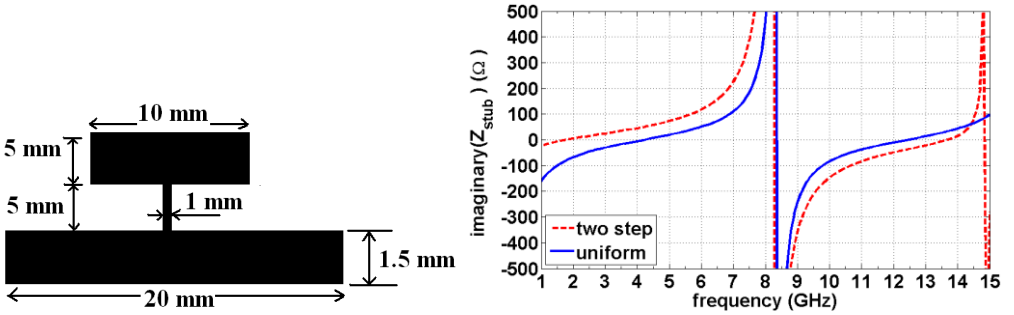

(a) (b)

Fig. 8.15: (a) The SISS geometry and (b) imaginary part of the input impedance of the stub.

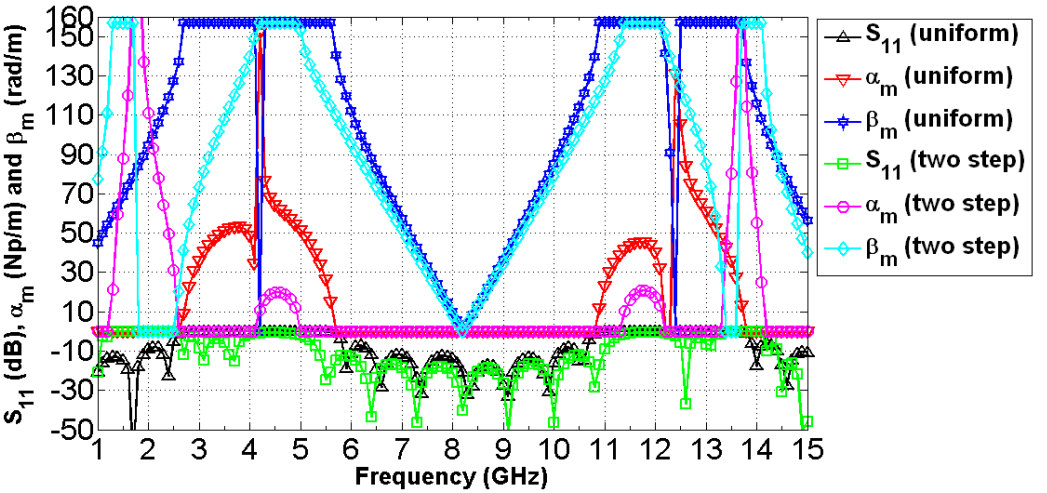

Fig. 8.16: β_m , α_m and S_{11} vs. frequency for microstrip line loaded periodically with this SISS

8.3.2.3. Stepped Impedance Shunt Stubs (SISS)

Use of stepped impedance stubs instead of simple rectangular stubs enhances the impedance bandwidth. The stepped impedance stubs is modeled as a cascade of piecewise linear segments. In Fig. 8.16c the dispersion characteristics

as well as S_{11} results for the 10 mm open circuited stub are compared with the stepped impedance shunt stub (SISS) of Fig. 16a. Evidently from Fig. 8.16c the SISS yields greater bandwidth than the uniform stub case. A fractional bandwidth of about 69% is achievable in case of the SISS while the uniform stub gives a fractional bandwidth of 58%. Primary reason behind this bandwidth enhancement is that the SISS pushes the quarter wavelength stopband (4.04 GHz for the OC stub) back to approximately 2 GHz while maintaining the half wavelength passband unperturbed. This in turn enhances the width of the passband. Input impedance of the SISS as well as that of a uniform stub is shown in Fig. 8.16b which clearly indicates this shift in zeros of the impedance function.

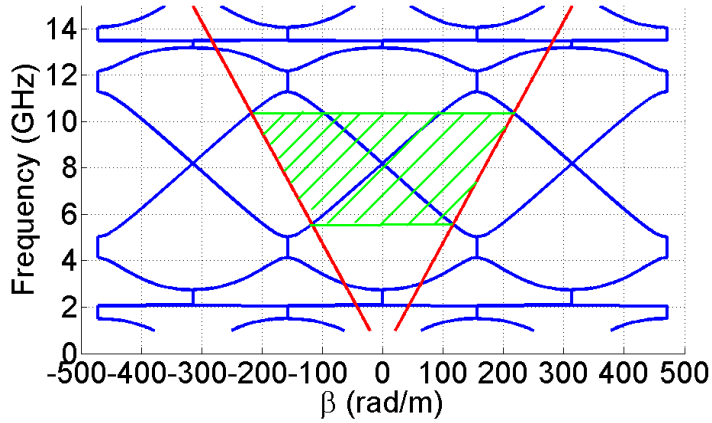

(a)

Fig. 8.17: leaky region shaded in green with the n= -1 mode radiating.

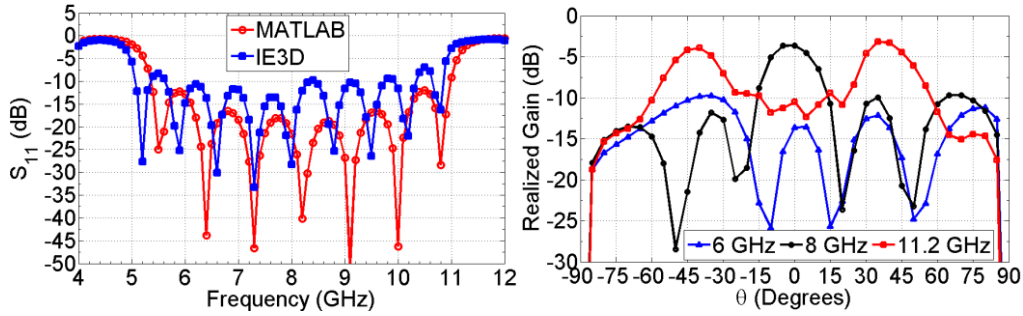

(a) (b)

Fig. 8.18: (a) S_{11} vs. frequency and (b) realized gain at three frequencies for the stepped impedance shunt stub of Fig. 8.16a.

8.3.3. SLOTS ON MICROSTRIP LINES

8.3.3.1. Notch from edge

Due to elongation of current path around the notch, the notch from the side edge (shown in Fig. 8.19a) introduces a series inductance (L_n) to the microstrip line [11].

L_n is given by the following approximate relation,

$$L_n = 2h\left(1-\frac{Z_0\sqrt{\varepsilon_{re}}}{Z_0'\sqrt{\varepsilon_{re}'}}\right)^2 \quad nH/\text{mm} \tag{8.9}$$

where ε_{re} and ε_{re}' are the effective dielectric constants for microstrip lines with widths W and W-b respectively and Z_0 and Z_0' are corresponding characteristic impedances. Here 'a' and 'b' are width and depth of the notch respectively (Fig. 8.19a). Dispersion characteristics with the leaky is shown in Fig. 8.20

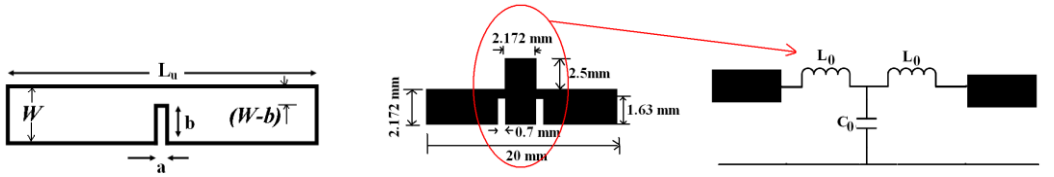

(a) (b)

Fig. 8.19: Unit cell for the (a) notch from the microstrip edge and (b) combination of stub and notches and the corresponding lumped model.

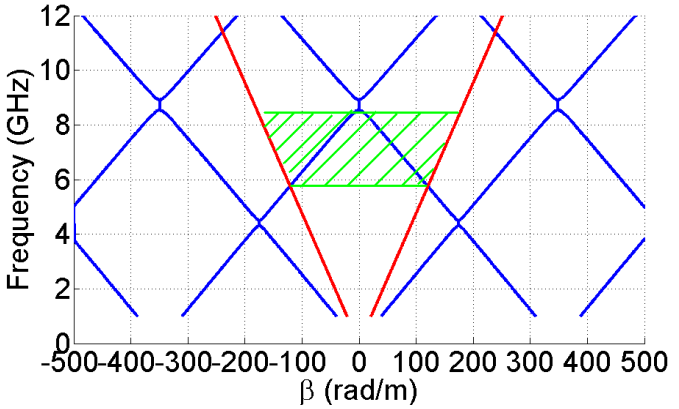

Fig. 8.20: Dispersion characteristics for microstrip line loaded with notch from the edge.

8.3.3.2. *Slot stub combinations*

This is an example of a distributed form of the T circuit discussed in section 8.3.1.3. The microstrip line geometry is loaded with a combination of stubs and notches (shown in Fig. 8.19b). Here the notches are modeled as series inductors while the open circuited stub is modeled as a shunt capacitor. Dimensions are shown in Fig. 8.19b and corresponding dispersion characteristics along with other antenna characteristics are shown in Fig. 8.21 and Fig. 8.22 respectively. respectively.

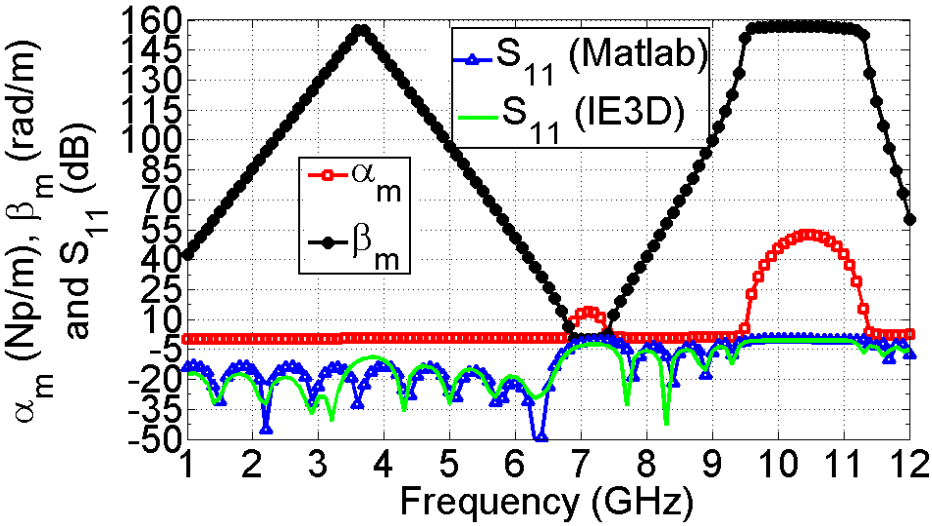

Fig. 8.21: (a) Phase constant, attenuation constant and S11 vs. frequency for the stub-notch loaded line.

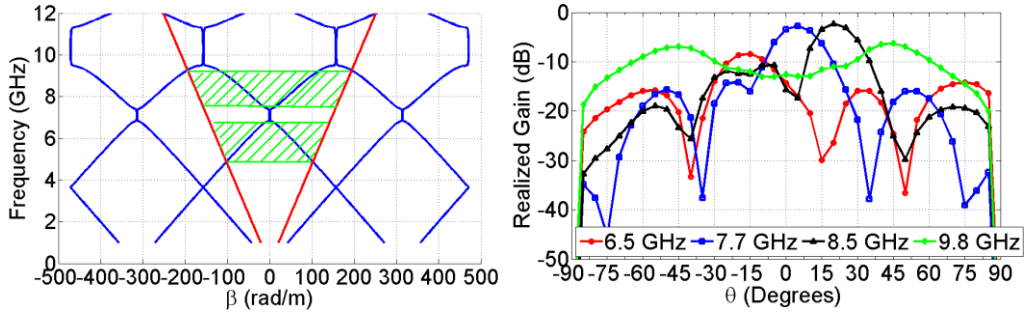

(a) (b)

8.22: (a) Dispersion characteristics with the leaky region and the radiation patterns for the stub-notch loaded line.

8.3.4. WIDTH MODULATED LINES

In this section, first an arbitrary width modulated microstrip line as periodic structures is discussed which is flowed by the effects of lumped loads and stubs on the width modulated line. Notations used are shown in Fig. 8.23a, b.

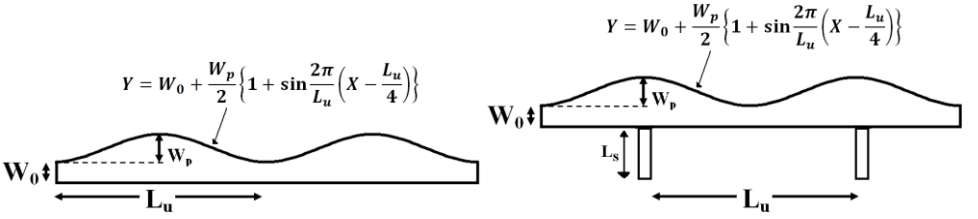

(a) (b)

Fig. 8.23: (a) Sinusoidal width modulated line and (b) stub loading in conjunction with sinusoidal width modulation.

8.3.4.1. Arbitrarily width modulated microstrip lines

Analysis of the periodic arbitrary width modulated microstrip line is performed using a piecewise uniform model [12]. Bragg frequency and consequently location of the stopbands are shifted when, instead of a series microstrip line, a continuous width modulated microstrip line is used. Amount of shift depends on the amount of width modulation. From an approximate piecewise calculation, the Bragg condition is derived as

$$\sum_{n=1}^{N} \beta_n l_n = m\pi \tag{8.10}$$

Here β_n and l_n are the phase constant and length of the n^{th} uniform subsection of the non uniform microstrip line respectively. From this, Bragg frequency (f_B) is calculated as

$$f_B = n\frac{mc}{2l_u \sum_{n=1}^{N} \sqrt{\varepsilon_{effn}}} \tag{8.11}$$

Here N is the number of subsections, l_u is the unit cell length and ε_{effn} is the effective dielectric constant of the nth subsection.

Width of a microstrip line with sinusoidal width modulation can be expressed as (Fig. 8.23a)

$$W = W_0 + \frac{W_p}{2} + \frac{W_p}{2}\sin\left\{\frac{2\pi}{l_u}\left(x - \frac{l_u}{4}\right)\right\} \tag{8.12}$$

where W_0 and (W_0+ W_p) are respectively the minimum and maximum width of the sinusoidal width modulated microstrip line and l_u is the unit cell length. It is observed that the location of the Bragg frequency is not substantially altered for small amount of width modulation. However, as the peak of the sinusoidal modulation increases, stopbands become wider and stopband attenuation increase monotonically (Fig. 8.24a).

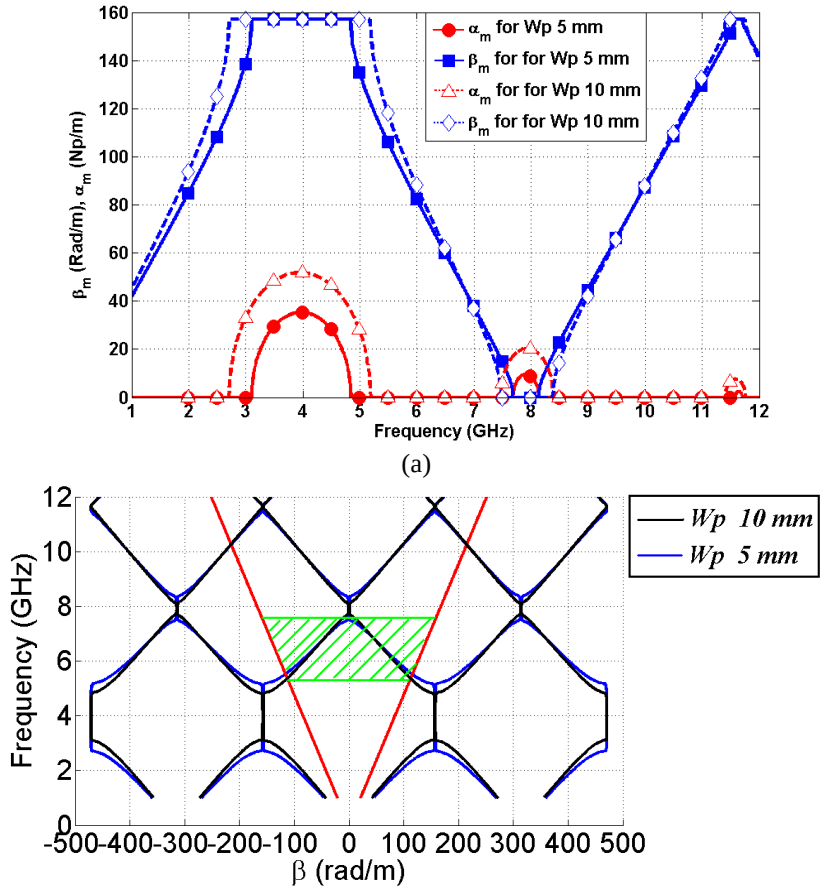

Fig. 8.24: (a) Phase constant and attenuation constant and (b) leaky region shaded in green for a sinusoidal width modulated line with peak non uniformity (Wp) of 5 mm and 10 mm.

For smaller width modulation, this modification in the propagation constant can be utilized to control the behavior of the passband and stopbands due to other periodic loads on the line such as lumped load, stubs or notch from the edge. Some of these geometries with multiple types of periodicities are discussed next.

8.3.4.2. Width modulation in conjunction with lumped loads

A sinusoidal width modulated microstrip line periodically loaded with a parallel LC circuit in shunt with respect to the line is investigated in this section.

f_0 at f_B: First, L_0 and C_0 are chosen so that resonant frequency of the parallel LC circuit is at the first Bragg frequency for the uniform periodic line with width W_0. As is expected, resonant behavior of the lumped network at f_0 shadows the stopband at f_B. Consequently we have a wideband behavior at f_0. Now, as peak of the sinusoidal width modulation (W_p) increases, attenuation at f_0 increases and consequently impedance matching degrades. As W_p increases further, attenuation in the next stopbands decreases upto a certain W_p, resulting in situation where two adjacent passbands near $2f_B$ merge to yield a very wideband behavior (Fig. 8.25a). As W_p increases further, attenuation at the stopband at $\sim 2f_B$ increases and the passbands push to the right. But after this point the sensitivity of the change in attenuation and matching is very slow.

f_0 not at f_B but near f_B: When f_0 is not at f_B but there is a little offset between them, a slight and appropriate amount of width modulation is capable of reducing the attenuation in the stopband near the first Bragg frequency considerably (Fig. 8.25b), thereby achieving better matching in that region. Thus it is observed that the width modulation is capable of controlling the passband bandwidth and consequently the matching at the passbands. However the effect is considerable only in the first two or three stopband regions. This is due to the fast diminishing nature of the attenuation for the width modulated case alone.

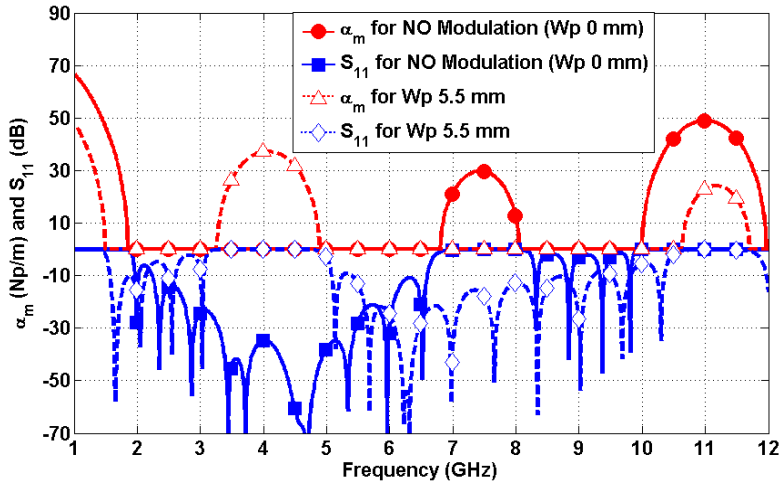

(a)

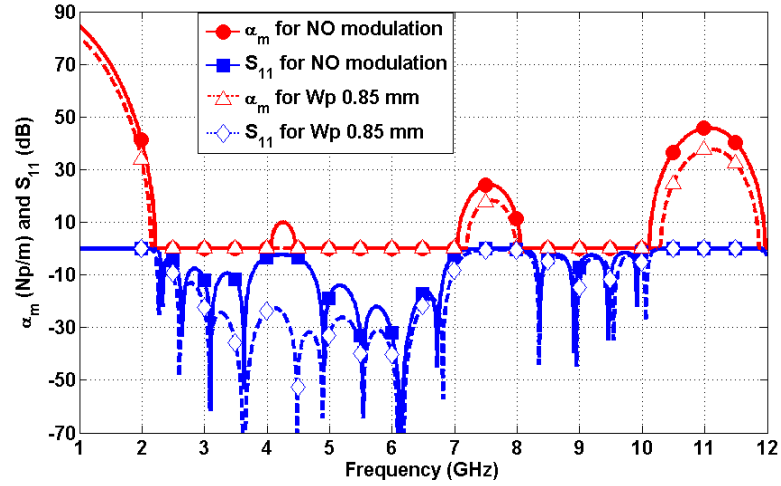

10

Fig. 8.25: (a) Resonant frequency of the parallel LC network at the first Bragg stopband and (b) resonant frequency of the parallel LC network near the first Bragg stopband but not exactly at that frequency.

8.3.4.3. Width modulation in conjunction with stub loading

To observe changes in dispersion characteristics due to width modulation, a microstrip line periodically loaded with OC stubs of 2.5 mm length is used (Fig. 8.26ba). Frequency (f_c) at which this stub length is $\lambda/4$ is 16.338 GHz. Thus we are working in the $f<f_c$ region.

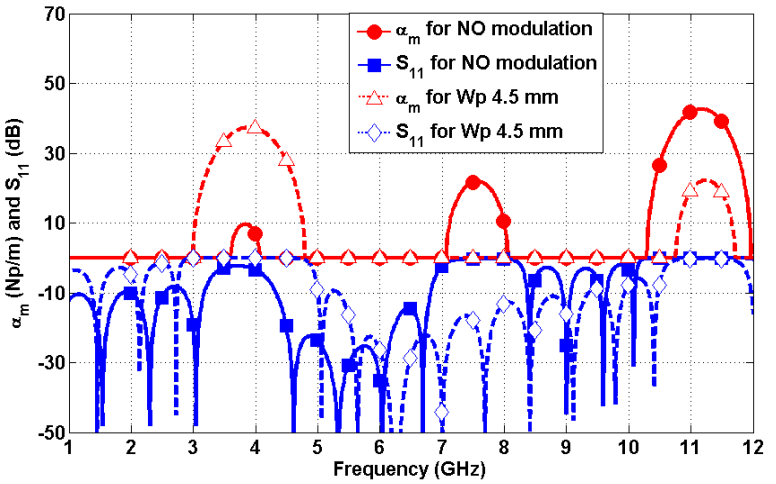

(a)

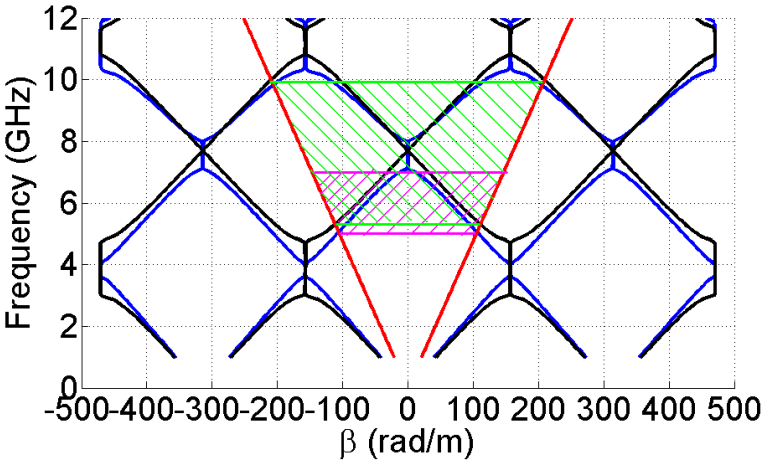

(b)

Fig. 8.26: (a) Attenuation constant and S_{11} and (b) complete dispersion characteristics with the leaky region for a width modulated line with stub loading

As is evident from Fig. 8.26b, there are stopbands at fundamental Bragg frequency (f_B=4.04 GHz) and its multiples, when there is no width modulation.

As peak (w_p) of the sinusoidal width modulation (as discussed earlier) is increased, attenuation near the first stopband keeps on increasing while that in the second stopband keeps decreasing. For an appropriate amount of width modulation (W_p= 4.5 mm for our case), attenuation in the second stopband is decreased to almost zero. Consequently, adjacent passbands merge to create a wide passband.

8.4 DESIGN GUIDELINES FOR SINGLE AND DUAL WIDEBAND LEAKY WAVE ANTENNAS

The primary objective of this section is to utilize the observations of the last sections and develop a set of design guidelines for designing leaky wave antennas with wideband, multi-band and multi-beam nature. In this regard we have used a combination of open and shorted stubs as the periodic load. The open stub is modeled as a shunt capacitor while the shorted stub acts like a shunt inductor. It is proposed that, placement of the resonant frequency of the parallel LC network thus created, by simultaneous use of the two stubs, near a Bragg stop band would suppress the corresponding stop band and merge the two adjacent pass bands to create a wide pass band. Observations in the dispersion characteristics for prediction of main radiation region are made and verified from practical measurement.

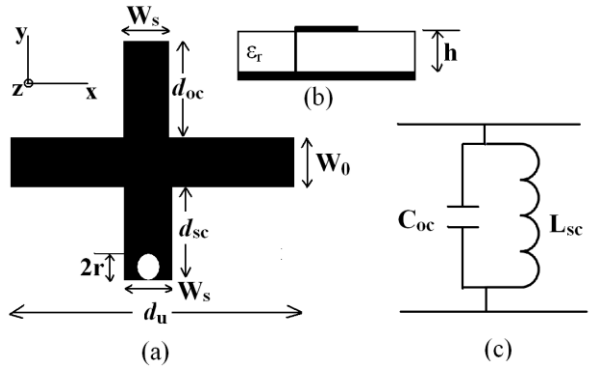

Fig. 8.27: Unit cell geometry (a) top view, (b) side view and (c) the equivalent circuit model.

8.4.1. BASIC IDEA:

8.4.1.1. Open and short circuited Stub reactance

The open stub behaves like a capacitor and the shorted stub like an inductor in the frequency range of choice. Input impedances for the open and the shorted lossless stubs are

$$Z_{in}\big|_{oc} = -jZ_{0s}\cot\beta_s d_{oc} \quad (8.13$$

$$Z_{in}\big|_{sc} = jZ_{0s}\tan\beta_s d_{sc} \quad (8.14)$$

Here Z_{0s}, β_s, d_{oc} and d_{sc} are the characteristic impedance, phase constant, length of the OC and SC stubs respectively. Corresponding values for the equivalent capacitance and inductances are calculated by comparing them with the reactance of a capacitor and an inductor as

$$C_{oc} = \frac{1}{j\omega Z_{in}\big|_{oc}} \text{ and } L_{sc} = \frac{Z_{in}\big|_{sc}}{j\omega} \quad (8.15)$$

The harmonic nature of the input impedances in (8.13) and (8.14) makes the nature of 'C_{oc}' and 'L_{sc}' harmonic as well. Consequently this model alters with frequency and the shorted stub behaves like a capacitor while the open stub behaves like an inductor. The effective circuit response remains equivalent to a parallel LC network connected in shunt.

8.4.1.2. Periodic structure analysis

Application of the Floquet's theorem to the periodic structure created by the unit cell shown in Fig. 8.27a leads to [13].

$$\cosh\gamma_p d_u = \cos\beta d_u + \frac{jZ_0 Y_{in}}{2}\sin\beta d_u \quad (8.16)$$

Here d_u is the unit cell length of the periodic structure and $Y_{in} = \frac{1}{Z_{in}\big|_{sc}} + \frac{1}{Z_{in}\big|_{oc}}$.

Using (8.13), (8.14) and (8.15), (8.16) can be written as follows

$$\cosh\gamma_p d_u = \cos\beta d_u + \frac{Z_0}{2}\frac{1-\omega^2 L_{sc}C_{oc}}{\omega L_{sc}}\sin\beta d_u \quad (8.17)$$

Here $\gamma_p=\alpha_p+j\beta_p$ is the complex propagation constant of the periodic structure and β is the phase constant of the unloaded line. Phase constants for the fundamental and higher order Floquet modes are calculated using the general solution of the form

$$\beta_p = \beta_0 + \frac{p\pi}{d_u}, \text{ where } p = 0, \pm 1, \pm 2, \ldots \tag{8.18}$$

Here β_0 (= β) is the phase constant of the unloaded microstrip line given by $\beta_0 = \omega\sqrt{\varepsilon_{eff}}\,/\,c$ where ε_{eff} is the effective dielectric constant of the substrate underneath the unloaded line.

8.4.1.3. Positioning of f_r around nf_B

It is evident from (8.17), when $1-\omega^2 L_{sc}C_{oc}$ =0, i.e. at the resonant frequency (f_r) of the parallel LC circuit shown in Fig. 8.27c, the load virtually vanishes. A forced pass band takes precedence at that frequency. Placement of this resonant frequency or its harmonic repetitions near the fundamental or higher order Bragg stop bands (nf_B) would then lead to elimination of the corresponding stop band. This would in turn give rise to a very wideband response.

Now, these resonant frequencies of the equivalent parallel LC network are given by the transcendental equation

$$f_r = \frac{1}{\sqrt{L_{sc}C_{oc}}} \tag{8.19}$$

The above condition can also be deduced from the input impedances of the two stubs with Y_{in}=0, which would in turn lead to

$$\tan\beta_{sc}d_{sc}\,\tan\beta_{oc}d_{oc} = \frac{Z_{0\_oc}}{Z_{0\_sc}} \tag{8.20}$$

Here Z_{0_oc} and Z_{0_sc} are the characteristic impedances of the open stub and shorted stubs respectively and $\beta_{sc} = 2\pi f\sqrt{\varepsilon_{eff\_sc}}\,/\,c$ and $\beta_{oc} = 2\pi f\sqrt{\varepsilon_{eff\_oc}}\,/\,c$ where ε_{eff_sc} and ε_{eff_sc} are the effective dielectric constants calculated from the widths of the shorted stub (W_{sc}) and open stub (W_{oc}) respectively.

Using stubs of identical lengths and widths simplifies above equation and the stub lengths (considering the principal values only) are calculated as $\lambda_g/8$ and $3\lambda_g/8$.

However solution of (8.20) becomes complicated when the practical shorting scheme using a metallic via is considered for the shorted stub. In this case, the via is modeled as a shunt inductor with impedance expressed as [14]

$$Z_{via} = jw\frac{\mu_0}{4\pi}\left[h\ln\left\{\frac{h+\sqrt{r^2+h^2}}{r}\right\}+1.5\left\{r-\sqrt{r^2-h^2}\right\}\right] \tag{8.21}$$

Input impedance for the shorted stub is then calculated by considering the impedance of (8.21) as load and using standard impedance transformation relation as follows

$$Z_{in}\big|_{sc} = Z_{0s}\frac{Z_{via}+jZ_{0s}\tan\beta_s d_{sc}}{Z_{0s}+jZ_{via}\tan\beta_s d_{sc}} \tag{8.22}$$

(8.13) and (8.22) are now used to calculate the condition for Y_{in} =0. After some simplification, this leads to the following equation

$$\tan\beta_s\left(d_{oc}+d_{sc}\right)=\frac{jZ_{0s}}{Z_{via}} \tag{8.23}$$

Using d_{oc}=d_{sc}=d, as a simplifying approximation, 'd' can be calculated from this (8.23).

It is clear from the harmonic nature of L_{sc} and C_{oc} in (8.15) that multiple resonances can be obtained by appropriately choosing the stub lengths. Summation of stub lengths ($d_{oc}+d_{sc}$) required for two such resonant frequencies placed at f_0 and $3f_0$, are calculated from the following two equations where (d_{oc}+d_{sc}) must simultaneously satisfy (8.24) and (8.25).

$$\tan\beta_{s1}\left\{d_{oc}+d_{sc}\right\}=\frac{jZ_{0s}}{Z_{via1}} \tag{8.24}$$

$$\tan\beta_{s2}\left\{d_{oc}+d_{sc}\right\}=\frac{jZ_{0s}}{Z_{via2}} \tag{8.25}$$

Here subscript '1' and '2' indicate the parameters at frequencies f_0 and $3f_o$ respectively.

It is to be noted here that during simulation or practical designing, d_{oc} would not be the physical length of the open stub. It includes length extension (ΔL) due to fringing at the open end. Consequently, $d_{oc}|_{physical}$ is chosen to be $d_{oc} + \Delta L$. On the other hand, the shorted stub length (while using a cylindrical metallic via for shorting) is calculated as $d_{sc}|_{physical} = d_{sc} + r_{via}$. Here $d_{sc}|_{physical}$ is the physical length of the stub and r_{via} is the via radius.

8.4.1.4.Higher order Floquet modes and leaky region

Observations regarding the radiation region and the beam scanning properties of the geometry are made from the dispersion characteristics calculated from (8.17) and (8.18). Higher order Floquet modes are plotted by varying m=±1, ±2… in (8.18). β_0 is calculated from the principal solution of (8.17). The free space dispersion characteristics (k_0 vs. frequency) are also plotted on the same graph. As was discussed in detail in chapter 6, regions where $\beta < k_0$ are leaky regions.

Systematic design steps for obtaining leaky wave microstrip line antennas (LWMLA) with specified centre frequencies are discussed in the following sections.

8.4.2. DESIGN GUIDELINES

8.4.2.1. Steps for designing a wideband LWMLA with centre frequency at f_0

Step 1: Unit cell length (d_u) is chosen so that the first Bragg stop band is near $f_0/2$. This places the second stop band ($2f_B$) near f_0.

Step 2: We intend to place the resonant frequency of the double stub near f_0. For this, first, (8.23) is solved with $\beta = 2\pi f_0 / v_p$ .where v_p is the phase velocity in the substrate underneath the stub. This yields

$$d_{oc} + d_{sc} = \frac{1}{\beta_s} \tan^{-1} \frac{jZ_{0s}}{Z_{via}} \tag{8.26}$$

Stub lengths ('d') are calculated by assuming $d_{oc} = d_{sc} = d$ Width of the microstrip line and that of the stubs are taken as same.

Step 3: Characteristic impedance of the microstrip line (Z_0) is varied and corresponding Bloch characteristic impedance (Z_B) is observed. W_0 is calculated by minimizing (Z_B-50 Ω) so as to achieve optimal matching.

8.4.2.2. Steps for designing a dual wideband LWMLA with centre frequencies near f_0 and $3f_0$.

Step 1: Unit cell length (d_u) is chosen so that the first Bragg stopband is near f_0. This places the third stop band ($3f_B$) near $3f_0$.

Step 2: We intend to place the two resonant frequencies of the double stub near f_0 and $3f_0$. For this, first, (8.24) and (8.25) are solved with $\beta_1 = 2\pi f_0 / v_p$ and $\beta_2 = 6\pi f_0 / v_p$. The general solution of (8.24) and (8.25) can be written as

$$(d_{oc} + d_{sc})_1 = \frac{n\pi + \tan^{-1} \frac{jZ_{0s}}{Z_{via1}}}{\beta_{s1}},\ n = 0,1,2... \tag{8.27}$$

$$(d_{oc} + d_{sc})_2 = \frac{p\pi + \tan^{-1} \frac{jZ_{0s}}{Z_{via2}}}{\beta_{s2}},\ p = 0,1,2... \tag{8.28}$$

An exact solution of (8.27) and (8.28) can be found with n=0 and p=1 only when Z_{via1}= Z_{via2}=0 (i.e. an ideal shorting stub).

To find a solution of (8.27) and (8.28) in approximate manner, we have taken average of the closest solutions of (8.27) and (8.28). We obtain

$$d_{oc} + d_{sc} = \frac{(d_{oc} + d_{sc})_{b1} + (d_{oc} + d_{sc})_{b2}}{2} \tag{8.29}$$

Here $(d_{oc} + d_{sc})_{b1}$ and $(d_{oc} + d_{sc})_{b2}$ are respectively the solutions of (8.27) and (8.28) that are closest to each other.

Step 3: Now that the resonant frequencies of the dual stub combination are placed properly to eliminate the stop bands at those frequencies. However, there is the issue of impedance matching near the pass bands. To obtain optimal impedance matching, Bloch impedances at the two frequencies (f_0 and $3f_0$) are to be flattened and brought near the characteristic impedance of the unloaded line. To do this, the following function (F) is minimized by varying d_{oc}.

$$F = \max\left(\left\|Z_{B1}(< f_0)\right| - Z_0\right|, \left\|Z_{B2}(< 3f_0)\right| - Z_0\right|\Big) \tag{8.30}$$

Here $Z_{B1}(<f_0)$ and $Z_{B2}(<3f_0)$ indicate the Bloch impedances at a frequency just below f_0 and 3 f_0 respectively. This function 'F' brings both Z_{B1} and Z_{B2} simultaneously closer to the characteristic impedance of the unloaded line (Z_0). This step accurately yields d_{oc}.

Step 4: Step 3 would only bring Z_{B1} and Z_{B2} simultaneously as close as possible to Z_0 (which is initially set to 50 Ω). Values of Z_{B1} and Z_{B2}, however, might not finally be near 50 Ω. To alleviate this problem and improve matching and bandwidth further, W_0 is varied so as to bring Z_B closer to 50 Ω.

8.4.2.3. Steps for designing a dual-beam LWMLA with centre frequency at f_0.

A dual beam leaky wave antenna can be designed by choosing to operate in a pass band where two different Floquet modes are simultaneously inside the fast wave region (both the n= -1 and n=-2 for example).

Following the steps outlined for single band antenna, a dual beam scanning leaky wave antenna around f_0 can be designed by placing the first Bragg stop-band near $f_0/3$. Next (8.26) is used to calculate the necessary stub lengths. Rest of the steps are as explained in the single band case.

These guidelines would act as starting point for designing single or dual band leaky wave antennas. Approximate values for stub length, widths, as well as the length and widths of the host lines are predicted. However, final practical design with cylindrical metallic vias necessitates the stub lengths to be tuned a little during full wave simulation for accurate placement of the resonant frequency of the stub combination.

8.4.3. SIMULATION AND OBSERVATIONS

8.4.3.1. Wideband Leaky Wave Antenna

We intend to design a wideband leaky wave antenna with center frequency near 8.4 GHz. Design steps using the guidelines defined in the previous section are illustrated below.

First, the Bragg frequency for the periodic structure is placed near 4.2 GHz by choosing unit cell length of 19.2 mm (substrate parameters as mentioned in subsection 8.3.1) using the equation

$$d_u = \frac{3\times10^8}{2 f_B \sqrt{\varepsilon_{eff}}} \tag{8.31}$$

Line width is taken initially as 1.5 mm which corresponds to a 50 Ω microstrip line in the substrate chosen.

Next, lengths for both the shorted and open stubs are taken as d_{oc}. d_{oc} is calculated from (8.26) at the resonant frequency of 8.4 GHz and is found to be 2.25 mm. A better matching near this wide pass band centered around 8.4 GHz is found by controlling the width of the host line W_0 (=W_s). As shown in Fig 8.28, choosing W_0=1 mm brings Z_B closest to 50 Ω for this case.

After inclusion of the cylindrical metallic via of 0.3 mm in the final design, the optimal physical stub lengths are found to be d_{oc}=1.7 mm and d_{sc} = 3.1 mm (Effective lengths in calculation are approximately d_{oc} = 2 mm and d_{sc} = 2.5 mm).

Simulated and measured S_{11} (five unit cells of the dual stub structure shown in Fig. 8.37a) shown in Fig 8.29a indicate that the stop band near 8.4 GHz has been eliminated and a wide pass band is obtained with start and stop frequencies at around 5.89 GHz and 11.57 respectively.

Observations on the radiation characteristics of the antenna are made from the dispersion characteristics of the unit cell. 'β_m' is plotted by varying 'm' as m=0,±1, ±2 etc. β_0 is taken as the principal solution of (8.18). This dispersion characteristic is shown in Fig 8.29b. Solutions for various 'm' are shown in blue line. The sign in the superscript here indicates the slope of corresponding mode i.e. m= -1^+ indicates the dispersion characteristic of the m= -1 mode having positive group velocity. The triangular region shaded in grey is the radiation region (i.e. the fast wave region with $\beta<k_0$). The region shaded in green (cross shading) indicates desired pass band. Point 'A' indicates the frequency at which the structure starts to radiate (around 6 GHz).

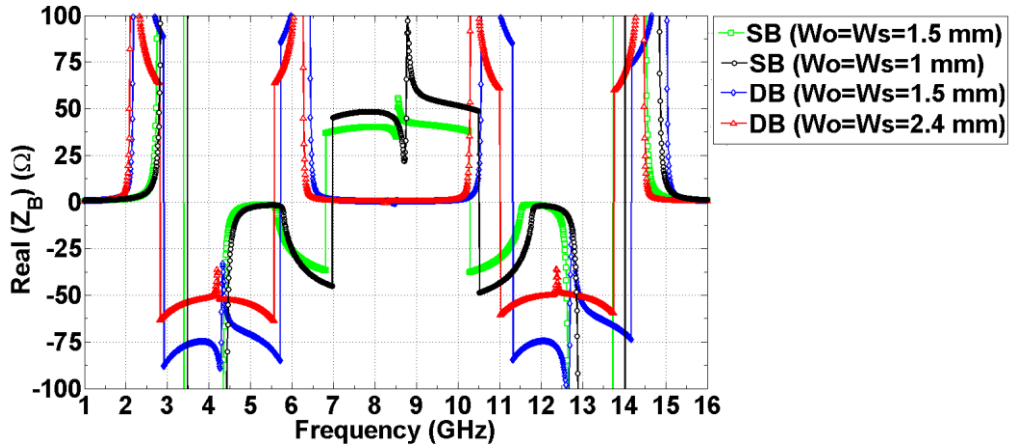

Fig. 8.28: Variation of real part of Z_B with frequency for different line width for the single band antenna

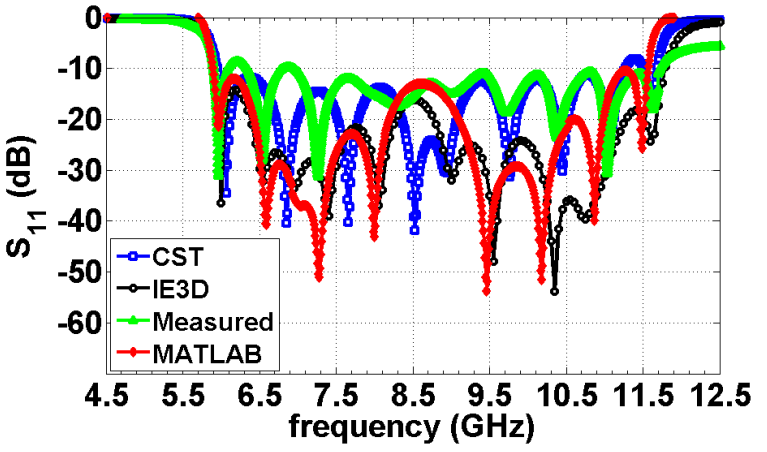

(a)

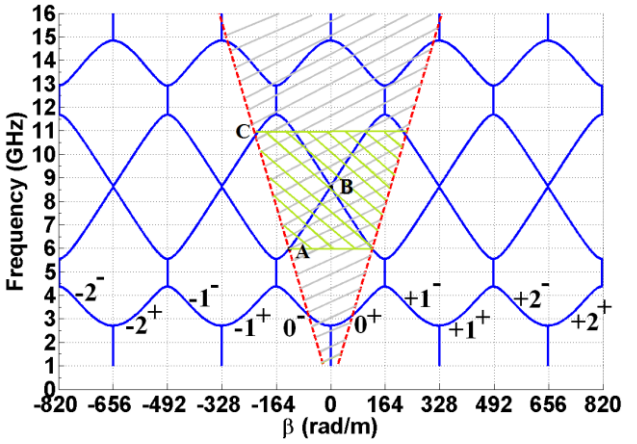

(b)

Fig. 8.29: (a) simulated and measured S_{11} with frequency and (b) calculated dispersion characteristics with point A, B and C indicating the entry into the radiation region, broadside radiating frequency and end frequency for the band respectively for the single band antenna with unit cell geometry of Fig. 8.37a.

It should be noted that the stop band edge located at 5.55 GHz is quite close to the frequency at which the structure enters the leaky fast wave region (which is near 6GHz). Since the antenna is fed from only one port and the other end is terminated, contribution to radiation is considered from modes with positive group velocity only (i.e. modes with positive slope). Near 6 GHz, only one mode is inside the leaky region (m= -1^+), but the n=0^+ mode passes very close to the fast wave region (Fig. 8.29b) and is considered to be only slightly slow at that frequency. This leads to a lack in distinct main lobe and increased side lobe

level. This is observable in radiation pattern of Fig. 8.31a. However, as we move to higher frequencies i.e. away from the stop band at 5.55 GHz, the main lobe becomes distinct as the n=0 mode moves further away from the fast wave region and interaction between multiple Floquet modes is reduced. A plot of the side lobe level vs. frequency for the single band antenna is shown in Fig. 8.30. It is clear that the side lobe level decreases as the frequency gets further away from the stop band, thereby giving a distinct main lobe. On the other hand, as we approach the other end of the stop band (nearing 11.5 GHz), there is another Floquet mode with positive group velocity (m= -2^{+}) that enters the leaky fast wave region. This introduces another main lobe in the radiation pattern.

Simulated and measured normalized radiated far fields for frequencies in the range 6 GHz to 11 GHz are plotted in Fig. 8.31 for the $\varphi=0^{0}$ plane (x-z plane) and in Fig. 8.32 for the $\varphi=90^{0}$ plane (y-z plane). A main beam scanning of -55^{0} to 33^{0} for the frequency range of 6 GHz to 11 GHz with broadside radiation near 8.6 GHz is observed.

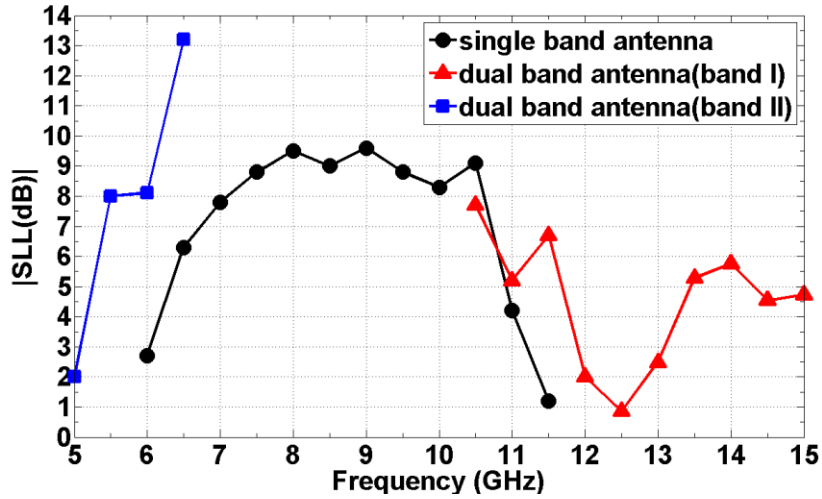

Fig. 8.30: Side lobe level with frequency for the both the single and the double band antenna.

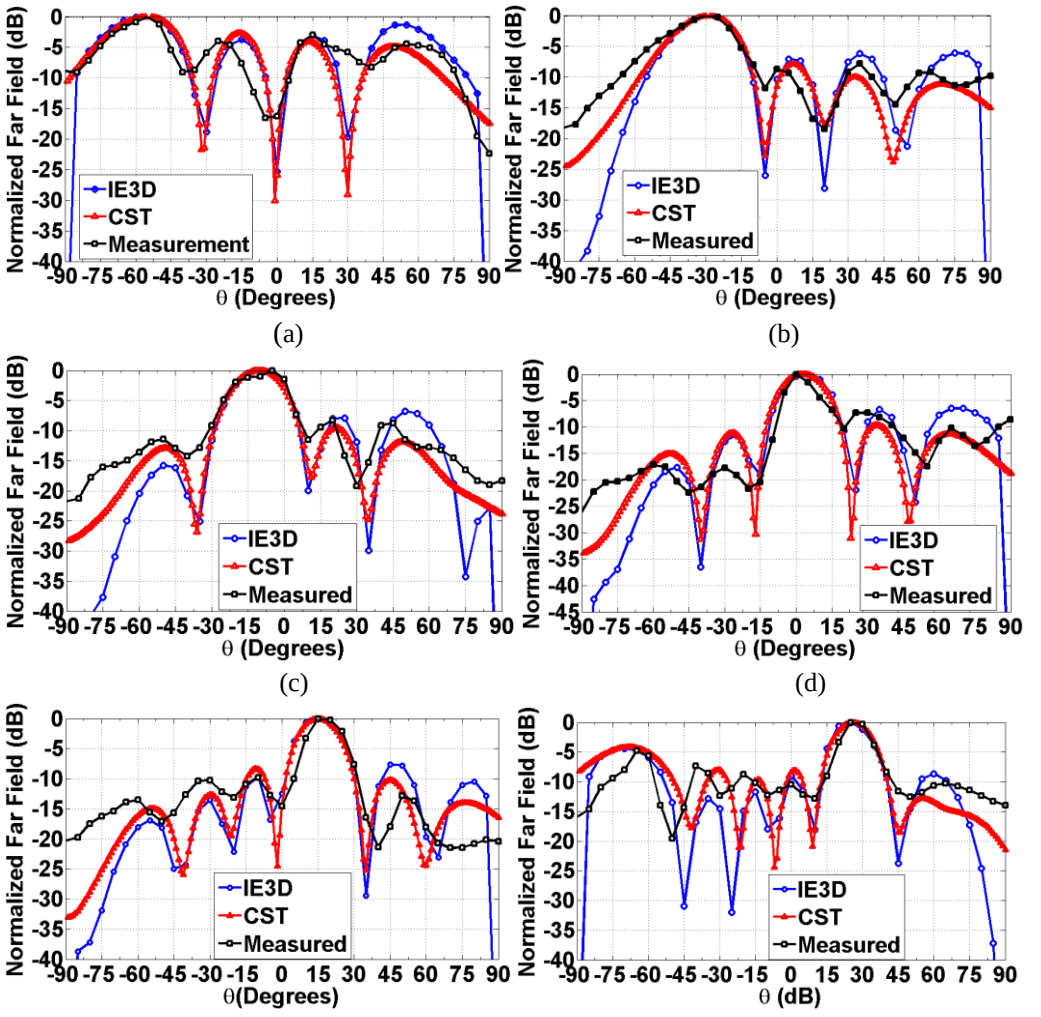

Fig. 8.31: Simulated and measured radiation patterns in the $\varphi=0^0$ plane i.e. the x-z plane at (a) 6 GHz, (b) 7 GHz, (c) 8 GHz, (d) 9 GHz, (e) 10 GHz and (f) 11 GHz for the single band antenna.

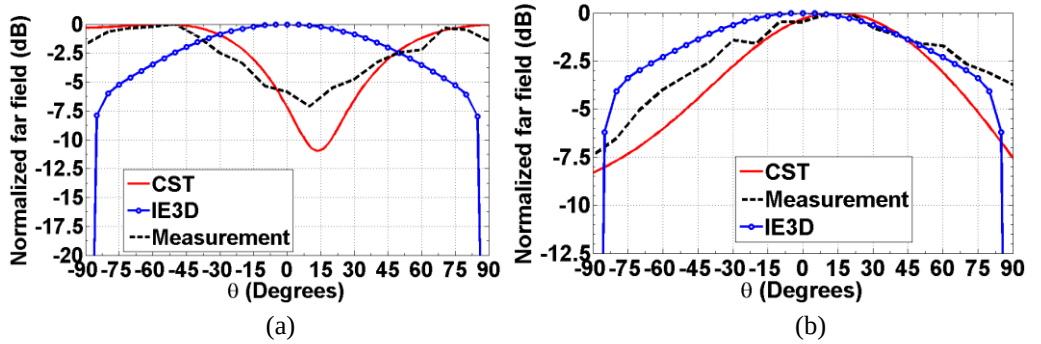

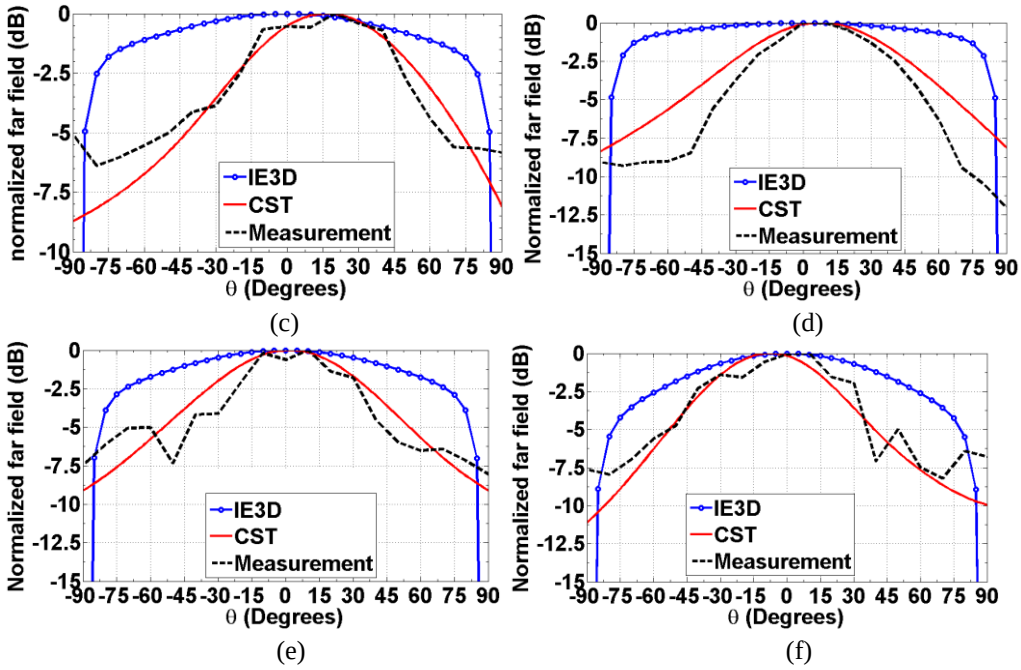

Fig. 8.32: Simulated and measured radiation patterns in the $\varphi=90^0$ plane i.e. the y-z plane at (a) 6 GHz, (b) 7 GHz, (c) 8 GHz, (d) 9 GHz, (e) 10 GHz and (f) 11 GHz for the single band antenna.

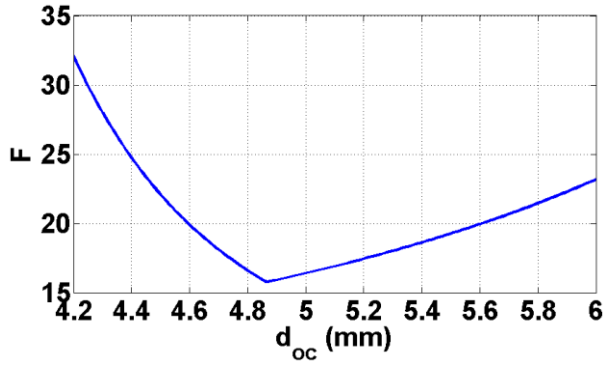

Fig. 8.33: Variation of F as expressed in (8.30) with the open stub length.

8.4.3.2. Multiband Leaky Wave Antenna

In this section, we intend to design a dual band leaky wave antenna with center frequencies near 4.25 GHz and 12.75 GHz. Design steps using the guidelines defined in section 8.3 are illustrated below. Unit cell length for the periodic line is kept at 19.2 mm as before. Line width is initially taken as 1.5 mm. However, an investigation of the Bloch impedance indicates that Z_B is greater than 50 Ω in this condition. Thus, W_0 (=Ws) is reduced further and a choice of W_0 (=W_s) =2.4 mm brings the Bloch impedance close to 50 Ω. Following the design steps outlined in the section 8.3, first, (d_{oc}+d_{sc}) is calculated from (8.27) with n=0

and is found to be 8.94 mm. (d_{oc}+d_{sc}) calculated from (8.28) with p=1 is then calculated as 8.79 mm. Finally (d_{oc}+d_{sc}) is thus taken as 8.87 mm. Next, d_{oc} is calculated by minimizing 'F' expressed in (8.30). Variation of this factor with d_{oc} is shown in Fig. 8.33.

d_{oc} calculated from the minimum value of the factor '*F*' is found to be 4.87 mm. After inclusion of the metallic via of 0.3 mm radius in the final design, the optimal physical stub lengths for fabrication are found to be 4.2 mm and 3.875 mm (Effective lengths in calculation are approximately 4.87 mm and 4 mm). Widths of the microstrip line as well as that of the stubs are tuned to obtain optimal matching in the simulation.

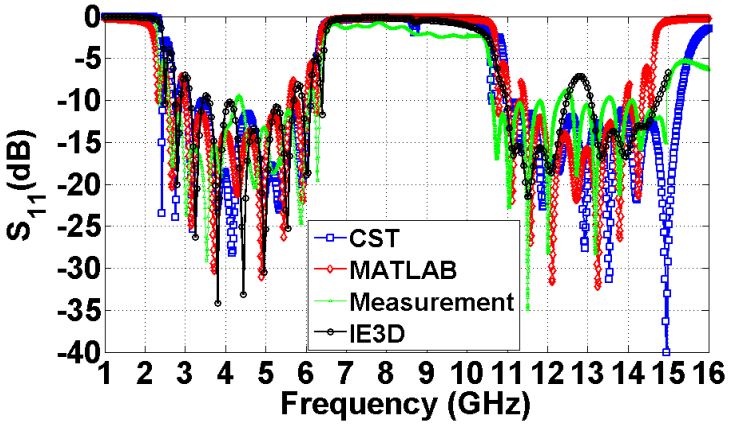

(a)

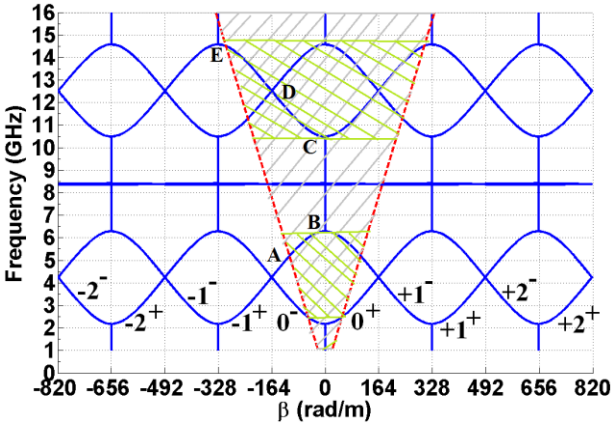

(b)

Fig. 8.34: (a) Simulated and measured S_{11} vs. frequency and (b) calculated dispersion characteristics with points A, B, C, D, E marked as entry of the first pass band into the radiation region, end frequency of the first band, entry of the second pass band into the radiation region, dual beam region in the second pass band and the end frequency of the second pass band respectively for dual band antenna.

Simulated and measured S_{11} shown in Fig. 8.34a clearly indicate the two pass-bands in the range 2.3 GHz to 6.5 GHz and 10.7 GHz to 14.7 GHz. The dispersion characteristics involving higher order Floquet modes are shown in Fig 8.34b. Blue lines indicate the β vs. frequency plots corresponding to different 'm' as indicated in (8.18). β_0 is taken as principal solution of (8.17).

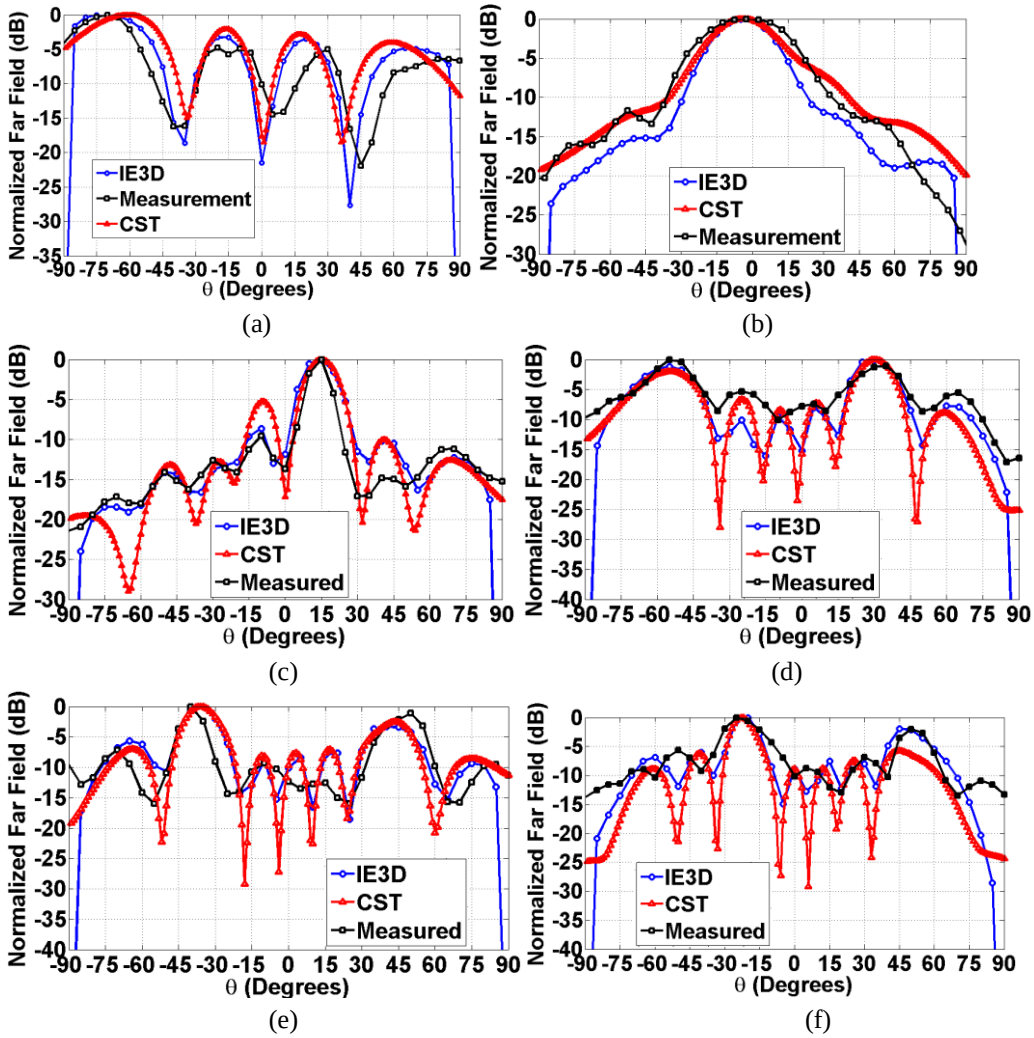

Fig. 8.35: Simulated and measured radiation patterns in the $\varphi=0^0$ plane i.e. the x-z plane at (a) 5 GHz, (b) 6.5 GHz, (c) 11 GHz, (d) 12 GHz, (e) 13 GHz and (f) 14 GHz for the dual band antenna.

Main radiating Floquet mode here is the m= -1^+ with minor interference from $n=0^+$ near 5 GHz. As shown in Fig. 8.30, side lobe level gets better with increasing frequency. On the other hand, for the second band at around 12.6 GHz,

Floquet modes corresponding to m= -1^{+} and m= -2^{+} space harmonics exist simultaneously inside the leaky fast wave region leading to a dual beam nature around this frequency.

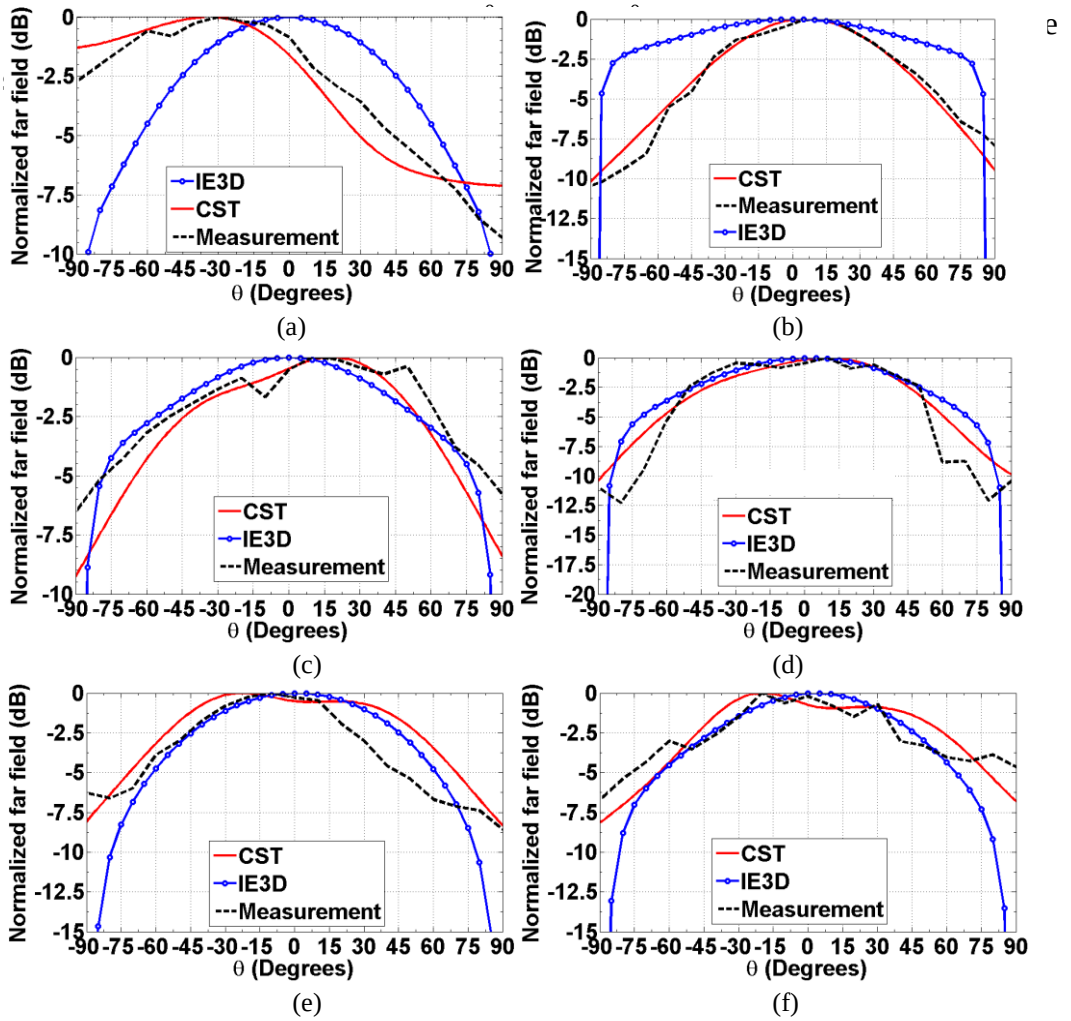

Fig. 8.36:Simulated and measured radiation patterns in the $\varphi=90^{0}$ plane i.e. the y-z plane at (a) 5 GHz, (b) 6.5 GHz, (c) 11 GHz, (d) 12 GHz, (e) 13 GHz and (f) 14 GHz for the dual band antenna.

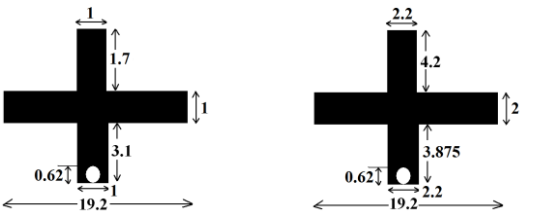

Fig. 8.37: (a) The single band and (b) the dual band cell geometry.

TABLE 8.2: MAIN LOBE DIRECTION WITH FREQUENCY FOR THE TWO ANTENNAS

Frequency (GHz)	Single band antenna			Dual band antenna		
	β/k_0	Main lobe direction (θ_m) (Calc.) $Sin^{-1}(\beta/k_0)$	Main lobe direction (θ_m) (Sim.)	β/k_0	Main lobe direction (θ_m) (Calc.) $sin^{-1}(\beta/k_0)$	Main lobe direction (θ_m) (Sim.)
5	-	-	-			-71.6
5.5	-	-	-	-0.781	-51	-45.2
6	-0.987	-80	-55.56	-51.7	-24	-25.46
6.5	-0.721	-46	-39.98	0	0	-5.09
7	-0.507	-30.4	-29.8	-	-	-
7.5	-0.326	-19	-19.2	-	-	-
8	-0.169	-9.73	-10	-	-	-
8.5	-0.029	-1.66	-4.34	-	-	-
9	0.088	5.02	4.94	-	-	-
9.5	0.198	11.4	10	-	-	-
10	0.298	17.32	15.12	-	-	-
10.5	0.391	22.98	19.9	-	-	-
11	0.480	28.69	25	0.3	17.5	14.2
11.5	0.58	35.45	30.1	0.43	25.48	22.14
12	0.651	40.61	33.99	-0.77, 0.532	-50.3, 32.2	-54.5, 28.96
12.5	-	-	-	-0.625, 0.625	-38.68, 38.68	-44.86, 34.6
13	-	-	-	-0.499, 0.703	-29.9, 44.67	-35.2, 40.32
13.5	-	-	-	-0.375, 0.782	-22, 51.47	-29.5, 42
14	-	-	-	-0.25, 0.867	-14.42, 60.1	-21.58, 47.1
14.5	-	-	-	-	-	-14.76, 54.51

Main beam directions at different frequencies for the two structures are shown in Table 8.2. It also includes an approximately calculated estimation of the main lobe direction using

$$\theta_m = \sin^{-1}\left(\beta / k_0\right) \tag{8.32}$$

Variation of maximum realized gain (using method of moment based full wave solver) with frequency for different number of unit cells of the single and dual band geometry are shown in Fig. 8.38a and Fig. 8.38b respectively. Both figures indicate that the overall antenna gain can be increased by increasing the number of unit cells being considered for fabrication, as expected. We have fabricated and measured prototype antennas with five unit cells (shown in Fig. 8.39a and Fig. 8.39b) to demonstrate the effectiveness of the design guidelines presented herein.

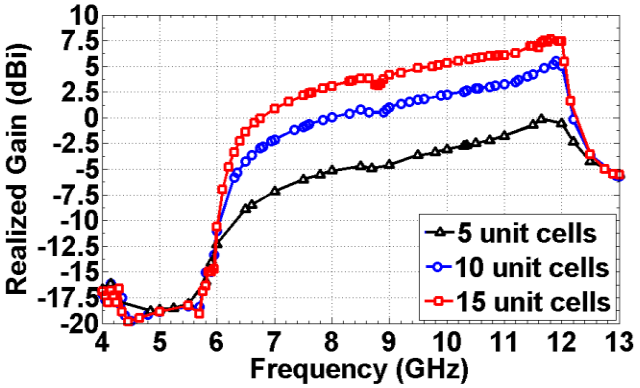

(a)

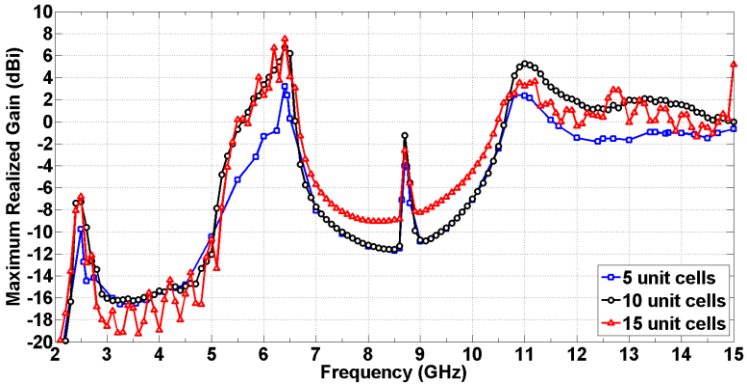

(b)

Fig. 8.38: Maximum realized gain vs. frequency for the (a) single band geometry and the (b) dual band geometry for different number of unit cells

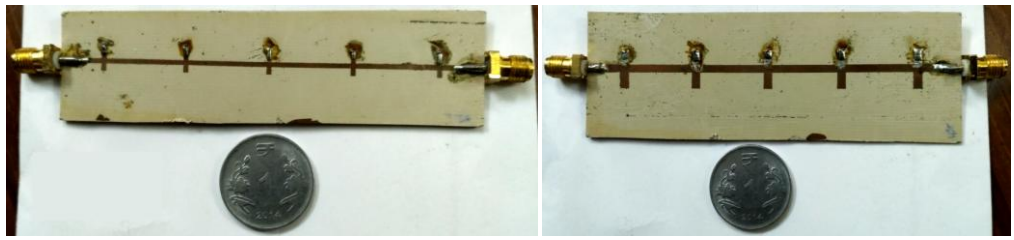

(a) (b)

Fig. 8.39: Fabricated prototypes for the (a) single band antenna and (b) the dual band antenna.

A tabulation of simulated and measured realized gain of the two antennas are shown in Table 8.3.

Table 8.3: Simulated and measured realized gain for the two antennas.

Frequency (GHz)	Single band antenna		Dual Band antenna	
	Simulated Gain	Measured Gain	Simulated Gain	Measured Gain
5			-10.5	-15
6	-12.2	-15	-1.34	-3
7	-7.2	-9	-8.07	-9
8	-5.2	-7.1	-11.3	-12.5
9	-4.6	-5.2	-10.8	-11.7
10	-3	-2	-7.1	-8
11	-1.8	-2.5	-2.45	-3
12	-0.5	-1	2.45	1.8

8.4.3.3. Additional Observations

As an additional observation, the unit cell length is varied and t is argued that increase in the unit cell length increases the number of passbands as well as stopbands. This in turn would lead to reduced bandwidth for the leaky wave antennas designed using them. To demonstrate this effect, three different unit cell lengths are taken (19.2 mm, 38.4 mm and 57.6 mm). Stub lengths are kept same as in the dual band case. Stub widths are varied for obtaining optimal impedance matching. Optimal stub widths are indicated in Table below.

TABLE 8.4: OPTIMAL LINE AND STUB WIDTHS FOR DIFFERENT UNIT CELL LENGTHS

Unit cell length (mm)	Line width (mm)	Stub width (mm)
19.2	2.2	2
38.4	1.1	1.6
57.6	1.6	1.8

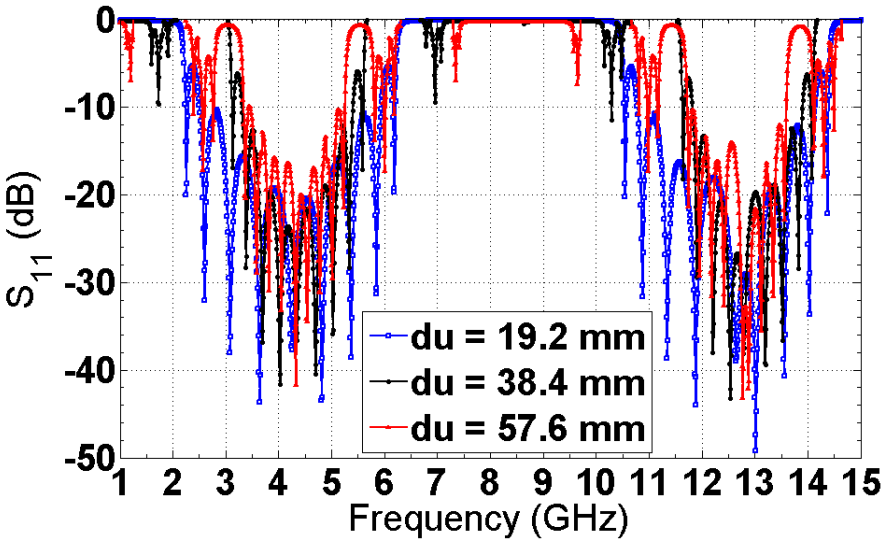

Fig. 8.40: Simulated S_{11} (Matlab) vs. frequency for dual band geometry using different unit cell lengths

Fig. 8.40 shows the variation of S_{11} with frequency for these three cases. It can be observed that the geometries with longer unit cell lengths yield smaller pass band bandwidth.

We would like to reflect on one limitation of the design guidelines presented here though. A simplifying assumption has been made regarding the identical stub lengths and width. Primary reason for such assumption is simplicity and ease of calculation for a robust starting point for leaky wave antenna design.

Assuming $d_{oc}=d_{sc}$ and $W_{sc}=W_{oc}$ leads to only two unknowns. Using (8.15) and the condition that $|(Z_B-Z_0)|$ should be minimized near the Bragg frequency under consideration helps in solving these two unknowns completely. On the other hand, if we used stubs of different lengths or widths or both, we would have needed more conditions. These could of course be generated by imposing additional criteria on impedance bandwidth i.e. minimizing $|(Z_B-Z_0)|$ at several frequencies instead of just one. However, these would turn this simple design guideline into a very rigorous optimization routine and would thus lose its applicability in providing a simple starting point for designing leaky wave antennas. This simplification brings forth some limitations to the design guidelines though. Fig. 8.41 shows the calculated S_{11} vs. frequency plot for three different cases of the single band antenna. In these three structures, the open and shorted stub lengths are made unequal and it is observed that the asymmetry in stub lengths lead to somewhat increase in the impedance bandwidth of the antenna. Three cases shown in the figure along with the impedance bandwidths achieved are summarized in Table 8.5 below.

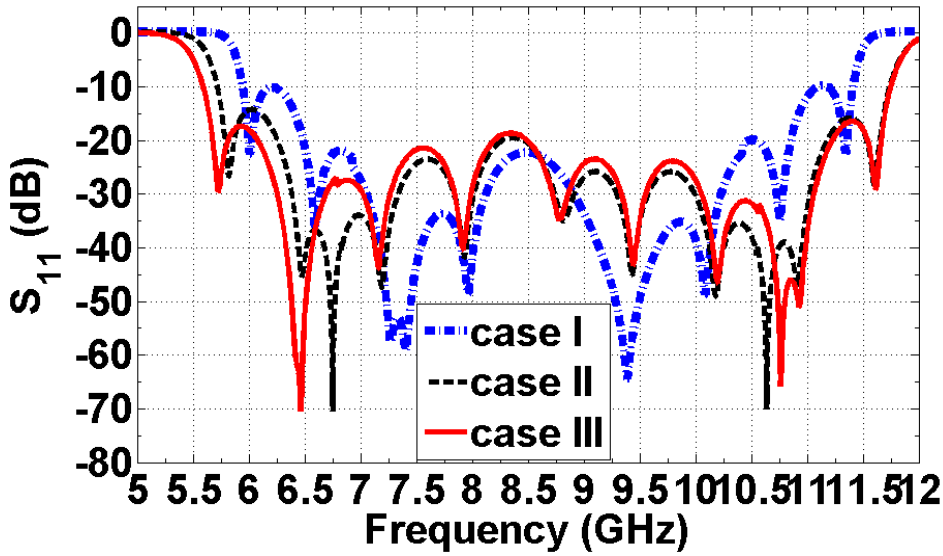

Fig. 8.41: S_{11} vs. frequency for the single band antenna for different stub length combinations

Table 8.5: Comparison of Impedance bandwidth for various stub length combinations

Case	Open stub length (mm)	Shorted stub length (mm)	Impedance bandwidth (GHz)	Other parameters
I	2.2	2.2	5.47	Stub width=line width=1 mm Substrate AD430 with 30 mils thickness
II	1.2	3.2	6.03	
III	0.2	4.2	6.16	

Observations presented in the previous section indicates that, operation closer to a stop band leads to possibility of very fast scanning (because of sharp variation in dispersion characteristics near a stop band) while operation away from a stop band and near the centre of the stop band gives rise to slower scanning. As can be seen from Table II, average scanning rate for the single band antenna is approximately 20^0/GHz below 8.5 GHz and 10^0-15^0/GHz above 8.5 GHz while that of the dual band antenna in the 1^{st} band is close to 40^0/GHz. Under practical scenarios, both fast scan and slow scan have requirements in different applications, For example, in Automotive radar [15] in vehicular applications, a faster scan is necessary while in frequency swept microwave imaging [16] and analog spectrogram [17], much better resolution is a requirement leading to necessity for greater scan sensitivity and in turn slower scan rate.

8.5 CONCLUSION

Several different non-resonant and resonant loads for microstrip line in both lumped and distributed configurations are considered in this chapter. Corresponding dispersion characteristics and the leaky fast wave regions are

observed. In most of the geometries the n= -1 and in some case at higher frequencies the m= -2 Floquet modes tend to enter the leaky region and radiate subsequently. However, it is the nature of the loading that presents interesting features in the antenna characteristics. Placement of a resonant frequency of the shunt resonator near a Bragg stopband tends to eliminate the corresponding stop band entirely thereby yielding a very wideband behavior. It is also observed that the radiation patterns near such an eliminated stop band tend to be of broadside nature. This proves to be a useful tool in design problems. Finally, these observations culminate in outlining systematic design guidelines for developing wideband, multiband and multi-beam leaky wave antennas. Results obtained using simulation is verified with data from practical measurement.

REFERENCES:

[1] M. Archbold, E. J. Rothwell, L. C. Kempel and S. W. Schneider, "Beam Steering of a Half-Width Microstrip Leaky-Wave Antenna Using Edge Loading," in *IEEE Antennas and Wireless Propagation Letters*, vol. 9, no. , pp. 203-206, 2010.

[2] D. K. Karmokar, Y. J. Guo, P. Y. Qin, K. P. Esselle and T. S. Bird, "Forward and Backward Beam-Scanning Tri-Band Leaky-Wave Antenna," in IEEE Antennas and Wireless Propagation Letters, vol. 16, pp. 1891-1894, 2017.

[3] D. Xie, L. Zhu and X. Zhang, "An EH_0-Mode Microstrip Leaky-Wave Antenna With Periodical Loading of Shorting Pins," in *IEEE Transactions on Antennas and Propagation*, vol. 65, no. 7, pp. 3419-3426, July 2017.

[4] D. Xie, L. Zhu, X. Zhang and N. Liu, "Gain-enhanced EH_1 mode microstrip leaky-wave antenna with periodical loading of shorting pins," in *IET Microwaves, Antennas & Propagation*, vol. 12, no. 2, pp. 230-236, 7 2 2018.

[5] D. K. Karmokar and K. P. Esselle, "Periodic U-Slot-Loaded Dual-Band Half-Width Microstrip Leaky-Wave Antennas for Forward and Backward Beam Scanning," in IEEE Transactions on Antennas and Propagation, vol. 63, no. 12, pp. 5372-5381, Dec. 2015

[6] D. K. Karmokar, K. P. Esselle and S. G. Hay, "Shifting the fixed-frequency beam scanning range of a leaky-wave antenna by slot loading," *2014 IEEE-APS Topical*

Conference on Antennas and Propagation in Wireless Communications (APWC), Palm Beach, 2014, pp. 640-643.

[7] D. K. Karmokar, K. P. Esselle and S. G. Hay, "Fixed-Frequency Beam Steering of Microstrip Leaky-Wave Antennas Using Binary Switches," in *IEEE Transactions on Antennas and Propagation*, vol. 64, no. 6, pp. 2146-2154, June 2016.

[8] J. Liu and Y. Long, "Analysis of a Microstrip Leaky-Wave Antenna Loaded with Shorted Stubs," in IEEE Antennas and Wireless Propagation Letters, vol. 7, pp. 501-504, 2008

[9] A. F. Harvey, Periodic and Guiding Structures at Microwave Frequencies, IRE Trans. Microw. Theory Tech., vol. 8, no. 1, pp. 30-61, January 1960.

[10] Pozar, David M. Microwave engineering. John Wiley & Sons, 2009

[11] W. J. R. Hoefer, "Equivalent Series Inductivity of a Narrow Transverse Slit in Microstrip," in *IEEE Transactions on Microwave Theory and Techniques*, vol. 25, no. 10, pp. 822-824, Oct. 1977.

[12] Nair, N.V. and Mallick, K., 1984. An analysis of a width-modulated microstrip periodic structure. *IEEE transactions on microwave theory and techniques*, *32*(2), pp.200-204.

[13] R. E. Collin, Foundations for Microwave Engineering, 2nd ed. NewYork: McGraw-Hill, 1992, ch. 8.

[14] M. E. Goldfarb and R. A. Pucel, "Modeling via hole grounds in microstrip," in *IEEE Microwave and Guided Wave Letters*, vol. 1, no. 6, pp. 135-137, June 1991.

[15] M. Ettorre, R. Sauleau, L. Le Coq and F. Bodereau, "Single-Folded Leaky-Wave Antennas for Automotive Radars at 77 GHz," in IEEE Antennas and Wireless Propagation Letters, vol. 9, pp. 859-862, 2010.Cd

[16] S. Li et al., "Study of Terahertz Superresolution Imaging Scheme With Real-Time Capability Based on Frequency Scanning Antenna," in IEEE Transactions on Terahertz Science and Technology, vol. 6, no. 3, pp. 451-463, May 2016.

[17] S. Gupta, S. Abielmona and C. Caloz, "Microwave Analog Real-Time Spectrum Analyzer (RTSA) Based on the Spectral–Spatial Decomposition Property of Leaky-Wave Structures," in IEEE Transactions on Microwave Theory and Techniques, vol. 57, no. 12, pp. 2989-2999, Dec. 2009.

Chapter 9

Conclusion

Contents	
	9.1 Overall summary of the thesis 9.2 Principal contributions 9.3 Future scope

9.1 OVERALL SUMMARY OF THE THESIS

The aim of this thesis is to present some analytical modeling tools for analyzing microstrip travelling wave antennas. These antennas have very interesting properties in terms of beam scanning with frequency and polarization agility. The simplicity of the beam scanning procedure is remarkable in comparison with the conventional phased array antennas where a much complicated feeding network is required. With the onset of 5G technology, antennas with wide bandwidth and beam steering abilities are becoming inseparable. In such a scenario, simple and approximate models within working precision are necessary. Full wave techniques can always be made toyield very accurate results but the cost is resource, time and physical insight.

Keeping these things in mind, we divided the thesis into two important parts: travelling wave antennas based on quasi TEM mode and higher order modes.

In Chapter 3, a transmission line based model is presented. This model is capable of analyzing the input characteristics as well as radiated far fields from any right angle bend based antennas. In calculating the radiated far field, we have

used a combination of both electric and magnetic current densities. This technique has the advantage over the conventional far field Green's function based technique in the fact that it can be applied to calculate the radiated near field from the antenna as well. Several geometries have been analyzed using the model and results seem to agree with both full wave simulation and practical measurements. In the later part of the chapter, an empirical formula for the bend reactance of non right angle bends is developed. This extends the transmission line model to acute and obtuse angle bend based geometries as well. Consequently, square loop line, Z line, zig-zag lines can now be analyzed using the transmission lie model.

In chapter 4, our objective is to investigate appropriate models for curved microstrip lines. First, a piecewise linear model is presented. Internal fields as well as radiated far fields from the line are calculated using the superposition principle. Since this model required greater number of segments when the curvature increase, consequently the analysis time required is increased. A transmission line model in the Serret-Frenet reference frame is presented next for calculation of the radiated far fields. Both these models proved to provide accurate results when the microstrip line harbors a quasi TEM mode. For microstrip lines supporting higher order modes, the transmission line model fails. A mode matching based technique is developed for such situations. In this sequential mode matching technique, the geometry is segmented into several piecewise circular segments and a mode matching procedure is applied at their interfaces. The source and the terminating load are modeled as boundary conditions. Performance of the three models is compared with simulation results as well as those from practical measurements wit good agreement.

Next in chapter 5, the problem of non uniform microstrip line is dealt with. First, a Fourier series based technique is presented for lines with smaller non uniformity supporting the fundamental quasi Tem mode of propagation. Propagation characteristics and a complete field solution are calculated. Radiated

far fields from the structure are calculated using the Serret-Frenet reference frame. Next, a mode matching based analysis is presented for non uniform lines with greater amount of non uniformity having the possibility of supporting higher order microstrip line modes. The non uniform line is segmented into several piecewise linear segments and a mode matching routine is applied at their interfaces. Radiated far fields from the structure are calculated by superposition of radiation from individual segments. Results obtained using the two models are validated against results from simulation as well as that from practical measurement.

A summary and comparison of the radiation mechanism of uniform and periodic leaky wave antennas are presented in chapter 6.

In chapter 7 a Floquet theorem based mode matching technique is applied to analyze periodic microstrip line with fundamental mode and higher order modes. The complete dispersion characteristics are evaluated and leaky regions are identified. Results are verified against simulation data and conventional ABCD matrix based technique.

Finally in chapter 8, effects of periodic loading on microstrip line are observed for corresponding leaky region. Several different kinds of lumped and distributed loads are considered. Finally, appropriate design guidelines for designing wideband, multiband a multi beam leaky wave antennas using open and shorted stub load microstrip line is presented.

9.2 PRINCIPAL CONTRIBUTIONS

- Development of a transmission line model suitable for travelling wave antennas based on bent microstrip lines.
- Development of a piecewise linear model, a transmission line model and a mode matching technique for analyzing curved microstrip lines.

- Development of a Fourier series based technique for microstrip lines with smaller non uniformity and a mode matching based technique when the non uniformity increases.

- Development of a Floquet theorem based mode matching technique for periodically loaded microstrip lines and based on the calculated dispersion characteristics outline some design guidelines for wideband and multi-beam leaky wave antennas.

9.3 FUTURE SCOPE

Several different open and potential areas have come up during the course of this work. These are outlined below:

- Travelling or leaky wave antennas require a great amount of length for potential radiation to occur from them. This makes fractals a natural choice. However, as the arms of the antenna come closer to each other in fractal geometry, the problem of mutual coupling creeps in. Modeling and controlling the effects of mutual coupling inside the transmission line problem would thus be a challenging task.

- Near field focusing using non uniform or curved leaky wave antenna is a very interesting topic of research in recent times. Efficient analysis of near fields from the antenna would thus allow one to appropriately reconfigure or control the focusing problem.

- The combination of Floquet theory and mode matching technique is a very efficient technique for analyzing the dispersion characteristics of periodically loaded planar line antennas. Application of this technique to analyze ladder lines, spur line and slot loaded microstrip lines would be interesting and fruitful if one could find them to be a suitable candidate for leaky wave antenna design.

Appendix

The Serret-Frenet Reference Frame

The Serret-Frenet Reference Frame: An orthogonal co-ordinate system for curved structures:

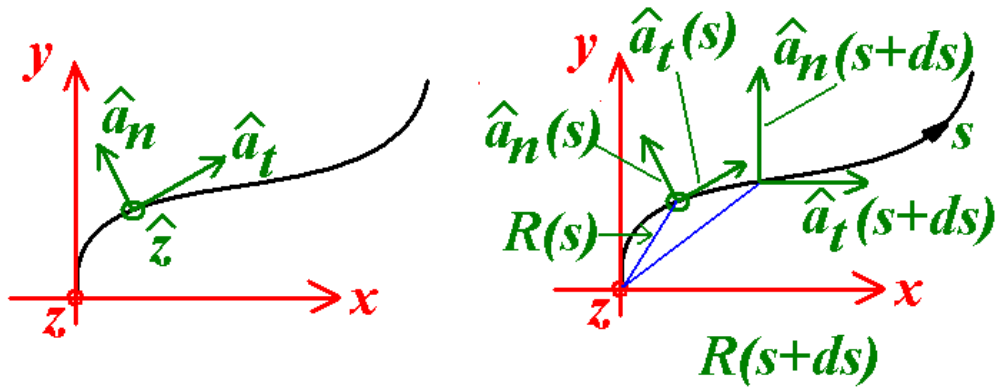

(a) (b)

Fig. A.1: The curved line with the dynamic co-ordinate system and (b) calculation of the unit vectors.

A co-ordinate system along the curve shown in Fig. A.1 is defined here and the corresponding unit vectors are derived.

We denote the unit vectors along and across the curve as $\hat{a}_t$ and $\hat{a}_n$ respectively. Now, $\hat{a}_t$ is calculated using the following formula

$$\vec{R}(\mathrm{s}+\mathrm{ds}) = \vec{R}(\mathrm{s}) + \hat{\mathrm{a}}_{\mathrm{t}}\mathrm{ds}$$
$$\hat{\mathrm{a}}_{\mathrm{t}} = \underset{ds\to 0}{Lt}\frac{\vec{R}(\mathrm{s}+\mathrm{ds}) - \vec{R}(\mathrm{s})}{ds} \tag{A.1}$$
$$\hat{\mathrm{a}}_{\mathrm{t}} = \frac{d\vec{R}}{ds}$$

Now we consider a planar space curve undulating on the xy plane. The parametric representation of the space curve can be expressed in the following manner:

$$x = g(t)$$
$$\mathrm{y} = \mathrm{h(t)} \tag{A.2}$$
$$\vec{R}(\mathrm{t}) = \mathrm{g(t)}\,\hat{\mathrm{i}} + \mathrm{h(t)}\,\hat{\mathrm{j}}$$

Here ‘t’ represents the parametric variable.

Now, unit vector tangential to the curved line can be written as

$$\hat{\mathrm{a}}_{\mathrm{t}} = \frac{d\vec{R}}{ds} \tag{A.3}$$

$$\hat{\mathrm{a}}_{\mathrm{t}} = \underset{ds\to 0}{Lt}\frac{(\vec{\mathrm{R}}(\mathrm{s}+\mathrm{ds}) - \vec{\mathrm{R}}(\mathrm{s}))}{ds}\frac{ds}{|(\vec{\mathrm{R}}(\mathrm{s}+\mathrm{ds}) - \vec{\mathrm{R}}(\mathrm{s}))|} \tag{A.4}$$

$$\hat{\mathrm{a}}_{\mathrm{t}} = \frac{g'(\mathrm{t})\,\mathrm{i} + \mathrm{h}'(\mathrm{t})\,\mathrm{j}}{\sqrt{g'^{2}(\mathrm{t})\,\mathrm{i} + \mathrm{h}'^{2}(\mathrm{t})\,\mathrm{j}}} \tag{A.5}$$

After calculation of $\hat{\mathrm{a}}_{\mathrm{t}}$, $\hat{\mathrm{a}}_{n}$ is calculated in a simple manner. For the space curve under consideration (Fig. A.1) the bi-normal vector is fixed and is equal to z. The following identities hold true:

$$\hat{\mathrm{a}}_{\mathrm{t}} \times \hat{\mathrm{a}}_{n} = \hat{z}, \quad \hat{z} \times \hat{\mathrm{a}}_{\mathrm{t}} = \hat{\mathrm{a}}_{n}. \tag{A.6}$$

Using the second relationship we obtain

$$\hat{\mathrm{a}}_{n} = \hat{z}\left\{\frac{-h'(\mathrm{t})\,\hat{\mathrm{j}} + g'(\mathrm{t})\,\hat{\mathrm{i}}}{|-h'(\mathrm{t})\,\hat{\mathrm{j}} + g'(\mathrm{t})\,\hat{\mathrm{i}}|}\right\} \tag{A.7}$$

This set of unit vectors are now utilized to calculate the dispersion

REFERENCES

[1] C. H. Tang, "An Orthogonal Coordinate System for Curved Pipes (Correspondence)," in *IEEE Transactions on Microwave Theory and Techniques*, vol. 18, no. 1, pp. 69-69, January 1970.

[2] Electromagnetic Waves and curved structures. Lewin L, Chang. David C, and Edward F Kuester. Peter Peregrinus.1977